Strong vortex pinning by natural linear defects in thin YBa$_2$Cu$_3$O$_{7-\delta}$ films

Sterke pinning van vortices door natuurlijke lijndefecten in dunne YBa$_2$Cu$_3$O$_{7-\delta}$ lagen

Strong vortex pinning by natural linear defects in thin YBa$_2$Cu$_3$O$_{7-\delta}$ films

ACADEMISCH PROEFSCHRIFT

ter verkrijging van de graad van doctor aan
de Vrije Universiteit Amsterdam,
op gezag van de rector magnificus
prof.dr. T. Sminia,
in het openbaar te verdedigen
ten overstaan van de promotiecommissie
van de faculteit der Exacte Wetenschappen
op dinsdag 26 februari 2002 om 13.45 uur
in de aula van de universiteit,
De Boelelaan 1105

door

Frodobertus Cornelis Klaassen

geboren te 's-Hertogenbosch

promotor: prof.dr. R.P. Griessen
copromotor: dr. B. Dam

Aan mijn ouders

Contents

i

Chapter 1

Introduction

1.1 Superconductivity

The phenomenon of superconductivity, discovered by Kamerlingh Onnes in 1911 [1], has ever since attracted a lot of attention both from a theoretical and a practical point of view. Theoretically, superconductivity poses an intriguing challenge due to its complexity as a macroscopic quantum phenomenon. Because of the phenomenon of zero resistivity the application of superconductors as strong magnets and other high current applications seemed to be very promising. However, the low critical temperature and the loss of superconductivity at relatively low current and magnetic field have been serious drawbacks for practical applications.

An enormous step forward was made in 1986 with the discovery of superconductivity in a LaBaCuO ceramic compound, with a critical temperature $T_c = 30$ K [2]. The discovery of superconductivity in this new class of materials, the cuprates, triggered a large boost of research on superconductivity. Soon the first superconductor with a T_c above the boiling point of nitrogen was found, namely $YBa_2Cu_3O_{7-\delta}$ with $T_c = 92$ K [3]. The high critical temperature, attainable by (inexpensive) cooling with liquid nitrogen, would make widespread applications within reach. Unfortunately, a lot of material problems still need to be resolved, before high-T_c superconductors can be easily implemented in large-scale applications. At present, large superconducting magnets are still mostly made from conventional superconductors, such as Nb_3Sn or NbTi.

The application of superconductivity carries in itself a strange paradox: it is closely related to applying high currents or large magnetic fields, but at the same time one of the essential characteristics of superconductors is the *expulsion* of magnetic flux, the Meissner effect [4]. Superconductors are forced to maintain a flux free interior, and therefore lose their superconducting properties at low magnetic fields already. However, in some superconductors (type-II superconductors, to which also the high-T_c cuprates belong) topological defects with locally suppressed superconductivity are formed above a certain magnetic field H_{c1}. These defects are called vortices. They consist of a (non-superconducting) core of typical size ξ, the coherence length, and surrounding supercurrents, falling off in strength over a typical length λ, the pene-

tration depth. Each vortex carries a quantized amount of flux $\Phi_0 = 2.07 \cdot 10^{-15}$ Wb, which implies that the magnetic induction $B = n_v \Phi_0$, with n_v the vortex density. The superconductor is now in a mixed phase, made up of material in the normal state carrying magnetic flux (the vortices), surrounded by superconducting material with zero resistivity. As soon as the vortex cores start to overlap, at the upper critical field $H_{c2} \sim 1/\xi^2$, the material is fully normal and superconductivity is lost. As the penetration of flux starts at a magnetic field $H_{c1} \sim 1/\lambda^2$, the size of the mixed phase ($\sim H_{c2}/H_{c1}$) is determined by the quotient of the penetration depth and the coherence length $\kappa \equiv \lambda/\xi$, which is called the Ginzburg Landau parameter. All cuprate superconductors have a large κ and, consequently, a large mixed phase region. For YBa$_2$Cu$_3$O$_{7-\delta}$ the Ginzburg Landau parameter $\kappa \approx 100$, with a field of first penetration $\mu_0 H_{c1} \approx 0.04$ T[1], and an upper critical field $\mu_0 H_{c2} \simeq 150$ T. In figure 1.1 the $B - T$ phase diagram of a type-II superconductor is depicted schematically.
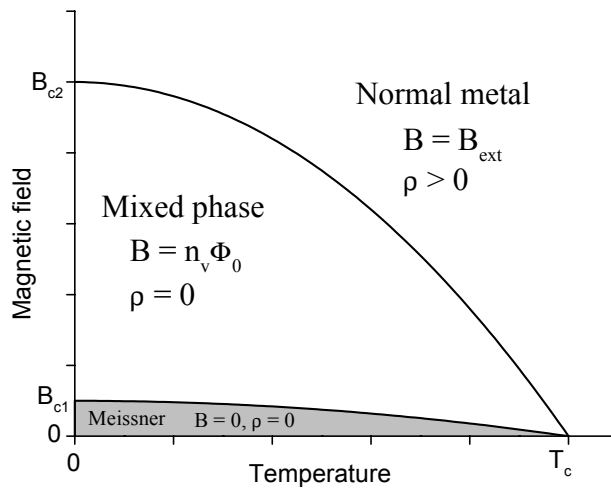
Figure 1.1: $B - T$ phase diagram of a type-II superconductor. At low magnetic fields the superconductor is completely flux-free (Meissner state). At magnetic fields $\mu_0 H > B_{c1}$ flux penetrates in the form of vortices. As each vortex carries a quantized amount of flux, the magnetic induction determines the vortex density n_v. The resistivity in the mixed phase $\rho = 0$ as long as the applied current density $j < j_c$, the critical current density. At $\mu_0 H = B_{c2}$, the upper critical field, the vortex cores start to overlap, and the material becomes normal.

---

[1]Due to demagnetization the field of first penetration in thin films is, however, much smaller.

For most applications of superconductivity it is essential to prevent vortex motion. Since vortices carry magnetic flux, moving vortices generate an electric field and therefore cause dissipation. In a completely defect-free superconductor, vortices will move due to the Lorentz force as soon as a current is applied. However, material defects may locally suppress superconductivity. At these preferential sites vortices are *pinned*. As long as the pinning force of the defect is larger than the Lorentz force acting on the vortex, the applied current runs through the superconductor without resistivity. The *critical* current density j_c, defined as the current density where the pinning force and the Lorentz force are equal, determines the onset of resistivity.

In type-II superconductors with an externally applied current there is thus a subtle, but fundamental difference between the thermodynamic superconducting phase, and the phenomenological feature of zero resistivity, as the latter is determined by the *pinning* of vortices. A good understanding of the vortex properties is of great importance, since vortex pinning determines the critical current. One can choose two different approaches. On the one hand we have the thermodynamic approach, i.e. a description of the general features of the vortex phase diagram and vortex phase transitions. This research has lead to a rich world of vortex phases, including various glass phases, vortex solid and vortex liquid phases [5]. On the other hand one can choose to identify vortex pinning in connection with the defect structure and describe in detail the pinning characteristics. This approach we take in the present thesis.

Specifically we investigate the *intrinsic* pinning mechanism of $YBa_2Cu_3O_{7-\delta}$ thin films. The reason for this choice is, that thin films of $YBa_2Cu_3O_{7-\delta}$ show very high critical current densities, in the order of $j_c = 10^{11} - 10^{12}$ Am^{-2} at $T = 4.2$ K. This is close to the thermodynamic limit, given by the depairing current $j_0 = 4 \cdot 10^{12}$ Am^{-2}, which indicates that a very efficient pinning mechanism must be present.

1.2 Vortex pinning mechanisms

To identify what kind of defect is responsible for the observed high current densities in thin $YBa_2Cu_3O_{7-\delta}$ films is not straightforward, because thin films contain many defects of various kinds. The different pinning centers can be divided into four main groups: point defects, linear defects, planar defects and thickness modulations. They are schematically depicted in figure 1.2.

1. Point defects, such as oxygen vacancies or interstitials are small, but densely distributed. Many defects collectively pin a vortex, but due to the randomly directed pinning forces, the total pinning force of the ensemble of point defects is much smaller than the sum of the individual pinning forces. Furthermore a straight vortex deforms in order to find as much (and as strong) pinning sites as possible and thus pays elastic energy. The balance between the total pinning energy on one hand, and the elastic energy plus Lorentz force on the other hand determines the size of the critical current density, which for $YBa_2Cu_3O_{7-\delta}$ single crystals is of the order of $j_c \simeq 10^9$ Am^{-2}. The theory of weak collective pinning accurately describes vortex pinning by small point defects [6] (see also
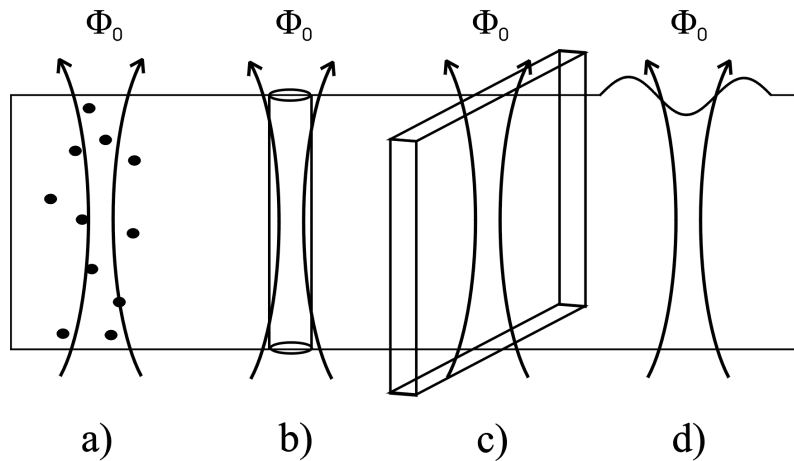
Figure 1.2: Schematic illustration of various pinning centers. The vortex is indicated by the magnetic field lines and is pinned by a) many point defects, b) a linear defect, c) a planar defect and d) surface roughness, which reduces locally the thickness of the film.

the extensive review by Blatter *et al.* [5]). Extended point defects, such as secondary phases, provide for stronger pinning energy but they are also less abundant [7].

2. Linear defects form potentially the most efficient pinning source, when the size of the defect coincides with the vortex, and when the defect is aligned with the applied magnetic field. In other words, when a vortex nicely "fits" inside a linear defect, it is optimally pinned over its full length. In single crystals the intrinsic density of linear defect is quite low, but it can be artificially enhanced by heavy-ion irradiation. The irradiation damage produces columnar tracks with a very strong pinning capacity. Consequently, the critical current density in irradiated single crystals increases by orders of magnitude [8].

   In thin films natural linear defects are found to be aligned along the c-axis with a density of $n_{disl} \approx 10 - 100 \ \mu\text{m}^{-2}$. It has been suspected for a long time, that a particular type of linear defects (screw dislocations) is responsible for the large intrinsic current density of thin $\text{YBa}_2\text{Cu}_3\text{O}_{7-\delta}$ films [9, 10]. In this thesis we will show that *all* linear defects (both screw and edge dislocations) have to be taken into account to explain the high critical current in thin $\text{YBa}_2\text{Cu}_3\text{O}_{7-\delta}$ films [11].

3. Planar defects, such as twin boundaries or grain boundaries, are effective in pinning vortices perpendicular to the plane of the defect only, whereas they form channels for easy flux flow along the plane [12].

This results in a highly anisotropic pinning force and critical current density [13]. The most important planar defects are twin and grain boundaries. Twin boundary pinning has been seen mainly in single crystals [14]. Grain boundaries are often formed in films deposited on polycrystalline substrates. When describing grain boundary pinning, one can define two critical currents, namely the *intra*grain critical current and the *inter*grain critical current. The former runs locally inside the grains and is usually larger, whereas the intergrain critical current is limited by the weak coupling between adjacent grains. Especially in tapes, used as high current carriers, grain boundaries limit the critical current.

Some models, describing vortex pinning in thin $YBa_2Cu_3O_{7-\delta}$ films, assume grain boundary pinning [16]. However, we never found any evidence for weak links between the growth islands in thin $YBa_2Cu_3O_{7-\delta}$ films.

4. A fourth pinning mechanism is formed by thickness modulations. Thin films of $YBa_2Cu_3O_{7-\delta}$ have a rough surface, i.e. they exhibit thickness modulations. Since a vortex wants to minimize its total length, thickness variations may form an additional source of pinning, eventually in combination with other material defects.

In this thesis we describe vortex pinning in thin superconducting $YBa_2Cu_3O_{7-\delta}$ films. By carefully examining the defect structure of $YBa_2Cu_3O_{7-\delta}$ thin films, in relation to the behaviour of the critical current density, we will prove that natural linear defects are the most dominant pinning source in $YBa_2Cu_3O_{7-\delta}$ thin films. In the second part of this thesis we describe the general features of linear defect pinning and the effect of i) temperature, ii) magnetic field and iii) film thickness on the vortex pinning properties of thin $YBa_2Cu_3O_{7-\delta}$ films.

1.2.1 Determination of the pinning properties

A serious drawback in the investigation of vortex pinning is, that essential pinning parameters, such as the critical current density and the pinning energy are not directly accessible within experiment. This is due to the hopping of vortices over their pinning barriers, a phenomenon known as vortex creep. This hopping is predominantly a thermally activated process at temperatures $T \gtrsim 10$ K, whereas at lower temperatures vortex hopping takes place via quantum creep [17]. Schematically we can picture the situation as follows (figure 1.3): a vortex is pinned by a defect with pinning energy U_c. When a current is applied, the pinning potential is tilted due to the Lorentz force exerted on the vortex. Without activated process the critical current density j_c is reached, when the pinning force $F_p = dU_c/dx \mid_{\max}$ equals the Lorentz force. However, in reality thermal activation causes vortex movement already at lower currents. The chance for a vortex to jump over the activation barrier is given by $P \propto \exp(-U(j)/k_BT)$, with the activation energy $U(j)$ a function of the applied current density j, the true critical current density j_c and the pinning energy U_c. The *measured* current density j_s corresponds to the current density at which the activation barrier $U(j)$ is comparable to the thermal energy of the vortex. It is thus
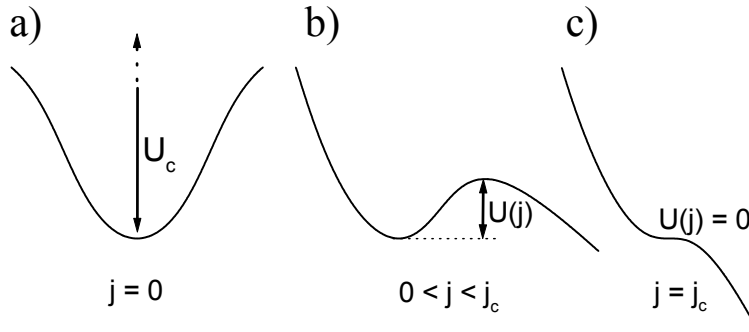
Figure 1.3: Due to thermal activation the measured current density j_s is smaller than the true critical current density j_c. a) When no current is applied the pinning potential is undistorted and a vortex is pinned with pinning energy U_c. b) Due to an external current j the pinning potential is tilted by the Lorentz force. An activation barrier $U(j)$ develops, which depends on j. As soon as $U(j)$ is comparable with the thermal energy of the vortex, at a certain current density $j = j_s < j_c$, the vortex can hop over the barrier. c) When the applied current density equals the critical current density, the activation barrier just disappears and the vortex depins without activation. Experimentally, this situation never occurs, since a vortex is always driven by either quantum or thermal fluctuations.

always smaller than the *critical* current density j_c. A proper measure for the activated motion of vortices is the magnetic relaxation rate, which can be measured directly. From the measurement of the current density j_s and the relaxation rate Q, we can set up a method to derive the pinning energy U_c and the critical current density j_c. Naturally this inversion method depends on the assumptions made regarding the pinning mechanism and activation model. Note, that for thin films the relaxation rate is measured dynamically, i.e. $Q \equiv d\ln j_s/d\ln(dB/dt)$, whereas in many studies, especially of single crystals, the conventional (or time) relaxation $S \equiv d\ln j_s/d\ln t$ is used. Both parameters are essentially equivalent [18].

1.3 YBa$_2$Cu$_3$O$_{7-\delta}$ thin films as a model system

Linear defect pinning in thin films is directly comparable to pinning by amorphous columnar tracks, formed by irradiating single crystals with heavy ions. The irradiation damage forms columnar tracks of typically 3-5 nm radius, which is somewhat larger, but comparable to the size of natural linear defects in thin films. But also in other

systems the linear extension of the pinning centers is characteristic, for example in antidot films, which have a regular array of large holes [19, 20]. Although natural linear defects are much smaller than antidots, their lateral distribution is more or less regular, as in antidot films, because the linear defects are situated in the trenches between growth islands. As a result natural linear defects show for example clear matching effects, more profound than in heavy-ion irradiated single crystals, in which the columnar tracks are distributed completely random. On the other hand, due to its size a natural defect can pin at most one vortex, whereas antidots usually accommodate tens of vortices.

A great advantage of natural linear defects is, that the defect itself is well-defined. For example, collateral damage in the form of dense point defects as a result of heavy-ion irradiation is absent. The possibility to change the linear defect density opens new ways for investigating vortex pinning by linear defects on a fundamental basis. As Huijbregtse showed, one can even stimulate the formation of linear defects by depositing small Y_2O_3 precipitates on the substrate prior to the film deposition [21]. With this technique the linear defect density can be increased even further, or one can, for example, play with the distribution of linear defects.

In chapter 7 we investigate the implications of the film thickness for the critical current density, which links to the maximum attainable critical current in for example tapes. Thick superconducting films on flexible metallic substrates are currently being developed for high current applications. Apart from an enhanced mosaic spread of the constituent grains, which reduces the intergrain current, these tapes are characterized by a superconducting layer thickness of several microns. Our results show that vortices in thick films are probably bent due to the self-field, while the current primarily runs at the surface and at the film-substrate interface. Effectively this reduces the total critical current. Whereas at the moment the critical current in tapes is limited due to the mosaic spread of the constituent grains, in the long run vortex bending from linear defects due to self-fields may become the limiting factor for developing tapes sustaining larger critical currents.

1.4 Outline of this thesis

This thesis forms the second part of a joint research of the Solid State Physics group at the Vrije Universiteit about the relationship between the defect microstructure of thin $YBa_2Cu_3O_{7-\delta}$ films and the vortex pinning properties. The first thesis, by Jeroen Huijbregtse [22], focussed on the deposition and *material properties* of $YBa_2Cu_3O_{7-\delta}$ thin films. In this thesis the strong *pinning properties* in thin $YBa_2Cu_3O_{7-\delta}$ films are described.

Specifically we investigate vortex pinning by means of torque magnetometry and magneto-optical imaging. In chapter 2 we explain the experimental technique to measure the current density and the relaxation rate in thin superconducting films, and the preparation of $YBa_2Cu_3O_{7-\delta}$ thin films. In chapter 3 we show that the density of *linear defects* in thin $YBa_2Cu_3O_{7-\delta}$ films is closely related to the pinning properties. We find that the current density is constant up to a characteristic magnetic field B^*,

which scales with the dislocation density n_{disl}. It is for the first time that an explicit quantitative relation is found, proving that linear defects are the most dominant pinning centers in $YBa_2Cu_3O_{7-\delta}$ films. Recently it was confirmed by magnetic force microscopy, an imaging technique enabling a direct visualization of vortices, that the vortices are indeed situated inside the trenches between growth islands, where the linear defects are located [23].

After establishing the importance of linear defects, we continue to describe the characteristics of linear defect pinning, both theoretically and experimentally. In chapter 4 we extend the Bose-glass theory [24] to calculate the general pinning potential for linear defects. Our calculation is not only valid in limiting cases, i.e. when the vortex is either much smaller or much larger than the linear defect, but also when vortex and defect are comparable in size, as is the case for $YBa_2Cu_3O_{7-\delta}$ thin films. Additionally we calculate explicitly the temperature dependence and the effect of thermal fluctuations on the pinning potential and on the critical current density.

The characteristic features of vortex pinning by natural linear defects are described in chapter 5, in terms of the critical current density, the relaxation rate and the pinning energy. We show, that the temperature dependence of the critical current below B^* is in accordance with linear defect pinning. Furthermore we find, that half-loop excitations form the most probable elementary vortex excitations at low magnetic fields, explaining the pinning energy $U_c \approx 600$ K. At high magnetic fields the current density decreases according to a power law, with a slope depending on the linear defect density. Our results provide a preliminary framework, predicting how the critical current density can be optimized specifically at high temperatures ($T \simeq 77$ K) and high magnetic fields ($\mu_0 H \simeq 1$ T).

In chapter 6 flux penetration in ring-shaped thin films is studied by means of magneto-optics. Due to the specific ring-shape, the penetration of flux shows highly peculiar features during first penetration and immediately after reverting the sweep direction in a hysteresis loop. Furthermore we can separate the penetration field from the characteristic field B^*, and show that the Bean model is valid in thin films as well.

Finally, in chapter 7, the effect of post-annealing and the film thickness on the pinning properties is investigated. Post-annealing has a profound influence on the surface morphology, but the pinning properties are still related to the linear defect lattice. This indicates, that pinning by surface roughness is negligible compared to linear defect pinning. For films with thickness $d > 150$ nm, vortex bending reduces the total critical current, and the current runs primarily in a small layer at the surface and the film-substrate interface. Secondly vortex bending causes an asymmetry in the magnetic hysteresis loop, due to the formation of Meissner areas within the film.

References

[1] H. Kamerlingh Onnes, Leiden Comm. **120b**, **122b**, **124c** (1911)

[2] J.G. Bednorz and K.A. Müller, Z. Phys. B **64**, 189 (1986)

[3] M.K. Wu, J.R. Ashburn, C.J. Torng, P.H. Hor, R.L. Meng, L. Gao, Z.J. Huang, Y.Q. Wang, and C.W. Chu, Phys. Rev. Lett. **58**, 908 (1987)

[4] W. Meissner and R. Ochsenfeld, Naturwissenschaften **21**, 787 (1933)

[5] G. Blatter, M.V. Feigel'man, V.B. Geshkenbein, A.I. Larkin, and V.M. Vinokur, Rev. Mod. Phys. **66**, 1125 (1994)

[6] I.A. Larkin, Zh. Eksp. Teor. Fiz. **58**, 1466 (1970),
I.A. Larkin and Yu.N. Ovchinnikov, J. Low Temp. Phys **34**, 409 (1979)

[7] J.M. Huijbregtse, F.C. Klaassen, A. Szepielow, J.H. Rector, B. Dam, R. Griessen, B.J. Kooi, and J.Th.M. de Hosson, Supercond. Sci. Technol. **15**, 1 (2002)

[8] For a review, see L. Civale, Supercond. Sci. Technol. **10**, A11 (1997), and references therein

[9] M. Hawley, I.D. Raistrick, J.G. Beery, and R.J. Houlton, Science **251**, 1587 (1991)

[10] J. Mannhart, D. Anselmetti, J.G. Bednorz, A. Catana, Ch. Gerber, K.A. Müller, and D.G. Schlomm, Z. Phys. B **86**, 177 (1992)

[11] B. Dam, J.M. Huijbregtse, F.C. Klaassen, R.C.F. van der Geest, G. Doornbos, J.H. Rector, A.M. Testa, S. Freisem, J.C. Martínez, B. Stäuble-Pümpin, and R. Griessen, Nature **399**, 439 (1999), and chapter 3 of this thesis

[12] R.J. Wijngaarden, R. Griessen, J. Fendrich, and W.-K. Kwok, Phys. Rev. B **55**, 3268 (1997)

[13] A. Gurevich and L.D. Cooley, Phys. Rev. B **50**, 13563 (1994)

[14] I. Maggio-Aprile, Chr. Renner, A. Erb, E. Walker, and Ø. Fischer, Nature **390**, 487 (1997)

[15] D. Dimos, P. Chaudhari, and J. Mannhart, Phys. Rev. B **41**, 4038 (1990)

[16] E. Mezzetti, R. Gerbaldo, G. Ghigo, L. Gozzelino, B. Minetti, C. Camerlingo, A. Monaco, G. Cuttone, and A. Rovelli, Phys. Rev. B **60**, 7623 (1999),
G. Ghigo, A. Chiodoni, R. Gerbaldo, L. Gozzelino, E. Mezzetti, B. Minetti, C. Camerlingo, G. Cuttone, and A. Rovelli, Supercond. Sci. Technol. **12**, 1059 (1999),
E. Mezzetti, A. Chiodoni, R. Gerbaldo, G. Ghigo, L. Gozzelino, B. Minetti, C. Camerlingo, and A. Monaco, Physica C **332**, 115 (2000)

[17] A.C. Mota, A. Pollini, P. Visani, K.A. Müller, and J.G. Bednorz, Phys. Rev. B **36**, 4011 (1987),
A.F.Th. Hoekstra, A.M. Testa, G. Doornbos, J.C. Martínez, B. Dam, R. Griessen, B.I. Ivlev, M. Brinkmann, K. Westerholt, W.K. Kwok, and G.W. Crabtree, Phys. Rev. B **59**, 7222 (1999)

[18]   A.J.J. van Dalen, M.R. Koblischka, and R. Griessen, Physica C **259**, 157 (1996)

[19]   M. Baert, V.V. Metlushko, R. Jonckheere, V.V. Moshchalkov, and Y. Bruynser-
       aede, Phys. Rev. Lett. **74**, 3269 (1995),
       V.V. Moshchalkov, M. Baert, V.V. Metlushko, E. Rosseel, M.J. van Bael, K.
       Temst, R. Jonckheere, and Y. Bruynseraede, Phys. Rev. B **54**, 7385 (1996)

[20]   A. Castellanos, R. Wördenweber, G. Ockenfuss, A. VonderHart, and K. Keck,
       Appl. Phys. Lett. **71**, 962 (1997)

[21]   J.M. Huijbregtse, B. Dam, R.C.F. van der Geest, F.C. Klaassen, R. Elberse,
       J.H. Rector, and R. Griessen, Phys. Rev. B **62**, 1338 (2000)

[22]   J.M. Huijbregtse, *Growth, Defect Structure and Critical Currents in*
       $YBa_2Cu_3O_{7-\delta}$ *Thin Films*, PhD-thesis, Vrije Universiteit (2001)

[23]   A. Volodin, K. Temst, C. van Haesendonck, Y. Bruynseraede, M.I. Montero,
       I.K. Schuller, B. Dam, and R. Griessen, to be published in Physica C

[24]   D.R. Nelson and V.M. Vinokur, Phys. Rev. B **48**, 13060 (1993)

Chapter 2

Experimental techniques

To investigate the pinning properties of vortices in thin $YBa_2Cu_3O_{7-\delta}$ films we use capacitive torque magnetometry. This technique yields an accurate quantitative measurement of the global magnetic moment, which we measure as a function of temperature and applied magnetic field. From the magnetic moment we directly determine the superconducting current density $j_s(B,T)$ and the dynamical relaxation rate $Q(B,T)$. These two parameters contain all pinning information and can be used to determine the critical current density $j_c(B,T)$ and the pinning energy $U_c(B,T)$, by applying an appropriate model. We explain the basic principles of capacitive torque magetometry, the design of our torquemeters and the measurement setup, capable of measuring over the whole temperature range from 1.7 K up to 300 K, and in magnetic fields up to 7 T. Furthermore we present the microstructural details and the basic superconducting properties of our thin $YBa_2Cu_3O_{7-\delta}$ films, deposited by pulsed laser ablation.

2.1 Introduction

There are various techniques to measure the magnetic properties of high-T_c super-conducting films. We can divide the different techniques roughly into two categories: methods to obtain *global* information, such as torque magnetometry [1, 2], ac-susceptibility [3, 4, 5], vibrating sample magnetometry (VSM) [6, 7], and dc SQUID magnetometry [8, 9], and methods that give a *local* picture of the magnetic properties, such as scanning SQUID magnetometry [10], magneto-optical imaging [11, 12] and Hall-probe measurements [13, 14].

In this thesis we measure the superconducting current density and the relaxation rate by means of capacitive torque magnetometry, a technique originally developed to study the Haas-van Alphen effect and the magnetorestriction of the Fermi-surface in pure metals [15]. Torque magnetometry makes use of the fact that a torque is exerted by a sample when the applied magnetic field and the magnetic moment are not aligned, for example due to vortex pinning. The measurement technique is non-invasive and inductive, so contact-free. The latter point is an advantage in thin films, because films exhibit very large critical currents, especially at low temperatures (up to 10^{12} Am^{-2} in YBa$_2$Cu$_3$O$_{7-\delta}$ thin films). Electrical contacts in transport measurements thus have to withstand very large currents, which puts high demands on the quality of the contacts, and secondly causes problems of self-heating. Inductive techniques obviously do not suffer from this problem. Moreover torque magnetometry is flexible, since the sensitivity of the torquemeter can be changed easily by changes in design and material. This makes the technique suitable for investigating tiny single crystalline samples, for which extremely sensitive micro-torquemeters have been designed with a resolution up to 10^{-14} Nm [16]. At the same time the large critical currents in thin YBa$_2$Cu$_3$O$_{7-\delta}$ films (exerting torques of typically 10^{-4} Nm) can be easily measured. A drawback of torque magnetometry is, that the torque vanishes at zero magnetic field, which makes it hard to determine the current density at very low magnetic fields. A second drawback is that it is a global technique in the sense that it measures the total magnetic moment of a sample. Small imperfections and local variations in the sample are therefore not observed. To obtain a picture of the *local* field distribution, magneto-optical imaging, which is used in our laboratory as well, is a good alternative. However, to determine the magnitude of the current density from a magneto-optical image, one has to perform a rather complicated inversion [17, 18, 19], and the results are less accurate than in torque magnetometry. Both techniques are therefore in many respects complementary, torque magnetometry giving very accurate, but global, quantitative results, whereas magneto-optics yields local information about the field and current distribution, and also about flux penetration. In this chapter we describe the details of torque magnetometry, the measurement setup and the preparation of superconducting YBa$_2$Cu$_3$O$_{7-\delta}$ thin films. First the basic principles of torque magnetometry are explained. Next we give a description of the torquemeter and the cryomagnetic setup. In the last section we give the details of the deposition of the superconducting YBa$_2$Cu$_3$O$_{7-\delta}$ films and about the general microstructural properties of these films. In chapter 6 of this thesis both torque magnetometry and magneto-optics are used to investigate the penetration of flux in superconducting rings. The
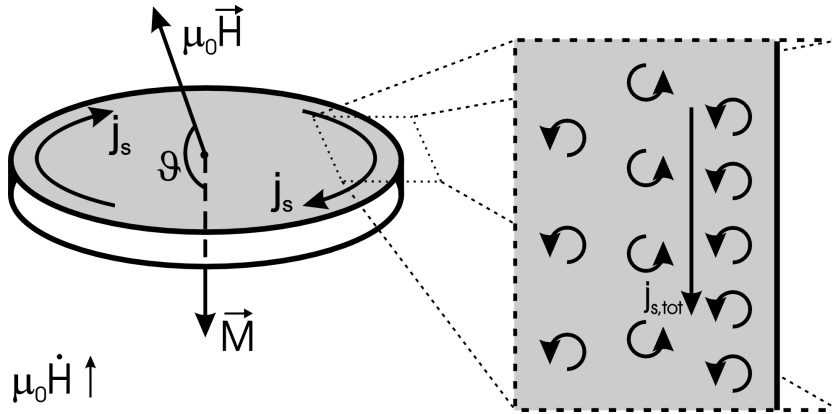
Figure 2.1: When sweeping the magnetic field with $\mu_0 dH/dt > 0$, vortices nucleate at the border of the disk and are pushed inside. This results in a vortex density gradient creating a net supercurrent j_s running concentrically around the disk and setting up the magnetic moment $\vec{M}$. Note that, in order to have a finite torque, one has to apply the magnetic field under an angle $\vartheta \neq 0, 180°$ with respect to the normal to the film plane.

description of the magneto-optical setup is included there, since magneto-optics is used only in chapter 6.

2.2 Basic principles of torque magnetometry

When we place a superconducting sample in a magnetic field $\mu_0 \overrightarrow{H}$ under a specific angle and sweep the field with constant sweep rate $\mu_0 dH/dt$, superconducting currents are induced in the sample, which set up a magnetic moment $\overrightarrow{M}$ perpendicular to the plane in which the currents flow. A torque is exerted, given by [20]:

$$\overrightarrow{\tau} = \mu_0 \left(\overrightarrow{M} \times \overrightarrow{H} \right) \tag{2.1}$$

Because the superconducting current is *induced* by the sweeping of the magnetic field, it is obvious that the direction of the magnetic moment depends on whether the magnetic field is swept up or down. This seems a trivial consequence of Lenz' law, but it is easily overlooked, since it is implicit in equation (2.1), where the direction of $\overrightarrow{M}$ depends on the sweep direction. In a vortex picture we can illustrate what happens in the following way. If the magnetic field $\mu_0 H > B_{c1}$ is being increased, i.e. $\mu_0 dH/dt > 0$, more and more vortices enter the sample. They are nucleated at the border of a sample and pushed inside by the newly created vortices. This results in a gradient in the vortex density, depicted in figure 2.1. From the supercurrents
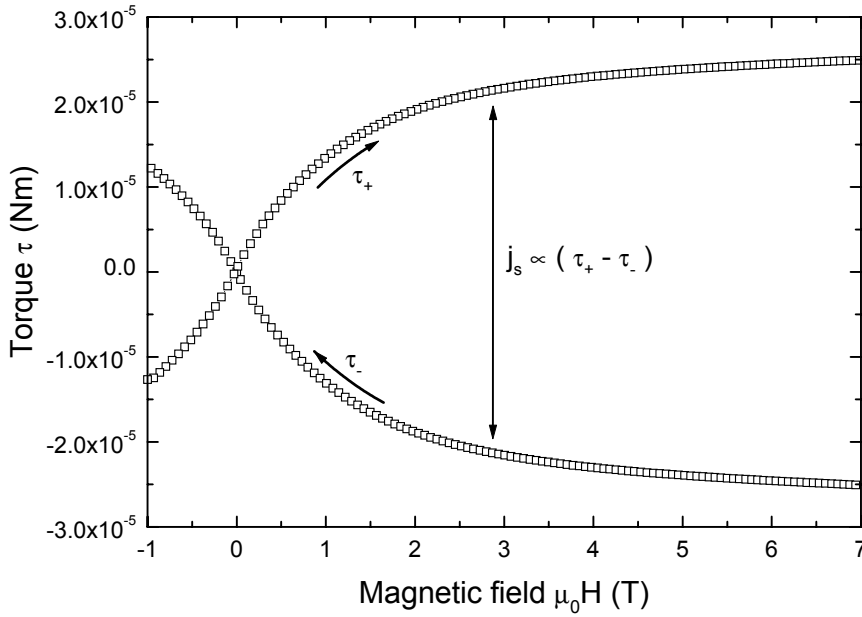
Figure 2.2: Typical torque hysteresis loop for a magnetic field sweep from $\mu_0 H = -1$ to 7 T. The width of the hysteresis is directly proportional to the superconducting current density j_s.

shielding the vortices we directly see that there is a net current setting up $\overrightarrow{M}$. When the field is being decreased, vortices escape from the sample, and the vortex density is largest inside the superconductor and smallest at the sides. The effect is, that the magnetic moment $\overrightarrow{M}$, and consequently the torque, are reversed in direction. We can therefore make hysteresis loops. As the size of the vortex density gradient depends on the pinning strength, the width of a magnetic hysteresis loop directly reflects the size of the critical current density.

Apart from the irreversible torque due to vortex pinning there is also a reversible torque contribution due to an anisotropy of the magnetic properties [21, 22]. This reversible torque, which in thin films is usually small compared to the irreversible torque, can be used in angle dependent measurements to determine the anisotropy constant γ [23] or, for example, to obtain the symmetry of the superconducting order parameter [24].

A typical example of a hysteresis loop is depicted in figure 2.2. From the irreversible torque $\tau_{irr} = (\tau_+ - \tau_-)/2$, with τ_+ the ascending and τ_- the descending branch of a magnetic hysteresis loop, we obtain $M_{irr} = \tau_{irr}/(\mu_0 H \sin \vartheta)$. The superconducting current density is directly proportional to the magnetic moment, depending only on a geometrical factor. Using the Bean critical state model [25], we find for the relation between the magnetic moment and the superconducting current density j_s:

$$M_{irr} = \frac{1}{4}a^2 d(b - a/3) \cdot j_s \tag{2.2}$$

$$M_{irr} = \frac{\pi}{3}d(r_o^3 - r_i^3) \cdot j_s \tag{2.3}$$

for rectangular and ring-shaped samples, respectively. In eqs. (2.2) and (2.3) d denotes the sample thickness, a and b the longer and shorter side of the rectangle, and r_o and r_i the outer and inner radius of the ring, respectively.

The measured superconducting current density j_s from a hysteresis loop is in general not the true critical current density j_c, i.e. the current density for which the pinning force and Lorentz force are equal. The difference is caused by magnetic relaxation of the vortex lattice due to thermally activated vortex hopping [26] or quantum creep [27]. In $YBa_2Cu_3O_{7-\delta}$ films the relaxation rate is typically a few percent at low magnetic fields and temperatures. The difference between j_s and j_c is a general experimental feature, also encountered in I-V measurements. The electric field associated with the induced current in a ring according to Faraday's law is:

$$E(R) = -\frac{\mathfrak{L}(R)d}{2\pi}\frac{\partial j}{\partial t} - \frac{R}{2}\frac{dB}{dt} \propto \frac{dB}{dt}, \tag{2.4}$$

with $\mathfrak{L}(r)$ the self-inductance of the ring, d the film thickness, and R the radius of the ring. Because $d \ll R$ the term with $\partial j/\partial t$ can be neglected. From eq. (2.4) we see that fixing a sweep rate corresponds exactly to choosing a certain voltage criterium as is usually done in I-V measurements to determine j_c.

The relaxation rate is usually determined by measuring the decay of the magnetic moment in time, after having stopped a field sweep. The normalized relaxation rate is then defined as:

$$S \equiv -\frac{d \ln j_s}{d \ln t} \tag{2.5}$$

There are, however, a few drawbacks in using this method to determine the relaxation rate in thin films. First of all the method is time consuming, since the relaxation, especially at low temperatures, is very slow. Secondly, because of the large demagnetization factor of a thin film, the penetration field is small. Therefore a small overshoot at the end of a field sweep causes dramatic changes in the microscopic field and current distribution, making it impossible to relate the measured magnetic moment to the current density, especially at short time scales. Since most of the relaxation takes place in the first few seconds after a field sweep has stopped, this overshoot seriously hampers an accurate measurement of the relaxation in thin films.
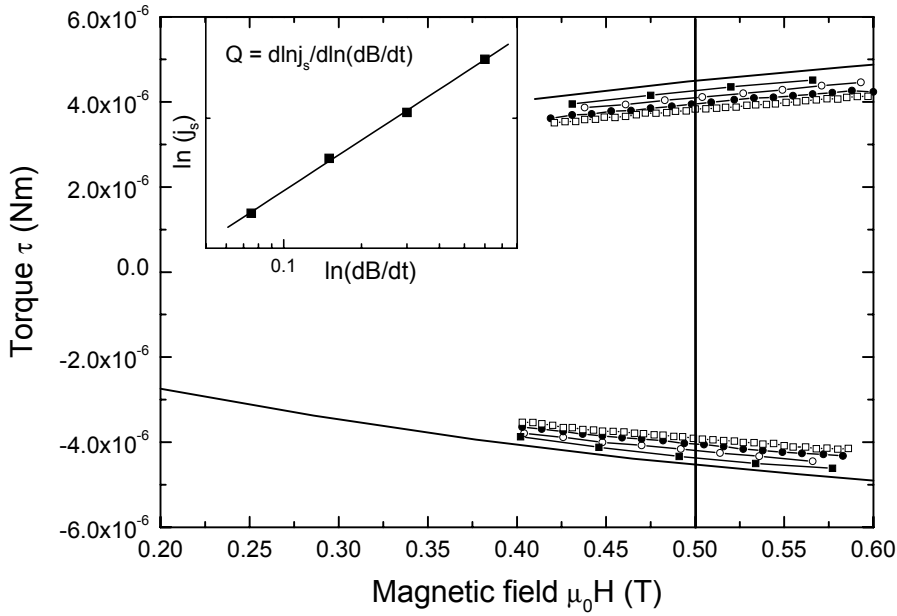
Figure 2.3: Hysteresis loop around $\mu_0 H = 0.5$ T with sweep rates (from outer to inner loop) $\mu_0 dH/dt = 40$ (solid line), 20 ($-\blacksquare-$), 10 ($-\circ-$), 5 ($-\bullet-$), and 2.5 ($-\square-$) mT/s. Inset: by plotting the hysteresis width versus the sweep rate on a double logarithmic scale, we obtain the dynamical relaxation rate Q.

One can conveniently avoid these problems, by making small hysteresis loops around a certain field, with ever decreasing sweep rates (see figure 2.3). Due to relaxation the width of the hysteresis loop decreases with decreasing sweep rate. We obtain the dynamical relaxation rate

$$Q \equiv \frac{\mathrm{d}\ln j_s}{\mathrm{d}\ln\left(\mathrm{d}B/\mathrm{d}t\right)} \tag{2.6}$$

by plotting the hysteresis against the sweep rate on a double logarithmic plot (inset of figure 2.3). The ring shape of our sample assures a well-defined, uniform relaxation rate. It was shown, both experimentally and theoretically, that both conventional and dynamical relaxation measurements essentially yield the same value for the relaxation [28].

Since $E(r) \propto \frac{dB}{dt}$ we find that making hysteresis loops, such as in figure 2.3, is in fact analogous to measuring *I-V* curves, and the slope of an *I-V* curve on a double logarithmic plot equals $1/Q$. The equivalence of torque and transport measurements was confirmed experimentally by Doornbos [29]. Note that the induced electric field in torque measurements is of the order of $10^{-4} - 10^{-5}$ Vm^{-1}, which is typically three to four orders of magnitude smaller than in transport measurements. Torque magnetometry thus provides useful technique to extend the window of *I-V* measurements by several decades. In this way *I-V* curves up to 14 (!) decades have been measured (see chapter 5 of ref. [29]).

2.3 The measurement setup

2.3.1 Design of the torquemeter

There are numerous ways to measure the torque, but in our setup it is measured by capacitance torque magnetometry [2]. The torquemeter consists of two or three capacitance plates. One of the plates, that carries the superconducting sample, can rotate via a spring system. When a torque is exerted by the sample, the plate with the sample bends slightly until the magnetic torque is counterbalanced by the mechanical torque of the springs. Since the capacitance depends on the distance between the plates, this bending results in a capacitance change ΔC. To first order, i.e. for not too large bending angles ϕ, the capacitance change is proportional to the torque $\Delta C \propto \phi \propto \tau$.

We used two different designs for our torquemeter, the two-plate and the three-plate geometry. The two-plate torquemeter (figure 2.4) consists of two U-shaped phosphorbronze plates, fixed on the circuit board with a clamping screw between teflon spacers. The capacitance plates are separated from each other by two glass spacers, leaving a distance between the two plates of $d \approx 0.4$ mm. This corresponds to capacitance of a few pF. The superconducting sample is glued with GE-varnish or vacuum grease on top of the second plate. In this geometry we measure directly the capacitance between the plates. The sensitivity of the torque meter can be changed by using capacitance plates of different thicknesses, ranging from 0.1 to 0.25 mm.

The three-plate torquemeter, depicted together with the rotation insert in figure 2.5, consists of two fixed copper plates on a printed circuit board, and one movable phosphorous-bronze plate. The movable plate with the sample is mounted with small bolts and ring spacers about 0.4 mm above the fixed plates. It has two U-shaped cuts that enables the plate to slightly rotate when a torque is exerted. The sensitivity of the torquemeter can be changed by varying the distance between the cuts, or the length over which the two cuts overlap.

There are a few advantages of the three-plate geometry over the two-plate capacitance torquemeter. First the system is more easy to assemble and disassemble, and secondly the design offers more flexibility in changing the sensitivity of the torquemeter.
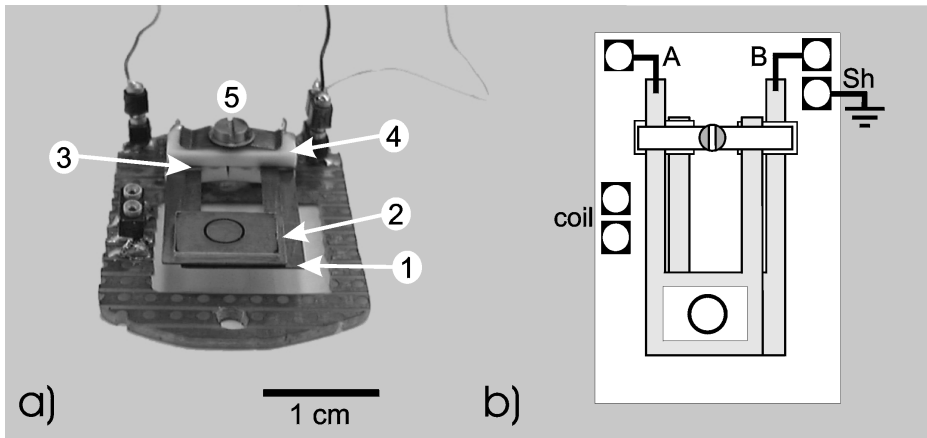
Figure 2.4: a) The two-plate torquemeter consists of a lower capacitance plate (1) and an upper plate with superconducting sample (2). They are separated from each other by glass spacers (3). The plates are mounted on the printplate with teflon spacers (4) and a clamping screw (5). b) Schematic view of the design with two connectors to both capacitance plates (A and B), shielding (Sh) and connections for the calibration coil.

This is the reason why we mostly worked with the three-plate torquemeter design. A third advantage is that the system is in mechanical and electrical equilibrium when no torque is exerted, whereas in the other torquemeter the upper plate bends slightly due to the weight of the sample.

The two-plate geometry is particularly useful when doing rotation measurements, since the influence of gravitation can be reduced by mounting an equally heavy counterbalance, for example a bare substrate, on the second plate. When rotating the three-plate torquemeter, a sinusoidal background signal reveals the influence of gravity. A second disadvantage of the three-plate torquemeter is, that eddy currents give a small background signal. The contribution of eddy currents to the torque is negligible at low temperatures, but it becomes important close to the irreversibility line, where the irreversible magnetic moment of the sample vanishes. One can substract the background signal by measuring a hysteresis loop at $T > T_c$, where eddy currents form the only contribution to the torque.

The torquemeter is calibrated by glueing a copper-wired coil of known dimensions onto the plate (see figure 2.5), and measuring the torque exerted by the coil as a function of applied current, or, alternatively, by making a hysteresis loop with fixed current through the coil. Typically the copper coil consists of 10 windings with a diameter of $D \approx 9$ mm.
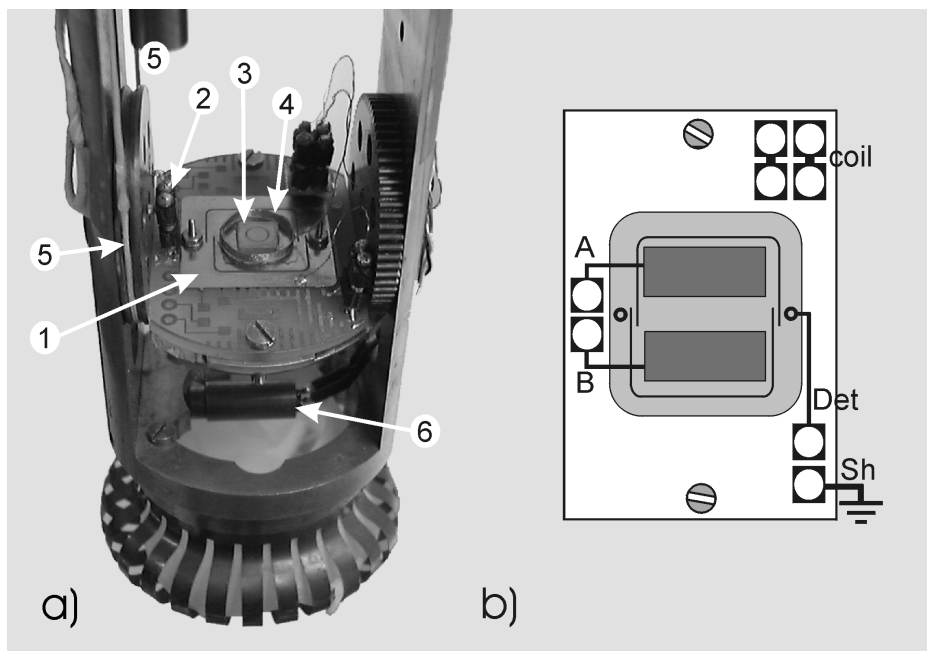
Figure 2.5: a) The three-plate torquemeter, mounted on the variable temperature insert. The movable plate with the U-cuts (1) is screwed on the printplate with small bolts and spacers, about 0.4 mm above the two fixed capacitance plates (2 points to the connectors to those). The movable plate carries the superconducting sample (3) and the calibration coil (4). The sample can be rotated via wires (5) that are connected with glass rods (not visible) to the stepper motor on top of the insert (not visible). The temperature is monitored by means of a RhFe temperature sensor (6). b) Schematic overview of the three-plate design with the fixed capacitance plates (connected to A and B), and the movable plate with the U-cuts (connected to Det). Additional connections concern the shielding (Sh) and the calibration coil (coil).

The printplate is fixed on the rotatable variable temperature insert [30], as is depicted in figure 2.5. The wheel on which the printplate is screwed, can be rotated over about 180° via a steppermoter on top of the insert, that is connected to the rotating ball by wires in the wedge-shaped rim of the ball. Glass rods cover the distance between the top of the insert with the steppermotor (not visible in figure 2.5) and the bottom with the printplate and sample. Two springs on top of the insert keep the wires and rods under tension. Most measurements were done at a fixed angle, with the magnetic field directed at an angle of 10° from the c-axis of the $YBa_2Cu_3O_{7-\delta}$ film. To obtain an accurate recording of the temperature during a measurement, a RhFe temperature sensor is mounted close to the sample.
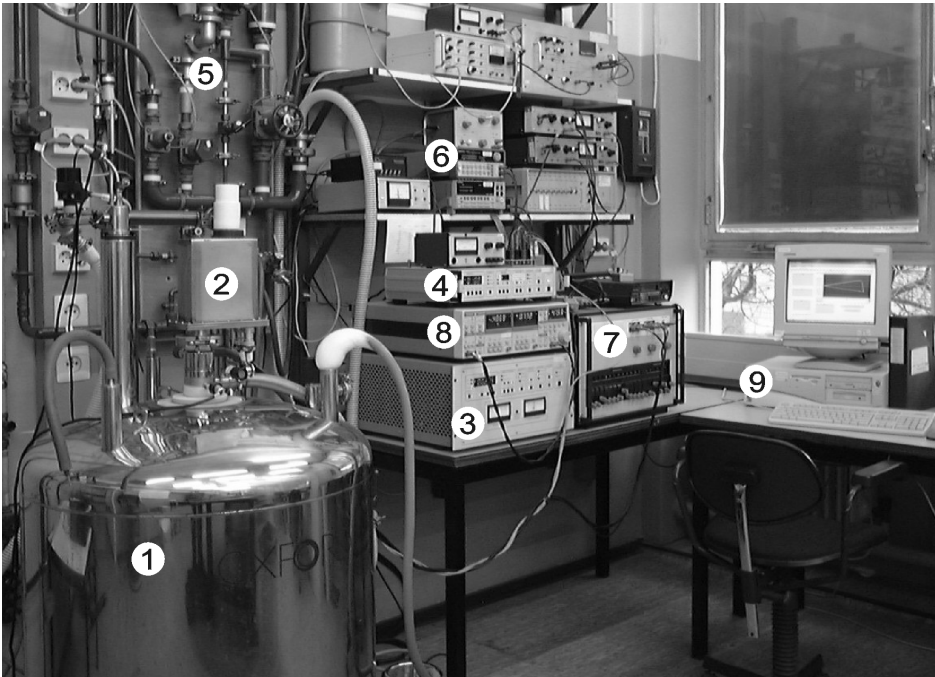
Figure 2.6: Overview of the measurement setup. It consists of a 7 T-magnet cryostat (1) with variable temperature insert (2). The magnetic field is controlled with the magnet controller PS120 (3), the temperature with the temperature controller ITC4 (4) and the helium gas handling system (5). The electrical circuit consists of a function generator HP33120A (6) with transformer (not visible), capacitance bridge GE1616 (7) and a vector lock-in amplifier SR830 (8) as detector. The data acquisition is controlled by the measurement computer Nadezjda (9).

2.3.2 The measurement setup

An overview of the setup is given in figure 2.6. We can distinguish two separate parts of the setup, the cryomagnetic part that controls the temperature and the magnetic field during a measurement, and the electric circuitry used to measure the torque.

The heart of the cryomagnetic system is formed by a 7 T magnet in a standard low-loss OXFORD cryostat. The magnet consists of a solenoid NbTi-coil, generating a vertical magnetic field up to 7 T. The magnet is situated in the main liquid helium bath of the cryostat and therefore permanently superconducting. A PS120-10 magnet controller controls the current (up to 100 A) through the magnet, and the sweep rate of the magnetic field. The magnetic field can be set with a resolution of approximately 0.7
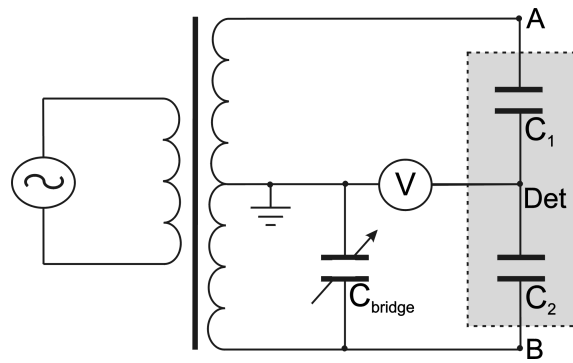
Figure 2.7: Equivalent electric circuit of the capacitive torque magnetometry setup. The torque-plates are excited with the function generator and transformer. The shaded area represents the torquemeter, that effectively consists of one capacitor (C_1, in the two-plate geometry C_2 is absent) or two capacitors (C_1 and C_2, in the three-plate geometry). A capacitance bridge is used to compensate for any offset capacitance, so that the lock-in amplifier measures zero volt in equilibrium (i.e. when no torque is exerted).

mT, and the sweep is done by digital steps of 0.13 mT, with a maximum sweep rate of 40 mT/s. In order to make very slow continuous sweeps, we connect a KEITHLEY 2400 source meter in combination with home-built a voltage to current converter parallel to the current leads of the magnet. We fix a certain magnetic field B_0 with the PS120 controller, and make hysteresis loops of $\Delta B = 74$ mT around B_0 with the external current source. In this way one can reach very low sweep rates in the order of μT/s.

The temperature is stabilized with an ITC4 temperature controller. Via a needle valve we pump helium from the liquid helium bath along the sample chamber. A PID-controlled heater and a Carbon-glass temperature sensor near the sample set the desired temperature in equilibrium with the cooling power of the flowing helium. To reach temperatures below 4.2 K, we open the helium flow valve completely, and regulate the pump pressure by a external PID-controller. In this way we are able to measure in the whole temperature range from $T \approx 1.7$ to 300 K.

The electric circuit is schematically depicted in figure 2.7. A HP33120A function generator in combination with a 15.6 : 1 transformer excites the capacitance plates. The shaded area represents the three-plate torquemeter, consisting of capacitance C_1 and C_2 (in the case of the two-plate design C_2 is absent). The signal is detected by a STANFORD INSTRUMENTS SR830 vector lock-in amplifier. A GENERAL RADIO 1616 capacitance bridge is used to compensate for any offset capacitance or conductance present in the system, so that the lock-in amplifier reads zero voltage when no torque is exerted. In this case we obtain maximum sensitivity to the capacitance *change* ΔC.
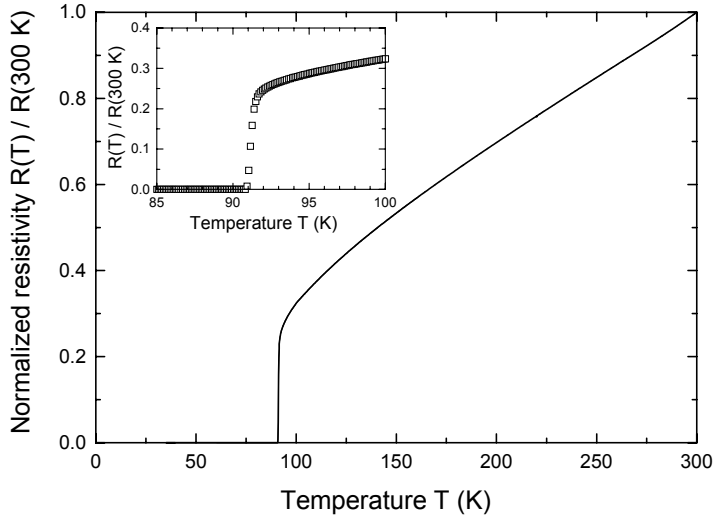
Figure 2.8: Resistance versus temperature of a typical $YBa_2Cu_3O_{7-\delta}$ thin film. The superconducting transition temperature $T_c(R = 0) = 90.6$ K. The transition width, determined by taking the FWHM of dR/dT around the transition, yields $\Delta T_c = 0.4$ K.

2.4 Preparation of $YBa_2Cu_3O_{7-\delta}$ thin films

$YBa_2Cu_3O_{7-\delta}$ thin films were deposited by means of Pulsed Laser Deposition (PLD) on (100) $SrTiO_3$ substrates. The PLD-system consists of a KrF excimer laser (QUESTEK IMPULSE 4750GL, with wavelength 248 nm, pulse time 30 ns, frequency 5 Hz)[1] and a UHV system in combination with projection optics to ensure a stoichiometric deposition from the $YBa_2Cu_3O_{7-\delta}$ target. XRD analysis shows a good overall crystallinity of all films. The c-axis of the films c = 11.68(3) Å is very close to the single crystal value of 11.677 Å, while the (005) rocking curve full width at half maximum $\Delta\omega_{(005)} \lesssim 0.1°$. The transition temperature T_c was measured resistively using a four point method. The average transition temperature, obtained by measuring a large collection of $YBa_2Cu_3O_{7-\delta}$ films, was $T_c = 90.4$ K with a standard deviation

---

[1]Recent films were deposited by a second PLD system, with a LAMBDA PHYSIK KrF laser ($\lambda = 248$ nm, $\tau = 25$ ns). The labeling of the films used in this thesis, is LAD[number] for the films produced by the QUESTEK laser, and LP[number] for the films deposited by the LAMBDA PHYSIK laser. Both deposition systems produced films of equally high quality and no noticeable differences in microstructural or superconducting properties were observed.
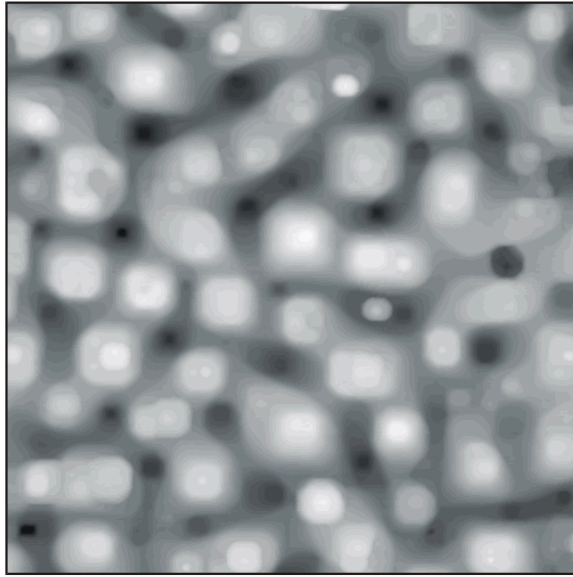
Figure 2.9: 1.5x1.5 μm^2 Surface topography of a 140 nm thick YBa$_2$Cu$_3$O$_{7-\delta}$ film, obtained by Atomic Force Microscopy. The island structure can be clearly distinguished. The average island diameter is $D = 200$ nm. Vertical scale: black-white ~ 40 nm.

of 0.4 K and a transition width $\Delta T_c \lesssim 0.5$ K [31]. In figure 2.8 a typical resistance measurement is shown.

To determine the defect structure *and* the pinning properties of the same film, we cut each film into four pieces. For critical current measurements one piece was patterned by standard UV photolithography into a ring of typically 3-5 mm in diameter and 125-500 μm width. In this geometry we can safely assume a well-defined current distribution and relaxation rate, which we confirmed by magneto-optical measurements [32]. The other pieces were used for microstructural analysis, such as AFM, XRD and wet chemical etching (see chapter 3), and as a backup piece.

The surface morphology of the films is studied by a tapping mode AFM, using a NANOSCOPE IIIA. In figure 2.9 a typical AFM image is shown of the surface of a laser ablated YBa$_2$Cu$_3$O$_{7-\delta}$ film (film LAD496). Characteristic for all PLD films is the 2D island structure, with an island diameter of typically 100 - 500 nm, separated by deep trenches (up to 20% of the film thickness). By using different substrate temperatures during deposition between $T_{sub} \approx 700°$C and $T_{sub} \approx 850°$C we are able to tune reproducibly the island size of the films between $D = 80$ nm to $D = 500$ nm [33]. In the next chapter we investigate how this affects the defect structure of thin films. We introduce wet chemical etching as a tool to reveal linear defects, and show, that by changing the island size, the number of linear defects changes. By relating

this to the low magnetic field behaviour of the current density, we prove that linear defects are the most important pinning centers in $\mathrm{YBa_2Cu_3O_{7-\delta}}$ thin films [34].

References

[1]   D.E. Farell, J.P. Rice, D.M. Ginsberg, and J.Z. Liu, Phys. Rev. Lett. **64**, 1573 (1990)

[2]   M. Qvarford, K. Heeck, J.G. Lensink, R.J. Wijngaarden, and R. Griessen, Rev. Sci. Instrum. **63**, 5726 (1992)

[3]   D.X. Chen, R.B. Goldfarb, J. Nogues, and K.V. Rao, J. Appl. Phys. **63**, 980 (1988)

[4]   T. Ishida and R.B. Goldfarb, Phys. Rev. B **41**, 8937 (1990)

[5]   D.X. Chen and A. Sanchez, J. Appl. Phys. **70**, 5463 (1991)

[6]   S. Foner, Rev. Sci. Instrum. **30**, 548 (1959),
A. Zieba and S. Foner, Rev. Sci. Instrum. **53**, 1344 (1982)

[7]   I.J. Daniel and D.P. Hampshire, Phys. Rev. B **61**, 6982 (2000)

[8]   R. Gross, P. Chaudhari, M. Kawasaki, M.B. Ketchen, and A. Gupta, Appl. Phys. Lett. **57**, 727 (1990)

[9]   M. Siegel, F. Schmidl, K. Zach, E. Heinz, J. Borck, W. Michalke, and P. Seidel, Physica C **180**, 288 (1991)

[10]   J.R. Kirtley, M.B. Ketchen, K.G. Stawiasz, J.Z. Sun, W.J. Gallagher, S.H. Blanton, and S.J. Wind, Appl. Phys. Lett. **66**, 1138 (1995)

[11]   M.R. Koblischka and R.J. Wijngaarden, Supercond. Sci. and Techn. **8**, 199 (1995), and references therein

[12]   R.J. Wijngaarden, K. Heeck, M. Welling, R. Limburg, M. Pannetier, K. van Zetten, V.L.G. Roorda, and A.R. Voorwinden, Rev. Sci. Instrum. **72**, 2661 (2001)

[13]   M. Konczykowski, F. Holtzberg, and P. Lejay, Supercond. Sci. Technol. **4**, S331 (1991)

[14]   E. Zeldov, D. Majer, M. Konczykowski, V.B. Geshkenbein, V.M. Vinokur, and H. Shtrikman, Nature **375**, 373 (1995)

[15]   R. Griessen, Cryogenics **13**, 375 (1973),
R.Griessen, M.J.G. Lee, and D.J. Stanley, Phys. Rev. B **16**, 4385 (1977)

[16]   C. Rossel, P. Bauer, D. Zech, J. Hofer, M. Willemin, and H. Keller, J. Appl. Phys. **79**, 8166 (1996),
M. Willemin, C. Rossel, J. Brugger, M. Despont, H. Rothuizen, P. Vettiger, J. Hofer, and H. Keller, J. Appl. Phys. **83**, 1163 (1998)

[17]   W. Xing, B. Heinrich, H. Zhou, A.A. Fife, and A.R. Cragg, J. Appl. Phys. **76**, 4244 (1994)

[18]   A.E. Pashitski, A. Gurevich, A.A. Polyanskii, D.C. Larbalestier, A. Goyal, E.D. Specht, D.M. Kroeger, J.A. DeLuca, and J.E. Tkaczyk, Science **275**, 367 (1997)

[19]   R.J. Wijngaarden, H.J.W. Spoelder, R. Surdeanu, and R. Griessen, Phys. Rev. B. **54**, 6742 (1996),
       R.J. Wijngaarden, K. Heeck, H.J.W. Spoelder, R. Surdeanu, and R. Griessen, Physica C **295**, 177 (1998)

[20]   J.D. Jackson, *Classical Electrodynamics*, John Wiley and Sons Inc., New York (1975)

[21]   V.G. Kogan, Phys. Rev. B **38**, 7049 (1988)

[22]   D.E. Farell, C.M. Williams, S.A. Wolf, N.P. Bansal, and V.G. Kogan, Phys. Rev. Lett. **61**, 2805 (1988)

[23]   J.C. Martínez, S.H. Brongersma, A. Koshelev, B. Ivlev, P.H. Kes, R.P. Griessen, D.G. de Groot, Z. Tarnavski, and A.A. Menovsky, Phys. Rev. Lett. **69**, 2276 (1992)

[24]   C. Rossel, M. Willemin, J. Hofer, H. Keller, Z.F. Ren, and J.H. Wang, Physica C **282-287**, 136 (1997),
       M. Willemin, C. Rossel, J. Hofer, H. Keller, Z.F. Ren, and J.H. Wang, Phys. Rev. B **57**, 6137 (1998)

[25]   C.P. Bean, Phys. Rev. Lett. **8**, 250 (1962)

[26]   Y. Yeshurun and A.P. Malozemoff, Phys. Rev. Lett. **60**, 2202 (1988)

[27]   A.C. Mota, A. Pollini, P. Visani, K.A. Müller, and J.G. Bednorz, Phys. Rev. B **36**, 4011 (1987)

[28]   A.J.J. van Dalen, M.R. Koblischka, and R. Griessen, Physica C **259**, 157 (1996)

[29]   G. Doornbos, *Pinning and Crossovers in the Vortex-Dynamics of High-T_c Thin Films*, PhD thesis, Vrije Universiteit (2001)

[30]   H.G. Schnack, R. Griessen, P. Noordeloos, K. Heeck, Physica C **266**, 285 (1996)

[31]   J.M. Huijbregtse, B. Dam, J.H. Rector, and R. Griessen, J. Appl. Phys. **86**, 6528 (1999)

[32]   M. Pannetier, F.C. Klaassen, R.J. Wijngaarden, M. Welling, K. Heeck, J.M. Huijbregtse, B. Dam, and R. Griessen, Phys. Rev. B **64**, 144505 (2001), and chapter 6 of this thesis

[33]   J.M. Huijbregtse, B. Dam, R.C.F. van der Geest, F.C. Klaassen, R. Elberse, J.H. Rector, and R. Griessen, Phys. Rev. B **62**, 1338 (2000)

[34]   B. Dam, J.M. Huijbregtse, F.C. Klaassen, R.C.F. van der Geest, G. Doornbos, J.H. Rector, A.M. Testa, S. Freisem, J.C. Martínez, B. Stäuble-Pümpin, and R. Griessen, Nature **399**, 439 (1999)

Chapter 3

Strong vortex pinning by natural linear defects

In this chapter the origin of the high critical current density in $YBa_2Cu_3O_{7-\delta}$ thin films ($10^{11} - 10^{12}$ Am^{-2} at $T = 4.2$ K) is explained in terms of strong vortex pinning by linear defects. We introduce wet chemical etching to determine the total number of linear defects in thin films. The superconducting current density $j_s(B)$ exhibits a plateau at low magnetic fields. From measuring many films with various linear defect density, we find that the size of the plateau, which we denote by B^*, is directly proportional to the density of linear defects n_{disl}, i.e. $B^* = 0.7n_{disl}\Phi_0$. This proves that linear defects form the most important pinning centers in $YBa_2Cu_3O_{7-\delta}$ thin films. Changing the surface roughness of the film has no effect on B^*, which strongly supports the model of linear defect pinning. In many respects vortex pinning by linear defects in thin films is similar to strong vortex pinning by columnar tracks in heavy-ion irradiated single crystals. There are, however, three essential differences: i) typical matching fields are at least one order of magnitude smaller, ii) linear defects are smaller than columnar tracks and iii) the distribution of natural linear defects is non-random, whereas columnar tracks are randomly distributed. We give a preliminary explanation of the observed pinning mechanism in terms of the Bose glass theory[1].

3.1 Introduction

In high-T_c superconducting $YBa_2Cu_3O_{7-\delta}$ thin films, very high critical currents up to 10^{12} Am^{-2} are observed. This is roughly two orders of magnitude higher than in high quality single crystals, and comparable to the depairing current j_0. These current densities indicate that a large amount of *correlated* defects is present in thin films [1]. Such defects provide for strong vortex pinning, whereas in single crystals vortices are only weakly pinned by randomly distributed point defects. Strong vortex pinning is an important aspect for high-T_c applications, but the nature of the defect responsible for the observed large current densities in thin films remained unresolved for a long time. One of the reasons for this is the complex defect structure of $YBa_2Cu_3O_{7-\delta}$ thin films, having many different defects that can act as a strong pinning source [2]. It is therefore hard to distill one typical defect and establish a quantitative relation between the defect microstructure and the pinning properties or, more specifically, the critical current density.

In general we can distinguish three types of defects, namely *point defects*, such as large extended precipitates [3] or oxygen vacancies [4], *linear defects* such as as-grown screw and edge dislocations [4, 5, 6, 7, 8, 9] or columnar tracks as a result of heavy ion irradiation [10], and *planar defects* such as twin boundaries [11], (low angle) grain boundaries [12], anti-phase boundaries [13] or surface roughness [14, 15]. All types have been extensively studied, but most studies are based on samples with an *artificially induced* defect structure, by using doping or heavy ion irradiation, or specially chosen (miscut, bicrystal) substrates in order to study various pinning mechanisms. However, the reason for the near to perfect pinning properties, i.e. $j_c \simeq j_0$ of high quality *as-grown* films remained unexplained.

In order to identify the mechanism responsible for strong pinning in *as-grown* thin films it is essential to analyse systematically and quantitatively the intrinsic pinning properties in connection with the defect structure. It was suspected for a long time that linear defects are the most effective pinning centers in thin $YBa_2Cu_3O_{7-\delta}$ films. The reason is that both the *radius* and *shape* of a linear defect and a vortex are comparable. A vortex has a normal core of radius $\sim \sqrt{2}\xi$, with ξ the coherence length. Also within the core of a linear defect the superconducting order parameter is heavily, if not completely, suppressed. A vortex inside a linear defect does not have to provide its own condensation energy, and is therefore strongly pinned. The extension of a linear defect along the c-axis allows a vortex to be pinned over its full length. Note that the condensation energy involved is quite large $\mathcal{E} \simeq \frac{1}{2}\mu_0 H_c^2 \cdot 2\pi\xi^2 d \approx 4$ eV for a film with thickness $d = 100$ nm. If the vortex and defect are of equal size, pinning is most effective. For smaller defects, the vortex has to pay some condensation energy itself, in other words is does not 'fit' completely inside the defect. For defects much larger than the vortex, the shielding currents around the vortex have to flow partially through the non-superconducting core of the defect, thereby causing dissipation.

The importance of pinning by linearly extended defects was observed also in single crystals. After irradiating single crystals with heavy ions, linear (columnar) tracks are formed of highly amorphous material, that have very strong pinning properties.

As a result the critical current increased by several orders of magnitude [16], and is almost as high as in thin films.

In an early attempt to relate the large critical currents of thin films to the number of linear defects, growth spirals were taken as a measure for the number of natural linear defects [5, 6, 17]. However, screw dislocations do not always form growth spirals. For example in Pulsed Laser Deposited (PLD) $YBa_2Cu_3O_{7-\delta}$ films, which have equally high critical currents, deposition takes place via 2D growth and dislocations cannot be discerned by looking at the as-grown surface morphology [18]. Moreover, edge dislocations which pin vortices equally well [9], do not form any topographic feature at all, and are therefore not counted. This indicates that by looking at the surface topology only, one severely underestimates the number of linear defects. This does not mean that linear defects cannot be important pinning centers in $YBa_2Cu_3O_{7-\delta}$ thin films. However, to investigate the influence of linear defects on the pinning properties, one has to use a different method to obtain an accurate estimate of the total density of linear defects.

In this chapter we introduce wet chemical etching as a method to determine the density of *all* linear defects, irrespective of the type. We show that etching provides accurate information about the density, distribution and the length of the linear defects in $YBa_2Cu_3O_{7-\delta}$ thin films. Moreover we demonstrate that linear defects have a profound influence on the superconducting current density j_s at low magnetic fields. A direct quantitative relation between the dislocation density n_{disl} and the size of the low field plateau of j_s proves that linear defects are indeed the most important pinning centers in $YBa_2Cu_3O_{7-\delta}$ thin films.

3.2 Measuring the total linear defect density by wet chemical etching

A well-known technique to visualize dislocations is wet chemical etching [19]. Etching is a nucleation process, where a critical nucleus has to be formed to initiate the dissolving process. When the surface is flat and defect-free, there is no preferential position for the etching process to start, and the film will dissolve homogeneously. When the surface exhibits roughness, step edges at the surface serve as a nucleation center. As a result the etching process will flatten the surface before dissolving the film further. However, when there are linear defects present at the surface, the energy required to form a critical nucleus is lower at the position of the defect, and the etching process starts preferentially at the position of the defect. Etch pits are formed which reveal the position of a dislocation. Figure 3.1 shows a typical picture of a $YBa_2Cu_3O_{7-\delta}$ film, etched in a 1 vol% Br in ethanol solution. By counting the total number of etchpits we determine the linear defect density. Note that this preferential etching does not distinguish between edge or screw dislocations. We obtain therefore the *total* linear defect density.
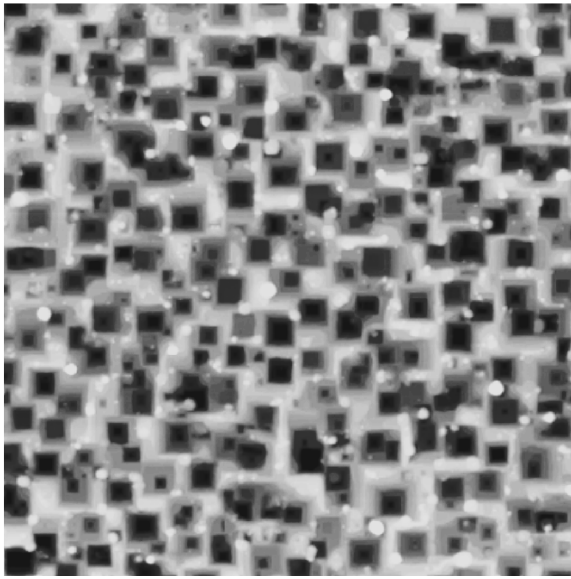
Figure 3.1: 3 x 3 μm^2 AFM picture of a 140 nm thick $YBa_2Cu_3O_{7-\delta}$ film (LAD496), etched in a 1 vol% Br in ethanol solution. Square etch pits reveal the position of all linear defects. From this picture we obtain $n_{disl} = 34\ \mu m^{-2}$. Note that the material, which is etched away forms precipitates on the surface. This makes the surface look dirty.

To prove that wet chemical etching shows both screw and edge dislocations, we depict in figure 3.2 a AFM image of a sputtered film Y67[2]. Sputtered films exhibit spiral growth, which results in the formation of very large growth islands (diameter $D \sim 1-2$ μm). In figure 3.2 film Y67 has been etched for about 20 s in a 1 vol% Br in ethanol solution, but the island structure is still visible. We know that the end of a growth spiral must be the outcrop of a screw dislocation. In fact the part of the film shown consists of a double spiral, and indeed we observe etch pits appearing at both ends of the double spiral (horizontal arrows in figure 3.2). Additionally other etch pits are formed that are not related to a growth spiral, and therefore cannot be screw dislocations. These dislocations (vertical arrows in figure 3.2) must therefore be of edge nature. We conclude that wet chemical etching shows all dislocations, and is thus a better method than that used by Hawley *et al.* [5] and Mannhart *et al.* [6], which discerns only screw dislocations.

By repeatedly etching and looking at the surface at the same position on the film we can follow individual etch pits. From this repeated etching, and also from the symmetric shape of an individual etch pit, we find that the linear defects are directed along

---

[2]This film has been made by S. Freisem at Leiden University. Details of the deposition process can be found in ref. [20].
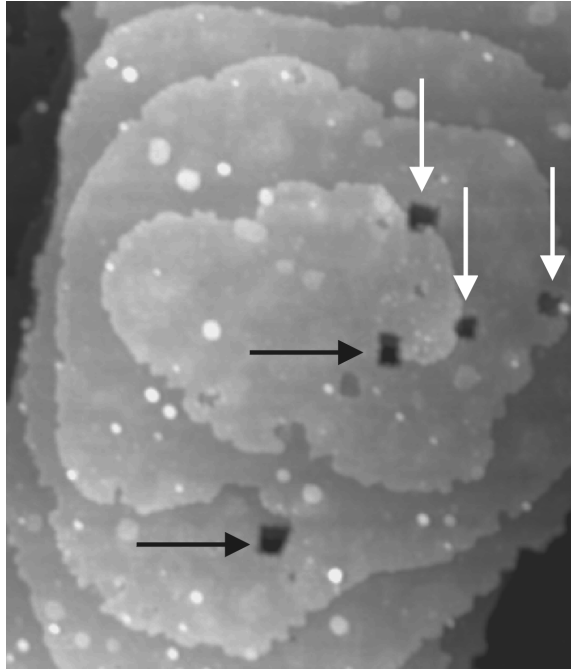
Figure 3.2: 0.85 x 1.0 μm^2 AFM image of a YBa$_2$Cu$_3$O$_{7-\delta}$ film (Y67), sputtered on SrTiO$_3$(100). After etching for 20 s the linear defects can be distinguished together with the island structure. At either end of the double growth spiral screw dislocations are revealed by small etch pits (horizontal arrows). Additionally etch pits have appeared, that are not connected to any growth features (vertical arrows). They correspond to edge dislocations.

the c-axis. Nearly all (> 85 %) linear defects continue down to the film-substrate interface [21]. Only a few etch pits are flat bottomed, i.e. ending inside the film. This shows that dislocations are formed almost exclusively at the film-substrate interface, i.e. during the first stages of film growth. An extensive investigation of the mechanism of film growth revealed, that dislocations are formed after a crossover from a pseudomorphic growth of the first few monolayers (film thickness $d < 7.3$ nm for SrO-terminated substrates) towards coherent 3D growth islands at larger thicknesses (above a critical thickness $d \gg 25$ nm) [22].

In figure 3.3 we compare the surface morphology of a YBa$_2$Cu$_3$O$_{7-\delta}$ film, as-grown and after etching for 5 s in a 1 vol% Br in ethanol solution. Both AFM images were taken at the same position of the film, so that we can distinguish the various islands, and determine the position of the dislocations with respect to the island structure. We clearly observe that the etch pits are situated in the trenches between the islands. Especially at the connection point where three growth islands meet, linear defects
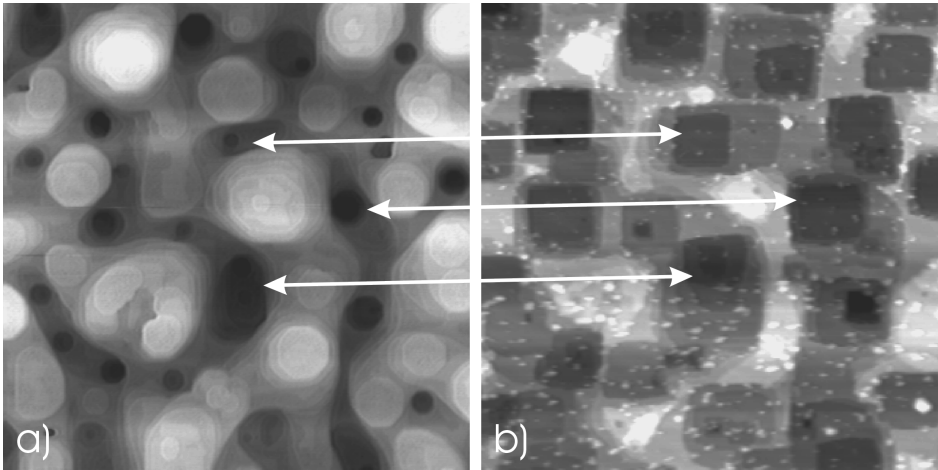
Figure 3.3: 2 x 2 μm^2 AFM images of a YBa$_2$Cu$_3$O$_{7-\delta}$ film, a) as-grown and b) etched for 5 s. Both AFM pictures are taken at the same position on the film. In this way we can map the position of the etch pits to the original location of the linear defects. The white arrows show this mapping for three dislocations, but every etch pit can be translated back to the original position of the linear defect. The position of the etch pits in figure 3.3b) indicates that the linear defects are located mainly in the trenches connecting the growth islands.

are found. This has two important consequences. First we expect a relation between the size of the island, or consequently the island density, and the number of linear defects. Indeed we find that the density of linear defects is directly proportional to the island density, with on average 0.9 dislocation per growth island [21]. Since we are able to change the island density by choosing a different substrate temperature during growth, we can tune the density of linear defects. We thus have a tool to determine the linear defect density (by wet chemical etching), but also we are able to make films with any desired dislocation density from $n_{disl} \approx 8 - 100$ μm^{-2} (by setting the appropriate substrate temperature from $T_{sub} \approx 700°C - 850°C$).

A second consequence of the predominant occurrence of dislocations inside the trenches is, that they are not randomly distributed. The radial distribution function of the etch pits shows that the distribution of linear defects is non-random, with almost no defects very close to each other [21]. This means that vortices that are pinned by the linear defects, form a more or less ordered vortex lattice, which has a configurational energy not much larger than an ideal Abrikosov lattice. We therefore expect that this array of linear defects pins vortices even more effectively than columnar tracks in irradiated crystals, that are randomly distributed.

3.3 Critical current density in films with various dislocation density

The superconducting current density j_s of a number of laser ablated films [23] is measured by means of capacitive torque magnetometry (see chapter 2 and ref. [24]). For each film we performed two sweeps; one fast sweep from $\mu_0 H = -1 \longleftrightarrow 7$ T with a sweep rate of $\mu_0 dH/dt = 40$ mT/s, and a slow sweep from $\mu_0 H = -0.3 \longleftrightarrow 1$ T with a sweep rate of $\mu_0 dH/dt = 1 - 2$ mT/s. The first sweep concentrates on the high field behaviour of the current density, whereas with the slow sweep we acquire enough data points to focus on the low field behaviour. Both data sets do not overlap completely due to magnetic relaxation, but between $\mu_0 H = 0.5$ and 1 T, the ratio between the current densities of both sweeps is virtually constant. This corresponds to a relaxation rate independent of magnetic field, and we can map both measurements on top of each other[3]. In this way we obtain complete picture of $j_s(B)$ both at low and high magnetic fields.

In figure 3.4 $j_s(B)$ is plotted for three films, with dislocation densities $n_{disl} = 19$, 48 and 71 μm^{-2} for low magnetic fields up to $\mu_0 H = 0.5$ T and temperature $T = 4.2$ K. The most remarkable feature of $j_s(B)$ is a plateau at low magnetic fields. Note that this plateau is not an artefact of the logarithmic scale, used for $\mu_0 H$; it persist in a linear plot (inset of figure 3.4). The plateau extends to larger field values for films with a larger dislocation density. This is a strong indication that dislocations are important for vortex pinning at low magnetic fields.

We denote the size of the plateau with a characteristic field B^*, which we determine by fitting $j_s(B)$ with an empirical expression:

$$j_s(B) = \frac{j_s(0)}{1 + k_1 \exp(-1/x) \cdot x^\alpha}, \text{ with } x = B/k_2 \qquad (3.1)$$

In eq. (3.1) k_1, k_2 and α are fit parameters. The parameter k_2 scales the magnetic field, i.e. $B^* \sim B/k_2$, and the factor x^α in the denominator reflects the power law behaviour, which is found at high magnetic fields $\mu_0 H \gg B^*$. The characteristic field B^* is found by taking the crossing of $j_s(0)$ with the tangent at the inflection point, as shown in the inset of figure 3.4.

In figure 3.5a the characteristic field is given for a number of YBa$_2$Cu$_3$O$_{7-\delta}$ films with various dislocation density at $T = 4.2$ K. The films from figure 3.4 are denoted by the solid circles. We find that B^* is directly proportional to the dislocation density, with a slope $dB^*/dn_{disl} = 1.4 \cdot 10^{-15} = 0.7 \Phi_0$. This proves that linear defects are the most important pinning centers at low fields, and furthermore that every linear defect can pin exactly one vortex.

We can describe strong pinning by linear defects within the framework of a Bose glass phase [25, 26]. At low fields $\mu_0 H \ll B^*$, vortices are localized on linear defects, which results in pinning with maximum efficiency and constant current density of the order of j_0, the depairing current. With increasing field, there are less defects available

---

[3]In chapter 5 of this thesis we measure the dynamical relaxation rate, and we show that at low temperatures the relaxation rate is indeed constant for $\mu_0 H > 0.5$ T.
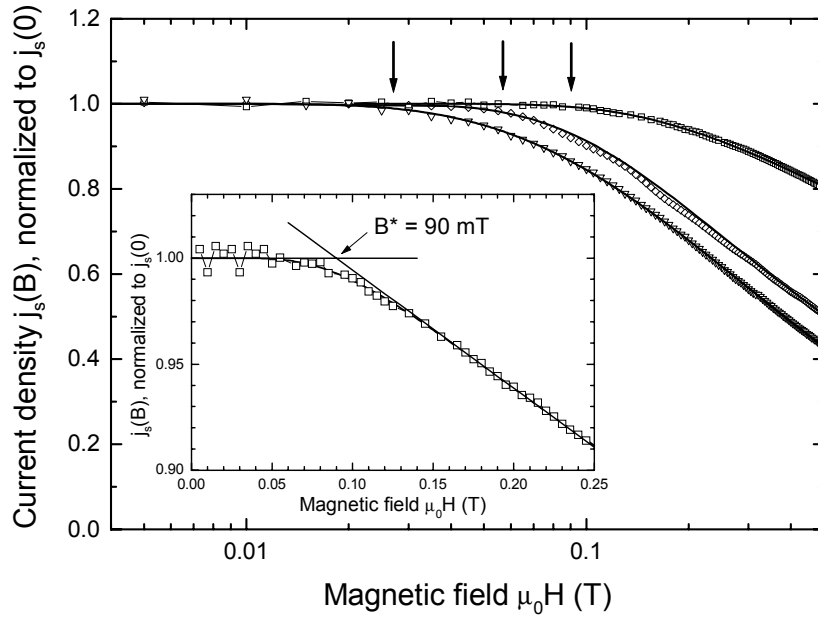
Figure 3.4: Normalized superconducting current density j_s for three films with $n_{disl} = 20$ (LAD323, $\triangledown$), 48 (LAD561, $\lozenge$), and 71 μm^{-2} (LAD493, $\square$). Solid lines are fits to $j_s(B) = j_s(0)/(1 + k_1 \exp(-1/x)x^{\alpha})$ with $x = B/k_2$. The size of the plateau scales with the dislocation density. Inset: The characteristic field $B^* = 90$ mT for LAD493 is determined from the crossing of the tangent at the inflection point with the plateau.

and also the vortex-vortex interaction increases. At fields $\mu_0 H \gtrsim B^*$, newly entering vortices cannot be accommodated any more by the defects, and the superconducting current density decreases. From this consideration it follows that the characteristic field B^*, that we observe experimentally, should be exactly the accommodation field, defined in the Bose glass theory[4]. Due to vortex-vortex interactions B^* is in general smaller than the matching field $B_\Phi \equiv n_{disl}\Phi_0$, the field when the vortex density equals the linear defect density.

---

[4]Note that in the review of Blatter *et al.* [26], the symbol B_{rb} is used for the accommodation field, instead of B^*.
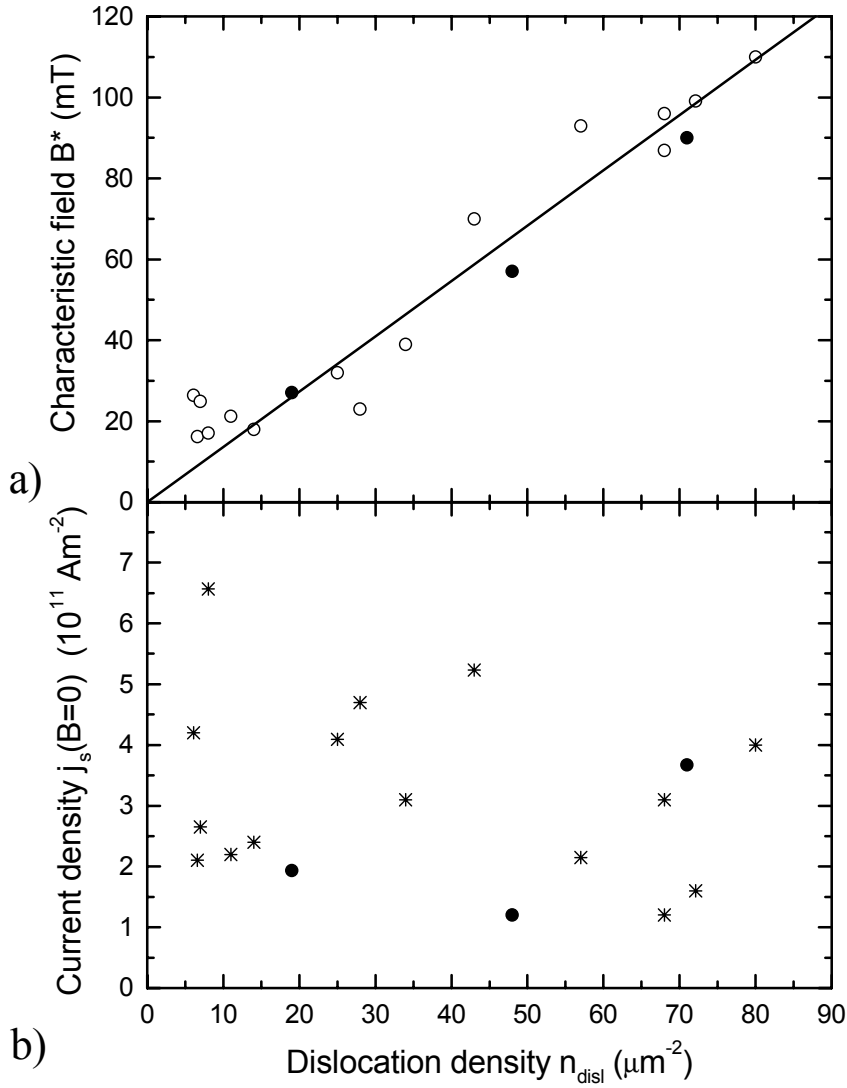
Figure 3.5: a) Characteristic field B^* for various films at $T = 4.2$ K, plotted versus the dislocation density. We find that $B^* = 0.7 n_{disl} \Phi_0$, showing that linear defects are the most important pinning source at low magnetic fields. b) The superconducting current density $j_s(B = 0)$ at $T = 4.2$ K is roughly constant for the many films we investigated, independent of n_{disl}. Solid circles denote the films, plotted in figure 3.4.

Theoretically B^* is determined by balancing the (attractive) vortex-pinning interaction and the (repulsive) vortex-vortex interaction, which leads to [25, 26]:

$$B^* \approx \frac{4\varepsilon_r}{\varepsilon_0} B_\Phi \approx 2 \left[\ln \left(1 + \frac{r_r^2}{2\xi_{ab}^2(T)} \right) \right] n_{disl} \Phi_0, \qquad (3.2)$$

where $\varepsilon_r \approx \frac{\varepsilon_0}{2} \ln \left(1 + \frac{r_r^2}{2\xi_{ab}^2} \right)$ is the depth of the pinning potential for linear defects, r_r is the radius of a linear defect, ξ_{ab} is the in-plane coherence length, and $\varepsilon_0 \equiv \Phi_0^2/4\pi\mu_0\lambda^2$ a characteristic vortex energy per unit length. From our result $B^* \approx 0.7 n_{disl}\Phi_0$ and eq. (3.2) we find $4\varepsilon_r/\varepsilon_0 \approx 0.7$, indicating that the radius of the dislocation core and the coherence length are of the same order of magnitude $r_r/\xi_{ab} \approx 0.9$. This is in good agreement with TEM experiments from Gao *et al.* [27], who found that the core radius of edge dislocations in thin YBa$_2$Cu$_3$O$_{7-\delta}$ films is typically $r_r \approx 1$ nm.

The superconducting current density of all the films measured is plotted in figure 3.5b. We find that the magnitude of $j_s(B = 0)$ does *not* depend systematically on the dislocation density. This is due to the fact, that at low magnetic fields, vortices are individually pinned and the pinning force depends only on the (single) vortex-pin potential. This explains why other groups, that have tried to compare the (screw) dislocation density with the *magnitude* of the current density [6], have not been able to establish a quantitative relationship between the pinning properties and the dislocation density. In a single vortex pinning regime the critical current is simply not the right quantity to compare with the defect density, which is evident from figure 3.5b.

From figure 3.5 we can also conclude that the self-field $\mu_0 H_{self} \approx \frac{1}{2} j_s d$ [28, 29] (d is the thickness of the sample) does not influence the measurement of B^*. Although the self-field is of the same order of magnitude as the characteristic field, B^* is proportional to n_{disl}, and it does not depend on j_s or the sample dimensions like $\mu_0 H_{self}$. We conclude therefore that the plateau of $j_s(B)$ is not an artifact connected to the self-field, but indeed related to the strong pinning of vortices by linear defects. In addition the field of first penetration, measured for various samples both by torque magnetometry and magneto-optics $\mu_0 H_{pen} \approx 10 - 25$ mT $< B^*$ [30]. However, self-fields might become important at magnetic fields below B_{pen}. This imposes extra experimental difficulties on determining the characteristic field, and it might explain why the characteristic field seems to level off at $B^* \approx 20$ mT for films with a low dislocation density $n_{disl} \lesssim 15$ μm^{-2}.

The characteristic field is strongly temperature dependent, contrary to the matching field B_Φ, which is by definition temperature *in*dependent. The temperature dependence of B^* is plotted in figure 3.6. Note that, since the torque vanishes at zero field, and because $j_s \sim \tau/B$, the data for $j_s(B)$ at very low fields become increasingly more noisy. This makes it hard to determine $B^*(T)$, especially at higher temperatures. In appendix 3A we investigate different methods to analyse the plateau-like features in j_s. From this analysis we find, that fitting with eq. (3.1), as was done in figure 3.4 and ref. [31], and the criterion $j_s(2B^*) = 0.95 j_s(0)$ give similar results at $T = 4.2$ and 10 K. In figure 3.6 we therefore used the more convenient criterion $j_s(2B^*) = 0.95 j_s(0)$
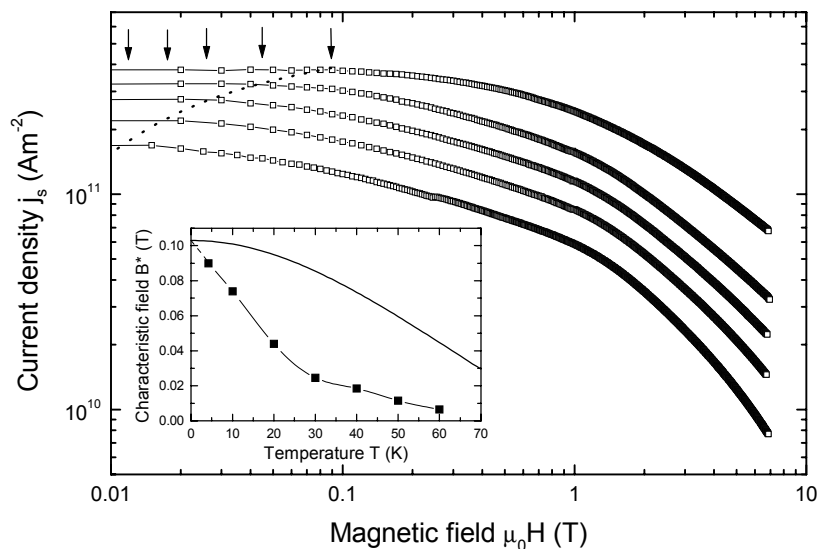
Figure 3.6: Current density $j_s(B)$ for film LAD493 at various temperatures. From top to bottom $T = 4.2$, 20, 30, 40, and 50 K. The characteristic field decreases strongly with temperature (dashed line). Inset: The characteristic field $B^*(T)$, determined via the criterion $j_s(2B^*) = 0.95j_s(0)$ (■, the line is a guide to the eye), decreases faster than expected by theory $B^*(T) \sim 1/\xi^2(T)$. The solid line is theoretical dependence, using eq. (3.2) and $r_r = 0.9\xi(0)$.

to find $B^*(T)$ at higher temperatures. $B^*(T)$ decreases with temperature due to the increase of $\xi_{ab}(T) \sim \sqrt{(1+t^2)/(1-t^2)}$, with $t = T/T_c$. Physically, the increase of the vortex core radius implies that the vortex does not completely fit in the linear defect, thus reducing the pinning energy $\varepsilon_r(T)$ in eq. (3.2). However, estimating $B^*(T)$ from eq. (3.2), we find that this intrinsic temperature effect is too weak to fully explain the strong decrease of the characteristic field (inset of figure 3.6). There must be additional temperature effects, such as thermal activation of vortices, that reduce $B^*(T)$ further. In chapter 5, where we discuss the general features of linear defect pinning in YBa$_2$Cu$_3$O$_{7-\delta}$ thin films, we will investigate the temperature dependence of B^* more thoroughly and discuss a possible mechanism to explain the strong decrease of $B^*(T)$.

3.4 Thin films versus heavy-ion irradiated single crystals

In many respects the structure of linear defects in thin films resembles the columnar tracks in heavy-ion irradiated single crystals. Both the irradiation damage in the columnar tracks, and the strong lattice distortions around a dislocation core cause a heavy suppression of the superconducting order parameter. Furthermore both have a similar linear shape and they are directed along the c-axis, although heavy-ion radiation has also been done under an angle [16], or while rotating the sample (splay, see for example ref. [32]). It is therefore not surprising that the pinning properties in both systems show many similarities as well. Clear matching effects are observed in both systems, and both give rise to very high critical currents (one to two orders of magnitude larger than in high quality single crystals). There are, however, some important differences between thin films and irradiated crystals.

The density of dislocations in thin films ($B_\Phi \simeq 100$ mT) is typically one order of magnitude smaller than in irradiated crystals ($B_\Phi \simeq 1$ T). Secondly the distribution of dislocations is non-random, as they are situated around growth islands. Heavy-ion irradiation causes columnar tracks, that are randomly distributed. Both differences indicate that in irradiated crystals vortex-vortex interactions will have a larger influence at the same reduced magnetic field $b = B/B_\Phi$. This has important consequences for i) the manifestation of the matching field, ii) the temperature dependence of B^*, and iii) the behaviour of $j_s(B)$ at high magnetic fields $\mu_0 H \gg B_\Phi$. Whereas we observe in thin films a plateau in $j_s(B)$ below the characteristic field, the critical current in single crystals was found to increase exponentially below the accommodation field. This means that a different criterion should be used to determine B^*. In thin films the size of the plateau is determined either by using an empirical fit of $j_s(B)$ [31] or the simple criterion $j_s(B^*)/j_s(0) = 0.9$ [33]. In appendix 3A we found an alternative method, namely the criterion $j_s(2B^*)/j_s(0) = 0.95$, which gave similar results as the empirical fit. In irradiated single crystals B^* was defined as the field that marks the transition of the field dependence of the critical current from an exponential decrease towards $j_s(B) \propto 1/B$. Alternatively, a similar value for $B^*(T)$ was derived from the maximum in $\mathrm{d}\ln j_s/\mathrm{d}T \,|_B$ [34].

In figure 3.7a we compare $j_s(B/B_\Phi)$ at high magnetic fields for a thin film and an irradiated crystal. Both exhibit a power law behaviour, but in thin films we find $j_s(B) \sim 1/\sqrt{B}$ and in irradiated crystals $j_s(B) \sim 1/B$. The latter is a clear feature of collective pinning, whereas the power law behaviour in thin films $j_s(B) \sim 1/\sqrt{B}$ points towards a shear mechanism of unpinned vortices along the strongly pinned vortices in the linear defects [35]. Note that for films with many dislocations $n_{disl} \gtrsim 60$ μm^{-2}, such as for example LAD493, the power law decrease of the current density resembles that of the irradiated crystals $j_s(B) \sim B^\alpha$, with $\alpha = -0.8$ to -1.1. Whether there is collective pinning or shear pinning thus depends on the average distance between defects[5].

---

[5]In chapter 5 we will investigate this the high field behaviour of $j_s(B)$ more thoroughly.
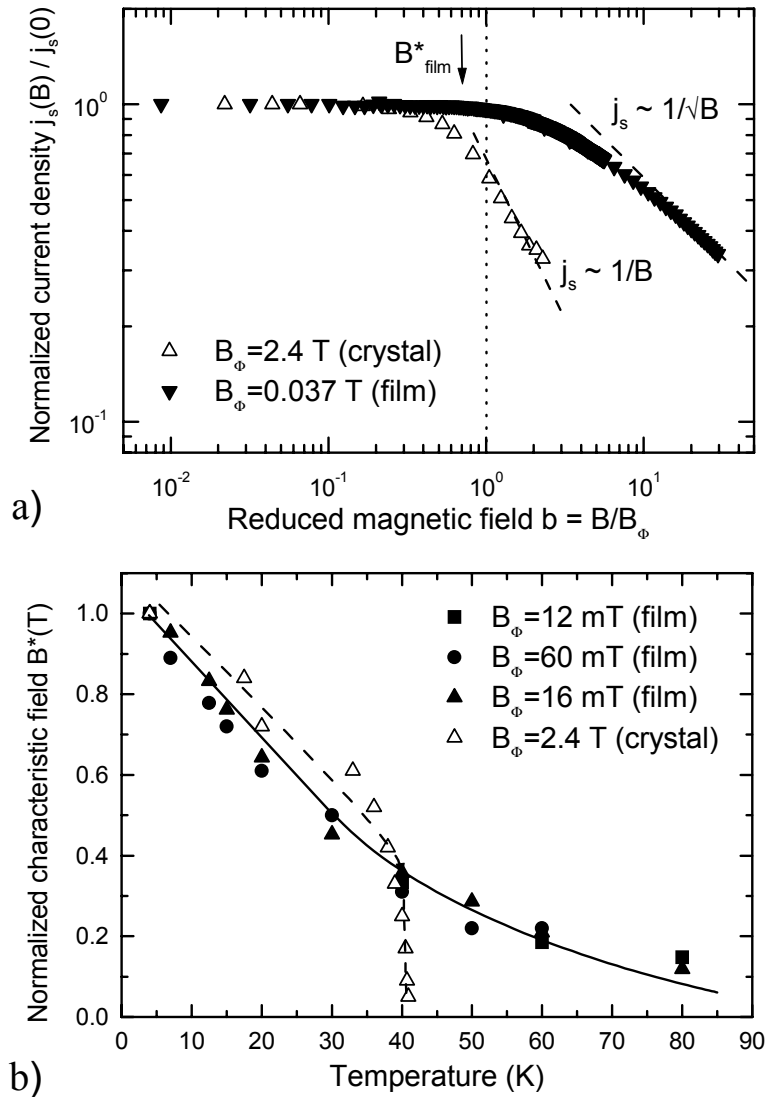
Figure 3.7: a) Comparison of the current density of a thin $YBa_2Cu_3O_{7-\delta}$ film ($B^* = 0.037$ T) with a heavy-ion irradiated $YBa_2Cu_3O_{7-\delta}$ single crystal ($B^* = 2.4$ T, from ref. [34]). At high magnetic fields $\mu_0 H \gg B_\Phi$ the current density decreases more strongly in irradiated single crystals ($j_s(B) \sim 1/B$) than in thin films ($j_s(B) \sim 1/\sqrt{B}$). b) At low temperatures the decrease of $B^*(T)$ is similar in thin films and irradiated single crystals. However, thin films do not exhibit a reduction of the depinning temperature T_{dp} and have a finite B^* also at higher temperatures $T > 40$ K.

The temperature dependence of $B^*(T)$ of thin films is similar to that of irradiated crystals at low temperatures (figure 3.7b). However the strong decrease of B^* in irradiated crystals around $T = 40$ K, is not present in thin films. Instead at higher temperatures $B^*(T)$ levels off somewhat. The exponential decrease of $B^*(T)$ at $T = 40$ K in irradiated crystals was attributed to an anomalous reduction of the depinning energy T_{dp}, marking a crossover from variable range hopping towards a bundle pinning regime [36]. A reduction of T_{dp}, however, does not occur in thin films: thermal fluctuations are found to be important only at higher temperatures $T \gtrsim 80$ K [37].

3.5 Surface roughness effects

By changing the island size we can tune the number of dislocations, but at the same time we change the surface roughness. How can we be sure that the observed plateau is indeed connected to linear defect pinning and not to changes in the surface morphology? The spatial variations could easily lead to pinning, since in the trenches between two islands the vortex can reduce its length. In a surface pinning model one would assume that vortices fill up the trenches of an island, until the inter-vortex distance becomes of the order of the penetration depth λ. Then the repulsive interactions between vortices become important, preventing new vortices to be pinned inside a trench. Qualitatively this gives the same behaviour for the superconducting current density as pinning by linear defects. When the average distance between vortices in a trench becomes of the order of the penetration depth λ, additional vortices will be located outside the trench, and the current density will decrease. This leads to the following matching condition:

$$B_\Phi \simeq \frac{2\Phi_0}{\lambda \cdot D} \propto \sqrt{n_{disl}} \qquad (3.3)$$

with D the island diameter. From eq. (3.3) it is clear that surface effects do not determine the plateau features in j_s, since we find $B^* \propto n_{disl}$, which is in contradiction with eq. (3.3).

Further evidence supporting dislocation pinning, is found by checking directly the influence of the surface on the matching field. A very simple way to do this is to etch a film as described in section 3.2. Evidently etching drastically changes the surface morphology. In figure 3.8 we show AFM pictures of the same film (LAD323, $n_{disl} = 20$ μm^{-2}, $D = 228$ nm), that we separated into two parts. One part was left untreated, and the other part was etched for 70 s in a 1.0 vol% Br in ethanol solution. From cross section height images we find that the surface in the etched film exhibits more roughness, with a completely erased island structure and very steep etchpits. In the untreated film the thickness varies more smoothly. Figure 3.9 shows the critical current densities of the untreated and etched sample at $T = 4.2$ K. There is no change in matching behaviour between the two samples: $B^* = 27$ mT in the as-grown sample, compared to $B^* = 28$ mT in the etched film.

In the case of surface roughness pinning vortices are strongly pinned in the trenches between islands, where the vortex length and, therefore, its condensation energy is
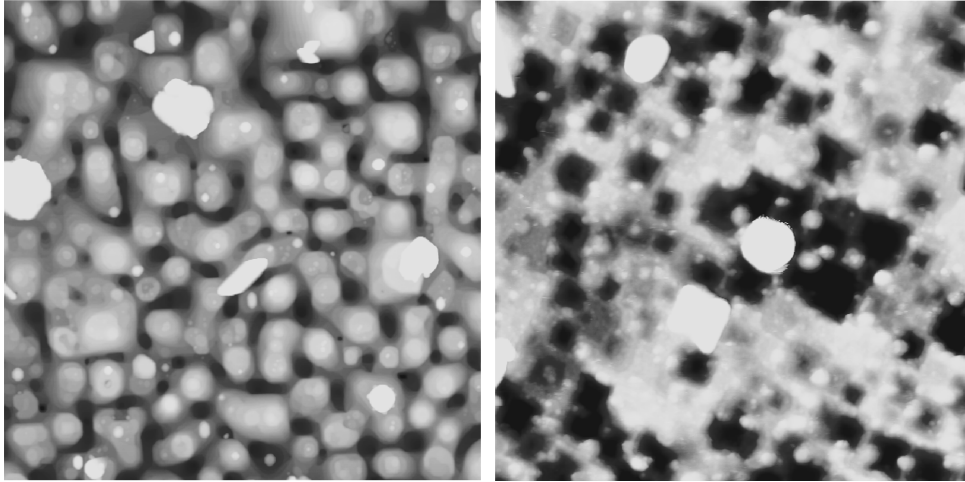
Figure 3.8: 3 x 3 μm^2 AFM image of a 140 nm YBa$_2$Cu$_3$O$_{7-\delta}$ film (LAD323), that has been cut in two parts. a) shows the untreated part and b) the same film, etched for 70 s. The surface of the etched part exhibits steep etch pits, whereas the as-grown part is characterized by trenches that are less steep.

reduced. The maximum pinning force per unit length is thus related to the thickness variations in the film [2]:

$$f_{p,\mathrm{max}} \simeq \varepsilon_l \frac{\partial \ln d}{\partial x} \tag{3.4}$$

with ε_l the vortex line energy and d the film thickness. Equating this to the Lorentz force $f_L = j_c \Phi_0$ and using $\varepsilon_l = (\varepsilon_0/\gamma^2)\ln(\lambda/\xi)$, we obtain for the maximum critical current density:

$$j_c \simeq \frac{\Phi_0}{4\pi\mu_0\gamma^2\lambda^2}\ln\kappa \cdot \frac{1}{d}\frac{\partial d}{\partial x}, \text{ for } \mu_0 H < B_\Phi \tag{3.5}$$

Analysis of the AFM pictures in figure 3.8, gives rms thickness variations $\partial d/\partial x = 0.15$ and $\partial d/\partial x = 0.49$ for the as-grown and etched part respectively. Taking $\lambda = 140$ nm, $\kappa = 100$, $\gamma^2 = 25$ (which yields $\varepsilon_l \approx 0.2\varepsilon_0$), and $d = 150$ nm, we obtain for the maximum critical current density due to surface roughness: $j_c \approx 1.4 \cdot 10^9$ Am^{-2} for the untreated film and $j_c \approx 6.3 \cdot 10^9$ Am^{-2} for the etched film[6]. We measure $j_s(B{=}0) = 1.9 \cdot 10^{11}$ Am^{-2} for the untreated and $j_s(B{=}0) = 1.15 \cdot 10^{11}$ Am^{-2} for the etched film.

---

[6]Here we have assumed that the thickness of the etched film is reduced to $d = 100$ nm, compared to the as-grown film.
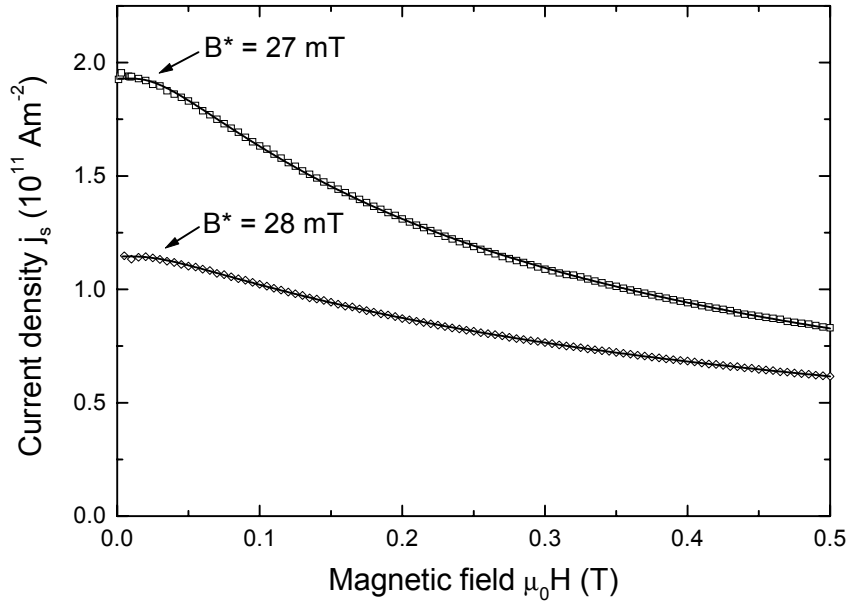
Figure 3.9: Current density $j_s(B)$ for the as-grown ($\square$) and etched part ($\lozenge$) of film LAD323. Solid lines are fits to eq. (3.1). Since the characteristic field is not affected by the drastic surface treatment, one can conclude that surface roughness does not play a role in strong vortex pinning.

The as-grown film has critical currents an order of magnitude higher than expected on the basis of eq. (3.5). Furthermore the thickness variations $\partial d/\partial x$ are bigger in the etched sample. We thus expect stronger pinning in the case of the etched film by a factor three, which is in contradiction with the observation that critical current density is lower in the etched film.

We therefore conclude that in $YBa_2Cu_3O_{7-\delta}$ films surface roughness pinning by the trenches between the islands cannot explain the low field behavior of the critical currents, because i) the matching field is proportional to n_{disl} and not to $\sqrt{n_{disl}}$, ii) etching does not change the characteristic field, although the island structure is completely erased, and iii) increased thickness variations do not lead to an increase in the measured superconducting current density. In chapter 7 we will investigate the influence of surface treatments and also the influence of film thickness on j_s further.

The conclusions of this investigation will support the model of linear defect pinning even more.

3.6 Conclusions

By investigating the superconducting properties of pulsed laser ablated $YBa_2Cu_3O_{7-\delta}$ films in relation with the defect microstructure, we found that linear defects are the dominant pinning centers at low magnetic fields. First we identified threading dislocations by means of wet chemical etching. Secondly the superconducting current density $j_s(B)$ exhibits a plateau at low magnetic fields up to a characteristic field B^* that is directly proportional to the density of linear defects, i.e. $B^* = 0.7n_{disl}\Phi_0$. In addition we found, that surface effects play a minor role in vortex pinning, by comparing two parts (one etched and one untreated) of the same film, exhibiting a different surface roughness.

For the first time, that an unambiguous *quantitative* relationship has been established between the superconducting properties and the as-grown defect microstructure of thin $YBa_2Cu_3O_{7-\delta}$ films. In many ways pinning by linear defects resembles the trapping of vortices by columnar tracks in heavy-ion irradiated single crystals. In both systems clear matching effects are observed. The characteristic field is strongly temperature dependent, and the temperature dependence of $B^*(T)$ is similar for both thin films and irradiated crystals up to $T = 40$ K. At higher temperature B^* levels off in thin films, whereas it decreases rapidly to zero at $T = 40$ K in irradiated crystals. At high magnetic fields the current density exhibits a power law decrease, $j_s(B) \sim B^\alpha$, with $\alpha = -1/2$ for thin films (shear pinning) and $\alpha = -1$ for irradiated single crystals (collective pinning).

Now that we have identified that linear defects are responsible for strong vortex pinning, we can proceed to describe the general features of vortex pinning by linear defects. The Bose glass theory has been very successful in explaining pinning by columnar tracks in irradiated single crystals. In the next chapters we treat linear defect pinning in thin films within the same framework. First we explain the theory behind the Bose glass phase and extend it to be valid for linear defects as well. In chapter 5 we present a full experimental overview of the features of strong vortex pinning in thin $YBa_2Cu_3O_{7-\delta}$ films, in terms of the current density, dynamical relaxation and pinning energy.

APPENDIX 3A: Various methods to determine the characteristic field B^*

Since the matching field B_Φ is purely a microstructural parameter, connected to the linear defect density or the density of columnar tracks, one can determine B_Φ unambiguously. In thin films B_Φ is obtained by counting the number of etchpits [21], and in irradiated samples from the irradiation dose. The characteristic (or accommodation) field B^*, however, is related to the interaction between the vortex lattice and the defect lattice. An unambiguous experimental determination of B^* is therefore not straightforward, as it is not a priori clear how B^* influences the current density $j_s(B)$.

In thin films B^* marks the end of a plateau in the critical current density. The small value of typical characteristic fields, in the order of a few tens of mT, with a maximum of $B^* \sim 100$ mT imposes experimental difficulties on the accurate measurement of B^*. Moreover, with increasing temperature B^* decreases strongly, which makes the determination of B^* even more troublesome.

In this appendix we compare three methods to determine B^* on various $YBa_2Cu_3O_{7-\delta}$ films. Up to now we used exclusively an empirical fit

$$j_s(B) = j_s(0)/\left(1 + k_1 \exp(-k_2/B) \cdot (B/k_2)^\alpha\right) \tag{A3.1}$$

with k_1, k_2 and α fit parameters, as explained in section 3.3. We find B^* from the crossing of the tangent at the inflection point and the low field plateau on a lin-lin plot (as shown in the inset of figure 3.4). This is the most relevant method, as it catches the essential physics of a constant current density for $\mu_0 H < B^*$, but it is not the most convenient way to find B^*. As a second method we use the same fit of $j_s(B)$, but we determine B^* by taking the crossing of the plateau and the tangent at the inflection point of the *log-lin plot*, i.e. of j_s versus $\ln B$. In this case the horizontal axis is extended which makes the matching behaviour more pronounced. Thirdly we determine B^* by the simple criterion $j_s(B^*)/j_s(0) = 0.95$, as in Mezzetti *et al.* [38]. From the comparison we hope to find a second method, or a useful relationship between various methods, to have at least two independent methods to determine B^*. The results on the determination of B^* on various films are shown in figure 3.10 for $T = 4.2$ K. We find that looking at the crossing in a log-lin graph and the simple 0.95-criterion give too large values for B^* compared to the original lin-lin fits, used in ref. [31]. Moreover B^*, determined from the log-lin plots, increases faster than linearly for films with many dislocations. However, using the 0.95-criterion and taking the half of $B^*(0.95)$, i.e. using the criterion $j_s(2B^*)/j_s(0) = 0.95$, we find a nice agreement with our original lin-lin fits, both at $T = 4.2$ and $T = 10$ K (inset of figure 3.10). We thus have obtained a quick and accurate alternative method of finding B^*, which we can compare with the linear fits at low temperatures. Secondly the new method allows us to find $B^*(T)$ also at high temperatures to satisfactory accuracy.
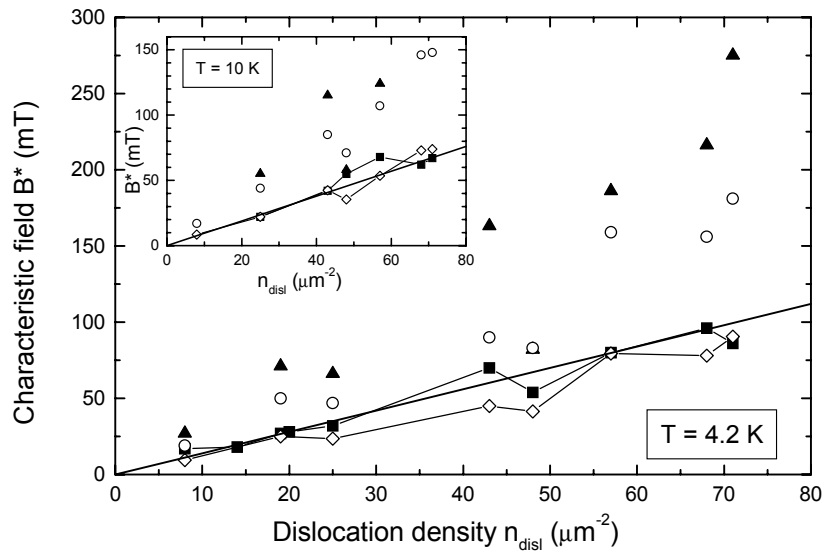
Figure 3.10: Comparison of various methods to determine B^* experimentally. $T = 4.2$ K. $-\blacksquare-$ fit according to eq. (3.1) on a *lin-lin* plot, $\blacktriangle$ idem, but B^* determined from the crossing of the plateau and the tangent at the inflection point on a *log-lin* plot, $\circ$ simple criterion $j_s(B^*)/j_s(0) = 0.95$, $-\diamond-$ idem with $j_s(2B^*)/j_s(0) = 0.95$. Inset: as the main plot, at $T = 10$ K.

References

[1]   T.L. Hylton and M.R. Beasley, Phys. Rev. B **41**, 11669 (1990)

[2]   For an overview of various pinning mechanisms, see e.g. P.H. Kes, in E. Kaldis (ed.), *Materials and Crystallographic Aspects of HTc-Superconductivity*, Kluwer Academic Publishers, 401 (1994)

[3]   M. Murakami, M. Morita, K. Doi, and K. Miyamoto, Jap. J. of Appl. Phys. **28**, 1189 (1989)

[4]   H. Douwes, P.H. Kes, Ch. Gerber, and J. Mannhart, Cryogenics **33**, 486 (1993)

[5]   M. Hawley, I.D. Raistrick, J.G. Beery, and R.J. Houlton, Science **251**, 1587 (1991)

[6]   J. Mannhart, D. Anselmetti, J.G. Bednorz, A. Catana, Ch. Gerber, K.A. Müller, and D.G. Schlomm, Z. Phys. B **86**, 177 (1992)

[7]   H. Douwes and P.H. Kes, J. Alloys & Compounds **195**, 451 (1993)

[8]   V.M. Pan, A.L. Kasatkin, V.L. Svetchnikov, and H.W. Zandbergen, Cryogenics **33**, 21 (1993)

[9]   A. Díaz, L. Mechin, P. Berghuis, and J.E. Evetts, Phys. Rev. Lett. **80**, 3855 (1998)

[10] L. Civale, Supercond. Sci. Technol. **10**, A11 (1997), and references therein

[11] I. Maggio-Aprile, C. Renner, A. Erb, E. Walker, and Ø. Fischer, Nature **390**, 487 (1997)

[12] A. Gurevich and L.D. Cooley, Phys. Rev. B **50**, 13563 (1994)

[13] Ch. Jooss, R. Warthmann, H. Kronmüller, T. Haage, H.-U. Habermeier, and J. Zegenhagen, Phys. Rev. Lett. **82**, 632 (1999),
      Ch. Jooss, R. Warthmann, and H. Kronmüller, Phys. Rev. B **61**, 12433 (2000)

[14] Ch. Jooss, A. Forkl, R. Warthmann, H.-U. Habermeier, B. Leibold, and H. Kronmüller, Physica C **266**, 235 (1996),
      Ch. Jooss, A. Forkl, and H. Kronmüller, Physica C **268**, 87 (1996)

[15] E. Sheriff, R. Prozorov, Y. Yeshurun, A. Shaulov, G. Koren, and C. Chabaud-Villard, J. Appl. Phys. **82**, 4417 (1997)

[16] L. Civale, A.D. Marwick, T.K. Worthington, M.A. Kirk, J.R. Thompson, L. Krusin-Elbaum, Y. Sun, J.R. Clem, and F. Holtzberg, Phys. Rev. Lett. **67**, 648 (1991)

[17] C. Gerber, D. Anselmetti, J.G. Bednorz, J. Mannhart, and D.G. Schlom, Nature **350**, 279 (1991)

[18] B. Dam, J.H. Rector, J.M. Huijbregtse, and R. Griessen, Physica C **305**, 1 (1998)

[19] D. Hull and D.J. Bacon, *Introduction to Dislocations*, Pergamon Press, 3rd edition (1984)

[20] S. Freisem, A. Brockhoff, D.G. de Groot, B. Dam, and J. Aarts, J. Magn. Mat. **165**, 380 (1997)

[21] J.M. Huijbregtse, B. Dam, R.C.F. van der Geest, F.C. Klaassen, R. Elberse, J.H. Rector, and R. Griessen, Phys. Rev. B **62**, 1338 (2000)

[22] J.M. Huijbregtse, B. Dam, A. Mendoza, J.H. Rector, R. Griessen, B.J. Kooi, and J.Th.M. de Hosson, accepted for publication in Phys. Rev. B (2002)

[23] J.M. Huijbregtse, B. Dam, J.H. Rector, and R. Griessen, J. Appl. Phys. **86**, 6528 (1999)

[24] M. Qvarford, K. Heeck, J.G. Lensink, R.J. Wijngaarden, and R. Griessen, Rev. Sci. Instrum. **63**, 5726 (1992)

[25] D.R. Nelson and V.M. Vinokur, Phys. Rev. B **48**, 13060 (1993)

[26] G. Blatter, M.V. Feigel'man, V.B. Geshkenbein, A.I. Larkin and V.M. Vinokur, Rev. Mod. Phys. **66**, 1125 (1994)

[27] Y. Gao, K.L. Merkle, G. Bai, H.L.M. Chang and D.J. Lam, Physica C **174**, 1 (1991)

[28] M. Däumling and D.C. Larbalestier, Phys. Rev. B **40**, 9350 (1989)

[29] L.W. Conner and A.P. Malozemoff, Phys. Rev. B **43**, 402 (1991)

[30] M. Pannetier, F.C. Klaassen, R.J. Wijngaarden, M. Welling, K. Heeck, J.M. Huijbregtse, B. Dam, and R. Griessen, Phys. Rev. B **64**, 144505 (2001), and chapter 6 of this thesis

[31] B. Dam, J.M. Huijbregtse, F.C. Klaassen, R.C.F. van der Geest, G. Doornbos, J.H. Rector, A.M. Testa, S. Freisem, J.C. Martínez, B. Stäuble-Pümpin, and R. Griessen, Nature **399**, 439 (1999)

[32] L. Civale, L. Krusin-Elbaum, J.R. Thompson, R. Wheeler, A.D. Marwick, M.A. Kirk, Y.R. Sun, F. Holtzberg, and C. Feild, Phys. Rev. B **50**, 4102 (1994), L. Krusin-Elbaum, A.D. Marwick, R. Wheeler, C. Feild, V.M. Vinokur, G.K. Leaf, and M. Palumbo, Phys. Rev. Lett. **76**, 2563 (1996)

[33] E. Mezzetti, R. Gerbaldo, G. Ghigo, L. Gozzelino, B. Minetti, C. Camerlingo, A. Monaco, G. Cuttone, and A. Rovelli, Phys. Rev. B **60**, 7623 (1999), G. Ghigo, A. Chiodoni, R. Gerbaldo, L. Gozzelino, E. Mezzetti, B. Minetti, C. Camerlingo, G. Cuttone, and A. Rovelli, Supercond. Sci. Technol. **12**, 1059 (1999), E. Mezzetti, A. Chiodoni, R. Gerbaldo, G. Ghigo, L. Gozzelino, B. Minetti, C. Camerlingo, and A. Monaco, Physica C **332**, 115 (2000)

[34] L. Krusin-Elbaum, L. Civale, J.R. Thompson, and C. Feild, Phys. Rev. B **53**, 11744 (1996)

[35] R. Wördenweber, Phys. Rev. B **46**, 3076 (1992), R. Wördenweber, Cryogenics **32**, 1098 (1992)

[36] J.R. Thompson, L. Krusin-Elbaum, L. Civale, G. Blatter, and C. Feild, Phys. Rev. Lett. **78**, 3181 (1997)

[37]   G. Doornbos, *Pinning and Crossovers in the Vortex-Dynamics of High-T_c Thin Films*, PhD thesis, Vrije Universiteit Amsterdam (2001)

[38]   Note, that Mezzetti *et al.* [33] use the criterion $j_s(B^*)/j_s(0) = 0.9$, whereas we choose to take $j_s(B^*)/j_s(0) = 0.95$

Chapter 4

Bose glass theory for pinning by natural linear defects

We present the theoretical framework to describe strong pinning by linear defects. Strong pinning by linear defects is usually described in terms of a Bose glass phase [1]. However, many results of the Bose glass theory are valid only when the linear defects are either much larger or much smaller than the vortex core. We extend the Bose glass theory to include also linear defects that are approximately equal in size with respect to the vortex. General expressions for the vortex pinning potential $\varepsilon_r(R)$ and for its renormalization due to thermal fluctuations are derived. The temperature dependence of the true critical current density can be fitted with $j_c(T) \sim 1/\left(\lambda^2(T)\xi^\nu(T)\right)$, with $\nu = 1 - 3$ a fit parameter depending on the ratio between the linear defect radius r_r and the vortex core radius $\sqrt{2}\xi$. The renormalization function of the pinning potential $f(k_B T/\tilde{T}_{dp}^r)$, with $\tilde{T}_{dp}^r$ the depinning energy, becomes linear in temperature $f(k_B T/\tilde{T}_{dp}^r) \simeq 1 - k_B T/\tilde{T}_{dp}^r$ at low temperatures. We show, using typical parameters for YBa$_2$Cu$_3$O$_{7-\delta}$ thin films, how the various temperature effects influence the pinning potential $\varepsilon_r(R,T)$ and the critical current density $j_c(T)$[1].

---

[1]This chapter is based on the theoretical section of the paper by F.C. Klaassen, G. Doornbos, J.M. Huijbregtse, R.C.F. van der Geest, B. Dam, and R. Griessen, *Vortex pinning by natural linear defects in thin films of YBa$_2$Cu$_3$O$_{7-\delta}$*, Phys. Rev. B. **64**, 184523 (2001)

4.1 Introduction

A general theory describing vortex pinning by many point defects was established already long before the discovery of high-T_c superconductors [2, 3]. In this so-called theory of weak collective pinning a single vortex is pinned by many pinning centers, that are randomly distributed and have a random pinning force. The vortex tries to increase its total pinning energy $\sim \sum f_{pin}$ by taking advantage of as many pinning centers as possible, while on the other hand a vortex wants to minimize its elastic energy by remaining straight. As a result of this competition between pinning energy ε_r and elastic energy ε_l, the vortex breaks up in correlated pieces of length L_c, the correlation length.

This picture works very well in describing the situation in single crystals of high-T_c superconductors, but it is not appropriate for strong pinning in thin films, where vortices are pinned over their full length by extended defects. Particularly, it cannot explain the plateau like features in $j_c(B)$ observed in thin films at low magnetic fields, nor the strong magnetic field dependence of $j_c(B)$ at high magnetic fields [4].

A second important phenomenon not described in the theory of weak collective pinning, is the thermal activation of vortices. In high-T_c superconductors vortex motion due to thermal activation is particularly important, because of the short coherence length and the high transition temperature. This results in a large relaxation rate, extending to logarithmic timescales, and a strongly current dependent activation barrier $U(j) \sim U_c \left[(j_c/j)^\mu - 1 \right]$, with U_c the pinning energy, j_c the critical current density, and j the applied current density [5]. This behaviour of $U(j)$ is fundamentally different from the classical Kim-Anderson activation energy $U(j) \sim U_c \left[1 - j/j_c \right]$ [6], since it results in a diverging activation barrier for small currents $j \to 0$, whereas the Kim-Andersen creep barrier stays finite for arbitrary small currents. This typical creep behaviour for high-T_c compounds, implying a vanishing linear resistivity $\rho(j \to 0) \to 0$, has triggered the idea of glassy-like behaviour in the mixed phase (hence the exponent μ is called the glass exponent) [7]. At the so-called glass line a phase transition takes place to a vortex liquid phase with a non-vanishing linear resistivity. Experimental evidence for the existence of a vortex glass, obeying the predicted scaling laws, was first observed in thin films [8], but soon also in single crystals [9]. Since then extensive work has been devoted to understanding the scaling behaviour associated with the vortex glass phase, and to the nature of the phase transition from vortex glass to vortex liquid [10].

Whereas the vortex glass phase is directly associated with pinning by point-like disorder, in the case of correlated, or extended defects, the nature of the vortex phase is different. Whereas point-like disorder stimulates vortex *wandering* and entanglement, correlated disorder promotes *localization* due to the extended nature of the defect. Nelson and Vinokur, following similar considerations on the superfluid to insulator transition in ^{4}He [11], observed that the localization of vortices, pinned by extended defects, is analogous to the binding of bosonic particles in a potential minimum [12]. In fact the Hamiltonian describing the binding and the elementary excitations (hopping) of 2D bosons in a random static potential can be mapped onto the vortex system. Therefore this vortex phase is called a Bose glass. Both vortex and

Bose glass show the same scaling behaviour at the glass transition. However, when the magnetic field is tilted away from c-axis, the vortex glass line shows a smooth, parabolic angular dependence, whereas the Bose glass phase is heavily suppressed, and the Bose glass line exhibits a profound cusp [1]. This is a direct consequence of the correlated nature of extended defects, that pin vortices in a specific direction (usually along the c-axis). Point-like disorder incoherently pins vortices in random directions, and is therefore not sensitive to tipping away the magnetic field off the c-axis. The predicted angular dependence of the Bose glass line has indeed been observed in single crystals with columnar tracks [13] and with a high density of twin planes [14, 15].

As the Hamiltonian of the 2D boson system can be rewritten into vortex language, a simple mapping of the relevant quantities was constructed to interpret the 2D boson characteristics in terms of strong vortex pinning: $\hbar \rightarrow T$, $a \rightarrow 2b_0$, $m \rightarrow \varepsilon_l$ and $U_0 \rightarrow \varepsilon_r$ [1]. We can understand this mapping in the following way: vortex pinning involves the competition between elastic energy and pinning energy. In this sense the pinning energy ε_r is related to the potential minimum for the boson U_0, and the elastic energy ε_l corresponds to the inertia of the vortex, or, equivalently, to the mass m of the boson. The width of the trapping potential a in the boson system is transferred to the extension of the pinning potential $b_0 \equiv \max(r_r \sqrt{2}\xi)$ (r_r is the linear defect radius and $\sqrt{2}\xi$ the vortex core radius). Finally the thermal fluctuations T of the vortex system represent the quantum scalar of the boson system $\hbar$. The boson-vortex mapping concerns both i) the free energy of both systems, and the elementary excitations from one defect (potential minimum) to another.

The Bose glass theory [1], derived for extended (linear or planar) defects, has successfully described many results of the strong pinning mechanism in irradiated single crystals [16]. As there is no essential difference between natural linear defects and columnar tracks as a result of heavy-ion irradiation [17], we will use the same theory to describe pinning by natural linear defects in thin films. An essential parameter in our description is the ratio $x \equiv r_r / \sqrt{2}\xi$ between the radius of a linear defect and the vortex core. In thin films both quantities are comparable in size, which changes the description appreciably. Note that our description is an extension of the Bose glass theory: using the same basic ideas, we generalize the results of the Bose glass theory to become valid for all defect sizes.

4.2 Basic elements from the Bose glass theory

The irradiation of single crystals or films with heavy ions creates columnar tracks where the crystal structure is heavily distorted, causing a suppression of the superconducting order parameter. Similarly the core of a dislocation in thin films is characterized by strong deformations of the crystal lattice and a corresponding suppression of the order parameter. Mkrtchyan and Shmidt [18] calculated the pinning properties of a cylindrical hole in a superconductor, which provides an accurate description

for large linear defects $1 \ll x \ll \kappa$.[2] For small defects Blatter *et al.* [3] calculated the pinning potential from the suppression of the order parameter inside a defect. In this section we describe the main aspects of the Bose glass theory that are relevant for strong vortex pinning in thin films. We mainly follow the description used by Blatter *et al.* [19], which is completely analogous to the original paper by Nelson and Vinokur [1].[3]

4.2.1 Pinning potential and critical current

The starting point in the Bose glass theory is, that at low magnetic fields a single vortex is strongly pinned by a linear (columnar) defect. The vortices can freely accommodate to the lattice of pinning sites until the shear energy exceeds the pinning energy per unit length ε_r. Then a crossover to a collective pinning regime occurs at the crossover or accommodation field $B^* \approx 4 \left(\varepsilon_r / \varepsilon_0 \right) B_\Phi$, with $\varepsilon_0 = \Phi_0^2 / 4\pi\mu_0\lambda^2$ a characteristic vortex energy per unit length and $B_\Phi \equiv n_{disl}\Phi_0$ is the matching field, the field where the vortex density exactly equals the defect density.

In the limit of very large, $x \gg 1$, and very small defects, $x \ll 1$, the pinning potential per unit length yields [19]:

$$\varepsilon_r(R) = \frac{\varepsilon_0}{2} \ln\left(1 - \frac{r_r^2}{R^2}\right) \qquad\qquad \text{for } x \gg 1 \qquad\qquad (4.1)$$

$$\varepsilon_r(R) = -\frac{\varepsilon_0}{2} \frac{r_r^2}{R^2 + 2\xi^2} \qquad\qquad \text{for } x \ll 1 \qquad\qquad (4.2)$$

with R the distance of the vortex from the center of the pinning site. Since the pinning potential diverges in eq. (4.1) at $R = r_r$, a cutoff of the pinning potential is used for small R inside the defect:

$$\varepsilon_r(R < r_r) = -\varepsilon_0 \ln(r_r/\sqrt{2}\xi) \qquad\qquad (4.3)$$

The critical current density j_c is determined by the balance between the Lorentz force per unit length $f_L = j_c\Phi_0$ and the maximum pinning force $-d\varepsilon_r/dR\,|_{\max}$. For large defects the pinning force on a vortex at $R = r_r + \sqrt{2}\xi$ is used to determine j_c, giving $f_{pin} \approx \varepsilon_r/\sqrt{2}\xi$ [19]. The critical current density is now:

---

[2]The results of Mkrtchyan and Shmidt are strictly valid only for small length scales compared to the penetration depth ($r_r \ll \lambda$, or $x \ll \kappa$). As the Ginzburg Landau parameter κ is large for high-T_c compounds $\kappa \approx 100$, this condition is always satisfied in our system, and we omit it for convenience.

[3]The paper by Nelson and Vinokur [1] and the review by Blatter *et al.* [3] use different and sometimes even confusing symbols. The analogy in notation between ref. [1] and ref. [3] is: $c_0 \to r_r$, $T_0 \to T_{r\xi}$, $T_1 \to T_{dp}$, $T_{dp} \to T_{dl}$, and $T^* \to \tilde{T}_{dp}^r$. Our notation follows that of Blatter *et al.*, with one exception that the accommodation field or characteristic field is denoted by B^* (like in refs. [1, 4, 17]) instead of B_{rb}.

$$j_c = \frac{3\sqrt{3}}{4\sqrt{2}} j_0 \simeq j_0 \qquad\qquad \text{for } x \gg 1 \qquad\qquad (4.4)$$

$$j_c = \frac{27\sqrt{2}}{64} \left(\frac{r_r}{2\xi(T)} \right)^2 j_0 \qquad\qquad \text{for } x \ll 1 \qquad\qquad (4.5)$$

In real samples the measured critical current density is usually smaller, because the defects do not have a completely suppressed order parameter, contrary to real cylindrical holes. For columnar tracks this difference is accounted for by including an extra factor $\eta \approx 0.1 - 0.2$, denoting the pinning efficiency [20]. The physical meaning of η is somewhat ill-defined; η incorporates effects of a non-ideal pinning center, the reduced size of the defect compared to the vortex, and also it includes errors coming from the approximations and assumptions in the Bose Glass theory [21]. The pinning efficiency η thus serves more as a convenient empirical factor than a physical quantity, taking care of any numerical inconsistencies between the "ideal" theoretical system and the actual experimental situation.

Note that the results of eqs. (4.1) to (4.5) are valid for limiting cases only, i.e. either for $x \gg 1$ or $x \ll 1$. As we saw in the previous chapter, the vortex core and the dislocation core in thin films are comparable in size. Even in irradiated crystals the size of a columnar track has a radius $r_r \lesssim 5$ nm, i.e. $x \approx 3$, which is not in the limit of Mkrtchyan and Shmidt. We conclude that for describing linear defects in thin films and also columnar tracks in irradiated single crystals, we need to derive an interpolation between the results of the Bose glass theory. The results of Mkrtchyan and Shmidt are, however, useful for films with antidots, that have a typical radius $r_r \simeq 0.1 - 0.2\ \mu$m, i.e. $x \gg 1$. They explain the experimentally observed matching effects in antidot films and predict how many vortices can be pinned by a single antidot [22, 23, 24].

4.2.2 Crossovers with increasing temperature

As the coherence length $\xi(T)$ increases with increasing temperature, the ratio $x(T) \sim 1/\xi(T)$ decreases. Various crossovers occur in pinning behaviour when increasing the temperature from zero to T_c. Because we describe linear defect pinning in YBa$_2$Cu$_3$O$_{7-\delta}$, we take $T_c = 90$ K in all calculations throughout this chapter. Starting with a linear defect somewhat larger than the vortex ($x \gtrsim 1$) at $T = 0$, we meet the following crossovers; at a temperature $T = T_{r\xi}$ the defect size and vortex core radius are equal, i.e. $r_r = \sqrt{2}\xi(T_{r\xi})$ ($x(T_{r\xi}) = 1$). The crossover temperature $T_{r\xi}$ thus describes the crossover between pinning by large defects and pinning by small defects (with respect to the vortex size). At the depinning temperature T_{dp}, thermal fluctuations of the vortex are comparable to the depth of pinning potential. In this situation the fluctuations are so strong that the vortex can spontaneously depin from its defect. Beyond T_{dp} the critical current decreases exponentially. Finally at the delocalization temperature T_{dl} the thermal fluctuations become of the order of the average defect
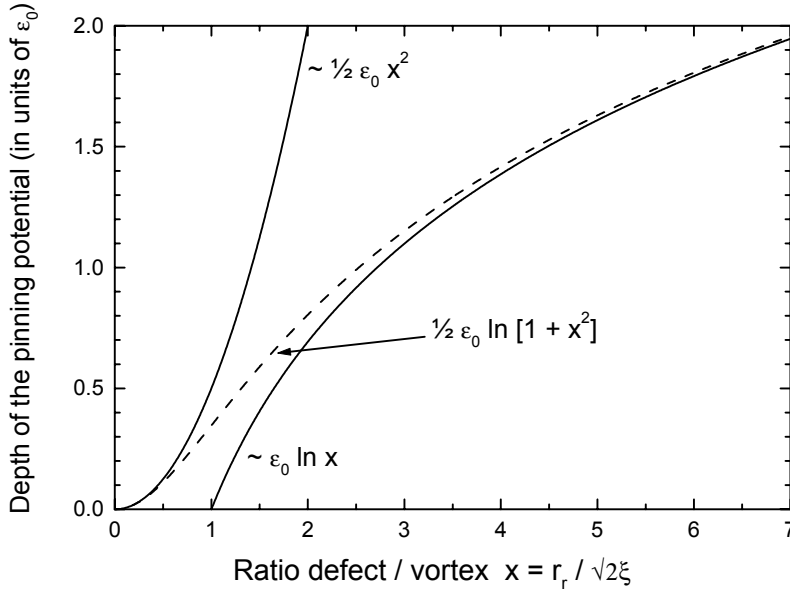
Figure 4.1: The depth of the vortex pinning potential can be described by a convenient interpolation formula $\varepsilon_r(0) \sim \frac{1}{2}\varepsilon_0(1+x^2)$ (dashed line), interpolating between the theoretical results for small defects ($\varepsilon_r(0) \sim \frac{1}{2}\varepsilon_0 \cdot x^2$) and large defects ($\varepsilon_r(0) \sim \varepsilon_0 \ln x$) (solid lines). Note that the expressions for large x are valid for $1 \ll x \ll \kappa$. At very large $x \lesssim \kappa$ the depth of the pinning potential saturates around $\varepsilon_r(0) \sim \varepsilon_0 \ln \kappa$.

distance between the linear defects d_r, i.e. $\left\langle u^2(T) \right\rangle_{th} \simeq d_r^2$. The vortex cannot be considered localized on a single defect, but instead is collectively pinned by all linear defects within a certain correlated area of size $l_{loc} \simeq d_r(T/T_{dl})^2$.

In general $T = 0 \leq T_{r\xi} < T_{dp} < T_{dl} < T_c = 90$ K. For small defects with $x(0) < 1$ we have $T_{r\xi} = 0$ K, and we are always in the small defect limit. Taking $r_r = 3$ nm $\approx 2\xi(0)$ which is a reasonable estimate for screw dislocations [4], we find for the crossover temperature $T_{r\xi} \approx 0.58T_c = 52$ K. The depinning and delocatization temperature have to be determined self-consistently as the depinning energy, scaling the thermal fluctuations, $\tilde{T}_{dp}^r \equiv b_0\sqrt{\varepsilon_l\varepsilon_r}$, is itself temperature dependent. Comparing the fluctuation length with the defect size r_r and average defect distance d_r, we obtain the following estimates for T_{dp} and T_{dl}, respectively:

$$T_{dp}, T_{dl} \approx \frac{\nu}{\nu+1} T_c, \text{ with } \nu = \frac{r_r}{4\xi_{ab}(0)} \frac{\alpha_{dp,dl}}{\sqrt{G_i}} \text{ and } \alpha_{dp} = 1, \alpha_{dl} = \ln \frac{d_r^2}{b_0^2} \qquad (4.6)$$

Taking $r_r = 2\xi(0)$, $d_r = 140$ nm, and the Ginzburg number $G_i = 0.01$, we obtain $T_{dp} \approx 0.83 T_c = 75$ K and $T_{dl} \approx 0.97 T_c = 87$ K for thin $YBa_2Cu_3O_{7-\delta}$ films. The delocalization temperature is very close to T_c which is not surprising, as the average defect distance is very large. We will therefore not consider delocalization, but focus on the crossover in defect size at $T_{r\xi}$, and on the influence of thermal fluctuations on the depinning of vortices.

4.3 The pinning potential $\varepsilon_r(R)$ for $x \approx 1$

As we have explained, the solutions for the pinning potential, derived within the Bose glass theory, are not applicable, when the vortex core size and the defect radius are comparable. The expressions eqs. (4.1) to (4.3) connect only for $R \to \infty$, i.e. when the vortex is far away from the linear defect. When the vortex is pinned inside the defect, i.e. for $R \lesssim r_r$, both equations deviate strongly in the limit $x \to 1$. In fact the proposed cut off in eq. (4.3) implies that the pinning potential $\varepsilon_r(R)$ vanishes for $x \downarrow 1$, which is clearly unphysical.

To interpolate between both limits for x, a convenient interpolation formula for the depth of the pinning potential has been introduced [1]:

$$\varepsilon_r(0) \approx -\frac{\varepsilon_0}{2} \ln \left[1 + \frac{r_r^2}{2\xi^2} \right] = -\frac{\varepsilon_0}{2} \ln \left[1 + x^2 \right] \qquad (4.7)$$

Eq. (4.7) connects the pinning potential in both limits, as depicted in figure 4.1, however only for $R = 0$. Figure 4.1 indicates, that eqs. (4.2) and (4.3) give a reasonable estimate for $\varepsilon_r(R = 0)$ for $x \lesssim 0.5$ and $x \gtrsim 3$. This suggests that the results of the Bose glass theory are applicable within these ranges of x, also at $R \neq 0$. The typical size of edge and screw dislocations is $r_r \approx 1-3$ nm, i.e. $x \approx 0.5-1.5$, which lies outside the range for which eqs. (4.1) to (4.5) are reasonably accurate. In order to make a quantitative comparison between theory and experiment, a more general derivation for the pinning potential is thus required. Even for the larger columnar tracks, we find that $x \lesssim 3$ and the limiting cases of the Bose glass theory are not very accurate. Note, that the coherence length $\xi(T)$ increases with temperature. When at zero temperature $x = r_r/\sqrt{2}\xi(0) > 1$, there is always a crossover in behaviour from $x > 1$ to $x < 1$, namely at $T = T_{r\xi}$. This indicates that a general expression, valid for $x \approx 1$, is always required to describe the temperature dependence of $\varepsilon_r(R,T)$.

To obtain the pinning potential for all defect sizes we calculate how much the order parameter is reduced at the position of the defect. For small defects a similar derivation leads to eq. (4.2), where it is assumed that $|\Psi(R)|^2 = |\Psi(0)|^2$ for all R inside the defect [19]. This is a good approximation when the linear defect is much smaller than the vortex. However, when both vortex and defect are comparable in size, the su-

perconducting order parameter $|\Psi(R)|^2$ varies significantly inside the defect, and we should integrate the reduction of the order parameter $1 - |\Psi(R)|^2$ over the full defect. For a vortex having its center at a position R from the center of the defect, situated in the origin of the coordinate system, the pinning potential is:

$$\varepsilon_r(R) = -\frac{1}{2}\mu_0 H_c^2 \int_0^{2\pi} \int_0^{r_r} \left[1 - \left|\Psi\left(|\vec{r} - \vec{R}|\right)\right|^2\right] r\, dr\, d\vartheta, \tag{4.8}$$

with $\left|\Psi\left(|\vec{r} - \vec{R}|\right)\right|^2$ the size of the superconducting order parameter at a point (r, ϑ). Taking for the vortex core $\Psi(R') = f(R')\exp[i\varphi]$, with $f(R') = R'/(R'^2 + 2\xi^2)^{1/2}$ [25], we obtain (see appendix 4A for a derivation):

$$\varepsilon_r(R) = -\frac{\varepsilon_0}{2}\left\{\mathrm{arcsinh}\left[\frac{1}{2}\frac{\sqrt{2}\xi}{|R|}\left(\frac{r_r^2 - R^2 + 2\xi^2}{2\xi^2}\right)\right] - \mathrm{arcsinh}\left[\frac{1}{2}\frac{\sqrt{2}\xi}{|R|}\left(\frac{-R^2 + 2\xi^2}{2\xi^2}\right)\right]\right\} \tag{4.9}$$

The depth of the pinning potential at $R = 0$ is given by (see appendix 4A):

$$\varepsilon_r(0) = -\frac{\varepsilon_0}{2}\ln\left[1 + x^2\right] \tag{4.10}$$

Note that eq. (4.10) is exactly the interpolation formula eq. (4.7), proposed by Nelson and Vinokur [1], showing that it is not only a convenient expression interpolating between two limiting cases, but physically describes the minimum of the pinning potential of linear defects for all x.

In figure 4.2 the pinning potentials according to eq. (4.9) are drawn together with eqs. (4.1) and (4.2), for $r_r = 3\xi$, $r_r = 2\xi$, $r_r = \sqrt{2}\xi$ and $r_r = \xi$. In the limit of large R eq. (4.9) approaches the theoretical results of Mkrtchyan and Shmidt, and of Nelson and Vinokur, but for small R, i.e. when the vortex is inside the defect, strong deviations occur. The depth of the potential eq. (4.10) is smaller than in eqs. (4.1) and (4.2) when $r_r \approx \xi$. This corrects for the unphysical divergence of the pinning potential in eq. (4.1) at $R = r_r$. Also the quadratic increase of $\varepsilon_r(0)$ with x for small defects (eq. (4.2)) is clearly too strong when $x \uparrow 1$.

The analytical expression eq. (4.9) is not convenient for calculating, for example, the critical current. We therefore seek a more convenient form. The Taylor expansion of eq. (4.9) is

$$\varepsilon_r(\mathbf{R}) = \varepsilon_r(\mathbf{R} = \mathbf{0}) + \frac{\varepsilon_0}{2}\frac{r_r^2}{\left(r_r^2 + 2\xi^2\right)^2}\mathbf{R}^2 + \frac{\varepsilon_0}{2}\frac{r_r^2\left(r_r^2 - 4\xi^2\right)}{2\left(r_r^2 + 2\xi^2\right)^4}\mathbf{R}^4 + O(\mathbf{R}^6), \tag{4.11}$$

with $\varepsilon_r(\mathbf{R} = \mathbf{0})$ given by eq. (4.10). This Taylor expansion is especially useful when calculating the effect of thermal fluctuations (section 4.4.2). Unfortunately it cannot be used to estimate of the maximum pinning force $f_{p,\mathrm{max}} = -d\varepsilon_r/dR\,|_{\mathrm{max}}$. Note, that the 4th order term changes sign and vanishes for $r_r = 2\xi$. For large defects $r_r > 2\xi$ eq. (4.11) does not have an inflection point, and for small defect sizes the inflection point of eq. (4.9) and of the Taylor expansion give strongly deviating results.
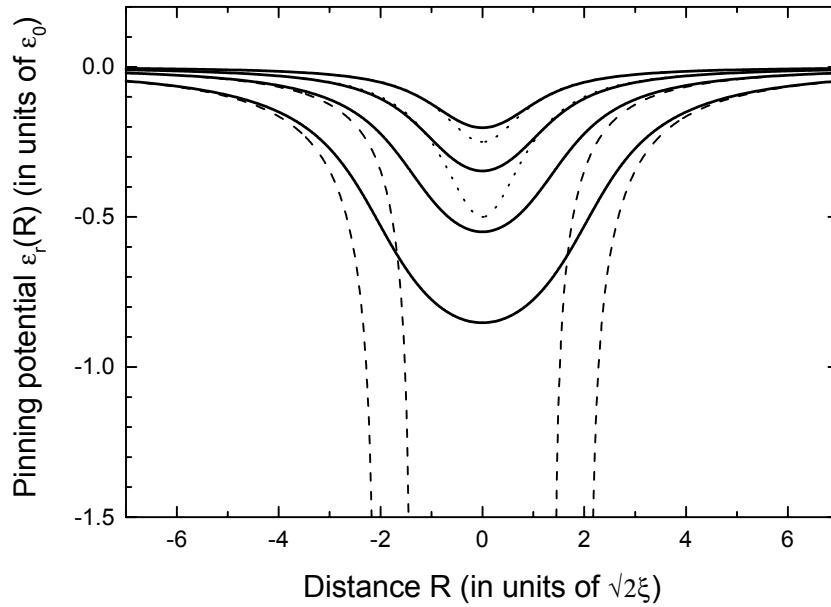
Figure 4.2: Pinning potential $\varepsilon_r(R)$ for (from bottom to top) $r_r = 3\xi$, 2ξ, $\sqrt{2}\xi$ and ξ, together with the theoretical limits of the Bose glass theory (dashed lines for large defects $x > 1$, and dotted lines for small defects $x < 1$). The expressions, derived in the limit of small or large defects are appropriate at large distances, $R \gg r_r$. However, when the vortex is inside the defect, strong deviations occur with the general pinning potential $\varepsilon_r(R)$, derived in this chapter.

Therefore we have to go back to the original function and calculate the maximum pinning force numerically. In figure 4.3 we have plotted the maximum pinning force versus the defect size, determined numerically from eq. (4.9). As it is quite cumbersome to determine the critical current density, including its temperature dependence, numerically, we like to find an easy analytical solution that approaches the numerical results reasonably well. We propose that the pinning force is maximum, when the center of the vortex is exactly at the edge of the linear defect, i.e. when $R = r_r$. Physically this seems reasonable since the vortex is exactly on the edge of i) being dragged into the defect (pinning), and of ii) flying off from the defect (depinning). The line for $f_p = -d\varepsilon_r/dR \mid_{R=r_r}$ is plotted in figure 4.3 as well (dashed line) together with the relative error from the numerically calculated $f_{p,\mathrm{max}}$ (inset of figure 4.3). The approximation is quite good, with a relative error $\Delta f_{\mathrm{max}}/f_{\mathrm{max}} < 10\%$ for $x > 0.5$. This leads to the following expression for the maximum pinning force, for not too small defect sizes:

$$f_{p,\mathrm{max}} \approx -\frac{d\varepsilon_r(R)}{dR} \mid_{R=r_r} = \frac{\varepsilon_0}{2r_r} \left(\frac{\xi^2 + r_r^2}{\xi\sqrt{(2r_r^2 + \xi^2)}} - 1 \right) \tag{4.12}$$

For smaller defect sizes one can use Blatter's estimate from eq. (4.2):
$f_{p,\mathrm{max}} = \frac{9\sqrt{2}}{16\sqrt{3}}\varepsilon_0 \left(\frac{r_r}{2\xi}\right)^2$ (dotted line in figure 4.3).
The eqs. (4.11) and (4.12), derived in this section, provide us with a relatively simple framework to calculate the temperature dependence of the critical current density. Note, that our derivation is also useful for columnar tracks, that have a size not much larger than the vortex core, at least at higher temperatures. The determination of $f_{p,\mathrm{max}}$ gives the intrinsic temperature dependence of $j_c(T)$, the Taylor expansion is particularly useful to calculate the effect of thermal fluctuations. Both phenomena are treated in more detail in the next section.

4.4 The influence of temperature on the critical current density

There are two effects that determine the temperature dependence of $j_c(T)$. First there is an intrinsic temperature dependence, due to the parameters $\lambda(T)$ and $\xi(T)$. With increasing temperatures the pinning potential becomes more shallow. This is not an thermal effect in the sense that it is connected to the thermal movement of the vortex, but it is a direct consequence of the temperature dependence of the Ginzburg Landau parameters $\lambda(T)$ and $\xi(T)$. In different words, the "strength" of superconductivity itself decreases with temperature (more physically one can say that the thermodynamical field H_c, or the superconducting order parameter $|\Psi|^2$, decreases with increasing temperature). The second effect is directly connected to the vortex movements: it is the effect of thermal fluctuations.
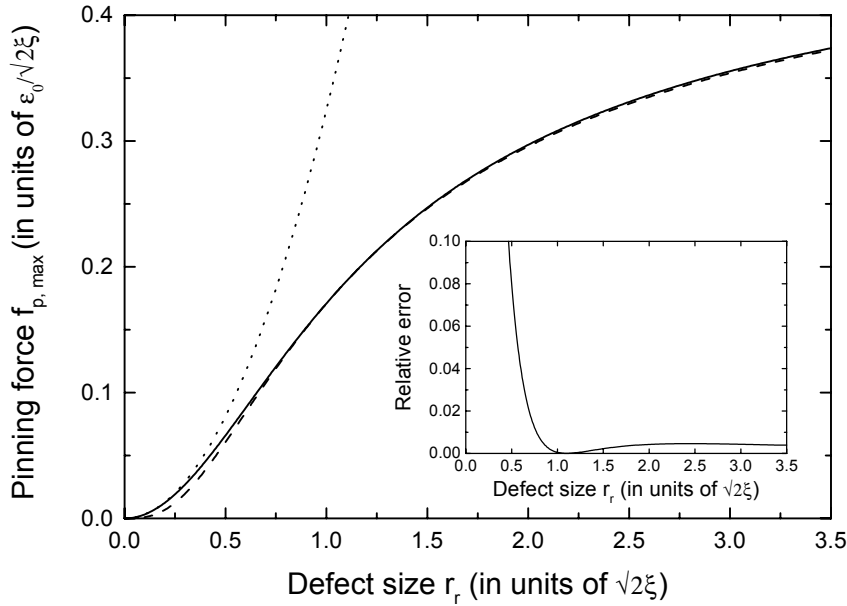
Figure 4.3: Maximum pinning force $f_{p,\mathrm{max}} = -d\varepsilon_r/dR \mid_{\mathrm{max}}$ versus the defect size for linear defects (solid line). The dashed line is an approximation, assuming $f_{p,\mathrm{max}} = f_{p,R=r_r}$, i.e. at the border of a linear defect. The dotted line represents the small defect limit from Blatter *et al.* [3]. Inset: The relative error between $f_{p,\mathrm{max}}$ and the approximation $f_{p,R=r_r}$ shows that our approximation is accurate for $x > 0.5$. For smaller defect sizes we can use the expressions, derived by Blatter *et al.* [3]

Note, that there is a third temperature effect as well, namely thermal activation of vortices. This activation causes relaxation, and is responsible for the difference between the experimentally measured j_s and the true critical current density j_c. As we consider only the true critical current in this chapter, we do not go into the details of thermal activation or relaxation, which are extensively investigated in chapter 5.

4.4.1 Intrinsic temperature effects

The temperature dependence of the Ginzburg Landau parameters $\lambda(T)$ and $\xi(T)$ immediately affects the critical current. Both the energy scale $\varepsilon_0(T) \sim 1/\lambda^2(T)$ and the depairing current $j_0 \sim 1/\left(\lambda^2(T)\xi(T)\right)$ decrease with increasing temperature. For large and small linear defects we can summarize the temperature dependence of $j_c(T)$
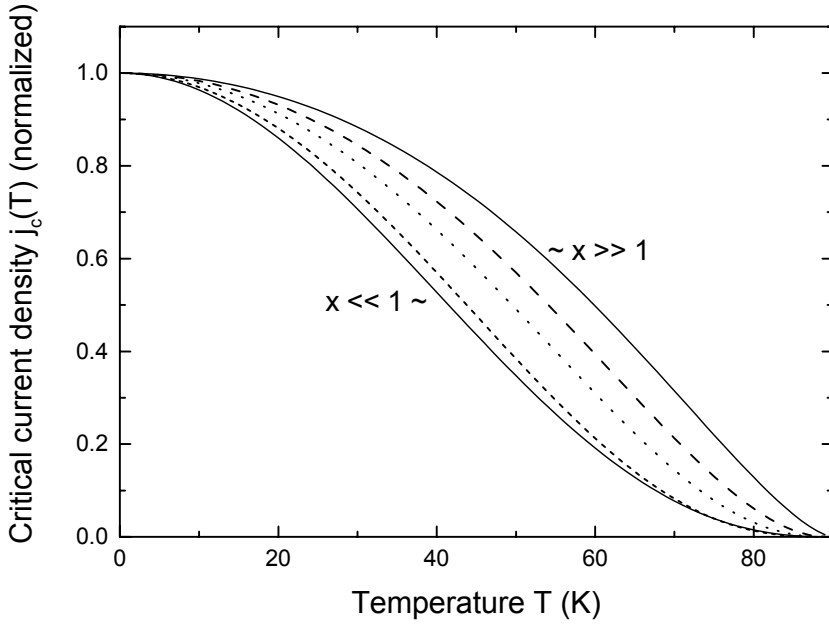
Figure 4.4: Intrinsic temperature dependence of the critical current density $j_c(T)$ for $r_r = 4\xi$ (dashed line), $r_r = 2\xi$, (dotted line) $r_r = \xi$ (short dashed line), normalized to $T = 0$. The curves lie in between the limits for small $(x \ll 1)$ and large defects $(x \gg 1)$ (solid lines), but have qualitatively a similar temperature dependence.

in the Bose Glass theory as (eqs. (4.4) and (4.5)):

$$j_c(T) \sim 1/\left(\lambda^2(T) \cdot \xi^\nu(T)\right), \tag{4.13}$$

with $\nu = 1$ and $\nu = 3$ for large and small defects, respectively. For the general pinning potential, eq. (4.9), we find the maximum pinning force from eq. (4.12), which leads to:

$$j_c(T) \approx \frac{\varepsilon_0}{2\Phi_0 \xi} \frac{1}{r_r} \left(\frac{r_r^2 + \xi^2}{\sqrt{2r_r^2 + \xi^2}} - \xi \right) = \frac{3\sqrt{3}}{8} \left(\frac{r_r^2 + \xi^2(T)}{r_r \sqrt{2r_r^2 + \xi^2(T)}} - \frac{\xi(T)}{r_r} \right) j_0(T). \tag{4.14}$$
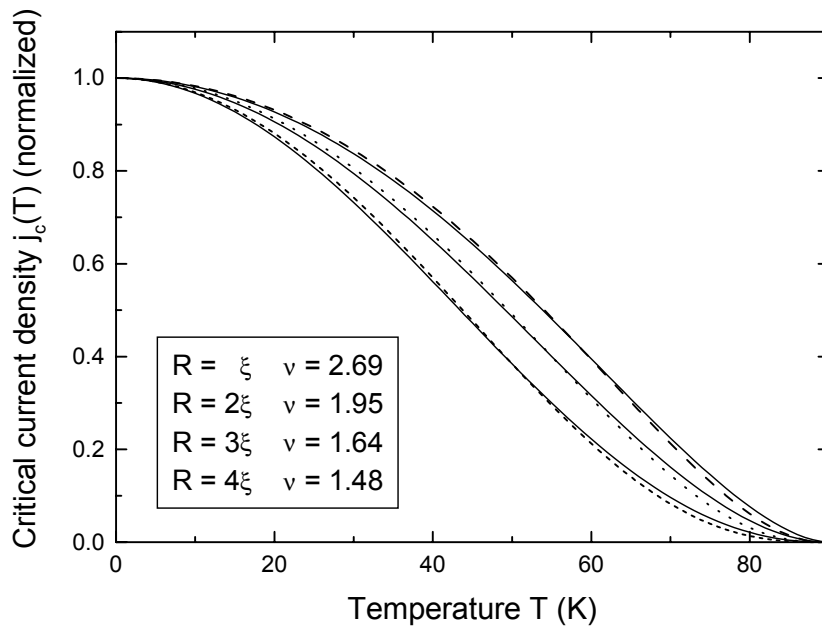
Figure 4.5: The intrinsic temperature dependence of $j_c(T)$ can be fitted to $j_c(T) = j_c(0)/\left(\lambda^2(T)\xi^\nu(T)\right)$ with ν a fit parameter depending on the defect radius. Dashed lines represent the curves from figure 4.4 (from top to bottom $r_r = 4\xi$, 2ξ, and ξ) and solid lines are the fits. Values for ν are given for some defect sizes.

In figure 4.4 the normalized critical current density is plotted for $r_r = \xi$, 2ξ, and 4ξ ($x = 0.7$, 1.4, and 2.8). The limits for small and large defects are plotted as well. We used the empirical temperature dependences $\lambda(T) = \lambda(0)/\sqrt{(1 - t^4)}$ and $\xi(T) = \xi(0)\sqrt{(1 + t^2)/(1 - t^2)}$, with $t = T/T_c$, although d-wave superconductors, such as the high-T_c compounds, have a different dependence of $\lambda(T)$. High quality crystals and thin films show a linear temperature dependence of $1/\lambda^2(T)$ at low temperatures [26, 27], but also quadratic temperature dependences of $1/\lambda^2(T)$ have been observed [28, 29]. There is quite some variation in the temperature dependences measured, and we do not a priori know how $\lambda(T)$ behaves in our samples. Also the temperature dependence of the coherence length is very hard to determine experimentally. Therefore we took a practical approach, using the empirical expressions from the two-fluid model and the Ginzburg Landau theory. However one should keep in

mind that in general the penetration depth for $YBa_2Cu_3O_{7-\delta}$ depends more strongly on temperature than assumed in our calculations

From figure 4.4 we observe that the temperature dependence for $x \approx 1$ is qualitatively quite similar to that of the limiting cases. This suggests that we may fit the temperature dependence of eq. (4.14) to $j_c(T) \sim 1/\left(\lambda^2(T) \cdot \xi^\nu(T)\right)$, with ν a fit parameter ranging from $\nu = 1$ to $\nu = 3$ for large and small defects, respectively. In figure 4.5 we have fitted $j_c(T)$ to eq. (4.13), with ν as a fit parameter. The fits approach the calculated values remarkably well! In other words eq. (4.13) can be used as an approximation of eq. (4.14) for all defect sizes, describing a smooth crossover from very large ($x \gg 1$, $\nu = 1$) to very small defects ($x \ll 1$, $\nu = 3$). In this way we obtained a simple and convenient fit for $j_c(T)$ from the general pinning potential eq. (4.9).

4.4.2 Thermal fluctuations

The second effect influencing $j_c(T)$ are thermal fluctuations. Due to the confinement of the vortices onto their pinning sites, the loss of entropy reduces the effective pinning depth of the pinning potential. The pinning potential has to be renormalized by an appropriate function $f(k_B T/\tilde{T}^r_{dp})$ to account for the influence of thermal fluctuations. The renormalization function $f(k_B T/\tilde{T}^r_{dp})$ is calculated using the analogy between the vortex system and the 2D boson system. We determine the energy eigenvalues of a boson, trapped in a potential well of the same form as the vortex pinning potential. The ground state energy level of the boson system is mapped back onto the vortex system, using the conversion as explained in the introduction of this chapter. In this way we obtain directly the renormalized pinning potential.

In the simplest form the pinning potential can be approximated by taking a cylindrical well of depth $\tilde{\varepsilon}_r$[4] and extension $b_0 \equiv \max(r_r, \sqrt{2}\xi)$ [19]. From transcribing into the vortex language the eigenvalues $E_B \simeq U_0 - c\,\hbar^2/2ma^2$ (see for example ref. [30]), of a particle of mass m, trapped in a well of depth U_0 and extension a (c is a constant of order unity), one obtains for the influence of thermal fluctuations at low temperatures:

$$\varepsilon_r(T) \sim \tilde{\varepsilon}_r \left[1 - \left(k_B T/\tilde{T}^r_{dp}\right)^2\right], \tag{4.15}$$

where k_B is the Boltzmann constant, and $\tilde{T}^r_{dp} \equiv b_0\sqrt{\varepsilon_l\varepsilon_r}$ is the depinning energy. Note that the depinning *energy* is temperature dependent itself, $\tilde{T}^r_{dp}(T) \sim 1/\lambda^2(T)$, and we have $\tilde{T}^r_{dp}(T_{dp}) \equiv k_B T_{dp}$, with T_{dp} the depinning *temperature*.

To use a cylindrical well as the pinning potential would be appropriate for very large defects, eq. (4.1) with the cutoff of eq. (4.3), but the actual pinning potential for $x \approx 1$ is different. To calculate the effect of thermal fluctuations more accurately we

---

[4]In this section $\tilde{\varepsilon}_r$ is used to denote the pinning potential without thermal fluctuations, whereas $\varepsilon_r(T)$ is the renormalized pinning potential, i.e. with thermal fluctuations. Note, that $\tilde{\varepsilon}_r$ itself depends on temperature via $\lambda(T)$ and $\xi(T)$. This notation is analogous to the one used by Blatter *et al.* (ref. [3]).
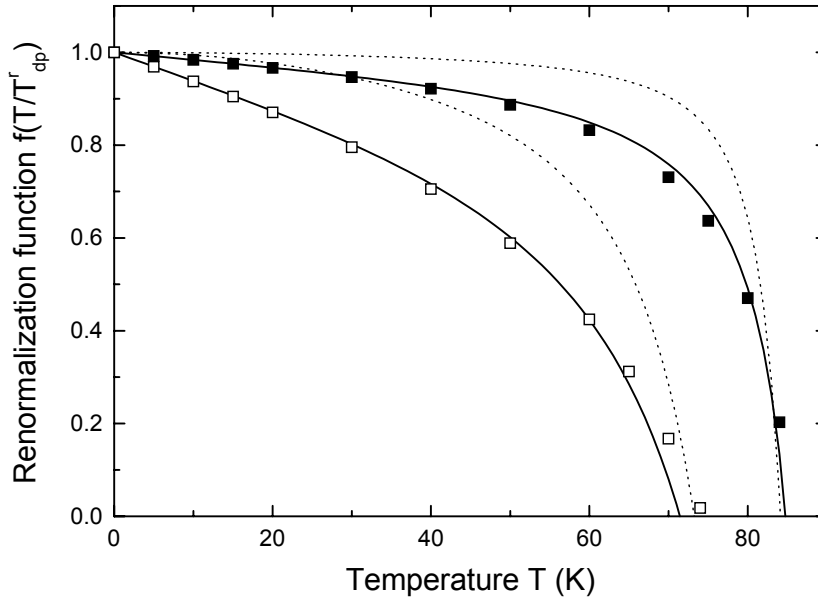
Figure 4.6: Renormalization function $f(k_B T/\tilde{T}^r_{dp})$, obtained from numerical calculations, with $\tilde{T}^r_{dp}(0) = 560$ K ($\blacksquare$) and $\tilde{T}^r_{dp}(0) = 145$ K ($\square$). The solid lines represent the harmonic oscillator approximation $f(k_B T/\tilde{T}^r_{dp}) = 1 - k_B T/\tilde{T}^r_{dp}$, which is obviously more accurate than the renormalization function, derived in the Bose glass theory $f(k_B T/\tilde{T}^r_{dp}) = 1 - (k_B T/\tilde{T}^r_{dp})^2$ (dashed lines). Note that the depinning energy is temperature dependent $\tilde{T}^r_{dp}(T) \sim 1/\lambda^2(T)$.

use the Taylor expansion of eq. (4.9) to lowest order, i.e.

$$\tilde{\varepsilon}_r(R,T) \approx \tilde{\varepsilon}_r(R = 0, T) + \frac{\varepsilon_0}{2} \frac{r_r^2}{\left(r_r^2 + 2\xi^2\right)^2} R^2, \qquad (4.16)$$

which is a harmonic oscillator potential. From the eigenvalues of the harmonic oscillator in two dimensions and the correct boson-vortex mapping (see appendix 4B for a derivation), we obtain:

$$\varepsilon_r(R,T) \sim \tilde{\varepsilon}_r(R,T) \left(1 - k_B T/\tilde{T}^r_{dp}\right) \text{ at low } T \qquad (4.17)$$

The thermal fluctuation factor is now linear in T, indicating that thermal fluctuations have a stronger effect on the pinning potential than was assumed up to now. In figure 4.6 the renormalization function is plotted, calculated numerically[5] from the pinning potential eq. (4.9). Also the approximations by Blatter *et al.* [19] and the harmonic oscillator model are plotted. We used two estimates for the depinning energy. First $\tilde{T}_{dp}^r(0) = 145$ K, corresponding to a depinning temperature $T_{dp} = 75$ K, as estimated in section 4.2.2. The other estimate is obtained by taking typical parameters for $YBa_2Cu_3O_{7-\delta}$ thin films: $\varepsilon_l = \varepsilon_r = 0.2\varepsilon_0$ and $b_0 = r_r = 2\xi(0)$, giving $\tilde{T}_{dp}^r(0) = b_0\sqrt{\varepsilon_l\varepsilon_r} \approx 560$ K. This corresponds to $T_{dp} = 84$ K. The approximation with a harmonic oscillator potential reflects the temperature dependence of $f(k_B T/\tilde{T}_{dp}^r)$ remarkably well. Note that with a large depinning energy, such as $\tilde{T}_{dp}^r(0) = 560$ K $\gg T_c$, thermal fluctuations only have a small effect at low temperatures. At higher temperatures, however, $\tilde{T}_{dp}^r(T) \sim 1/\lambda^2(T)$ is reduced appreciably, and the effect of thermal fluctuations becomes very large.

4.5 Conclusions

In this chapter we extended the results of the Bose glass theory and derived a modified pinning potential, that is also applicable when the vortex core and the defect radius are equal in size, i.e. when $x \approx 1$. In this way we obtained a general expression for $\varepsilon_r(R)$, valid for all defect sizes. This is especially important, when investigating the temperature dependence of the critical current density, because with increasing temperature the defect-to-vortex ratio experiences a crossover from $x > 1$ to $x < 1$. The temperature dependence of $j_c(T)$ is determined by an intrinsic contribution and by a renormalization factor due to thermal fluctuations. The former can be fitted to $j_c(T) = 1/\left(\lambda^2(T) \cdot \xi^\nu(T)\right)$, with $\nu \simeq 1-3$ a fit parameter depending on the defect size. The effect of thermal fluctuations is modified with respect to the original Bose glass result, from $f(k_B T/\tilde{T}_{dp}^r) \sim 1 - (k_B T/\tilde{T}_{dp}^r)^2$ to $f(k_B T/\tilde{T}_{dp}^r) \sim 1 - (k_B T/\tilde{T}_{dp}^r)$, indicating a stronger effect of thermal fluctuations on the pinning potential and critical current. In figure 4.7 we have summarized both temperature effects, for the pinning potential $\varepsilon_r(R, T)$ and for the critical current density $j_c(T)$. In the top figures the pinning potential is plotted for various temperatures, with $r_r = 2\xi(0)$ ($x = \sqrt{2}$) and $\tilde{T}_{dp}^r(0) = 560$ and 145 K. The pinning potential broadens and its depth decreases due to the increase of $\xi(T)$ and $\lambda(T)$. The renormalization is stronger for a lower depinning energy, as depicted in figure 4.6, but $f(k_B T/\tilde{T}_{dp}^r)$ does not change the qualitative behaviour of $\varepsilon_r(R, T)$. In the lower figures the effect on the critical current density is plotted for large and small defects. Again the overall behaviour is mainly determined by intrinsic temperature effects. The corrections due to thermal fluctuations are reasonably small in the case of a large depinning energy (closed symbols in figure 4.7c and d), but can be significant when $\tilde{T}_{dp}^r \simeq k_B T$.

However, there is an important *qualitative* impact of thermal fluctuations.

---

[5]The eigenvalues were calculated using a quantum physics software package, Q-PHYS-LAB 1.5.
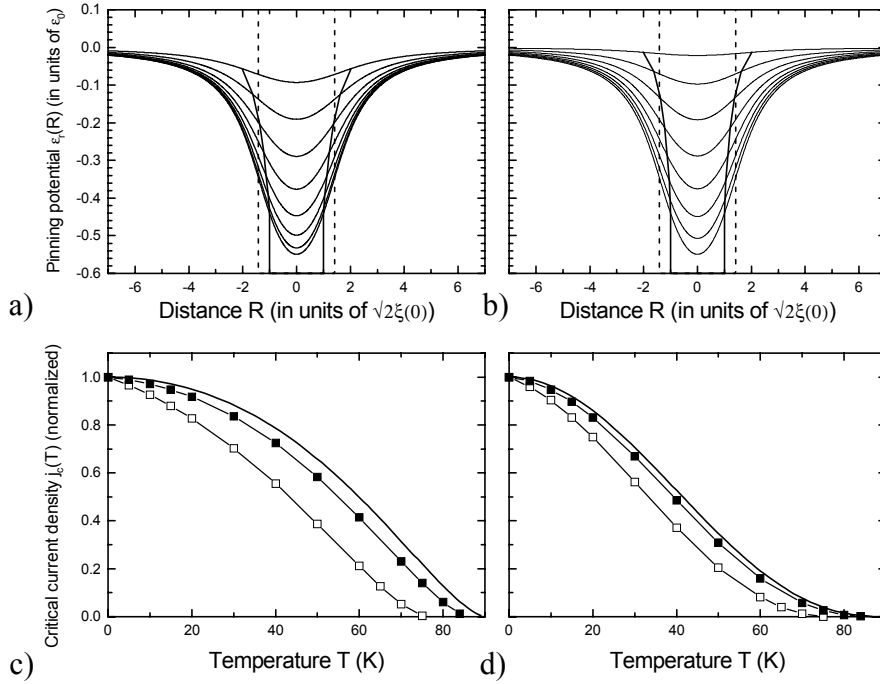
Figure 4.7: Overview of the influence of temperature on the pinning potential (upper graphs) and the critical current (lower graphs). a) Renormalized pinning potential $\varepsilon_r(T)$ of a linear defect with $r_r = 2\xi(0)$ at (from bottom to top) $T = 0, 10, 20, 30, 40, 50, 60$, and 70 K. $T_c = 90$ K and $\tilde{T}^r_{dp}(0) = 560$ K. The dashed lines depict the size r_r of the linear defect, the solid vertical lines the size of the vortex core $\sqrt{2}\xi(T)$. b) Idem, but with $\tilde{T}^r_{dp}(0) = 145$ K. c) Temperature dependence of the critical current density for large defects ($x \gg 1$). The solid line denotes the intrinsic temperature dependence, $-\blacksquare-$ include the renormalization due to thermal fluctuations, with $\tilde{T}^r_{dp}(0) = 560$ K, $-\square-$ with $\tilde{T}^r_{dp}(0) = 145$ K. d) Idem, for small defects ($x \ll 1$).

Because the renormalization function decreases linearly in temperature, the derivative at low temperatures is nonzero, i.e. $dj_c/dT \mid_{T\to 0} = -k_B/\tilde{T}_{dp}^r(0) \neq 0$, whereas all other temperature influences have a zero slope at low temperatures. Some models, such as the Generalized Inversion Scheme [31], used to calculate the true critical current $j_c(B,T)$ from the measured current $j_s(B,T)$ and relaxation $Q(B,T)$, make use of the assumption that the temperature derivative of various quantities, such as the critical current density or pinning energy, vanishes for $T \to 0$. These models have to be modified, although for large depinning energies, the effect of the linear term in $f(k_B T/\tilde{T}_{dp}^r)$ is probably small.

Having established an accurate framework for treating the properties of vortices, pinned by linear defects, we investigate in the next chapter the behaviour of the critical current, characteristic field and pinning energy experimentally and try to explain the pinning properties of $YBa_2Cu_3O_{7-\delta}$ thin films with the extended Bose glass theory.

APPENDIX 4A: Calculation of the vortex-pinning potential

To find the pinning potential we integrate eq. (4.9) over the full defect

$$\varepsilon_r(R) = -\frac{1}{2}\mu_0 H_c^2 \int_0^{r_r}\int_0^{2\pi}\left[1 - |\Psi(R')|^2\right]r\,dr\,d\vartheta, \qquad (A4.1)$$

with $R' = \left|\vec{r} - \vec{R}\right| = r^2 + R^2 - 2rR\cos\vartheta$. Here the origin is put at the center of the linear defect, R is the distance from the center of the vortex to the center of the defect, and R' is the distance from the vortex to the point (r, ϑ) (see figure 4.8). With $|\Psi(R')|^2 = R'^2/(R'^2 + 2\xi^2)$ we obtain:

$$\varepsilon_r(R) = -\frac{\varepsilon_0}{2\pi}\int_0^{r_r}\int_0^{2\pi}\frac{r\,dr\,d\vartheta}{r^2 + R^2 - 2rR\cos\vartheta + 2\xi^2} \qquad (A4.2)$$

Integrating over ϑ yields:

$$\varepsilon_r(R) = -\varepsilon_0\int_0^{r_r}\frac{r\,dr}{\sqrt{\left(r^2 + R^2 + 2\xi^2 + 2rR\right)\left(r^2 + R^2 + 2\xi^2 - 2rR\right)}} \qquad (A4.3)$$

which can be written as:

$$\varepsilon_r(R) = -\varepsilon_0\int_0^{r_r}\frac{r\,dr}{\sqrt{\left(r^2 - R^2 + 2\xi^2\right)^2 + 8R^2\xi^2}} \qquad (A4.4)$$
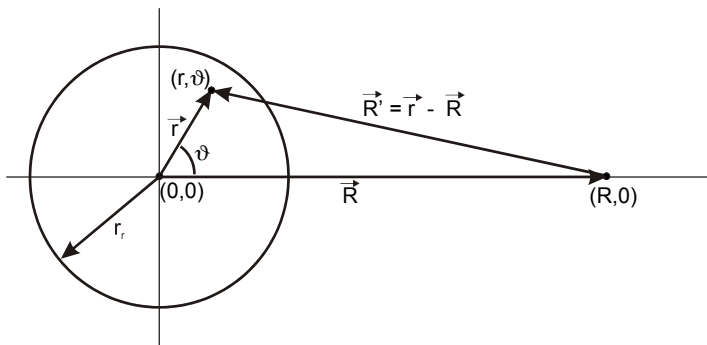
Figure 4.8: Geometrical situation for calculating the vortex pinning potential $\varepsilon_r(R)$. The linear defect with radius r_r is at the origin of the coordinate system. The center of the vortex is at position $(R, 0)$. To obtain the pinning potential, we integrate the reduction of the order parameter at (r, ϑ) over the full defect, i.e. from $r = 0 \rightarrow r_r$ and $\vartheta = 0 \rightarrow 2\pi$.

From integrating eq. (A4.4) we obtain:

$$\varepsilon_r(R) = -\frac{\varepsilon_0}{2} \operatorname{arcsinh} \left[\frac{1}{2} \frac{\left(r^2 - R^2 + 2\xi^2\right)}{\sqrt{2}\xi \cdot |R|} \right]_0^{r_r} \tag{A4.5}$$

and:

$$\varepsilon_r(R) = -\frac{\varepsilon_0}{2} \left\{ \operatorname{arcsinh} \left[\frac{1}{2} \frac{\left(r_r^2 - R^2 + 2\xi^2\right)}{\sqrt{2}\xi \cdot |R|} \right] - \operatorname{arcsinh} \left[\frac{1}{2} \frac{\left(-R^2 + 2\xi^2\right)}{\sqrt{2}\xi \cdot |R|} \right] \right\} \tag{A4.6}$$

The depth of the pinning potential $\varepsilon_r(0)$ can be calculated straightforwardly from eq. (A4.2) by putting in $R = 0$. The result is:

$$\varepsilon_r(0) = -\frac{\varepsilon_0}{2} \ln \left[1 + \frac{r_r^2}{2\xi^2} \right] \tag{A4.7}$$

APPENDIX 4B: The effect of thermal fluctuations on the pinning potential

To calculate the effect of thermal fluctuations on the pinning potential we use the same line of derivation as in ref. [19]. Instead of using a square well potential, we use the Taylor expansion of the pinning potential, eq. (4.11), to lowest order:

$$\varepsilon_r(R) \approx \varepsilon_r(R=0) + \frac{\varepsilon_0}{2}\frac{r_r^2}{\left(r_r^2 + 2\xi^2\right)^2}R^2 = \varepsilon_r(0) + \frac{1}{2}kR^2, \text{ with } k = \frac{\varepsilon_0 r_r^2}{\left(r_r^2 + 2\xi^2\right)^2}.$$
(B4.1)

The first term of eq. (B4.1) gives the depth of the potential and the second term is a harmonic oscillator potential. The binding energy of a particle trapped in this harmonic oscillator potential in two dimensions is given by:

$$E_B = U_0 + \hbar\omega, \text{ with } \omega = \sqrt{\frac{k}{m}}$$
(B4.2)

Eq. (B4.2) is translated back to the vortex picture according to the usual mapping $\hbar \rightarrow T$, $m \rightarrow \varepsilon_l$, $U_0 \rightarrow \varepsilon_r(0)$, $\tilde{T}_{dp}^r = b_0\sqrt{\varepsilon_l \varepsilon_r}$, and k from by eq. (B4.1). We obtain for the effective depth of the pinning potential at low temperatures (note that $\varepsilon_r(0) = -\frac{1}{2}\varepsilon_0 \ln\left[1 + r_r^2/2\xi^2\right]$ is negative):

$$\varepsilon_r(T) = \varepsilon_r(T=0)\left(1 - \gamma\frac{T}{\tilde{T}_{dp}^r}\right), \text{ with } \gamma = \frac{\sqrt{2}x^2}{\sqrt{\ln\left(1+x^2\right)}\cdot\left(1+x^2\right)}.$$
(B4.3)

The prefactor $\gamma \approx 0.85$ for $x > 1$ is only weakly dependent on x^2 and we put $\gamma = 1$ for convenience. Also we have omitted the Boltzmann constant k_B. Compared to the square well potential the effect of thermal fluctuations changes from $f(T/\tilde{T}_{dp}^r) = 1 - \left(T/\tilde{T}_{dp}^r\right)^2$ to $f(T/\tilde{T}_{dp}^r) = 1 - T/\tilde{T}_{dp}^r$. As a result the effective depth of the pinning potential decreases faster with temperature than it was assumed up to now. This immediately affects the temperature dependence of the critical current density $j_c(T)$. It is obvious that the harmonic oscillator approximation is valid in a limited range $T \ll \tilde{T}_{dp}^r$ only. At high temperatures $T > \tilde{T}_{dp}^r$, when the pinning potential is shallow, Blatter *et al.* calculated that $f(T/\tilde{T}_{dp}^r) = \exp(-T/\tilde{T}_{dp}^r)$ [19], at intermediate temperatures $T \lesssim \tilde{T}_{dp}^r$ we use numerical calculations to obtain an exact result for $f(T/\tilde{T}_{dp}^r)$, and to check the accuracy of our calculations.

References

[1]   D.R. Nelson and V.M. Vinokur, Phys. Rev. B **48**, 13060 (1993)

[2]   I.A. Larkin, Zh. Eksp. Teor. Fiz. **58**, 1466 (1970),
      I.A. Larkin and Yu.N. Ovchinnikov, J. Low Temp. Phys **34**, 409 (1979)

[3]   G. Blatter, M.V. Feigel'man, V.B. Geshkenbein, A.I. Larkin and V.M. Vinokur,
      Rev. Mod. Phys. **66**, 1125 (1994)

[4]   F.C. Klaassen, G. Doornbos, J.M. Huijbregtse, R.C.F. van der Geest, B. Dam,
      and R. Griessen, Phys. Rev. B **64**, 184523 (2001), and chapter 5 of this thesis

[5]   M.V. Feigel'man, V.B. Geshkenbein, A.I. Larkin, and V.M. Vinokur, Phys. Rev.
      Lett. **63**, 2303 (1989),
      M.V. Feigel'man, V.B. Geshkenbein, and V.M. Vinokur, Phys. Rev. B **43**, 6263
      (1991)

[6]   P.W. Anderson and Y.B. Kim, Rev. Mod. Phys. **36**, 39 (1964)

[7]   M.P.A. Fisher, Phys. Rev. Lett. **62**, 1415 (1989),
      D.S. Fisher, M.P.A. Fisher, and D.A. Huse, Phys. Rev. B **43**, 130 (1991)

[8]   R.H. Koch, V. Foglietti, W.J. Gallagher, G. Koren, A. Gupta, and M.P.A Fis-
      cher, Phys. Rev. Lett. **63**, 1511 (1989)

[9]   P.L. Gammel, L.F. Schneemeyer, and D.J. Bishop, Phys. Rev. Lett. **66**, 953
      (1991)

[10] G.W. Crabtree, W.K. Kwok, U. Welp, D. Lopez, and J.A. Fendrich, in. R.
      Kossowsky *et al.* (eds.), *Physics and Materials Science of Vortex States, Flux
      Pinning and Dynamics*, NATO Science Series **E356**, 357 (1999), and references
      therein

[11] M.P.A. Fisher, P. B. Weichman, G. Grinstein, and D.A. Fisher, Phys. Rev. B.
      40, 546 (1989)

[12] D.R. Nelson and V.M. Vinokur, Phys. Rev. Lett. **68**, 2398 (1992)

[13] W.K. Kwok, R.J. Olsson, G. Karapetrov, L.M. Paulius, W.G. Moulton, D.J.
      Hofman, and G.W. Crabtree, Phys. Rev. Lett. **84**, 3706 (2000)

[14] T.K. Worthington, W.J. Gallagher, D.L. Kaiser, F.H. Holtzberg, and T.R.
      Dinger, Physica C **153**, 32 (1988)

[15] S.A. Grigera, E. Morré, E. Osquiguil, C. Balseiro, G. Nieva, and F. de la Cruz,
      Phys. Rev. Lett. **81**, 2348 (1998)

[16] L. Civale, Supercond. Sci. Technol. **10**, A11 (1997), and references therein

[17] B. Dam, J.M. Huijbregtse, F.C. Klaassen, R.C.F. van der Geest, G. Doornbos,
      J.H. Rector, A.M. Testa, S. Freisem, J.C. Martínez, B. Stäuble-Pümpin, and
      R. Griessen, Nature **399**, 439 (1999), and chapter [**?**] of this thesis

[18] G.S. Mkrtchyan, and V.V. Shmidt, Sov. Phys. JETP **34**, 195 (1972)

[19] ref [3], page 1327 and further

[20] L. Civale, A.D. Marwick, T.K. Worthington, M.A. Kirk, J.R. Thompson, L. Krusin-Elbaum, Y. Sun, J.R. Clem, F. Holtzberg, Phys. Rev. Lett. **67**, 648 (1991)

[21] L. Krusin-Elbaum, L. Civale, J.R. Thompson, C. Feild, Phys. Rev. B **53**, 11744 (1996)

[22] M. Baert, V.V. Metlushko, R. Jonckheere, V.V. Moshchalkov, and Y. Bruynseraede, Phys. Rev. Lett. **74**, 3269 (1995)

[23] V.V. Moshchalkov, M. Baert, V.V. Metlushko, E. Rosseel, M.J. van Bael, K. Temst, R. Jonckheere, and Y. Bruynseraede, Phys. Rev. B **54**, 7385 (1996)

[24] A. Castellanos, R. Wördenweber, G. Ockenfuss, A. VonderHart, K. Keck, Appl. Phys. Lett. **71**, 962 (1997)

[25] J.R. Clem, J. Low Temp. Phys. **18**, 427 (1975)

[26] W.N. Hardy, D.A. Bonn, D.C. Morgan, Ruixing Liang, and Kuan Zhang, Phys. Rev. Lett. **70**, 3999 (1993)

[27] J.E. Sonier, R.F. Kiefl, J.H. Brewer, D.A. Bonn, J.F. Carolan, K.H. Chow, P. Dosanjh, W.N. Hardy, Ruixing Liang, W.A. MacFarlane, P. Mendels, G.D. Morris, T.M. Riseman, and J.W. Schneider, Phys. Rev. Lett. **72**, 744 (1994)

[28] L.A. de Vaulchier, J.P. Vieren, Y. Guldner, N. Bontemps, R. Combescot, Y. Lemaître, and J.C. Mage, Europhys. Lett. **33**, 153 (1996)

[29] B.J. Feenstra, F.C. Klaassen, D. van der Marel, Z.H. Barber, R. Perez Pinaya, and M. Decroux, Physica C **278**, 213 (1997)

[30] L.D. Landau and E.M. Lifshitz, *Quantum Mechanics*, Pergamon Press, 2nd edition (1965)

[31] H. Schnack, R. Griessen, J.G. Lensink, and H.H. Wen, Phys. Rev. B **48**, 13178 (1993)

Chapter 5

Vortex pinning in thin $\mathrm{YBa_2Cu_3O_{7-\delta}}$ films

In this chapter the general behaviour of the superconducting current density $j_s(B,T)$ and the dynamical relaxation rate $Q(B,T)$ of $\mathrm{YBa_2Cu_3O_{7-\delta}}$ thin films is presented. Both exhibit a number of features typical for strong pinning of vortices by growth induced linear defects. At low magnetic fields $j_s(B)$ and $Q(B)$ are constant up to a characteristic field B^*, that is directly proportional to the linear defect density n_{disl} of the film. The pinning energy $U_c(B{=}0) \approx 600$ K can be explained by half-loop excitations determining the thermal activation of vortices at low magnetic fields. Using the vortex pinning potential $\varepsilon_r(R,T)$, derived in chapter 4 and its renormalization due to thermal fluctuations, we explain the temperature dependence of the true critical current density $j_c(0,T)$ and of $U_c(0,T)$ at low magnetic fields. Moreover we find that the core radius of the linear defects $r_r \cong 1 - 2 \cdot \xi_{ab}(0)$, the in-plane coherence length. At high magnetic fields $\mu_0 H \gg B^*$ the current density experiences a power law behaviour $j_s(B) \sim B^\alpha$, with $\alpha \approx -0.58$ for films with low n_{disl} and $\alpha \approx -0.8$ to -1.1 for films with high n_{disl}. The pinning energy in this regime, $U_c(\text{high}B) \approx 60 - 200$ K is independent of magnetic field, but depends on the dislocation density. This implies that vortex pinning is still largely determined by the linear defects, even when the vortex density is much larger than the linear defect density.

Our results show, that natural linear defects in thin films form an analogous system to columnar tracks in irradiated samples. Therefore the Bose glass theory, that has successfully described many properties of pinning by columnar tracks, can be applied also to thin films. Vice versa a better understanding of pinning in thin films is also useful to put the properties of irradiated samples in a broader perspective[1].

---

[1]This chapter forms, together with the previous chapter, an extended version of the paper by F.C. Klaassen, G. Doornbos, J.M. Huijbregtse, R.C.F. van der Geest, B. Dam, and R. Griessen, *Vortex pinning by natural linear defects in thin films of $YBa_2Cu_3O_{7-\delta}$*, Phys. Rev. B. **64**, 184523 (2001).

5.1 Introduction

In the previous two chapters we have shown, i) that natural linear defects are responsible for the observed high critical currents in thin films of YBa$_2$Cu$_3$O$_{7-\delta}$ and ii) that linear defects can be described in terms of the Bose glass theory [1, 2], provided that we take into account that the vortex and the dislocation core are comparable in size. The importance of linear defects in thin films was already suspected by many other groups [3, 4, 5, 6, 7, 8], but little attempts have been made to describe vortex pinning in as-grown thin films in terms of strong pinning. Strong pinning theories, such as the Bose glass theory, have been extensively applied to irradiated single crystals [9], irradiated thin films [10, 11] or antidot films [12, 13], but surprisingly not to thin YBa$_2$Cu$_3$O$_{7-\delta}$ films, that still show the largest critical currents of all (up to 10^{12} Am$^{-2} \simeq j_0$, the depairing current).

An alternative strong pinning model, different from the Bose glass theory, has been proposed by Mezzetti *et al.* [14]. They relate vortex pinning in thin YBa$_2$Cu$_3$O$_{7-\delta}$ films to the island structure of the films. It is assumed that the islands are separated by planar defects, situated in the trenches between the islands. Planar defects, for example low angle grain boundaries or (hidden) weak links, can have strong pinning properties. An important aspect of pinning by planar defects, is the anisotropy of the critical current, being large perpendicular to the defect, and much smaller (up to two orders of magnitude) along the plane of the defect [15]. Effectively low angle grain boundaries are described as a network of Josephson junctions, where the critical current of each junction is given by a Fraunhofer-like expression [16, 17]. Mezzetti *et al.* [14] assume that their film consists of such a network of long Josephson junctions with a certain length variation, and they fit the measured magnetic field dependence of the critical current density $j_s(B)$ to a statistical length distribution of long Josephson junctions. Their approach fits the experimentally observed current density $j_s(B)$ well at intermediate temperatures. Unfortunately, Mezzetti *et al.* do not show if such a network of planar defects in thin YBa$_2$Cu$_3$O$_{7-\delta}$ films actually exist. Moreover they do not discuss whether the fit parameters, yielding the average length and standard deviation of the network of Josephson junctions, are reasonable with respect to the expected network of planar defects. However, in view of their model, we take a careful look at the island structure of our films, and discuss whether these islands are separated by strongly pinning grain boundaries.

Already in chapter 3 we gave some general features of the current density and characteristic field, and compared them with vortex pinning by columnar tracks. We showed that many aspects are well explained in terms of the Bose glass theory. In this chapter we present a systematic study on the behaviour of the superconducting current density $j_s(B,T)$ and the magnetic relaxation $Q(B,T)$ in YBa$_2$Cu$_3$O$_{7-\delta}$ films. We demonstrate the existence of a matching effect in the dynamical relaxation rate, similar to that in $j_s(B)$. The magnitude of the zero field pinning energy we measured, $U_c(B{=}0) \approx 600$ K, suggests that half-loop excitations are the elementary vortex excitations in thin films at low magnetic fields. We show that the observed temperature dependence of true critical current density $j_c(B{=}0,T)$ (where $j_c(0,T)$ is derived from the measured $j_s(0,T)$ and $Q(0,T)$, assuming linear defect pinning)

and $U_c(T)$ are in good agreement with the theoretical expressions, derived in chapter 4. This shows that the Bose glass theory describes vortex pinning at low magnetic fields in thin YBa$_2$Cu$_3$O$_{7-\delta}$ films. Moreover, it appears that far above B^* the critical current is still determined by (collective) strong pinning due to linear defects. We focus on the behaviour at low temperatures $T \lesssim 70$ K, since at higher temperatures the true critical current density j_c cannot be easily related to the measured superconducting current density j_s. Moreover, at temperatures close to T_c the vortex glass transition and the melting transition have already been investigated extensively by many groups [18, 19].

The chapter is organized as follows. In section 5.2 we describe briefly the properties of the YBa$_2$Cu$_3$O$_{7-\delta}$ films, used in this chapter and the experimental technique to measure $j_s(B,T)$ and $Q(B,T)$. Next we present the experimental results, in terms of the current density j_s, the relaxation rate Q and the pinning energy U_c. Section 5.4 is devoted to a discussion, mainly in terms of the extended Bose glass theory, described in chapter 4. Finally we summarize our results and give an overview of the remaining questions.

5.2 Experimental

5.2.1 Sample preparation

YBa$_2$Cu$_3$O$_{7-\delta}$ thin films were deposited by means of Pulsed Laser Deposition (PLD) on (100) SrTiO$_3$ substrates [20]. The films are all c-axis oriented and have a thickness of $d \approx 140$ nm. XRD analysis shows a good overall crystallinity of all films, with the c-axis of the films $c = 11.68(3)$ Å being very close to the single crystal value of 11.677 Å, while the (005) rocking-curve full width at half maximum $\Delta\omega_{(005)} \lesssim 0.1°$. The average transition temperature T_c, measured resistively using a four point method, T_c = 90.4 K with a standard deviation of 0.4 K and a typical transition width $\Delta T_c \lesssim 0.5$ K [21]. By using different substrate temperatures during deposition between $T_{sub} \approx$ 700°C and $T_{sub} \approx 850°$C we are able to tune reproducibly the island size of the films between $D = 80$ nm to $D = 500$ nm, and consequently the dislocation density [22]. To perform critical current measurements on the films, they are all patterned by standard UV photolithography into rings of typically 3-5 mm in diameter and 125-500 μm width. In this geometry we can safely assume a well-defined current distribution and relaxation rate, which we confirmed by magneto-optical measurements [23].

For comparison we measured a 70 nm thin film (film LAD493) and a film (film Y67), prepared by means of DC sputtering. This film was sputtered at $T = 840°$C and 3 mbar oxygen pressure with a substrate-target distance of 2 cm. After deposition the film was post-annealed for 1 hour at 650°C in 10^3 mbar O$_2$ in order to optimize the superconducting properties. In this way, films containing large growth spirals are obtained, resulting in island sizes with diameter $D = 2$ μm [24].

In table 5.1 an overview is given of the structural details of the films described in this chapter.

film	deposition	d (nm)	T_c (K)	ΔT_c (K)	n_{disl} (μm^{-2})	d_r (nm)
Y67	DC sputtering	192	90.6	0.6	7	378
LAD670	PLD	110	90.4	0.6	28	189
LAD496	PLD	140	90.6	0.3	34	171
LAD203	PLD	140	91	-	57	132
LAD493	PLD	70	89.7	0.4	72	118
LAD554	PLD	140	-	-	90	105

Table 5.1 General properties of pulsed laser deposited (PLD) and sputtered YBa$_2$Cu$_3$O$_{7-\delta}$ films on SrTiO$_3$ investigated in this work. d is the film thickness, T_c the transition temperature (not measured for all fillms), ΔT_c the width of the transition, n_{disl} the dislocation density and d_r the average defect spacing.

5.2.2 Defect structure

The surface morphology of the films is studied by a tapping mode AFM. Characteristic for all laser-ablated films is the island structure, with an island diameter of typically $D = 100 - 500$ nm. The islands are separated by deep trenches with a depth up to 20% of the film thickness. By means of wet chemical etching in a 1.0 vol% Br in ethanol solution we obtain the linear defect density n_{disl} from the density of etch pits. Most linear defects are found to be situated in the trenches, which results in a linear relationship between the island density and the linear defect density, with on average one linear defect per island [22].

Previously, we found indications for an anti-phase boundary network, due to the c-axis mismatch between YBa$_2$Cu$_3$O$_{7-\delta}$ and the SrTiO$_3$ substrate [25, 26]. However, recent TEM observations on our films show, that anti-phase boundaries are not a general feature in thin films, whereas the island morphology is. Moreover, we find no grain boundaries or weak links separating the islands [27]. Instead our films consist of large well-connected islands, and the dislocations found by TEM appear to be screw dislocations. We conclude that the trenches between the growth islands only reflect a reduction of the film thickness and that there is no network of planar defects related to them. Note, that the typical defect distance $d_r \approx 200$ nm is much larger than the defect radius $r_r \approx 1 - 3$ nm, which makes it impossible to view these dislocations to be correlated in such a way that they form a planar defect. In low angle grain boundaries the array of dislocations is much denser. For example, in the 4° grain boundary YBa$_2$Cu$_3$O$_{7-\delta}$ film, investigated by Diaz *et al.* [8], the distance between adjacent edge dislocations $d_r \approx 5.6$ nm $\lesssim r_r$, which means that the defect core sizes are almost overlapping. Even if all dislocations in our film would be aligned, we find (using the Shockley-Read formula $d_r = |b| / (2 \sin(\vartheta/2))$, with $|b| = 0.4$ nm the magnitude of the Burgers vector, and $d_r = 200$ nm), that the grain boundary angle $\vartheta \approx 0.1°$. This is clearly too small to give any noticeable grain boundary effect, for which the minimum angle would be $\vartheta \gtrsim \vartheta_0 \approx 3 - 5°$ [28, 29]. Hence, we may safely assume that in our films we are dealing with pinning at *individual* linear defects.

Therefore, the model of Mezzetti *et al.* [14] is not applicable to the films we measured. Note, that Mezzetti *et al.* report typical current densities $j_s \simeq 10^{10}$ Am^{-2}, one order of magnitude lower than in our films. This might reflect the presence of grain boundaries or weak links, although, as mentioned already in the introduction, they give no structural evidence for the existence of a grain boundary network.

For sputtered films the one to one correspondence between island density and defect density does not hold. The islands are very large and do not show deep trenches. Instead growth spirals are observed, that can be associated with screw dislocations. After etching additional dislocations (mostly edge dislocations) show up, which makes the dislocation density relatively large compared to the island size. Nevertheless, also in sputtered films the matching effect is related to the total measured linear defect density n_{disl} (ref. [30] and chapter 3). This proves once more that the linear defect density, and not the island size, determines the size of the low-field plateau in the current density.

5.2.3 Measurement of the current density and the relaxation

The superconducting current density is measured by means of capacitive torque magnetometry [31]. In a magnetic field $\mu_0 \overrightarrow{H}$ that is being swept with a sweep rate $\mu_0 dH/dt$, a superconducting sample experiences a torque

$$\overrightarrow{\tau} = \mu_0 \left(\overrightarrow{M} \times \overrightarrow{H} \right) \tag{5.1}$$

which is the result of induced supercurrents flowing in the sample. From the irreversible torque $\tau_{irr} = (\tau_+ - \tau_-)/2$, with τ_+ and τ_- the ascending and descending branch of a magnetic hysteresis loop respectively, we directly obtain the irreversible magnetic moment $M_{irr} = \tau_{irr}/(\mu_0 H \sin \vartheta)$. Since the current density j_s is confined to the film plane, it is proportional to M_{irr}, depending only on a geometrical factor. Using the Bean critical state model [32], we obtain for ring-shaped samples:

$$M_{irr} = (\pi/3)d(r_o^3 - r_i^3)j_s \tag{5.2}$$

with d the sample thickness and r_o and r_i the outer and inner radius of the ring, respectively. Note, that we assure that the sample is fully penetrated, by performing sweeps over a much larger range than the penetration field. In this situation the current density is directly reflecting the pinning strength.

The setup consists of a 7 T magnet in a Oxford cryostat that enables us to measure over a temperature range from 1.7 to 300 K. The magnetic field is applied at an angle of 10° from the c-axis. As this angle is well within the trapping angle for columnar tracks, we can safely assume that the vortices are parallel to the c-axis. Moreover, as shown by Brandt [33], vortices are straight and perpendicular to the surface over a length $l \sim \lambda$, indicating that even without linear defects vortices would be aligned with the c-axis over almost the full film thickness. Vortex kink creation at the surface, as proposed by Indenbom *et al.* [34], does therefore not occur in thin films with thickness $d \lesssim \lambda$.

Douwes *et al.* [5] showed by comparing transport measurements with torque magnetometry, that the applied magnetic field can be scaled to an effective field along the c-axis $\mu_0 H_{eff} = \mu_0 H_{appl} \cos \vartheta$, for angles at least up to $\vartheta = 30°$. In our measurements, with $\cos \vartheta = 0.985$, we set thus $\mu_0 H_{eff} = \mu_0 H_{appl}$.

Note, that the measured superconducting current density j_s is in general not the true critical current density j_c, i.e. the current density for which the pinning force and Lorentz force are equal. The difference is caused by the relaxation of the vortex lattice due to thermally activated vortex hopping [35] or quantum creep [36]. In YBa$_2$Cu$_3$O$_{7-\delta}$ films the relaxation rate is typically a few percent at low magnetic fields and temperatures. We measure the dynamical relaxation rate

$$Q \equiv \frac{\mathrm{d}\ln j_s}{\mathrm{d}\ln (\mathrm{d}B/\mathrm{d}t)} \tag{5.3}$$

by making small hysteresis loops around a certain field, with ever decreasing sweep rates from $\mu_0 dH/dt = 40$ mT/s down to 1.25 mT/s, and by plotting the hysteresis against the sweep rate on a double logarithmic plot. Due to the ring shape of our sample, we obtain a well-defined, uniform relaxation rate. From measuring the superconducting current density $j_s(B,T)$ and the dynamical relaxation rate $Q(B,T)$, one obtains in principle all experimental information to determine the behaviour of the critical current density $j_c(B,T)$ and the pinning energy $U_c(B,T)$. However, to construct j_c and U_c from the experimental data one has to use either an inversion model, such as the Generalized Inversion Scheme [37], or one has to make assumptions about the vortex pinning mechanism. Since we know that linear defects are the dominant pinning sites at low magnetic fields, we will use the Bose glass model to construct $j_c(B{=}0,T)$ and $U_c(B{=}0,T)$ from our experimental data.

5.3 Results

5.3.1 General properties of the superconducting current density j_s

The general behaviour of the superconducting current density j_s in thin films of YBa$_2$Cu$_3$O$_{7-\delta}$ has a number of distinct features. The most remarkable property is, that at low magnetic fields, the current density $j_s(B)$ exhibits a plateau. Note that this plateau is not an artefact of the logarithmic scale, used for $\mu_0 H$; it persists in a linear plot. In figure 5.1 and figure 5.2 we plot $j_s(B, T)$ as a function of magnetic field and temperature respectively, for two films with low and high dislocation density. Comparing many films we typically find that at $T = 4.2$ K, $j_s(B = 0) \approx 2$ to $6 \cdot 10^{11}$ Am^{-2}, while at $T = 77.5$ K, $j_s = 2 - 4 \cdot 10^{10}$ Am^{-2}. These high critical current values confirm, that the films are of excellent quality, like the materials parameters (cf. section 5.2.1) already suggested.

We find that the characteristic field B^* is directly proportional to the linear defect density as determined by wet chemical etching, $B^* \cong 0.7 n_{disl} \Phi_0$, which implies that linear defects are the most important pinning centers in YBa$_2$Cu$_3$O$_{7-\delta}$ thin films.

At higher magnetic fields we observe a transition to a power law behaviour for films with a low dislocation density $j_s(B) \sim B^\alpha$, with $\alpha \approx -0.58$. This is close to $j_s(B) \sim 1/\sqrt{B}$. Typically such a field dependence is described by plastic pinning [1], or a flux line shear model where the unpinned vortices are moving by shear forces through the lattice of strongly pinned vortices [38]. The power law behaviour sets in at $\mu_0 H \simeq 0.5$ T and extends to 7 T at low temperatures. At higher temperatures a faster decrease of $j_s(B)$ develops, that is accompanied by an exponential increase of the relaxation rate Q (see figure 5.6 and the next section). This does not necessarily mean that there is a crossover to another pinning *mechanism*. Merely a direct qualitative relation between j_s and the true critical current density j_c is lost, due to the exponentially increasing relaxation rate. Therefore we cannot make any statements about the pinning mechanism without determining $j_c(B, T)$ explicitly.

Eventually also in films with a large defect density a power law behaviour is reached. However, as shown in figure 5.3, for films with high n_{disl}, $\alpha(T)$ decreases with temperature to $\alpha \approx -1.1$ at $T = 50$ K, whereas $\alpha(T) \approx -0.58$ constant for all T for the films with low n_{disl}. The crossover in behaviour at high magnetic fields occurs when the dislocation density $n_{disl} \approx 60$ μm^{-2}. The reason for this crossover is possibly related to the distance between the linear defects in the film. For film LAD203 ($n_{disl} = 57$ μm^{-2}), the distance between defects is $d_r = 150$ nm $\simeq \lambda$, whereas for LAD554 and LAD493, that have many dislocations, $d_r \approx 100$ nm $< \lambda$. Since $j_s \sim 1/B$ is the typical behaviour for a collective pinning of the dislocation lattice, our result implies that the pinning mechanism changes from a shear ($\alpha = -\frac{1}{2}$) to a collective pinning regime ($\alpha = -1$). Note that also in irradiated single crystals (with $d_r \ll \lambda$) collective pinning with $j_s \sim 1/B$ is observed above B^* [39]. In section 5.4.3 we will address the high field behaviour of j_s more thoroughly.
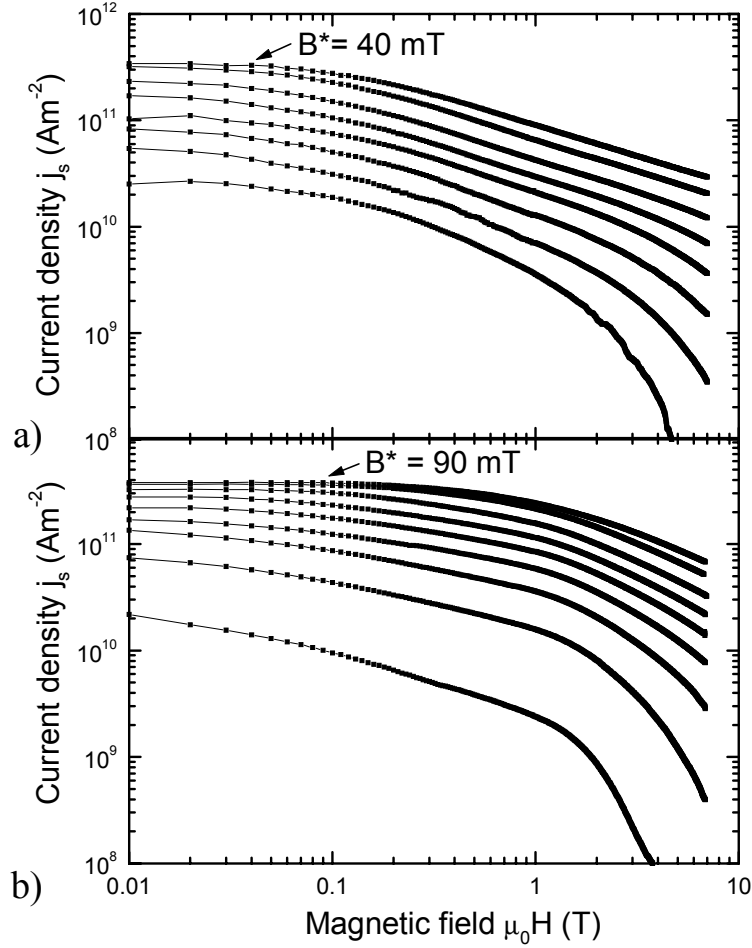
Figure 5.1: Superconducting current density $j_s(B)$ for two films with different dislocation density; a) LAD496 with $n_{disl} = 34$ μm^{-2} and b) LAD493 with $n_{disl} = 72$ μm^{-2}. From top to bottom $T = 4.2$, 10, 20, 30, 40, 50, 60, 70 and 80 K (only LAD493). The arrows indicate the characteristic field at $T = 4.2$ K.
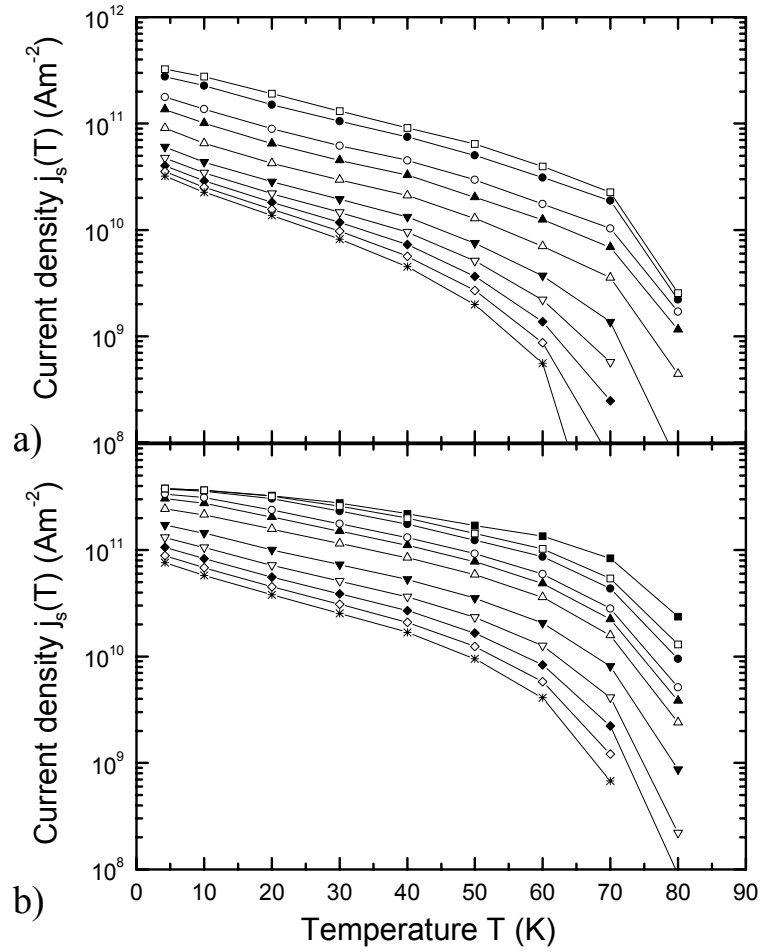
Figure 5.2: Current density $j_s(T)$ for various magnetic fields of a) LAD496 and b) LAD493. From top to bottom $B = 0.005$ (■, only LAD493), 0.05 (□), 0.1 (●), 0.3 (○), 0.5 (▲), 1.0 (△), 2.0 (▼), 3.0 (▽), 4.0 (◆), 5.0 (◇) and 6.0 T (*).
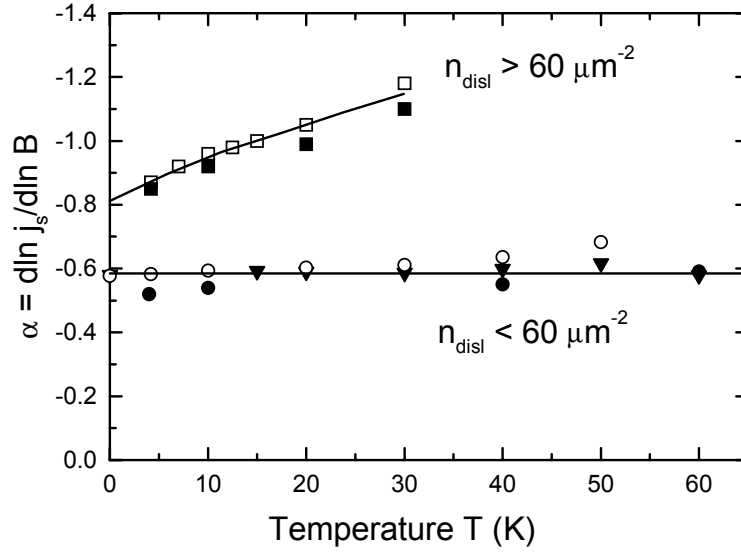
Figure 5.3: Exponents $\alpha \equiv -\mathrm{d}\ln j_s/\mathrm{d}\ln B$ at high magnetic fields for films LAD493 (■), LAD554 (□), LAD203 (●), LAD496 (○) and Y67 (▼). For films with a low dislocation density $\alpha \approx -0.58$, constant with temperature, whereas for films with many dislocations α is more negative and decreases with temperature. Note, that the vertical axis is negative. Lines are guides to the eye.

5.3.2 General properties of the dynamical relaxation rate Q

After describing the general properties of j_s, we turn to the dynamical relaxation rate. First we investigate the behaviour of Q at low fields $\mu_0 H < B^*$, where j_s exhibits a plateau. To measure the relaxation Q at these fields, we have to use very low sweep rates to acquire sufficient data points. Moreover, the torque disappears at vanishing magnetic field. We use an external current source in combination with the magnet power supply to obtain sweep rates down to 90 μT/s. In figure 5.4 the current density at four different sweep rates is plotted for film LAD203 (from Doornbos, ref [40]). As j_s exhibits a plateau at every sweep rate, so does the relaxation rate $Q(B)$ at fields below B^*. We thus observe in the relaxation the same matching effect as in j_s. The plateau in Q is also observed at higher temperatures (inset of figure 5.4) and like $B^*(T)$ from the current measurement (figure 3.6 on page 37), the size of the plateau decreases with increasing temperature. If we increase the magnetic field
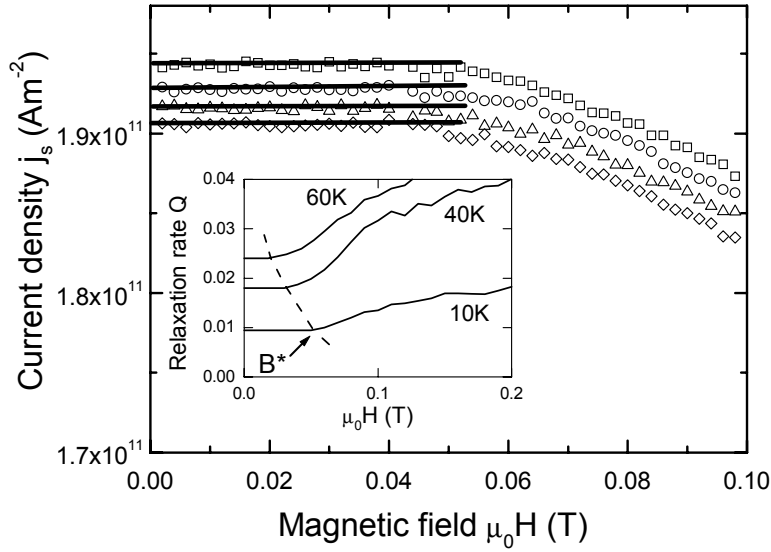
Figure 5.4: Current density $j_s(B)$ at low magnetic fields for various sweep rates (film LAD203), $T = 10$ K. $j_s(B)$ becomes constant at B^*, which is independent of the sweep rate used. From top to bottom; $dB/dt = 735, 368, 184$ and 92 μT/s. Inset: $Q(B)$ for LAD203 at $T = 10, 40$ and 60 K. The decrease of B^* with temperature is clearly observed (dashed line).

beyond the characteristic field B^*, $Q(B)$ increases steeply (see figure 5.5), especially at low temperatures. The relaxation rate rises until $\mu_0 H \approx 0.5$ T, and becomes roughly constant for high magnetic fields at low temperatures.

The sharp increase of the relaxation just above B^* can be understood as a consequence of the crossover from strong pinning by dislocations towards another (weaker) pinning regime. It is comparable to the crossover observed in $j_s(B)$ from a plateau at low fields to a power law decrease at high magnetic fields. When the current density decreases as a power law $j_s(B) \sim B^\alpha$, with $\alpha < 0$, $Q(B)$ is constant again. The behaviour of $Q(B)$ is thus closely related to the behaviour of $j_s(B)$.

There is an interesting difference in $Q(B, T)$ of films with low and high dislocation density; in films with a low dislocation density $Q(T)$ is constant at intermediate temperatures $20 < T < 50$ K (figure 5.6a). This plateau has been observed before and seems to be a common feature for YBa$_2$Cu$_3$O$_{7-\delta}$ [41]. However in films with high n_{disl}, Q increases monotonically with T (figure 5.6b).
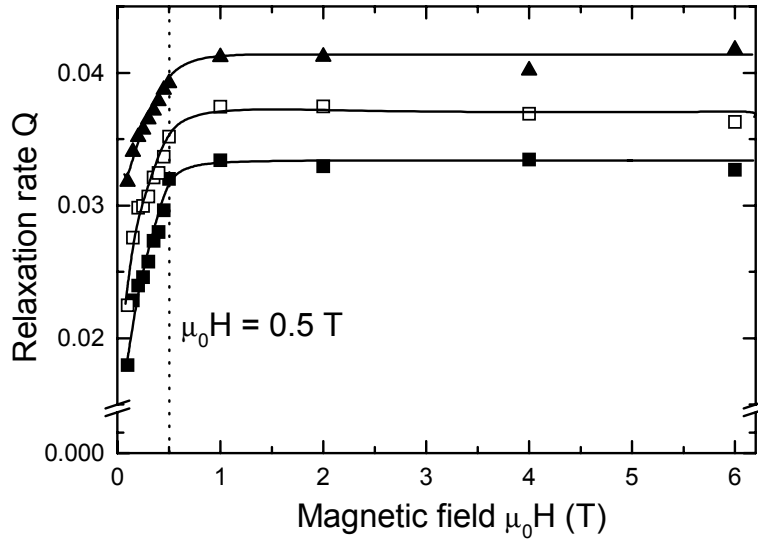
Figure 5.5: $Q(B)$ at various low temperatures for film Y67. At high magnetic fields, $Q(B)$ is constant, but when $\mu_0 H \lesssim 0.5$ T, the relaxation decreases sharply. From bottom to top $T = 7$ (■), 10 (□) and 15 K (▲). Lines are guides to the eye.

At low temperatures $T \leq 10$ K a transition from thermally activated creep to quantum creep takes place and $Q(T)$ becomes independent of temperature [42]. Especially in figure 5.6a for the lowest field values, $B = 0.1, 0.3$ T, one clearly distinguishes that $Q(T)$ starts to flatten. We do not discuss the effect of quantum creep, since it is described extensively elsewhere [43], but for describing thermally activated flux motion, we have to discard data for $T \lesssim 10$ K.
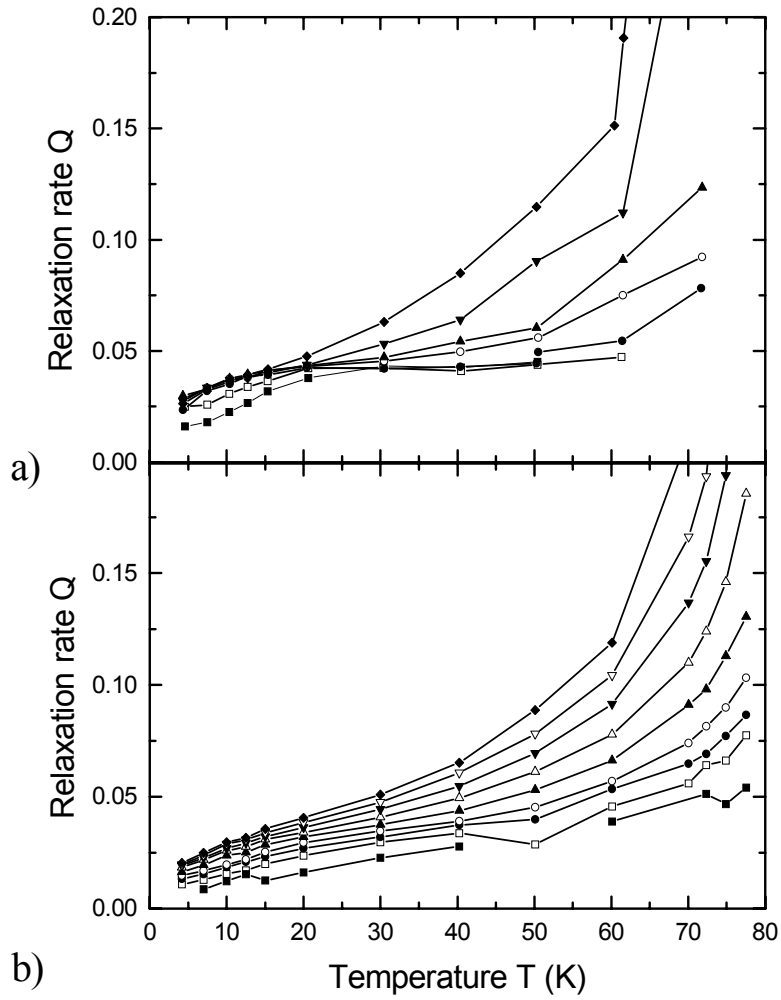
Figure 5.6: Dynamical relaxation rate $Q(T)$ for a) Y67 and b) LAD554. From bottom to top $B = 0.1$ (■), 0.3 (□), 0.5 (●), 1.0 (○), 2.0 (▲), 3.0 (△, only LAD554), 4.0 (▼), 5.0 (▽, only LAD554) and 6.0 T (◆).

5.3.3 Determination of the pinning energy U_c

The pinning energy U_c can be determined directly from the dynamical relaxation rate. For thermally activated flux creep, the probability for a vortex to jump from one pinning configuration to another is $P \propto e^{-U(j,B,T)/k_BT}$. The activation energy is given by [44]:

$$U\left(j\right) = \frac{U_c}{\mu}\left(\left(\frac{j_c}{j_s}\right)^{\mu} - 1\right) = Ck_BT, \tag{5.4}$$

where μ is a model dependent parameter, k$_B$ the Boltzmann constant and C a factor that incorporates the attempt frequency of the vortex to jump over a potential barrier and the geometry of the sample. C depends logarithmically on the sweep rate dB/dt. After extracting j_s from eq. (5.4) and differentiating to dB/dt one obtains the following relationship for U_c:

$$\frac{T}{Q} = \frac{U_c}{k_B} + \mu CT \tag{5.5}$$

Equation (5.5) provides us with a direct measure of U_c, if we plot T/Q vs. T and extrapolate to $T = 0$. Note that we have to neglect the data below $T \lesssim 10$ K, because of quantum creep. Figure 5.7 shows a plot of T/Q of the films Y67 and LAD554 ($n_{disl} = 7$ and $n_{disl} = 90$ μm^{-2}). Indeed at the lowest temperatures ($T = 4.2$ and 7 K) T/Q bends down towards $T = 0$, which corresponds to a constant relaxation rate $Q(T)$ due to quantum creep. At intermediate temperatures the relaxation rate is more or less constant and T/Q rises linearly. At higher temperatures however, thermal fluctuations become stronger and Q increases exponentially, which results in a sharp decrease of T/Q. An interesting feature is observed in figure 5.7a; at low magnetic fields $\mu_0H \lesssim 0.5$ T, an upturn develops. This feature is directly connected to the decrease of the relaxation rate, being constant at high magnetic fields and exhibiting a sharp decrease for $\mu_0H \lesssim 0.5$ T at low temperatures (figure 5.5). Especially in film Y67 the upturn is very clear but, although less pronounced, it is also observed in other films. At high magnetic fields the lines of T/Q fall almost on top of each other ($Q(B)$ is virtually constant at high magnetic fields), indicating that the pinning energy U_c is only weakly field dependent.

In figure 5.8 we plotted the pinning energy versus the magnetic field. We can distinguish the same field regimes as for the relaxation. At low magnetic fields U_c extrapolates to a value of $U_c \approx 600$ K. At high magnetic fields $U_c(B)$ is roughly constant with $U_c \approx 60 - 200$ K. The plateau in $U_c(B)$ scales with the square root of the dislocation density (inset of figure 5.8), which shows that the dislocation lattice is still important at high magnetic fields, when the vortices outnumber the strong pinning centers by far. Note that a similar field dependence of $U_c(B)$ in YBa$_2$Cu$_3$O$_{7-\delta}$ films was observed before by Douwes and Kes [6].
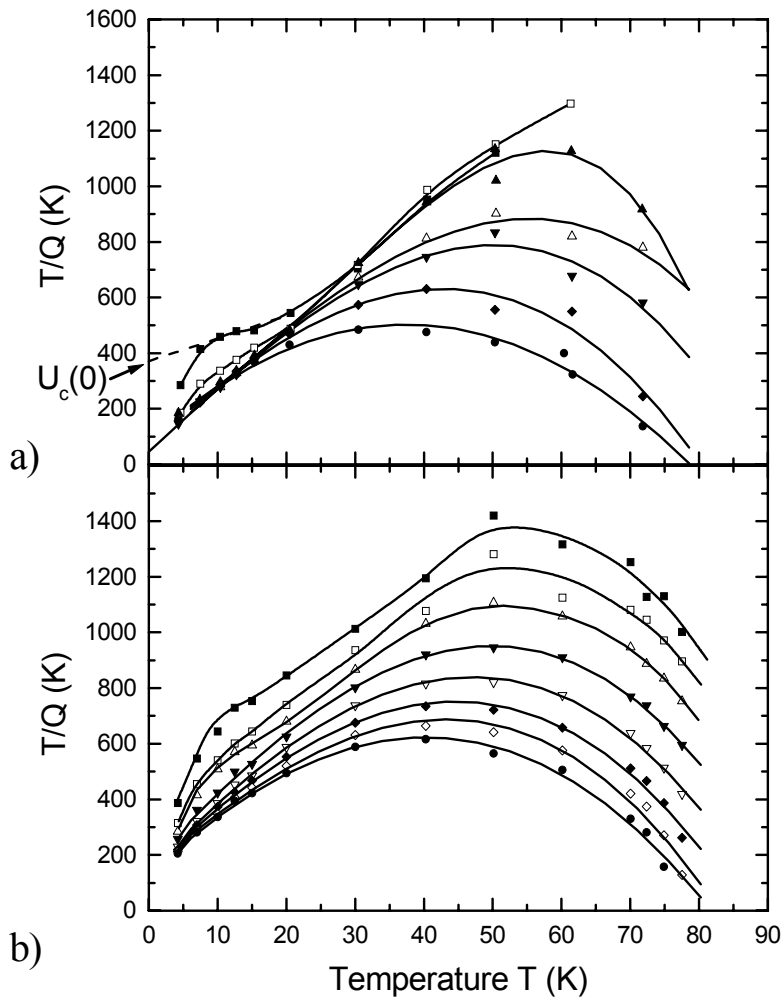
Figure 5.7: T/Q vs T plots for two films; a) Y67 and b) LAD554 at $B = 0.1$ (■, only Y67), 0.3 (□), 0.5 (▲), 1.0 (△), 2.0 (▼), 3.0 (▽, only LAD554), 4.0 (◆), 5.0 (◇, only LAD554) and 6.0 T (●). Lines are guides to the eye. Extrapolation of T/Q to $T = 0$, gives the pinning energy U_c. At high magnetic fields the pinning energy becomes independent of magnetic field. At low magnetic fields an upturn appears, that is specifically clear in Y67, resulting in an increase of $U_c(B)$. At low temperatures $T \lesssim 10$ K the curves bend down to zero due to quantum creep.

One might be tempted to conclude that $U_c(B = 0) = 600$ K is the pinning energy of a single vortex, pinned by a linear defect. However, a simple calculation of the pinning energy U_p, obtained by equating U_p to the Lorentz force $j_s\Phi_0 d$ times the range of the pinning potential ($\sim \xi$), yields $U_p \sim 10^4$ K, which is at least one order of magnitude higher than observed experimentally. The discrepancy between the experimental and theoretical pinning energies seems at first sight paradoxical, but one should realize that U_c is related to Q and thus to the elementary excitations of a vortex. The critical current density on the other hand is related to the depinning of a complete vortex from its defect, and therefore to the condensation energy ε_0 that is much larger. In section 5.4.5 we will investigate what kind of excitation is responsible for the observed pinning energy U_c.
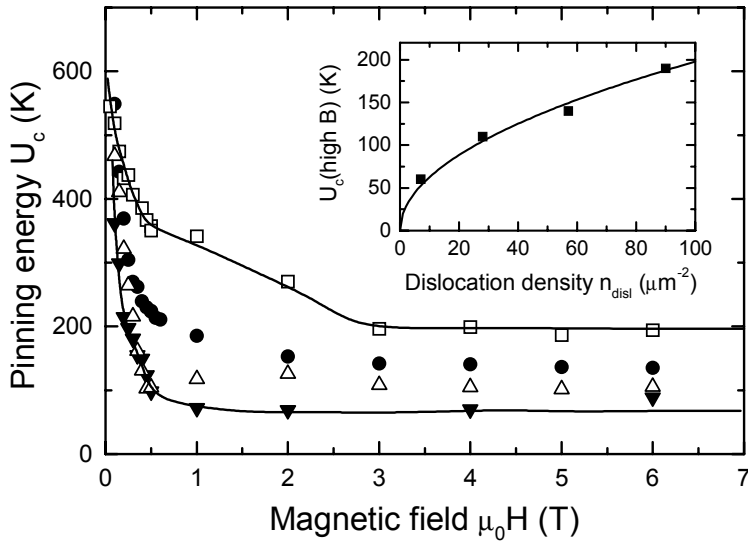
Figure 5.8: Pinning energies U_c for various films; Y67 (▼), LAD670 (△), LAD203 (●), and LAD554 (□). At high fields U_c exhibits a plateau, whereas at low magnetic fields, it rises steeply to $U_c(B = 0) \approx 600$ K. Lines are guides to the eye for Y67 and LAD554. Inset: The plateau of U_c at high magnetic fields scales with the square root of the dislocation density $\sqrt{n_{disl}}$.

5.4 Discussion

5.4.1 Current density at low magnetic fields

At low temperatures and for large defects the critical current $j_c \simeq \frac{3\sqrt{3}}{4\sqrt{2}} j_0$ is comparable to the depairing current. In thin films and in irradiated crystals the current density is typically reduced compared to the depairing current j_0, because neither the linear defect size in films nor the typical radius of columnar tracks is in the limit of $x \gg 1$. In chapter 4 we derived:

$$j_c(T) \approx \frac{3\sqrt{3}}{8} \left(\frac{r_r^2 + \xi^2(T)}{r_r \sqrt{2r_r^2 + \xi^2(T)}} - \frac{\xi(T)}{r_r} \right) j_0(T). \qquad (5.6)$$

It is convenient to put all current reducing effects into one parameter $\eta \equiv j_c/j_0$, denoting the pinning efficiency, like in ref. [45]. Experimentally we find, with $j_c \approx j_s \approx 5 \cdot 10^{11}$ Am^{-2} and $j_0 \approx 4 \cdot 10^{12}$ Am^{-2}, that $\eta = 0.13$, which is comparable to the values obtained for columnar tracks, $\eta = 0.17$ [39]. The maximum pinning efficiency can be calculated from eq. (5.6), and yields $\eta \approx 0.22$ for thin films (taking $r_r \approx 2\xi(0)$), and $\eta \approx 0.32$ for irradiated crystals (taking $r_r \approx 4\xi(0)$), see figure 4.3 in chapter 4. These maximum pinning efficiencies are close to the experimental values, which shows that the superconducting order parameter is almost completely suppressed inside the defect.

Upon heavy-ion irradiation of thin films an increase of the critical current density was observed compared to unirradiated films. The increase ranges typically from a few tens of percents [10] to a factor 2 [11, 14], which can be directly explained by the larger size of the columnar tracks compared to natural linear defects. From eq. (5.6) we find that for $r_r \approx \xi(0)$ the critical current density is roughly proportional to r_r. An increase of j_c by a factor 2 would imply that the columnar defects are about twice as large as natural linear defects, which is indeed the case. Schuster *et al.* [46] found that the relative increase of j_c in thin YBa$_2$Cu$_3$O$_{7-\delta}$ films before and after irradiation depends on the type of ion used. Heavy-ion irradiation by Pb-ions was most effective and showed an increase of j_c by a factor 5. This difference cannot be fully explained by the larger size of columnar defects, but the differences between intrinsic current densities measured in various films can be significant (see figure 3.5b on page 35). Moreover the maximum current, measured by Schuster *et al.* [46] in a Pb-irradiated film, $j_c = 6.7 \cdot 10^{11}$ Am^{-2} is about 30% larger than in our film LAD554. This implies that $r_r \approx 4$ nm for Pb-irradiated columnar defects, which is quite a reasonable estimate.

Other reports on irradiated thin films focus on the angular dependence of the pinning force, showing a peak in the irradiation direction [47, 48], or investigating Bose glass scaling in irradiated thin films [49, 50]. Unfortunately irradiation doses and, consequently, the magnetic fields considered, are usually much larger than the typical matching fields of natural linear defects ($B_\Phi \approx 100$ mT), which makes comparison to

our films difficult. To observe Bose glass scaling by natural linear defects, one would have to measure at very low fields. Note that Roas *et al.* [51] did observe a peak in the critical current density along the c-axis in as-grown YBa$_2$Cu$_3$O$_{7-\delta}$ thin films, that could well be caused by linear defects.

To compare the measured superconducting current density $j_s(T)$ with the true critical current density $j_c(T)$, whose temperature dependence was derived by theory, we need to compensate for relaxation effects. The relation between $j_s(B = 0, T)$ and $j_c(B = 0, T)$, derived from eqs. (5.4) and (5.5) is:

$$\frac{j_s}{j_c} = (1 - \mu C Q)^{1/\mu} \tag{5.7}$$

From the plots of T/Q versus T in figure 5.7 we find the product μC at low magnetic fields. The activation constant $C \approx 15-19,$[2] which results in $\mu \approx 1$. The ratio j_s/j_c is only weakly temperature dependent at intermediate temperatures 10 K $< T <$ 50 K. This is not surprising, because $Q(T)$ is roughly constant at intermediate temperatures (see figure 5.6a and ref. [41]). Furthermore j_s/j_c does not depend sensitively on μ, which enables us to treat pinning models for the critical current density at $B = 0$, provided that we correct the measured current density j_s via eq. (5.7).

In figure 5.9 the measured $j_s(T)$ is plotted for films Y67 and LAD554, together with $j_c(T)$, calculated using eq. (5.7) with $\mu = 1$ and $C = 15$ for Y67, and $C = 19$ for LAD554. Also included is the expected temperature dependence according to $j_c(T) \sim 1/\left(\lambda^2(T)\xi^\nu(T)\right)$, with $\nu = 1, 2$ and $\nu = 3$. For the temperature dependences we used $\lambda(T) = \lambda(0)/\sqrt{(1 - t^4)}$ and $\xi(T) = \xi(0)\sqrt{[(1 + t^2)/(1 - t^2)]}$, with $t = T/T_c$. We find good agreement with the measured current densities with $\nu = 3$ for Y67 and $\nu \approx 2$ for LAD554. Secondly we find that thermal fluctuations have a small effect on $j_c(T)$, which was expected, since $\tilde{T}^r_{dp} \approx 560$ K $\gg T$. From the values obtained for ν we tentatively conclude that the linear defects in Y67 are smaller in average than those in film LAD554. Indeed from AFM measurements we deduce, that the sputtered film Y67 contains twice as much edge dislocations as screw dislocations (cf. figure 3.2 on page 31), whereas in the laser ablated films, like LAD554, TEM observations revealed mostly screw dislocations. Since the Burgers vector of screw dislocations is directed along the c-axis, it is 3 times larger than for edge dislocations. We therefore expect that the defect core size, typically a few Burgers vectors, is larger in film LAD554. TEM observations from Gao *et al.* [52] indicate that $r_r \approx 1.0$ nm $\approx 2.5\,|b|$ for an edge dislocation in a YBa$_2$Cu$_3$O$_{7-\delta}$ thin film. For screw dislocations we then expect $r_r \approx 3.0$ nm $\approx 2\xi(0)$. A rough estimate for the average defect size in film Y67 yields $\bar{r}_r \approx 1.3$ nm $\approx 0.9\xi(0)$, whereas in film LAD554 we would get $r_r \approx 3.0$ nm $\approx 2\xi(0)$. Filling in $r_r = 0.9\xi(0)$ and $r_r = 2\xi(0)$ in the general equation for $j_c(T)$, eq. (5.6), and determining ν by fitting with $j_c(T) \sim 1/\left(\lambda^2(T)\xi^\nu(T)\right)$, we find $\nu = 2.0$ and $\nu = 2.8$ respectively, which is in excellent agreement with the values from figure 5.9.

---

[2] The value for C can be determined independently as it is given by $C = -\lim\limits_{T \longrightarrow 0} \frac{1}{Q}\frac{d \ln j_s}{d \ln T}$. In this way the values $C = 15$ and $C = 19$ were obtained for Y67 and LAD554 respectively.
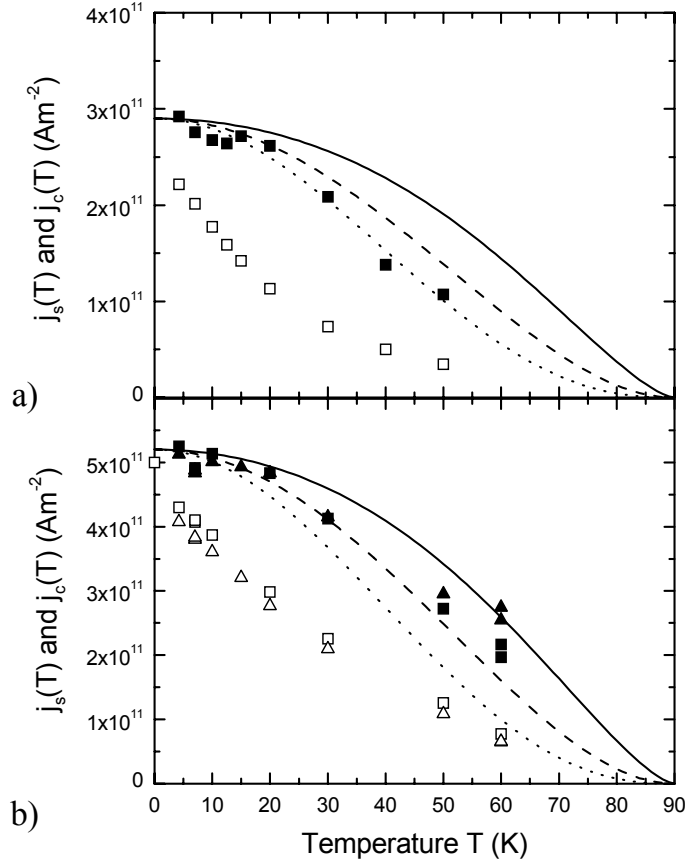
Figure 5.9: Temperature dependence of the current densities j_s (open symbols) and j_c (solid symbols) for a) Y67, $B = 0.1$ T ($\square$, $\blacksquare$), and b) LAD554, $B = 0.1$ T ($\square$, $\blacksquare$) and $B = 0.2$ T ($\triangle$, $\blacktriangle$). Lines depict the derived dependence $j_c(T) \sim 1/\lambda^2(T)\xi^\nu(T)$ with $\nu = 1$ (solid lines), $\nu = 2$ (dashed lines) and $\nu = 3$ (dotted lines). From the fits it is obvious that the average linear defect size of film Y67 is smaller than that of film LAD554.

Moreover, if we calculate $j_c(0)$ from $f_{\max} \approx -d\varepsilon_r/dR \mid_{R=r_r}$, we find $j_c(0) \approx 2.0 \cdot 10^{11}$ Am^{-2} for film Y67 and $j_c(0) \approx 5.1 \cdot 10^{11}$ Am^{-2} for film LAD554, again in good agreement with experiment.

Comparing the current density below the characteristic magnetic field for various films, we find that $j_s(B = 0)$ is essentially independent of the dislocation density. Some films with higher dislocation density $n_{disl} \gtrsim 50 \ \mu$m^{-2}, show a somewhat reduced current density at $T = 4.2$ K. We believe that this is due to the slightly reduced crystallinity for films with large n_{disl} (smaller T_c, wider rocking curve $\Delta\omega_{(005)}$), so

that the intrinsic current density is smaller in films with large n_{disl}. However, also the defect sizes may vary somewhat from film to film (as in Y67 and LAD554). The fact that $j_s(B = 0)$ is independent of the dislocation density implies that surface roughness pinning in films is, at least at low magnetic fields, not important, contrary to what has been claimed by some groups [53, 54]. Because the island density (and thus the surface roughness) increases with increasing dislocation density, surface roughness pinning would give a higher current density for high dislocation density films. This is not observed; in fact from all our measurements, we see that the current density is typically somewhat lower in films with many dislocations, compared to films with a low dislocation density. In chapter 7 we investigate the influence of the surface on the pinning properties in further detail.

5.4.2 Characteristic field

The characteristic field $B^* = 4 \left(\varepsilon_r / \varepsilon_0 \right) B_\Phi$ has the same physical origin in thin films as in irradiated single crystals, but in thin films B^* marks the end of a plateau in $j_s(B)$, whereas in single crystals the current density depends strongly on magnetic field, even below the matching field. The reason for this difference is the strong influence of vortex-vortex interactions in irradiated crystals, due to the high density and the random distribution of the columnar defects. The characteristic field in single crystals coincides with the matching field B_Φ, except for very high irradiation doses [39]. For YBa$_2$Cu$_3$O$_{7-\delta}$ thin films $B^* < B_\Phi$ and from the proportionality factor $B^*/B_\Phi = 0.7$ we estimate $\varepsilon_r/\varepsilon_0 \approx 0.18$.

The temperature dependence of $B^*(T)$, plotted normalized to its zero temperature value in figure 5.10, shows a similar dependence in films with low and high dislocation density. At low temperatures the reduction in B^* corresponds to the behaviour found in irradiated YBa$_2$Cu$_3$O$_{7-\delta}$ crystals (see the inset of figure 5.10 and figure 3.7b on page 39), but the sudden decrease of the matching field in irradiated crystals at around $T = 40$ K is absent in thin films.

To explain the decrease of $B^*(T)$ with increasing temperature we have to determine the temperature dependence of $\varepsilon_r/\varepsilon_0$, including the effect of thermal fluctuations, that facilitate the depinning of a vortex from its pinning site:

$$B^*(T) = B^*(0) \left(1 - \frac{T}{\tilde{T}_{dp}^r(T)} \right) \ln \left(1 + \frac{r_r^2}{2\xi(T)^2} \right). \tag{5.8}$$

If we use $\tilde{T}_{dp}^r(T) = \tilde{T}_{dp}^r(0) \left(\lambda^2(0)/\lambda^2(T) \right)$, with $\tilde{T}_{dp}^r(0) = 560$ K (solid lines in figure 5.10), there is no agreement with the experimental data. Both in irradiated crystals and in thin films (figure 5.10) the measured $B^*(T)$ decreases faster than theory predicts, which was noted already by Thompson *et al.* for the case of irradiated crystals [55]. To explain the fast decrease of $B^*(T)$ one can of course assume a lower depinning energy. For example taking $\tilde{T}_{dp}^r(0) = 70$ K for thin films (dashed line in figure 5.10) and $\tilde{T}_{dp}^r(0) = 95$ K for irradiated crystals (dashed line in the inset of figure 5.10) gives a good agreement with the experimental data at low temperatures.
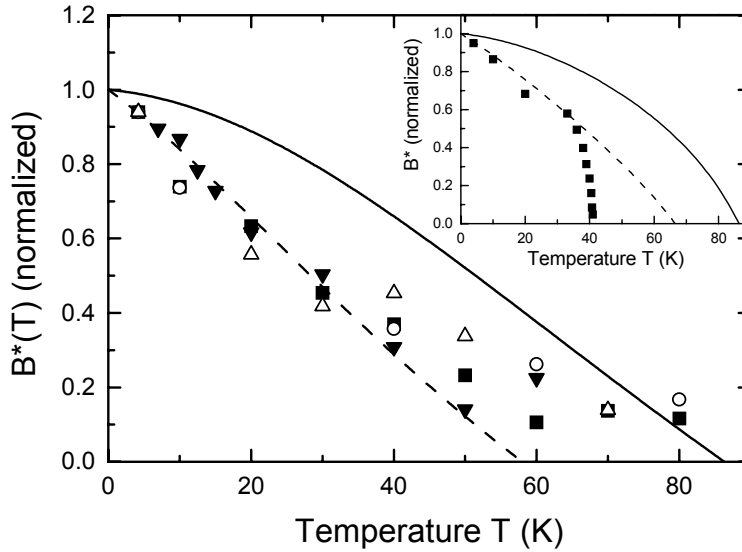
Figure 5.10: Normalized temperature dependence of the characteristic field $B^*(T)$ for films LAD670 ($\triangle$), Y67 ($\blacktriangledown$), LAD203 ($\bullet$), and LAD493 ($\blacksquare$). Lines are the expected temperature dependence with $\tilde{T}^r_{dp}(0) = 560$ K (solid line), and $\tilde{T}^r_{dp}(0) = 70$ K (dashed line). The latter is in good agreement with experiment at low temperatures. At higher temperatures $T \gtrsim 30$ K, deviations occur because the harmonic oscillator potential is only accurate when $T \ll \tilde{T}^r_{dp}(T)$. Inset: Normalized characteristic field $B^*(T)$ of an irradiated crystal (from ref. [39]), together with the expected temperature dependence with $\tilde{T}^r_{dp}(0) = 560$ K (solid line), and $\tilde{T}^r_{dp}(0) = 95$ K (dashed line). Note that $\tilde{T}^r_{dp}(T) \sim 1/\lambda^2(T)$.

But taking a different depinning energy changes the temperature dependence of $j_c(T)$ as well, and we cannot obtain a consistent picture for both $j_c(T)$ and $B^*(T)$ with a single $\tilde{T}^r_{dp}(0)$. To illustrate this inconsistency more clearly we have plotted in figure 5.11 the temperature dependence of $B^*(T)$ versus the superconducting current density $j_s(T)$ for various films. The solid line denotes the expected dependence, from eq. (5.8) and $j_s(T) = j_c(T)\,[1 - CQ]$ (taking $\tilde{T}^r_{dp}(0) = 560$ K, $C = 19$, $\nu = 2$, and $Q(T)$ from experiment), which clearly does not describe the behaviour observed in experiment. Note, that this does not depend on the choice for $\tilde{T}^r_{dp}(0)$, since both $B^*(T)$ and $j_s(T)$ contain the same factor $f(T/\tilde{T}^r_{dp})$.
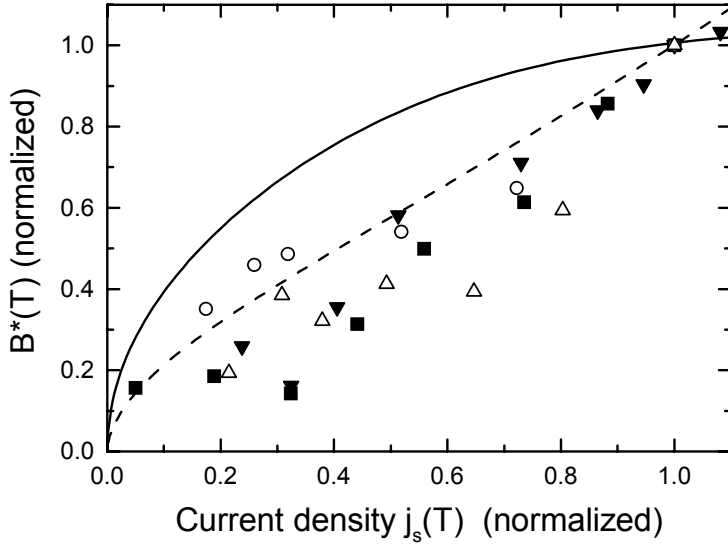
Figure 5.11: Characteristic field $B^*(T)$, plotted against $j_s(T)$ for films LAD670 ($\triangle$), Y67 ($\blacktriangledown$), LAD496 ($\circ$), and LAD493 ($\blacksquare$).   Both $B^*(T)$ and $j_s(T)$ are normalized to T = 10 K. Lines denote the expected dependencies with $j_s(T) = j_c(T)\left[1 - CQ(T)\right]$ and $B^*(T) \sim \ln(1 + x^2(T)) \cdot f(T/\tilde{T}_{dp}^r)$ (eq. (5.8), solid line) and $B^*(T) \sim \ln(1 + x^2(T)) \cdot f(T/\tilde{T}_{dp}^r) \cdot \left[1 - CQ(T)\right]$ (thermal activation included, dashed line).

However, we have to realize that the size and temperature dependence of $B^*(T)$ were derived for $j_s = 0$, whereas in our experimental situation large currents run through the film. As the pinning landscape tilts when applying a current, vortices escape more easily from the linear defect, and thus the characteristic field decreases. If we include the same factor $j_s/j_c = 1 - CQ(T)$ in the temperature dependence of $B^*(T)$, we obtain a good approximation of B^* (dashed line in figure 5.11). Apparently an increased relaxation rate results in a decrease of $B^*(T)$. Intuitively this is logical, but up to now there is no model available to describe this effect. A similar effect is observed in irradiated crystals, where the sudden decrease of $B^*(T)$ at $T = 40$ K (ref. [39], and the inset of figure 5.10), is accompanied by a sharp increase of the relaxation rate $S(T)$, resulting in a peak in $S(T)$ [39, 55].

5.4.3 Current density at high magnetic fields $\mu_0 H \gg B^*$

Whereas the pinning below the characteristic field is quite well understood, the situation at higher magnetic fields $\mu_0 H \gg B^*$ is less clear. Several models have been proposed. Douwes *et al.* [5] suggested, that at high magnetic fields, pinning is caused oxygen vacancies in the CuO_2-plane. Another possibility, suggested by Wördenweber [38], is that at high magnetic fields there is a strongly pinned vortex lattice on the linear defects, whereas the unpinned vortices move by shearing in channels through the pinned lattice. A similar shear model, giving rise to plastic pinning is described by the Bose glass theory [1]. At high magnetic fields individually pinned vortices experience a transition to bundle pinning. The large density of vortices and the variety of pinning defects and models make it hard to interpret unambiguously the experimental data, and up to now no consistent picture for pinning at high magnetic fields has emerged.

Experimentally the most remarkable feature of the high field behaviour of $j_s(B)$ is the change of slope $\alpha \equiv \mathrm{d}\ln j_s/\mathrm{d}\ln B$ from $\alpha = -0.58$ to $\alpha = -0.8$ to -1.1. This abrupt change of slope, observed when $n_{disl} > 60\ \mu\mathrm{m}^{-2}$ (which means that the average defect spacing $d_r < \lambda$), probably marks the onset of strong vortex interactions. The Bose glass theory [1], that distinguishes between plastic pinning and collective pinning, provides a useful framework to describe our observations.

In plastic pinning the vortices, not accommodated by the dislocations, are pinned via shear interactions with the strongly pinned vortex lattice. The maximum pinning force is given by $f_{p,\max} = c_{66}a_0$, where c_{66} is the shear elastic constant and a_0 the intervortex distance. The critical current density

$$j_c(B) \approx \eta \frac{\sqrt{\Phi_0}}{16\pi\mu_0\lambda_{ab}^2} \frac{B_\Phi}{\sqrt{B}} \approx \eta j_0 \frac{\xi}{\sqrt{\Phi_0}} \frac{B_\Phi}{\sqrt{B}} \tag{5.9}$$

gives a field dependence of the current $j_c \sim B^{-0.5}$. The collective pinning model relates the Lorentz force within a correlation area of size $\sim R_c^2$ to the elastic force of the vortices. Collective pinning becomes important when the correlation radius $R_c \simeq d_r \frac{\varepsilon_0}{\varepsilon_r} \frac{b_0}{a_0} \simeq d_r$, the average defect spacing. The critical current density in this case is given by:

$$j_c(B) \approx \eta \frac{\Phi_0}{4\pi\mu_0\lambda_{ab}^2\xi_{ab}} \frac{B_\Phi}{B} \approx \eta j_0 \frac{B_\Phi}{B} \tag{5.10}$$

The most important difference between eqs. (5.9) and (5.10) is the field dependence, changing from $j_c \sim 1/\sqrt{B}$ to $j_c \sim 1/B$. Exactly such a crossover we observe experimentally when the average defect spacing becomes smaller than λ. We propose that collective pinning is important when $d_r < \lambda$, whereas in a more dilute linear defect lattice vortices are plastically pinned. In irradiated single crystals, where $d_r \ll \lambda$, we expect collective pinning as well, which is indeed observed [45].

There are, however, still a number unresolved questions. First the plastic pinning model gives too low estimates for the critical current density, as noted before by Mannhart *et al.* [4] and Douwes and Kes [5]. For example, eq. (5.9) with $B_\Phi = 0.1$

T and $B = 1$ T gives $j_c \approx 1 \cdot 10^9$ Am^{-2}. This is much lower than the measured value of typically $j_s \approx 1 - 2 \cdot 10^{11}$ Am^{-2} at $T = 4.2$ K and $B = 1$ T. This also implies that the low field current density, eq. (5.6), and the high field current density, eq. (5.9), do not connect at the matching field B_Φ (contrary to the collective pinning case, with eqs. (5.6) and (5.10), note that $\eta \equiv j_c(0)/j_0$). Matching the linear defect pinning and plastic pinning regimes would imply a dramatic decrease of $j_s(B)$ over two orders of magnitude between B^* and B_Φ. Instead we observe a smooth crossover to a power law regime, with only a minor decrease of $j_s(B)$. On the other hand the plateau in U_c at high magnetic fields increases with the dislocation density (inset of figure 5.8), which can be perfectly understood in a plastic pinning model, since shearing through a defect lattice, filled with strongly pinned vortices, will be more difficult when the defect lattice is denser. Therefore a plastic pinning model is still a good candidate since it gives the right field dependence $j_s \sim 1/\sqrt{B}$ and explains why U_c increases with increasing dislocation density.

The discrepancy between theory and experiment points out that vortex-vortex interactions have a more profound influence on the current density than anticipated. One essential point, not considered up to now, is the non-random distribution of the linear defects in thin YBa$_2$Cu$_3$O$_{7-\delta}$ films. Due to the ordered distribution of the strongly pinned vortices at B^* they provide a natural way for additional vortices to distribute themselves regularly, which improves the pinning properties at higher fields as well. In order to fully explain the measured size of j_s and its field dependence into more detail, these effects have to be taken into account more explicitly.

Secondly the slopes α do not coincide exactly with the theoretical dependencies. For films with high dislocation density $\alpha \approx -0.8$ at low temperatures, which is too large for collective pinning, for which $\alpha \approx -1$. Moreover $|\alpha(T)|$ increases with temperature for films with high n_{disl}. Possibly the current density is determined by a mixture of collective and shear pinning. After all we are still in a relatively low field regime, where $R_c \ll d_r$, and it is surprising that collective pinning occurs at all.

We can give a rough quantitative argument why the slopes of the power law behaviour do not coincide exactly with the expected slopes in eqs. (5.9) and (5.10), and why $\alpha(T)$ is temperature dependent for films with high n_{disl}. Due to relaxation $\alpha \equiv \mathrm{d}\ln j_s/\mathrm{d}\ln B \neq \mathrm{d}\ln j_c/\mathrm{d}\ln B$. If we differentiate the general formula of thermally activated vortex creep, given by eq. (5.4), with respect to the magnetic field B, we obtain the following expression[3]:

$$\frac{d\ln j_c}{d\ln B} = \frac{d\ln j_s}{d\ln B} + Q - CQ\frac{d\ln U_c}{d\ln B} = \alpha + Q - CQ\frac{d\ln U_c}{d\ln B} \qquad (5.11)$$

Thus, to obtain the field dependence of the true critical current density $\mathrm{d}\ln j_c/\mathrm{d}\ln B$, we have to add to the slope α two positive terms (note that in general $\mathrm{d}\ln U_c/\mathrm{d}\ln B \leq 0$). So the measured slope α is always more negative than the field dependence of the true critical current density. Comparing this with the measured slopes (figure 5.3), we

---

[3]Hereby we neglect the field dependence of μ. We assume that, as we are in a specific pinning regime, μ is independent of B. This assumption is strictly speaking not true, but for a crude estimate it is not necessary to take the field dependence of μ into account.

observe that for films with low n_{disl}, $\alpha = -0.58$. This suggests that $j_c(B) \sim 1/\sqrt{B}$, with a correction of 0.08. Because α is constant with temperature, so should $Q(T)$ for these films. From figure 5.6a we learn that this is indeed the case for films with a low dislocation density. For films with high n_{disl}, $\alpha \approx -0.8$ at low temperatures. With increasing temperature the slope decreases, but $Q(T)$ increases (figure 5.6b), so the correction terms are higher at larger temperatures, suggesting that $\mathrm{d}\ln j_c/\mathrm{d}\ln B$ is roughly constant with temperature.

In numerical simulations a slope $\mathrm{d}\ln j_c/\mathrm{d}\ln B = -0.7 \pm 0.1$ has been found, by simulating the plastic deformations due to strong pinning, and allowing entanglement [56]. This entanglement as an additional ingredient could explain the observed slopes $\alpha = -0.8$ with a small correction according to eq. (5.11). However, an exact calculation of the field dependence of the critical current would require a more thorough derivation, that includes in eq. (5.11) also the field dependence of μ, which cannot be determined accurately within experiment.

5.4.4 Dynamical relaxation rate

Various pinning regimes are clearly seen in the field dependence of the relaxation rate $Q(B)$. Below B^* the relaxation rate is constant. Then it increases and becomes constant again for magnetic fields $\mu_0 H \gtrsim 0.5$ T. The same regimes are observed in $j_s(B)$ (showing first a constant plateau and in the second regime a power law behaviour), and also in the pinning energy $U_c(B)$. This suggests that there are at least two regimes, one below B^* with strongly pinned vortices on the linear defects, and one above $\mu_0 H \gtrsim 0.5$ T with plastically or collectively pinned vortices. In between these two regimes the relaxation rate increases steeply.

The reason why the crossover occurs at about 0.5 T is not clear at present. In any case it is observed in various films independently of the dislocation density. Also it has been observed by other groups [4, 6], and in quantum creep [43]. The change in behaviour at around $\mu_0 H = 0.5$ T is thus more general for $\mathrm{YBa_2Cu_3O_{7-\delta}}$ films, and may well be related to a stronger influence of vortex-vortex interactions. The intervortex distance at this field $a_0 \approx 63$ nm $\approx \frac{1}{2}\lambda$, so the vortex-vortex interactions become increasingly more important beyond this field.

The temperature dependence of the relaxation rate at low fields is different in irradiated single crystals. Whereas in thin films $Q(T)$ rises monotonically, in irradiated crystals the conventional relaxation rate $S(T)$ exhibits a peak for $\mu_0 H < B^*$ [39, 55]. This peak marks the crossover of a single vortex regime, where the motion of vortices takes place via variable range hopping, to a collective pinning regime involving vortex bundles [55]. In thin films a similar peak of $Q(T)$ is absent, because both variable range hopping and bundle pinning do not occur in thin films at $\mu_0 H \simeq B^*$. A necessary condition for variable range hopping is a strong dispersion in the pinning energies and/or distances between the strong pinning sites [2]. In single crystals irradiation indeed produces randomly distributed columnar tracks of various strength, but in thin films the dispersion in pinning energies of the dislocations is much smaller, as follows from the variation in distances between the defects [22]. Secondly, in thin films vortex bundles do not form immediately above the characteristic field $\mu_0 H \gtrsim B^*$, be-

cause the field value $B^* \lesssim 100$ mT is too small. In thin films B^* marks a different crossover in vortex pinning, namely dislocation pinning governed by half-loop excitations (sections 5.4.1 and 5.4.5) towards a plastic or collective pinning regime that sets in at higher magnetic fields (section 5.4.3).

The absence of a peak in the relaxation rate is consistent with the behaviour of $j_s(T)$, because $Q(T)$ is directly related to the behaviour $d\ln j_s/dT$. In irradiated crystals $d\ln j_s/dT$ shows a minimum when $\mu_0 H < B^*$, when $Q(T)$ experiences a peak. In thin films the minimum in $d\ln j_s/dT$ is absent, as is the peak in $Q(T)$. This illustrates once more the close relationship between the relaxation rate $Q(T)$, or equivalently $S(T)$, and the derivative of the current density $d\ln j_s/d\ln T$, as was found in the magnetic field dependence of the relaxation $Q(B)$, eq. (5.11). In fact an expression similar to eq. (5.11) was derived in ref. [39], relating the temperature dependence of $j_s(T)$ to the conventional relaxation rate $S(T)$.

5.4.5 Pinning energy U_c

According to the Bose glass theory the vortex excitations that determine the pinning energy U_c at high driving currents are half-loop excitations. For half-loop excitations the activation energy is calculated by balancing the driving force with the loss in pinning energy and the increase of elastic energy. It is given by [2]:

$$U(j) = \xi\sqrt{\varepsilon_l\varepsilon_r(T)}\left(\frac{j_c}{j_s}-1\right) = U_c(T)\left(\frac{j_c}{j_s}-1\right), \qquad (5.12)$$

with ε_r the depth of the pinning potential and ε_l the line tension, which is smaller than ε_0 due to anisotropy. Note that $\tilde{T}_{dp}^r \equiv b_0\sqrt{\varepsilon_l\varepsilon_r}$, which means that the depinning energy and half-loop energy are comparable in size. With $\xi = 1.5$ nm and $\varepsilon_l \approx \varepsilon_r \approx 0.2\varepsilon_0$ we estimate that $U_c(0) \approx 280$ K, which is smaller than the experimentally obtained value $U_c(0) \approx 600$ K, but given the uncertainty in the parameters used, the estimate is not so bad.

The temperature dependence of $U_c(T)$ is given by:

$$U_c(T) = U_c(0)\frac{\lambda^2(0)\xi(T)}{\lambda^2(T)\xi(0)}\sqrt{f\left(T/\tilde{T}_{dp}^r\right)} \sim \frac{\xi(T)}{\lambda^2(T)}\sqrt{f\left(T/\tilde{T}_{dp}^r\right)} \qquad (5.13)$$

To check whether or not this kind of excitation is consistent with experiment, we can use the temperature dependence of $U_c(T)$ to calculate the ratio j_s/j_c. Half-loop excitations impose that the glass exponent in eq. (5.4) $\mu = 1$, which implies that:

$$\frac{j_s(T)}{j_c(T)} = \frac{1}{1 + Ck_B T/U_c(T)} \qquad (5.14)$$

In figure 5.12 we plotted the ratio $j_s/j_c = 1 - CQ$ from experiment together with the expected temperature dependence, given by eq. (5.14). We took $\tilde{T}_{dp}^r(0) = 560$ K, and the usual temperature dependence for $\lambda(T)$ and $\xi(T)$. We find excellent agreement with experiment, if we take for $U_c(0) = 280$ K for Y67 and $U_c(0) = 600$ K for LAD554.
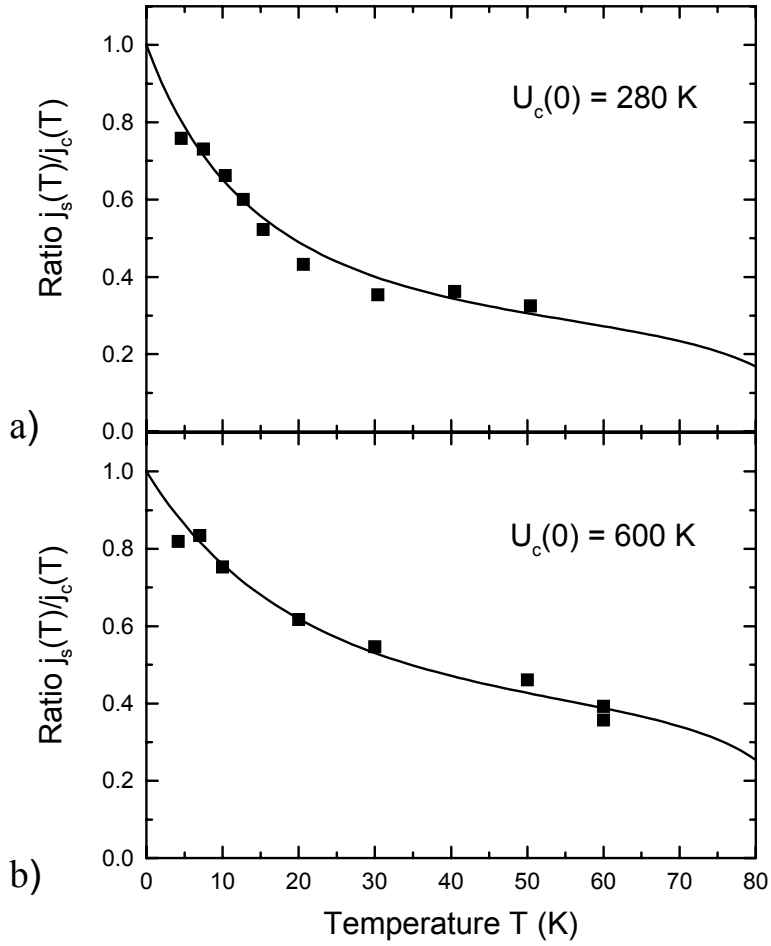
Figure 5.12: Ratio j_s/j_c from experiment and theory for films a) Y67 and b) LAD554. Solid squares are obtained from experiment. Solid lines correspond to the theoretical behaviour for half-loop excitations eqs. (5.13) and (5.14), with $\mu = 1$, $C = 15$ (Y67) or $C = 19$ (LAD554), $\tilde{T}_{dp}^r(0) = 560$ K, and $U_c = 280$ K for Y67 and $U_c = 600$ K for LAD554.

This agrees with the pinning energy, measured experimentally at $B = 0.1$ T, $U_c = 360$ K and $U_c = 520$ K for film Y67 and film LAD554 respectively. Note, that $B = 0.1$ T is larger than B^* for film Y67. Therefore $U_c = 360$ K < 600 K, since the pinning energy decreases steeply beyond B^*. Unfortunately no relaxation data was available at lower magnetic fields.

An important question is whether the assumption, that the glass exponent $\mu = 1$, is correct at low fields. From the low temperature slope of the plots T/Q vs. T, figure 5.7, we find $\mu \approx 1 - 1.3$ at high magnetic fields $\mu_0 H > 0.5$ T, but for low fields μ is decreasing towards $\mu \approx 0.5$ at $\mu_0 H = 0.1$ T. The order of magnitude of μ is reasonable, but its field dependence is puzzling. For variable range hopping, theory predicts μ to increase from $1/3$ to 1 with increasing magnetic field [1, 2], which is similar to the increase of $\mu(B)$ we observe in experiment. Assuming a somewhat higher C we find even quantitative agreement with the theory for variable range hopping. But, as we argued in the previous section, variable range hopping is unlikely to occur in our films, due to the large distances between defects. It involves a pinning energy of typically $U_c \simeq d_r \sqrt{\varepsilon_l \varepsilon_r}$, which is at least one order of magnitude larger than the energy required for half-loop excitations. On the other hand, in film Y67, that contains both edge and screw dislocations (with edge dislocations that are possibly uncorrelated, as they are not connected to any growth feature) we might have a larger dispersion in the pinning potential ε_r, which facilitates variable range hopping. Indeed in the T/Q versus T plot (figure 5.7a) the decrease of $\mu(B)$ with magnetic field is more apparent than in film LAD554.

The length ℓ_{hl} of the half-loop and the displacement u_{hl} of a half-loop excitation [57] are of the order of a few nanometer, in agreement with other estimates for the activation length. Hylton and Beasley [58] obtained similar values for the length of a vortex segment, being depinned from a linear row of point pins. Also Hoekstra *et al.* [59] found at very low temperatures, that the correlation length L_c is of the order of a few nanometers. We conclude that half-loops provide the most likely mechanism for vortex excitations at low magnetic fields, but the measured values of the glass exponent remain unexplained by theory. In any case the ratio j_s/j_c from experiment is consistent with a pinning energy $U_c(T)$ of half-loop excitations, and moreover it has the correct temperature dependence.

At high magnetic fields the pinning energy is essentially constant. Its magnitude appears to be proportional to the square root of the dislocation density (inset of figure 5.8). We propose that pinning of vortices in the high field regime is caused by the collective pinning of vortex bundles, between the array of strongly pinned vortices. Assuming that it involves plastic pinning of vortex bundles of volume V_c we have [2]:

$$U_c(B) \simeq \sqrt{c_{44}\bar{E}_{pin}}V_c \simeq \sqrt{c_{44} \cdot c_{66} \left(a_0/d_r\right)^2}V_c \simeq \frac{\Phi_0 \sqrt{B}}{16\pi\mu_0\lambda^2}\sqrt{B_\Phi}V_c \qquad (5.15)$$

which gives the observed dependence of $U_c(B) \propto \sqrt{B_\Phi} \propto \sqrt{n_{disl}}$. The field dependence of $U_c(B)$ implies that $V_c(B) \sim 1/\sqrt{B}$. The collective pinning volume at $\mu_0 H = 0.5$ T, according to eq. (5.15) and the inset of figure 5.8, is $V_c \approx 5.3 \cdot 10^{-24}$ m^3. Taking the intervortex distance at $\mu_0 H = 0.5$ T for the collective pinning radius,

i.e. $R_c = 63$ nm, we obtain $L_c \approx 1.3$ nm. A theoretical estimate for $R_c \simeq d_r \frac{\varepsilon_0}{\varepsilon_r} \frac{b_0}{a_0} \approx 24$ nm gives $L_c \approx 9.3$ nm. These values of typically a few c-axis lattice distances agree well with other estimates (see for example Doyle *et al.*, ref. [60]) for the collective pinning length and for the size of the half-loop excitations along the c-axis.

5.5 Conclusions

Natural linear defects have a profound effect on the pinning properties of high-T_c YBa$_2$Cu$_3$O$_{7-\delta}$ thin films. We have shown that indeed many features, both in the field and temperature dependence of the superconducting current density and the relaxation rate, can be described in terms of vortex pinning by growth-induced linear defects. Since the defect size is of the order of ξ and the average defect spacing of the order of λ, columnar defect models have to be adapted accordingly.

In figure 5.13 we give a schematic overview of the typical behaviour of $j_s(B)$, $Q(B)$ and $U_c(B)$ in various regimes. At low magnetic fields $\mu_0 H < B^*$ the vortices are strongly pinned by the dislocations resulting in a plateau both in $j_s(B)$ and $Q(B)$. To describe the pinning properties of the linear defects consistently with the Bose glass theory, we derived in chapter 4 a generalized expression for $\varepsilon_r(R)$, which is valid for all defect sizes. As a result, we find that the effect of thermal fluctuations is linear with temperature $f(T/\tilde{T}_{dp}^r) \approx 1 - T/\tilde{T}_{dp}^r$. Fitting the temperature dependence of $j_c(B = 0)$ with the modified expression for $\varepsilon_r(R,T)$ we find a defect size $r_r \approx 1.5 - 3$ nm $\approx 1 - 2 \cdot \xi_{ab}(0)$, which corresponds to the estimated core radius of edge and screw dislocations. The elementary excitations in this regime are half-loop excitations, involving a pinning energy of $U_c \approx 600$ K. The temperature dependence of $U_c(T) \sim \xi(T)/\lambda^2(T)$ for half-loop excitations gives a ratio j_s/j_c, in agreement with experiment. However, the strong temperature dependence of the characteristic field remains puzzling. We suspect that $B^*(T)$ is decreased due to the large currents running in the film, resulting in a small activation barrier for vortex jumps. Unfortunately, there is as yet not a model including the effect of the current density on the characteristic field $B^*(T)$.

At intermediate magnetic fields $B^* < \mu_0 H \lesssim 0.5$ T, the critical current density starts to deviate from its plateau value. The relaxation increases, whereas the pinning energy decreases steeply. Since at 0.5 T the inter-vortex spacing equals half the penetration depth, the crossover could mark the onset of a pinning regime where vortex-vortex interactions become increasingly more important.

At high magnetic fields $\mu_0 H \gg 0.5$ T, the superconducting current density decreases as $j_s(B) \sim 1/\sqrt{B}$ for films with low dislocation density $n_{disl} \lesssim 60 \ \mu\mathrm{m}^{-2}$. The pinning energy is independent of magnetic field, $U_c(B) \simeq 60 - 200$ K, and it is proportional to $\sqrt{n_{disl}}$. For films with a small defect spacing $d_r < 130$ nm $\approx \lambda$ the current density $j_s(B)$ decreases more strongly with magnetic field, $\alpha = -0.8$ to -1.1. This behaviour of α suggests a transition from plastic to collective pinning. The fact, that $U_c(B)$ and the behaviour of α depend on the dislocation density, indicates that the linear defects play an important role even far above the matching field.

An important question from an applications point of view is, how to make films with the largest possible current densities at 77 K, and at high magnetic fields.
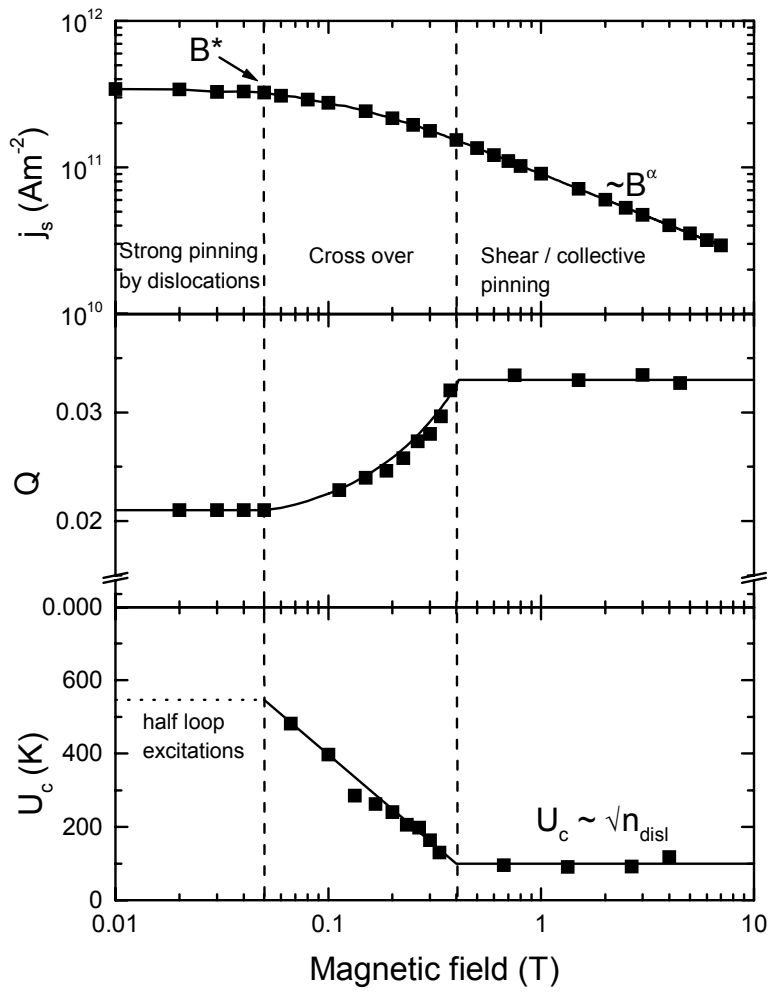
Figure 5.13: Different vortex regimes with increasing magnetic field in thin films of YBa$_2$Cu$_3$O$_{7-\delta}$. Three regimes can be clearly distinguished; (i) a strongly pinned vortex lattice below B^*, (ii) a crossover regime and (iii) a plastic / collective pinning regime at high magnetic fields. Lines are guides to the eye.

We have seen that, especially at elevated temperatures, thermal activation causes a large difference between the superconducting current j_s and the critical current j_c. Moreover, the critical current is reduced, as the vortices are pinned only plastically or collectively at high magnetic fields. The results presented in this paper show two possible options to optimize $j_s(B,T)$, namely (i) increasing the *density* of linear pinning sites, and (ii) increasing the *core size* of the linear pinning sites. We will consider here some aspects of both possibilities to achieve higher current densities.

For films with a high n_{disl} the plateau of constant j_s extends up to larger field values, but at high magnetic fields, $\mu_0 H \gg B^*$, $j_s(B)$ decreases faster in these films ($j_s \sim 1/B$ compared to $j_s \sim 1/\sqrt{B}$ for films with a low n_{disl}). Whether increasing the dislocation density also increases $j_s(\text{high}B)$ is therefore not a priori clear. Moreover it remains to be seen up to what n_{disl} the plateau-like features in $j_s(B)$ remain intact. We expect that to obtain larger current densities, the non-random distribution of natural linear defects is an advantage over the random distribution of columnar tracks, but on the other hand columnar tracks can be produced with far higher densities (several Teslas) than natural linear defects ($B_\Phi \lesssim 200$ mT). Experimentally we find at magnetic fields $\mu_0 H \sim 1-2$ T, that films with many dislocations still carry the largest currents. We conclude that increasing the dislocation density (eventually by heavy-ion irradiation) can be effective in achieving higher current densities, but it depends very much on what field and temperature range one is using.

A larger defect core size gives a deeper pinning potential and a larger pinning force $f_p = -d\varepsilon_r/dR \mid_{\max}$ (see figure 4.3 on page 59). Therefore, increasing the defect size gives intrinsically (i) a larger critical current density j_c and (ii) a higher pinning energy U_c. Also the temperature dependence $j_c(T) \sim 1/\left(\lambda^2(T)\xi^\nu(T)\right)$ is less strong for smaller ν, i.e. a larger defect size. From the lines for various ν in figure 5.9 we find at $T = 77$ K, that the critical current density $j_c(\nu = 2) \approx 2.5 \cdot j_c(\nu = 3)$. The measured critical current density j_s benefits even more from a larger defect size, since the ratio $j_s/j_c \approx 0.2$ (at $T = 77$ K and $\nu = 2$) becomes larger for larger pinning energies, see eq. (5.14). Since irradiation by heavy ions produces columnar defects with a radius, which is 2 to 3 times larger than that of linear defects, the reasoning above might explain why irradiation of thin films [10, 11, 14] is more effective in enhancing the critical currents at high ($T = 77$ K) temperatures [11]. In order to increase the diameter of *natural* linear defects, one would have to find ways to produce (screw) dislocations with a Burgers vector of several times the unit-cell.

Concluding, we find that the high critical currents in $YBa_2Cu_3O_{7-\delta}$ thin films are to a large extent due to natural linear defects. Due to half-loop nucleation vortices can depin rather easily, which reduces the measured current j_s compared to the true critical current density j_c. Theoretically, strong pinning in the high field regime, where vortex-vortex interaction competes with vortex pinning still needs to be explored. In order to obtain the maximum current density at high fields and temperatures, one has to find the optimum balance between (i) large defect density versus strong vortex-vortex interactions, and (ii) randomly distributed, but large defects (columnar tracks) versus regularly distributed, but small defects (growth-induced linear defects).

References

[1]   D.R. Nelson and V.M. Vinokur, Phys. Rev. B **48**, 13060 (1993)

[2]   G. Blatter, M.V. Feigel'man, V.B. Geshkenbein, A.I. Larkin and V.M. Vinokur, Rev. Mod. Phys. **66**, 1125 (1994), section IX-B (page 1327 and further)

[3]   M. Hawley, I.D. Raistrick, J.G. Beery, and R.J. Houlton, Science **251**, 1587 (1991)

[4]   J. Mannhart, D. Anselmetti, J.G. Bednorz, A. Catana, Ch. Gerber, K.A. Müller, and D.G. Schlomm, Z. Phys. B **86**, 177 (1992)

[5]   H. Douwes, P.H. Kes, Ch. Gerber, and J. Mannhart, Cryogenics **33**, 486 (1993)

[6]   H. Douwes and P.H. Kes, J. Alloys & Compounds **195**, 451 (1993)

[7]   V.M. Pan, A.L. Kasatkin, V.L. Svetchnikov, and H.W. Zandbergen, Cryogenics **33**, 21 (1993)

[8]   A. Díaz, L. Mechin, P. Berghuis, and J.E. Evetts, Phys. Rev. Lett. **80**, 3855 (1998)

[9]   L. Civale, Supercond. Sci. Technol. **10**, A11 (1997), and references therein

[10]   B. Roas, B. Hensel, G. Saemann-Ischenko, and L. Schultz, Appl. Phys. Lett. **54**, 1051 (1989),
B. Roas, B. Hensel, S. Henke, S. Klaumünzer, B. Kabius, W. Watanabe, G. Saemann-Ischenko, L. Schultz, and K. Urban, Europhys. Lett. **11**, 669 (1990)

[11]   M.P. Siegal, R.B. Vandover, J.M. Phillips, E.M. Gyorgy, A.E. White, and J.H. Marshall, Appl. Phys. Lett. **60**, 2932 (1992)

[12]   M. Baert, V.V. Metlushko, R. Jonckheere, V.V. Moshchalkov, and Y. Bruynseraede, Phys. Rev. Lett. **74**, 3269 (1995),
V.V. Moshchalkov, M. Baert, V.V. Metlushko, E. Rosseel, M.J. van Bael, K. Temst, R. Jonckheere, and Y. Bruynseraede, Phys. Rev. B **54**, 7385 (1996)

[13]   A. Castellanos, R. Wördenweber, G. Ockenfuss, A. VonderHart, and K. Keck, Appl. Phys. Lett. **71**, 962 (1997)

[14]   E. Mezzetti, R. Gerbaldo, G. Ghigo, L. Gozzelino, B. Minetti, C. Camerlingo, A. Monaco, G. Cuttone, and A. Rovelli, Phys. Rev. B **60**, 7623 (1999),
G. Ghigo, A. Chiodoni, R. Gerbaldo, L. Gozzelino, E. Mezzetti, B. Minetti, C. Camerlingo, G. Cuttone, and A. Rovelli, Supercond. Sci. Technol. **12**, 1059 (1999),
E. Mezzetti, A. Chiodoni, R. Gerbaldo, G. Ghigo, L. Gozzelino, B. Minetti, C. Camerlingo, and A. Monaco, Physica C **332**, 115 (2000)

[15]   A. Gurevich and L.D. Cooley, Phys. Rev. B **50**, 13563 (1994)

[16]   R. Fehrenbacher, V.B. Geshkenbein, and G. Blatter, Phys. Rev. B **45**, 5450 (1992)

[17]   X.Y. Cai, A. Gurevich, I-Fei Tsu, D.L. Kaiser, S.E. Babcock, and D.C. Larbalestier, Phys. Rev. B **57**, 10951 (1998)

[18] D.S. Fisher, M.P.A. Fisher, and D.A. Huse, Phys. Rev. B **43**, 130 (1991)

[19] G.W. Crabtree, W.K. Kwok, U. Welp, D. Lopez, and J.A. Fendrich, in. R. Kossowsky *et al.* (eds.), *Physics and Materials Science of Vortex States, Flux Pinning and Dynamics*, NATO Science Series **E356**, 357 (1999), and references therein

[20] J.M. Huijbregtse, B. Dam, J.H. Rector, and R. Griessen, J. Appl. Phys. **86**, 6528 (1999)

[21] The average transition temperature and transition width were determined by measuring a large collection of $YBa_2Cu_3O_{7-\delta}$ films (see ref. [20]), including the films listed in table 5.1.

[22] J.M. Huijbregtse, B. Dam, R.C.F. van der Geest, F.C. Klaassen, R. Elberse, J.H. Rector, and R. Griessen, Phys. Rev. B **62**, 1338 (2000)

[23] M. Pannetier, F.C. Klaassen, R.J. Wijngaarden, M. Welling, K. Heeck, J.M. Huijbregtse, B. Dam, and R. Griessen, Phys. Rev. B **64**, 144505 (2001), and chapter 6 of this thesis

[24] S. Freisem, A. Brockhoff, D.G. de Groot, B. Dam, and J. Aarts, J. Magn. Mat. **165**, 380 (1997)

[25] J.C. Martínez, B. Dam, B. Stäuble-Pümpin, G. Doornbos, R. Surdeanu, U. Poppe, and R. Griessen, J. Low Temp. Phys. **105**, 1017 (1996)

[26] B. Dam, C. Træholt, B. Stäuble-Pümpin, J. Rector, and D.G. de Groot, J. Alloys and Compounds **251**, 27 (1997)

[27] J.M. Huijbregtse, F.C. Klaassen, A. Szepielow, J.H. Rector, B. Dam, R. Griessen, B.J. Kooi, and J.Th.M. de Hosson, Supercond. Sci. Technol. **15**, 1 (2002)

[28] A. Gurevich and E.A. Pashitskii, Phys. Rev. B **57**, 13878 (1998)

[29] N.F. Heinig, R.D. Redwing, I. Fei Tsu, A. Gurevich, J.E. Nordman, S.E. Babcock, and D.C. Larbalestier, Appl. Phys. Lett. **69**, 577 (1996)

[30] B. Dam, J.M. Huijbregtse, F.C. Klaassen, R.C.F. van der Geest, G. Doornbos, J.H. Rector, A.M. Testa, S. Freisem, J.C. Martínez, B. Stäuble-Pümpin, and R. Griessen, Nature **399**, 439 (1999), and chapter 3 of this thesis

[31] M. Qvarford, K. Heeck, J.G. Lensink, R.J. Wijngaarden, and R. Griessen, Rev. Sci. Instrum. **63**, 5726 (1992)

[32] C.P. Bean, Phys. Rev. Lett. **8**, 250 (1962)

[33] E.H. Brandt, Phys. Rev. B **48**, 6699 (1993)

[34] M.V. Indenbom, C.J. van der Beek, M. Konczykowski, and F. Holtzberg, Phys. Rev. Lett. **84**, 1792 (2000)

[35] Y. Yeshurun and A.P. Malozemoff, Phys. Rev. Lett. **60**, 2202 (1988)

[36] A.C. Mota, A. Pollini, P. Visani, K.A. Müller, and J.G. Bednorz, Phys. Rev. B **36**, 4011 (1987)

[37] H. Schnack, R. Griessen, J.G. Lensink, and H.H. Wen, Phys. Rev. B **48**, 13178 (1993)

[38] R. Wördenweber, Phys. Rev. B **46**, 3076 (1992),
R. Wördenweber, Cryogenics **32**, 1098 (1992)

[39] L. Krusin-Elbaum, L. Civale, J.R. Thompson, and C. Feild, Phys. Rev. B **53**, 11744 (1996)

[40] G. Doornbos, *Pinning and Crossovers in the Vortex-Dynamics of High-T$_c$ Thin Films*, PhD thesis, Vrije Universiteit Amsterdam (2001)

[41] A.P. Malozemoff and M.P.A. Fischer, Phys. Rev. B **42**, 6784 (1990),
H.H. Wen, Z.X. Zhao, R.J. Wijngaarden, J.H. Rector, B. Dam, and R. Griessen, Phys. Rev. B **52**, 4583 (1995)

[42] I.L. Landau and H.R. Ott, Physica C **340**, 251 (2000),
J. Chen, D.L. Yin, P. Zheng, J. Hammann, G.C. Xiong, Q. Jiang, K. Wu, Z.J. Chen, and D. Jin, Physica C **282-287**, 2267 (1997)

[43] A.F.Th. Hoekstra, A.M. Testa, G. Doornbos, J.C. Martínez, B. Dam, R. Griessen, B.I. Ivlev, M. Brinkmann, K. Westerholt, W.K. Kwok, and G.W. Crabtree, Phys. Rev. B **59**, 7222 (1999)

[44] M.V. Feigel'man, V.B. Geshkenbein, A.I. Larkin, and V.M. Vinokur, Phys. Rev. Lett. **63**, 2303 (1989),
M.V. Feigel'man, V.B. Geshkenbein, and V.M. Vinokur, Phys. Rev. B **43**, 6263 (1991)

[45] L. Civale, A.D. Marwick, T.K. Worthington, M.A. Kirk, J.R. Thompson, L. Krusin-Elbaum, Y. Sun, J.R. Clem, and F. Holtzberg, Phys. Rev. Lett. **67**, 648 (1991)

[46] Th. Schuster, H. Kuhn, M.R. Koblischka, H. Theuss, H. Kronmüller, M. Leghissa, M. Kraus, and G. Saemann-Ischenko, Phys. Rev. B **47**, 373 (1993)

[47] B. Holzapfel, G. Kreiselmeyer, M. Kraus, G. Saemann-Ischenko, S. Bouffard, S. Klaumünzer, and L. Schultz, Phys. Rev. B **48**, 600 (1993)

[48] R. Prozorov, A. Tsameret, Y. Yeshurun, G. Koren, M. Konczykowski, and S. Bouffard, Physica C **234**, 311 (1994)

[49] G. Nakielski, A. Rickertsen, T. Steinborn, J. Wiesner, G. Wirth, A.G.M. Jansen, and J. Kötzler, Phys. Rev. Lett. **76**, 2567 (1996)

[50] T. Sueyoshi, N. Ishikawa, A. Iwase, Y. Chimi, T. Kiss, T. Fujiyoshi, K. Miyahara, Physica C **309**, 79 (1998)

[51] B. Roas, L. Schultz, and G. Saemann-Ischenko, Phys. Rev. Lett. **64**, 479 (1990)

[52] Y. Gao, K.L. Merkle, G. Bai, H.L.M. Chang and D.J. Lam, Physica C **174**, 1 (1991)

[53] Ch. Jooss, A. Forkl, R. Warthmann, H.-U. Habermeier, B. Leibold, and H. Kronmüller, Physica C **266**, 235 (1996),

Ch. Jooss, A. Forkl, and H. Kronmüller, Physica C **268**, 87 (1996)

[54] E. Sheriff, R. Prozorov, Y. Yeshurun, A. Shaulov, G. Koren, and C. Chabaud-Villard, J. Appl. Phys. **82**, 4417 (1997)

[55] J.R. Thompson, L. Krusin-Elbaum, L. Civale, G. Blatter, and C. Feild, Phys. Rev. Lett. **78**, 3181 (1997)

[56] A. Schönenberger, A. Larkin, E. Heeb, V. Geshkenbein, and G. Blatter, Phys. Rev. Lett. **77**, 4636 (1996)

[57] ref. [2], eqs. (9.105) and (9.106) on page 1336

[58] T.L. Hylton and M.R. Beasley, Phys. Rev. B **41**, 11669 (1990)

[59] A.F.Th. Hoekstra, R. Griessen, A.M. Testa, J. el Fattahi, M. Brinkmann, K. Westerholt, W.K. Kwok, and G.W. Crabtree, Phys. Rev. Lett. **80**, 4293 (1998)

[60] R.A. Doyle, W.S. Seow, J.D. Johnson, A.M. Campbell, P. Berghuis, R.E. Somekh, J.E. Evetts, G. Wirth, and J. Wiesner, Phys. Rev. B **51**, 12763 (1995)

Chapter   6

Flux penetration in ring-shaped YBa$_2$Cu$_3$O$_{7-\delta}$ thin films

By means of advanced magneto-optics, we study the field and current distributions in superconducting thin film rings of YBa$_2$Cu$_3$O$_{7-\delta}$, in an externally applied magnetic field. During the first penetration of flux a peculiar peak of *negative* magnetic field appears at the inner edge of the ring, which is due to the self-field of the current density. The occurrence of this peak allows an unambiguous definition of the penetration field H_{pen} in magneto-optical experiments, in agreement with the penetration field measured by torque magnetometry. The characteristic field B^*, which determines the matching of the vortex lattice with the linear defect lattice, is not influenced by any penetration effects.

During field reversal a highly non-uniform current distribution is observed with two concentric counter-rotating current loops. Our observations on the field profiles are in excellent agreement with numerical calculations, that we performed using the same ring-geometry. From the numerical simulations we conclude that the current density is uniform within a hysteresis loop, provided that the sample is i) fully penetrated and ii) not in a stage where the magnetic field profile is being reversed. The Bean model, although derived for an infinitely long cylinder, is therefore also valid in thin films.[1]

6.1 Introduction

In the previous chapters we have discussed the pinning properties in thin films of YBa$_2$Cu$_3$O$_{7-\delta}$. We have observed that the current density exhibits matching effects due to pinning by linear defects. Typical matching fields are however small; $B^* \lesssim 100$ mT, which is not much larger than the penetration field $\mu_0 H_{pen}$, and in a range where self-field effects are expected to be important. In order to determine the critical currents in superconducting thin films, we pattern the films into rings, because of the well-defined shape and constant sample width perpendicular to the current flow direction [1, 2, 3]. In fact many studies on superconductors use ring-shaped samples, to measure e.g. the flux relaxation rate [4], the magnetic flux noise [5], the levitation forces [6], or the photoresponse in the flux creep regime [7]. In addition, ring shapes also occur in practical applications e.g. in SQUID-loops. The interpretation of these experiments presupposes a knowledge of the current distribution. Most authors assume that this current distribution is uniform, and use the Bean model [8] to determine the current density from the magnetization. However, theoretical calculations of the magnetic field in superconducting rings and disks have shown that shielding effects cause deviations from the (ideal) Bean model [9, 10]. Experimentally, the behaviour of the magnetic field and current density distribution, and specifically the uniformity of the current density, have not been verified in detail in ring-shaped samples. For these reasons an experimental investigation of the exact current distribution in ring-shaped samples is strongly needed.

In this chapter we present an investigation of the flux penetration in ring-shaped thin films of YBa$_2$Cu$_3$O$_{7-\delta}$, using an improved magneto-optical technique [11]. We compare the magneto-optical results with measurements done by torque magetometry. Magneto-optical (MO) imaging [12] enables a direct measurement of the magnetic field above the superconductor, from which the current distribution can be derived for a 2-dimensional geometry [13, 14, 15]. A recent improvement [11] of the technique enables an accurate linear measurement of the local magnetic field, including an unambiguous determination of its sign. Results are presented for two superconducting rings with different widths. It is found that within the hysteresis loop, during first penetration and after reversing the sweep direction, the field and current distributions exhibit a peculiar behaviour, with positive and negative domains within the width of the ring. At other magnetic fields the current density is uniform over the whole width.

This chapter is organized as follows. In section 6.2 we present the details of the samples and the experimental technique. The numerical calculations, used for a direct comparison with experiment, are described in section 6.3. Experimental results are given in section 6.4. Specifically we focus on two aspects: i) on the homogeneity of the current density within a hysteresis loop and ii) on the peculiar flux behaviour during first penetration and immediately after reversing the sweep direction of the applied magnetic field.

6.2 Experimental technique

To study the penetration effects of rings of thin $YBa_2Cu_3O_{7-\delta}$ films we use both torque magnetometry and magneto-optical imaging. Torque magnetometry gives the total magnetic moment and an accurate quantitative determination of the current density, whereas with magneto-optics we obtain information about the local magnetic field and its distribution. In this section we describe the principles of magneto-optical imaging and the measurement setup. Torque magnetometry and the sample preparation, described in detail in chapter 2, are summarized briefly.

6.2.1 Magneto-optical imaging

The physical principle behind magneto-optical imaging is the Faraday effect. In a magneto-optical active material, the refractive indices for right- and left-handed circularly polarized light are slightly different when a magnetic field is present. The consequence of this asymmetry is, that *linearly* polarized light, which can be thought of as a superposition of right- and left-handed circularly polarized light, experiences a rotation of the polarization vector. The angle of this so-called Faraday rotation is given by:

$$\theta_F = V l H_z \tag{6.1}$$

where $\mu_0 H_z$ is the local magnetic field along the wave-vector of the incident light beam, l is the optical path-length in the medium and V is a material dependent constant, called the Verdet constant. Many materials exhibit this Faraday effect, but it is usually very small. For some materials however, such as the Eu chalcogenides (EuSe, EuTe, EuS) and Bi-doped Yttrium Iron Garnet (YIG) films, the Verdet constant is large, so that they can be used as magneto-optical indicators.

A schematic picture of how the Faraday effect is used to image the local magnetic field is given in figure 6.1. The magneto-optical layer (MOL) is deposited on a glass substrate. On top the MOL is coated with a highly reflecting mirror (for example Al). The system is mounted 'upside down' on top of the sample (non-destructively). Polarized light traverses the MOL twice. The polarization vector is rotated according to eq. (6.1), depending on the local magnetic field on the sample. The analyzer is placed perpendicularly to the polarizer, such that those parts of the film with zero local magnetic field (i.e. no rotation) appear black, whereas places with magnetic field (i.e. with rotated polarization) appear bright. In this way we obtain an image of the local magnetic field everywhere inside (and outside) the sample. The signal output has an intensity (for small rotation angles):

$$I = L \exp(-2\beta l)\sin^2(2\theta_F) \approx L \exp(-2\beta l) \cdot (2VlH_z)^2 \propto H_z^2 \tag{6.2}$$

with L the intensity of the incident light and β the absorption coefficient of the MOL. In this way the spatial variation of the perpendicular component of the local induction B_z at the sample is visualized as an intensity pattern.
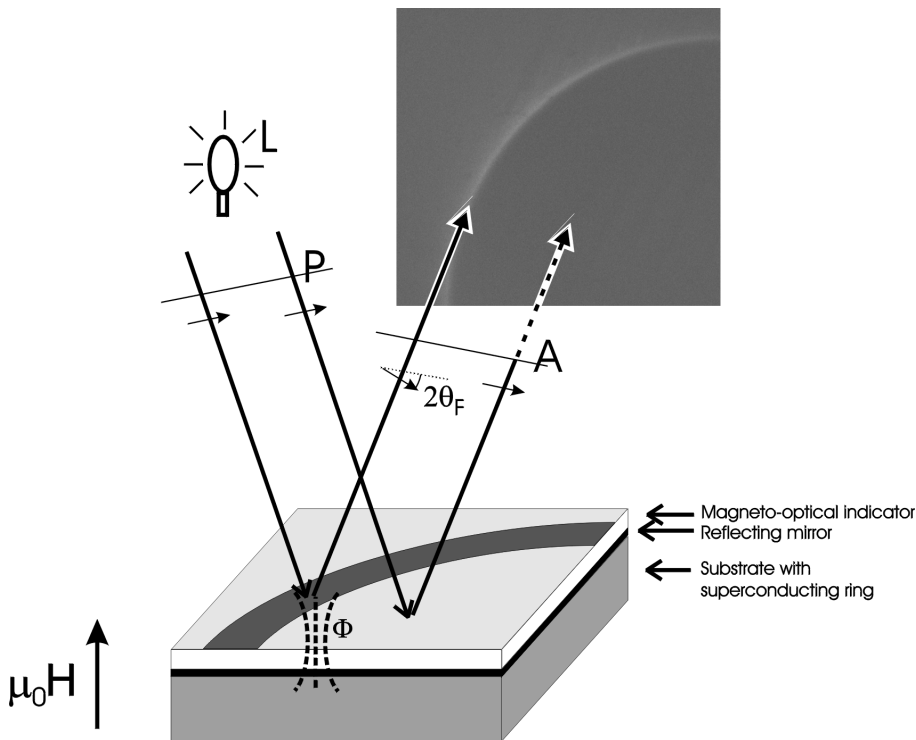
Figure 6.1: Schematic picture of magneto-optical imaging by means of the Faraday effect. Light from the light source L is polarized by the polarizer P and focussed on the sample (a superconducting ring in this case) with MO-indicator. When flux is present, the polarization angle of the reflected light is rotated over an angle $2\theta_F$ with respect to the incident light beam. It passes partly through the analyzer A, which is put at an angle $\alpha = 90°$ with respect to the polarizer. When no flux is present, the polarization angle remains unchanged, and the light is blocked by the analyzer. In this way we obtain an intensity image of the local magnetic field inside and outside the sample.

From the intensity images, the local field is calibrated, either by measuring the intensity far from the sample, for which $B_z = \mu_0 H_{appl}$ [16], or in a separate experiment without sample.

In our experiments we use dichroic sheet polarizers with an extinction ratio of 10^{-6} and as magneto-optical indicator we use a Bi-doped Yttrium Iron Garnet film (YIG) with in-plane anisotropy. These garnet films exhibit a large Faraday effect of typically $0.06°/$mT [17]. The YIG-indicators have a thickness of $d_{MOL} \approx 2-3$ μm, resulting in a magnetic resolution better than 0.1 mT and spatial resolution better than 0.5 μm. Moreover we can use the YIG-indicator in the full temperature range from $T = 1.5$ to

300 K due to the large Curie temperature $T_C = 800$ K. A drawback of YIG-indicators is that the use is limited to magnetic fields $\mu_0 H \lesssim 200$ mT as the indicator saturates at higher magnetic fields. Secondly in-plane magnetic domains are present in YIG-indicators, that can cause a rotation of the incident light. As a result these domains become visible in a magneto-optics picture. However by an appropriate rotation of the sample with indicator, such that the in-plane magnetization vector is at 45° with the polarization vector of the incident light, this effect can be avoided.

The sample with the magneto-optical indicator is mounted on a variable temperature insert (VTI) and put in a 1T cryostat similar to the one used for torque magnetometry (see chapter 2 for a description). A digital CCD camera is continuously taking pictures during a field sweep. In this way we can make hysteresis loops just like in torque magnetometry. In the next section, where we describe a recently developed improvement of the MO-setup, a schematic picture of the measurement setup is displayed (figure 6.2). A more detailed description of the conventional MO-setup can also be found in refs. [12] and [18].

6.2.2 Magneto-Optical Image Lock-In Amplifier

The conventional magneto-optical setup described in the previous section has three important drawbacks. First we measure an *intensity* profile $I \propto H_z^2$ (eq. (6.2)), and therefore we do not obtain information about the *sign* of the magnetic field. Secondly, the intensity is very insensitive to small rotation angles (i.e. small magnetic fields). Thirdly, a non-uniform illumination hinders an accurate calibration of the field profile. With a recently developed lock-in technique we are able to circumvent these problems. In this section we describe our new setup, the *Magneto-Optical Image Lock-In Amplifier* (*MO-ILIA*) [11].

In general the measured intensity of a polarization microscope between two polarizers is:

$$I = K + L\sin^2\left(\alpha + \theta_F\right) \simeq K + L\left(\alpha + \theta_F\right)^2, \tag{6.3}$$

with L the incident intensity, K an offset intensity (due to camera noise, straylight etc.), and $(90° - \alpha)$ the angle between polarizer and analyzer. In conventional magneto-optics $\alpha = 0$ (crossed polarizers)[2]. One can in principle use a lock-in technique to reduce the noise, by rotating the polarizer sinusoidally. However, the image processing in this case is very time consuming, and therefore not practical. Alternatively, we choose to measure the intensity for three values only $\alpha = +\alpha_0$, $\alpha = 0$, and $\alpha = -\alpha_0$, with α_0 typically a few degrees. From eq. (6.3) one finds straightforwardly that the corresponding intensities I_+, I_0, and I_- are related to L and θ_F as:

$$L = \frac{I_- - 2I_0 + I_+}{2\alpha_0^2} \tag{6.4}$$

---

[2]To increase the sensitivity at low magnetic fields, sometimes the polarizer and analyzer are not completely crossed, but put under a small offset angle $(90° - \alpha_{\mathrm{offset}})$.

$$\theta_F = \frac{(I_+ - I_-)}{4\alpha_0 L} \tag{6.5}$$

The incident intensity L is constant in time and can be determined by averaging over many images. We measure the intensities I_+, I_0, and I_- for each pixel, and with eqs. (6.4) and (6.5) we determine directly $\theta_F \propto H_z$, i.e. the *magnitude* and *sign* of the magnetic field.

The complete setup is depicted in figure 6.2. In addition to the conventional MO-setup, we added a polarization rotator (PR) to rotate the polarization vector of the incident light and a data-processing PC (PC2). The light source is a 250 W halogen lamp with a bandpass filter. The light is polarized by the fixed polarizer P and then travels through a polarization rotator PR. This polarization rotator consists of a 150 mm long rod of SF59 glass with a high Verdet constant. Around the glass rod a copper wire coil is wound, capable of making a homogeneous magnetic field of 100 mT. Specially designed electronics switches the magnetic field in 1 ms during the video blank time. After traversing the Faraday rotator the light is led into the MO-system by a beamsplitter (BS) and with a focal lens (L1) it is projected on the sample with MO-active layer (depicted in figure 6.1). The reflected light is going through the analyzer and projected via a second lens (L2) on a CCD camera. The CCD camera is a peltier-cooled MICROMAX CCD-782Y camera with 782 x 582 pixels and an active area of 6.49 x 4.83 mm^2. The camera is controlled by the computer PC1, which is linked via a high speed dynamic link (DL) to the image processing computer PC2. As the image processing is still very demanding, the latter PC, which is absent in the conventional MO-setup, contains specially dedicated hardware to do the calculation of eqs. (6.4) and (6.5). It is capable of sustaining 25 images per second with a size of 782 x 582 pixels (corresponding to the MICROMAX CCD-camera we use) and 16 bits per pixel. More details of the MO-ILIA system can be found in ref. [11].

The MO-ILIA is a considerable improvement compared to conventional magneto-optics due to the intrinsic linearity in field, the direct measurement of the sign of the field and the improved sensitivity at small magnetic fields. A drawback of the increased sensitivity is, that the domains of the YIG-indicator become visible again, and have to be filtered out.

6.2.3 Torque magnetometry

The penetration field and the superconducting current density are measured by means of capacitive torque magnetometry (see chapter 2 and ref. [19]). The sample is placed in a magnetic field $\mu_0 \overrightarrow{H}$ at a small angle $\vartheta = 10°$ with the applied field. When the applied field is increased with a sweep rate $\mu_0 dH/dt$, superconducting currents are induced in the sample. The corresponding magnetic moment $\overrightarrow{M}$ leads to a torque $\overrightarrow{\tau}$ given by:

$$\overrightarrow{\tau} = \mu_0 (\overrightarrow{M} \times \overrightarrow{H}). \tag{6.6}$$

The pinning of vortices is reflected by the irreversible magnetic moment in a hysteresis loop $M_{irr} = \tau_{irr}/(\mu_0 H \sin\theta)$. Assuming a uniform current distribution [8], the
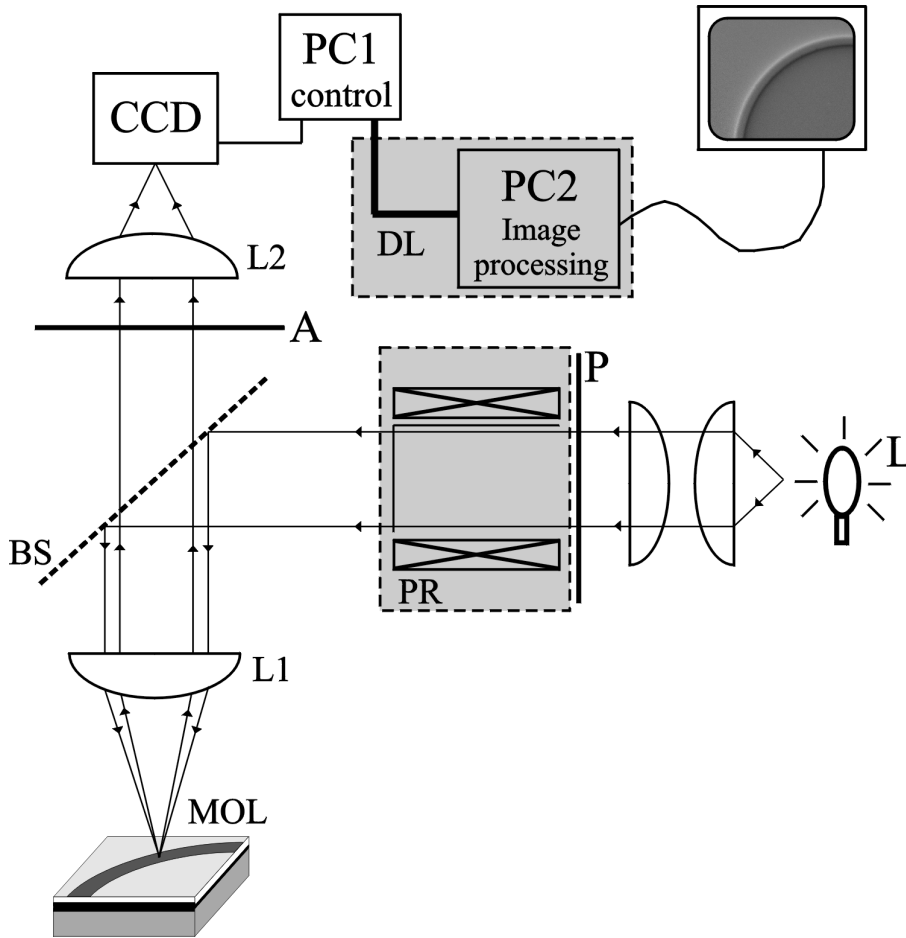
Figure 6.2: Schematic picture of the magneto-optical measurement setup. The incident light is linearly polarized by the polarizer (P), and passes the polarization rotator (PR), where the polarization angle is rotated between $-\alpha_0$, 0 and $+\alpha_0$. Via the beamsplitter (BS) and the lens L1 it is focussed on the MOL with sample. The reflected light passes through the analyser (A) and is focussed onto the MICROMAX CCD-camera, which is controlled by PC1. The data-processing is carried out by PC2 and the image is displayed on a TV-screen. In the conventional MO setup the devices in the shaded areas (PR and PC2) are absent, and the image, coming in on PC1, is directly displayed on the TV-screen.

current density j_s is directly related to the magnetic moment. For a ring of inner radius r_i, outer radius r_o and thickness d it is given by:

$$M_{irr} = (\pi/3)d(r_o^3 - r_i^3)j_s \tag{6.7}$$

The torque magnetometer is placed into the variable temperature insert of a OXFORD INSTRUMENTS low-loss dewar with 7 T magnet. The cryostat enables measurements from 1.5 K up to 300 K. Experiments are performed after zero field cooling (ZFC) by sweeping the field from $\mu_0 H = 0 \to +200$ mT $\to -200$ mT $\to +200$ mT $\to 0$ T, with a constant sweep rate of $\mu_0 dH/dt = 2$ or 1 mT/s. No qualitative differences were observed when using different sweep rates. From making a full hysteresis loop after ZFC, one can determine the penetration field H_{pen}. During first penetration the magnetic moment increases linearly with magnetic field, i.e. the torque increases quadratically (eq. (6.6)). As soon as the sample is fully penetrated, the magnetic moment is proportional to j_s, and τ depends linearly on magnetic field (provided that $j_s(B)$ is constant, i.e. when $\mu_0 H < B^*$). The crossover from quadratic to linear torque thus determines H_{pen}.

6.2.4 Samples

Results are presented for two rings patterned from YBa$_2$Cu$_3$O$_{7-\delta}$ thin films LAD632 and LP25, which we deposited on (100) SrTiO$_3$ substrates by means of Pulsed Laser Deposition. Similar results are obtained on other rings. The thickness of the rings is $d = 140$ and 100 nm respectively and the critical temperature is $T_c = 90$ K, with $\Delta T_c < 0.5$ K. The samples are characterized by Rutherford Backscattering, Atomic Force Microscopy and X-Ray Diffraction (XRD) [20]. The excellent crystallinity of these films enables even the observation of Laue finite size oscillations around the (001)-reflection of the XRD spectrum [21].

The films are patterned into rings using conventional UV-photolithography and chemical etching in H$_3$PO$_4$. The rings have an outer diameter of $D = 3$ mm, a width of $w = 500$ μm for LAD632, and $w = 125$ μm for LP25. The samples are checked for irregularities, scratches and weak spots by optical transmission and reflection microscopy and exhibit excellent quality. Subsequently, magneto-optics showed no inhomogeneous flux penetration along the circumference.

6.3 Numerical simulation

In order to obtain a complete description and a full understanding of the phenomena occurring in the ring, we investigate numerically the distribution of the current density while performing a hysteresis loop. With the help of a simulation, similar to a calculation by Brandt [10], we can calculate the field profiles and current distributions in the sample, which we compare with our experimental results. A numerical calculation is required due to the geometry, as the elliptic integrals of the problem make it analytically intractable.

In our calculation we express the time derivative of the position dependent current $dI(r)/dt$ in the ring as a function of the current $I(r)$ and sweep rate $\mu_0 dH/dt$ of the externally applied field. Note, that for thin films the thickness d is much smaller than the radius of the ring. The current is therefore effectively running in a plane, and we can treat the problem in 2 dimensions, ignoring the ϑ-direction. Moreover, the vector potential $\overrightarrow{A}(r, \vartheta)$ depends only on r, due to the radial symmetry. In this geometry, only the A_φ component is non-zero.

Hence, in spherical coordinates, the vector potential for a single loop of current I of radius a, is given by [22]:

$$A_\varphi(r, \vartheta) = \frac{\mu_0}{4\pi} I a \int_0^{2\pi} \frac{\cos\varphi' d\varphi'}{\sqrt{a^2 + r^2 - 2ar\sin\vartheta\cos\varphi'}} \tag{6.8}$$

For a thin ring with inner radius r_i and outer radius r_o we find in the plane of the ring (note that $\vartheta = \pi/2$):

$$A_\varphi(r) = \frac{\mu_0}{4\pi} \int_{r_i}^{r_o} \mathfrak{J}(a')a' \int_0^{2\pi} \frac{\cos\varphi' d\varphi'}{\sqrt{a'^2 + r^2 - 2a'r\cos\varphi'}} da' \tag{6.9}$$

with $\mathfrak{J}(a')$ the current per unit length. Note that the total current from eq. (6.8) $I = \int \mathfrak{J}(a')da'$ is related to the current density j by $I = j * wd$, with w the width of the ring.

By discretizing the space on the width of ring, we obtain:

$$A_\varphi(r) = \frac{\mu_0}{4\pi} \sum_{p=r_i}^{r_o} I(p)p \int_0^{2\pi} \frac{\cos\varphi' d\varphi'}{\sqrt{p^2 + r^2 - 2pr\cos\varphi'}} = \frac{\mu_0}{4\pi} \sum_{p=r_i}^{r_o} I(p)\mathcal{Q}(p, r) \tag{6.10}$$

where $I(p) = \mathfrak{J}(p)\Delta a'$ is now the current flowing between $p - \frac{1}{2}\Delta a'$ and $p + \frac{1}{2}\Delta a'$, $\Delta a'$ being the gridspacing. The second equal sign defines a kernel matrix $\mathcal{Q}(p, r)$.[3] In matrix notation, eq. (6.10) may be abbreviated as:

$$\overrightarrow{A_\varphi} = \frac{\mu_0}{4\pi} \overrightarrow{\mathcal{Q}} \cdot \overrightarrow{I}. \tag{6.11}$$

Here the arrow on A_φ and I is used to denote the position dependent quantities, written as a mathematical vector in discretized space.

The total vector potential is due to the current in the ring and the external field:

$$A_{\varphi,tot} = A_{\varphi,ring} + A_{\varphi,ext} \tag{6.12}$$

For a uniform external field along the $\hat{z}$-axis $A_{\varphi,ext} = \mu_0 \frac{r}{2} H_z$. Inserting this and eq. (6.11) in (6.12) gives:

$$\frac{\mu_0}{4\pi}\left(\overrightarrow{\mathcal{Q}} \cdot \overrightarrow{I}\right) = A_{\varphi,tot} - \mu_0 \frac{r}{2} H_z \tag{6.13}$$

---

[3]The kernel matrix $\mathcal{Q}(p, r)$ is not to be confused with the dynamical relaxation rate Q.

To proceed we need the relation between current density j and electrical field E in the superconductor. For simplicity [10] we use a power law relation:

$$E = \rho j = \rho_0 \left| \frac{j}{j_0} \right|^\sigma j = \gamma \left| I \right|^\sigma I, \tag{6.14}$$

with ρ the resistivity and γ a constant. For large σ (we take $\sigma = 30$) this captures the essential superconductor physics, where the electrical field rises sharply when the current density exceeds the value j_0 (close to the critical current density j_c)[4], while it is very convenient in the calculation.

By taking the time derivative of eq. (6.13) and using $\dot{A}_{\varphi,tot} = -E = -\rho j$, with ρ from eq. (6.14), one obtains the following expression:

$$\frac{\partial \overrightarrow{I}}{\partial t} = \left(\frac{4\pi}{\mu_0} \right) \overrightarrow{\overrightarrow{Q}}^{-1} \cdot \left(-R_0 \left| \overrightarrow{I} \right|^\sigma \overrightarrow{I} - \mu_0 \frac{r}{2} \dot{H}_z \right), \tag{6.15}$$

Equation (6.15) can be easily iterated numerically. The initial condition at $t = 0$ is to set the current and the magnetic field to zero all over the width of the ring, corresponding to a zero-field cooled situation with no applied magnetic field. The applied field is now increased linearly with time and for each timestep Δt_{i+1} the current distribution $I_{i+1}(r)$ is calculated from the previous current distribution $I_i(r)$. In this way a complete hysteresis loop with arbitrary sweep rate can be easily calculated. From the calculated current $I(r)$ in the ring, also the magnetic field in all space around the ring is determined, taking into account the external field (obtained from integrating $\dot{H}_z$) and the self-field from eq. (6.8).

6.4 Experimental results and analysis

We now compare the magnetic moment M_{irr}, obtained from torque measurements, with magneto-optical data of the total local magnetic field $B_{z,tot}$ perpendicular to the plane of the ring. In addition, both experimental results are compared with numerical simulations.

The magneto-optical experiments presented here are performed at $T = 4.2$ K after zero field cooling, by sweeping the field from $\mu_0 H = 0 \rightarrow +B_{max} \rightarrow -B_{max} \rightarrow +B_{max} \rightarrow 0$ T, with $B_{max} = 50$ or 200 mT, depending on the film. The sweep rate was constant $\mu_0 dH/dt = 1$ mT/s. The images are taken continuously with the CCD camera at a typical time interval of $\Delta t = 1.5$ s (hence the field difference between consecutive pictures is $\Delta(\mu_0 H) \approx 1.5$ mT). In figure 6.3 we have drawn a schematic picture of a typical hysteresis loop with $B_{max} = 50$ mT. The characters A to N denote the positions in the hysteresis loop where experimental profiles and/or simulations are determined (presented in the figures 6.7 and 6.9).

---

[4]From implicitly differentiating the logarithm of eq. (6.14), we find that $(\sigma + 1)$ is essentially the slope in an I-V-plot, which is the reciprocal of the dynamical relaxation rate Q.
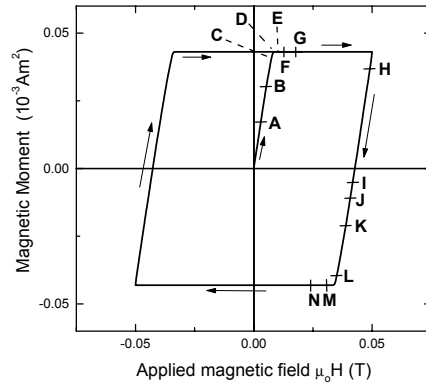
Figure 6.3: Schematic hysteresis loop starting from ZFC conditions. The characters refer to the curves in figure 6.7 (A to G) and figure 6.9 (H to N).

6.4.1 First penetration and penetration fields

In figure 6.4 we show the first penetration of flux in the wide ring (film LAD632) after zero-field cooling. The pictures were taken in increasing magnetic field wi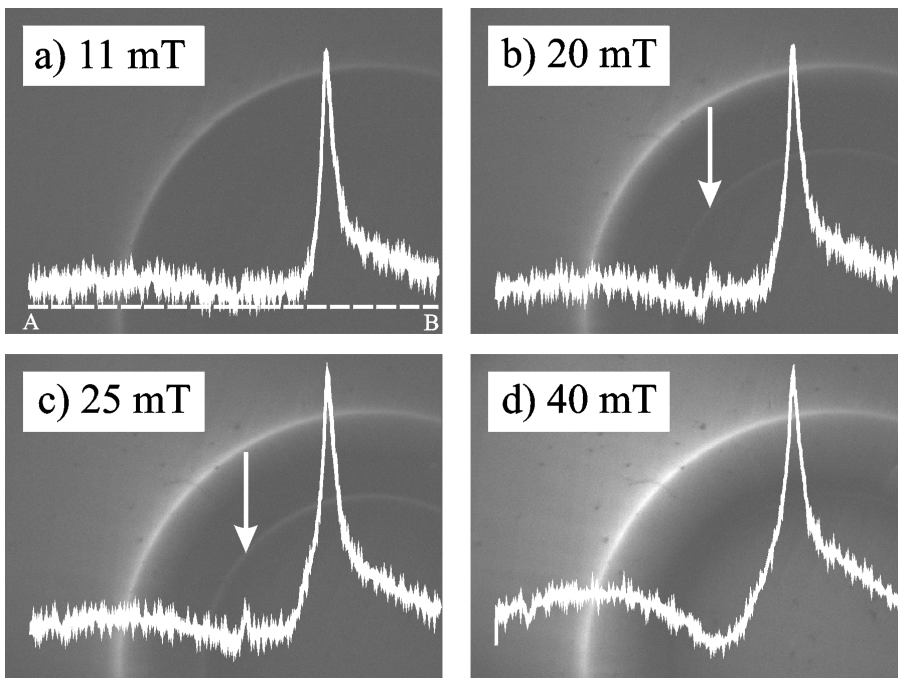th conventional magneto-optics, i.e. figure 6.4 shows intensity images. Also we depict the intensity profile for each field along the line A-B. At small magnetic fields we observe the usual intensity peak at the outer edge of the ring. This peak is caused by the self-field of the currents shielding the applied magnetic field. But surprisingly, at $\mu_0 H = 20$ mT also a bright rim at the *inside* of the ring shows up. This is the more remarkable, since this inner peak appears when the middle of the ring is still flux-free, i.e. when the vortices have not yet completely penetrated (crossed the whole width of the ring). The inner peak increases in intensity with a maximum when the applied magnetic field $\mu_0 H = 25$ mT, and then slowly disappears. At $\mu_0 H = 40$ mT the peak has disappeared completely. We measured also a narrow ring patterned from film LAD632 ($D = 3$ mm, $w = 125$ μm), but there the peak could not be found.

What is the reason for this peak? As the flux has not completely penetrated the sample yet, it is unlikely that the peak represents a positive flux. Instead we suspect that the inner peak stems from a *negative* local magnetic field preventing the flux from entering through the middle of the ring. One way of describing the observed effect is that our ring is equivalent to the superposition of a superconducting disk with the same outer diameter as the ring and ordinary shielding currents and a disk with same outer diameter as the inner diameter of the ring and counter-flowing shielding currents [23]. The latter currents produce a peaked field at the edge of the inner virtual disk, that is negative because the currents are counter-flowing.

Figure 6.4: Conventional magneto-optical intensity images (proportional to the local field squared), for $\mu_0 H = 11$, 20, 25 and 40 mT, on ring LAD632, at $T = 4.2$ K. The profiles along the dashed line A-B are shown in the picture. We note that a small peak starts to appear at the inner edge of the ring at 20 mT (see arrow). The peak reaches a maximum at 25 mT and then decreases and disappears at 40 mT. The screening peak at the outer edge of the ring continues to increase with magnetic field.

However, in this case the peak should also be present in the narrow ring, where it was not observed. Possibly the resolution of the conventional magneto-optical setup was not sufficient to see the inner peak. To confirm our hypothesis we decided to measure the flux penetration by the new MO-ILIA in a narrow ring, LP25.[5] With the new MO-ILIA we can determine the sign of the local magnetic field, and with the increased resolution we hope to observe the inner shielding peak in the narrow ring as well. In figure 6.5 we show a MO-image of film LP25, during first penetration after zero-field cooling, at $\mu_0 H = 8$ mT (point C in figure 6.3). We observe the intense bright outline at the outer edge of the ring, but also the peculiar peak at the inner edge. The outline at the inner edge of the ring is dark, corresponding to a local field *opposite* to the applied field. We conclude that also in the narrow ring the same

---

[5]The narrow ring patterned from film LAD632 was, unfortunately, not available for magneto-optics anymore.
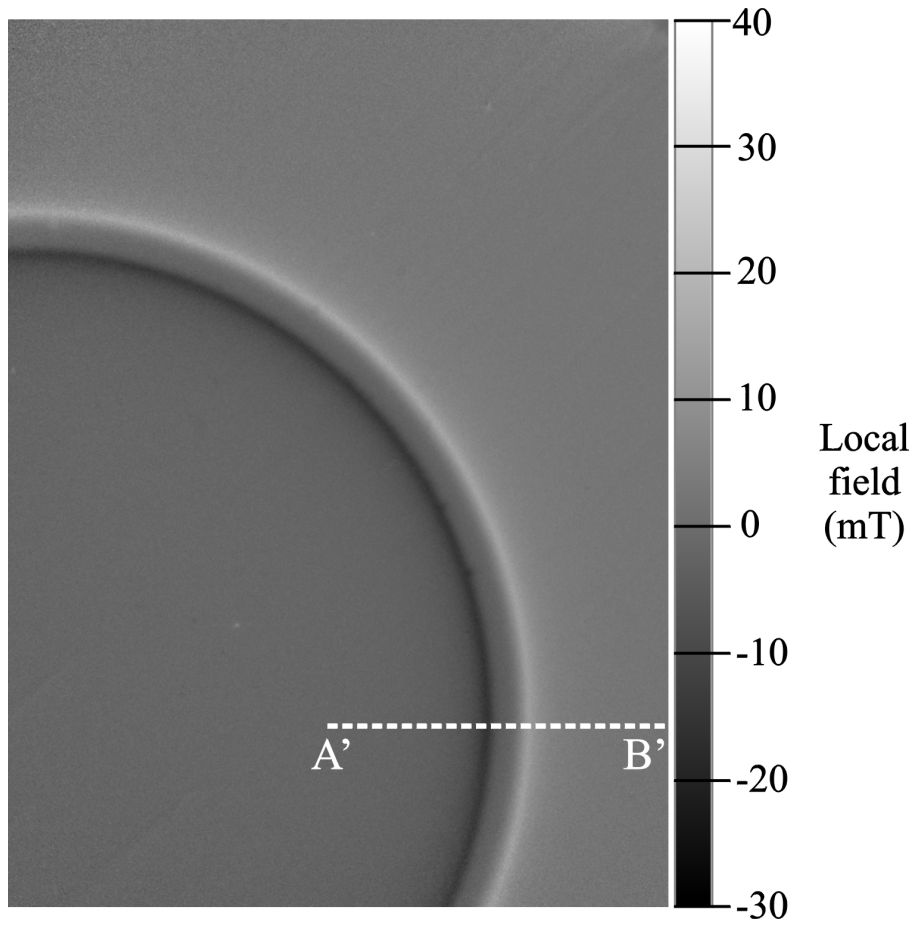
Figure 6.5: Local field map obtained from MO-ILIA magneto-optical imaging of LP25 (125 μm width), with an applied field of $\mu_0 H = 8$ mT, at $T = 4.2$ K. The scale bar gives the local field values in mT. We observe a positive bright outline at the outer edge of the ring, while a negative dark outline is visible at the inner edge of the ring. The profiles shown in the figures 6.7a and 6.9a are measured along the dashed line A'B'.
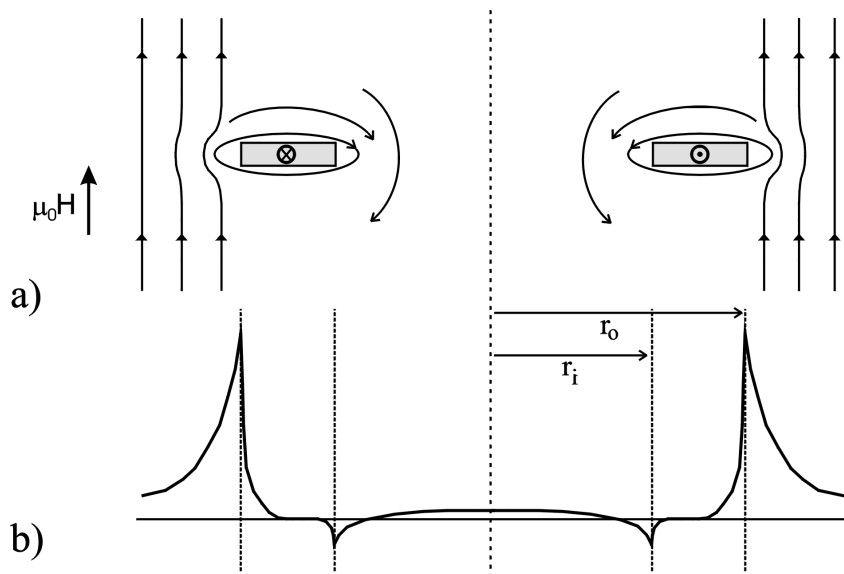
Figure 6.6: a) Schematic diagram showing magnetic field lines due to a current flowing in a ring of inner radius r_i, outer radius r_o and thickness d, in the presence of an externally applied field. Near the outer edges of the ring, the local field is high due to enhancement of the external field by the field generated by the current. At the inner edge of the ring, the external field and the self-field are directed opposite to each other. Close to the inner radius of the ring the total field becomes even negative. b) Schematic magnetic field profiles, indicating the sharp peak at the edges of the ring due to the large aspect ratio.

remarkable peak is observed, which is indeed related to the shielding of the flux, trying to thread through the hole of the ring.

To explain more explicitly what happens, we start with a ring in the virgin state, i.e. without flux anywhere (inside and outside). When a magnetic field is applied perpendicular to the film, a supercurrent will flow in the ring, in order to keep it in the Meissner state. On the outer edge of the ring, the field generated by the shielding currents adds to the applied field, as in the flat strip case (see for example ref. [24]). This results in a sharp peak, increasing with the applied field. But, because of the geometry of the ring, the flux lines of the self-field close by threading through the hole (see figure 6.6a), thereby generating a negative field at the edge of the hole. The resulting field profile is given in figure 6.6b. The strength of the inner peak is related to the thickness-to-width ratio of the patterned thin film, just as for the peak at the edge of a strip. This phenomenon has been studied analytically in the torus case [25], where a similar negative peak on the inner edge of the torus was found.

To illustrate the phenomenon experimentally, we plot in figure 6.7a magnetic field profiles along the line A'-B' for film LP25 at various applied fields. Also from these profiles it is clear that, as soon as an external field is applied, some negative field is present at the inner edge of the ring. The total magnetic field in the profiles is obtained by adding the applied magnetic field and the self-field. For not too large applied magnetic fields, the self-field is larger in size than the applied magnetic field, resulting in a negative total magnetic field (see figure 6.6). To the middle of the ring the self-field becomes smaller than the applied magnetic field, and the total flux is positive. The spatial distribution of the field inside the hole of the ring is dome shaped, which is particularly clear at higher applied fields, when $\left|\overrightarrow{H}_{appl}\right| > \left|\overrightarrow{H}_{self}\right|$ everywhere (see figure 6.4d).

The negative peak at the inner edge of the ring initially becomes stronger with increasing external field. This is due to an increase in total current flowing in the ring, because the width of the region where j_s flows increases with external field. At a certain external field, i.e. the penetration field, the current density j_s flows everywhere in the ring. The total current in the ring cannot increase anymore and therefore the self-field due to the shielding currents is constant. The only effect of an increasing external field is now a shifting of the whole field profile upwards. This implies that the negative field at the inner edge henceforth decreases in strength until it becomes positive.

6.4.2 Simulation of the flux penetration

With our simulation, as outlined in section 6.3, we can simulate the experiment and construct magnetic field profiles to compare with experiment. But additionally we can observe from the simulations how the current density behaves during a hysteresis loop. The results of the numerical calculation are plotted in figure 6.7b. We start with the first penetration from the ZFC situation, with initially the current density j zero all over the width of the ring, up to the state of full penetration, where $j \simeq j_s$, are shown in figure 6.7c. The corresponding points on the calculated and measured magnetization curves, shown in figure 6.3, are indicated with the characters A-G. From figure 6.7 we see that the numerical calculations for the field profile correspond remarkably well with the measured field profiles. We propose consequently, that the calculated current profiles also form an accurate approximation of the real currents running during an experiment.

Note, that even at relatively high fields the current density j only approaches, but never reaches the true critical current density j_c. There are several reasons for this. First, due to relaxation (which is implicitly present also in the numerical calculation due to the finite resistivity) one can never reach j_c, but obtains a lower value $j_s \lesssim j_c$. Secondly even j_s is reached only at the outer perimeter due to the geometry. The difference between $j(r_o)$ and $j(r_i)$ is, however very small, about 1% for the broad ring LAD632 and even four times smaller for the narrow ring LP25. The effect of this non-uniformity of $j(r)$ on the magnetization is therefore negligible, which shows that the Bean model is remarkably accurate.
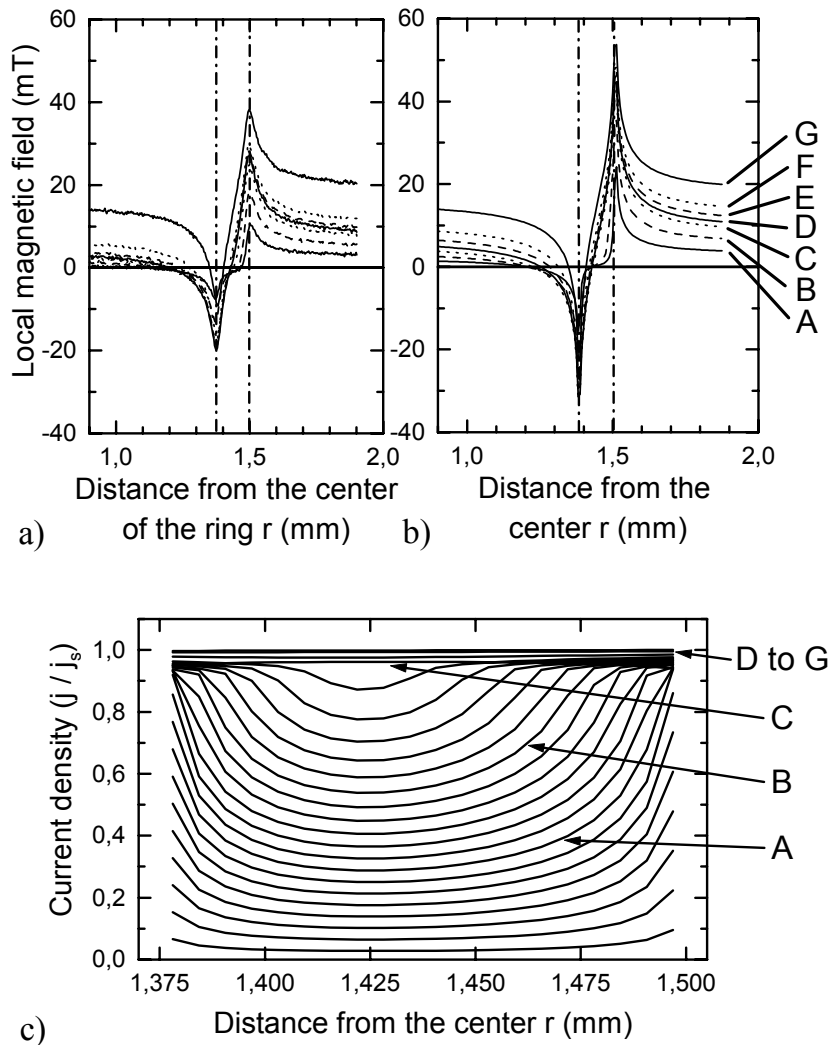
Figure 6.7: a) Experimental MO-ILIA field profiles and b) calculated field profiles (from bottom to top) for $\mu_0 H = 3$ mT (A), 5.5 mT (B), 7.9 mT (C), 9.1 mT (D), 10.5 mT (E), 12.7 mT (F) and 18 mT (G), in ring LP25 as a function of the distance r from the center of the ring. The positions of these fields in the hysteresis loop are indicated in figure 6.3. The dotted lines indicate the inner and outer edge of the ring. c) Local current density from ZFC (bottom) to full penetration (top) as a function of position in the ring, given in units of j_s. The characters A to G indicate the external field and are defined above.

With our magneto-optical images and the simulations, we are able to define a criterion of full flux penetration, and compare this with torque measurements. We investigate this in the next section.

6.4.3 Torque magnetometry versus Magneto-optics

From the magneto-optical results it is immediately clear that there is no sharply defined penetration field. Rather there is an abrupt but continuous change between increasing magnetization and constant magnetization. Coming back to figure 6.7, we note that the maximum of the inner peak occurs for the situation where, for the first time after zero field cooling, the current $j \simeq j_s$ over the whole superconducting sample. Therefore the maximum in the inner peak as a function of applied field can be used as an accurate magneto-optical determination of the value of the penetration field H_{pen}. To confirm this, we compare the values for H_{pen}, obtained according to this criterion, with the values measured from torque. In figure 6.8 we show torque loops of the first penetration after zero-field cooling for the films LAD632 and LP25. We find, as expected, a parabolic torque, corresponding to a linear increase of the magnetization. The penetration fields for the two rings are as follows:

	$\mu_0 H_{pen}^{Torque}$ (mT)	$\mu_0 H_{pen}^{MO}$ (mT)
LAD632	25.5 ± 0.5	25 ± 1
LP25	10.0 ± 0.5	10.0 ± 1

Here the penetration field in torque magnetometry is determined by the deviation from a quadratic increase of the torque (see figure 6.8), in magneto-optics from the maximum of the inner peak. Clearly, the two results for H_{pen} are in good agreement, which means that the maximum of the negative peak serves as a good criterion in MO-experiment for the penetration field.

It is obvious from figure 6.7c, that before this full penetration state is reached, the current flowing in the ring is far from uniform. In the beginning there are even two regions with current flowing, separated by a Meissner area. We see an even more complicated current distribution pattern below, in the region where the field profile is reversed, immediately after reversing the sweep direction. But outside these two regions (first penetration and profile reversal) the current density is uniform. This validates the use of the Bean model, eq. (6.7), to calculate the superconducting current density. Moreover, from figure 6.8 it is obvious, that the penetration field is much smaller than the characteristic field B^* (insets in figure 6.8). As B^* is determined in a region where j_s is uniform, penetration effects do not interfere with the matching of the vortex lattice.
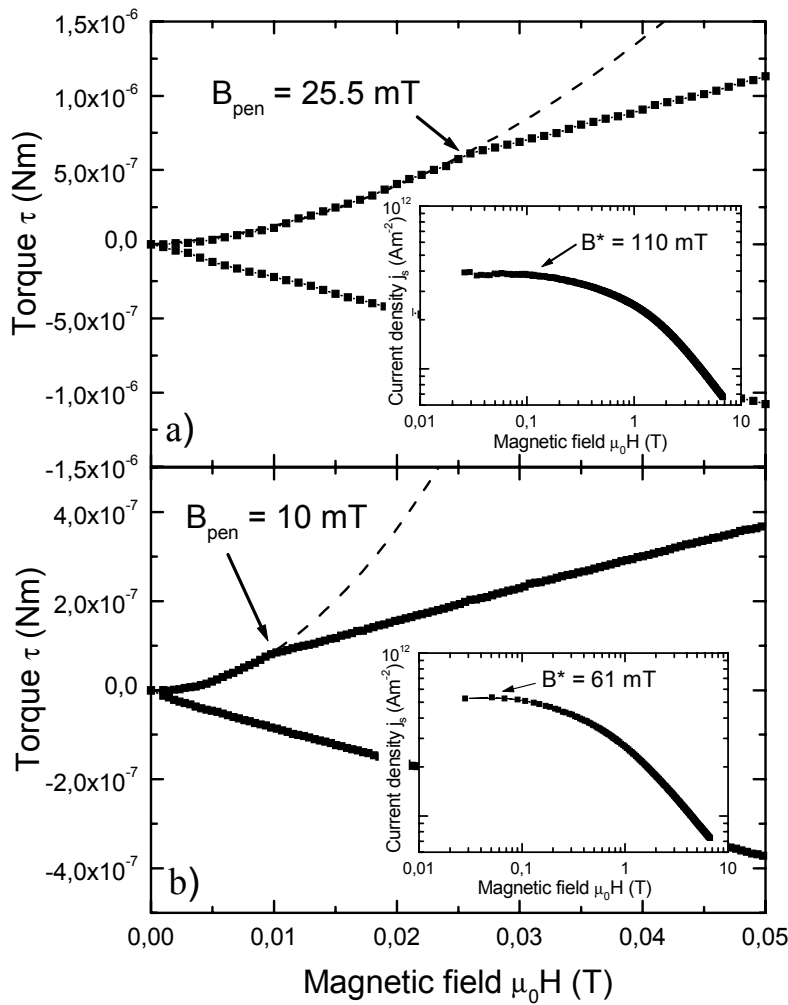
Figure 6.8: First penetration of flux after zero-field cooling of a) the broad ring ($w = 500$ μm, LAD632) and b) the narrow ring ($w = 125$ μm, LP25), measured with torque magnetometry. Dashed lines are parabolic fits to the first penetration, giving $B_{pen} = 25.5$ and 10 mT for LAD632 and LP25 respectively, in close agreement with the magneto-optical results. Insets: Current density $j_s(B)$ for both films, giving characteristic fields of $B^* = 110$ mT for LAD632, and $B^* = 61$ mT for LP25.

From the magneto-optically observed penetration fields we also calculate the current density j_s using the formulae from Brandt [10]:

$$\frac{H_{pen}}{j_s d} = \frac{2}{\pi}\left(\frac{1-x}{1+x}\right)[\ln 4\left(\frac{1+x}{1-x}\right) - 0.307] \qquad \text{for } x \geqslant 0.8 \qquad (6.16)$$

$$\frac{H_{pen}}{j_s d} = \frac{2p}{\pi}\left(\ln\frac{8}{p} - 1\right) - \frac{1}{2}\left(\ln x + 1 - x\right) \qquad \text{for } 0.6 < x < 0.8 \qquad (6.17)$$

$$\frac{H_{pen}}{j_s d} = \frac{1}{2}(-\ln x + 0.467) \qquad \text{for } x \leqslant 0.6 \qquad (6.18)$$

where $x = r_i/r_o$ and $p = (1-x)/(1+x)$. The first and last formulae are exact, while the middle is an interpolation. In our case $x = 0.67$ for LAD632 and $x = 0.92$ for LP25. The values for j_s obtained in this manner can be compared with the current density measured in the torque experiment, and calculated using the Bean model (insets in figure 6.8):

	$j_s^{Torque}(T = 4.2K)$	$j_s^{MO}(T = 4.2K)$
LAD632	3.9×10^{11} A/m^2	4.19×10^{11} A/m^2
LP25	5.3×10^{11} A/m^2	6.82×10^{11} A/m^2

The magneto-optical values for j_s are slightly higher than from the torque measurements, but the agreement is very reasonable.

6.4.4 Field reversal

We observe a rather surprising behaviour of the flux during field reversal. The profiles measured on ring LP25 are shown in figure 6.9, while the corresponding points in the hysteresis curve are again indicated in figure 6.3. For the profile at the top (curve H) the field reversal has just started. From top to bottom the applied field $\mu_0 H$ is decreased from 49 mT to 24 mT. At $\mu_0 H = 24$ mT the flux profile has completely reversed. A further decrease of $\mu_0 H$, first to zero applied field and then to negative applied field, only leads to a vertical shift of the curve, but no change in shape is observed. Note that between 49 and 24 mT, the profile goes through quite a complex sequence of patterns. For example, at $\mu_0 H_{appl} = 35$ mT (curve L), four peaks (counting both positive and negative peaks) are present in the ring. From the slope dB_z/dr, where r is the radial distance from the centre of the ring, one gets the impression that there are two counter-rotating current loops in the ring. To investigate this further, we compare the experimental result with our numerical simulations. Results for the current and field profiles from the numerical simulation are shown in figure 6.9b and 6.9c. Note the excellent correspondence between the experimental and the simulated field profiles shown in figure 6.9a and 6.9b.
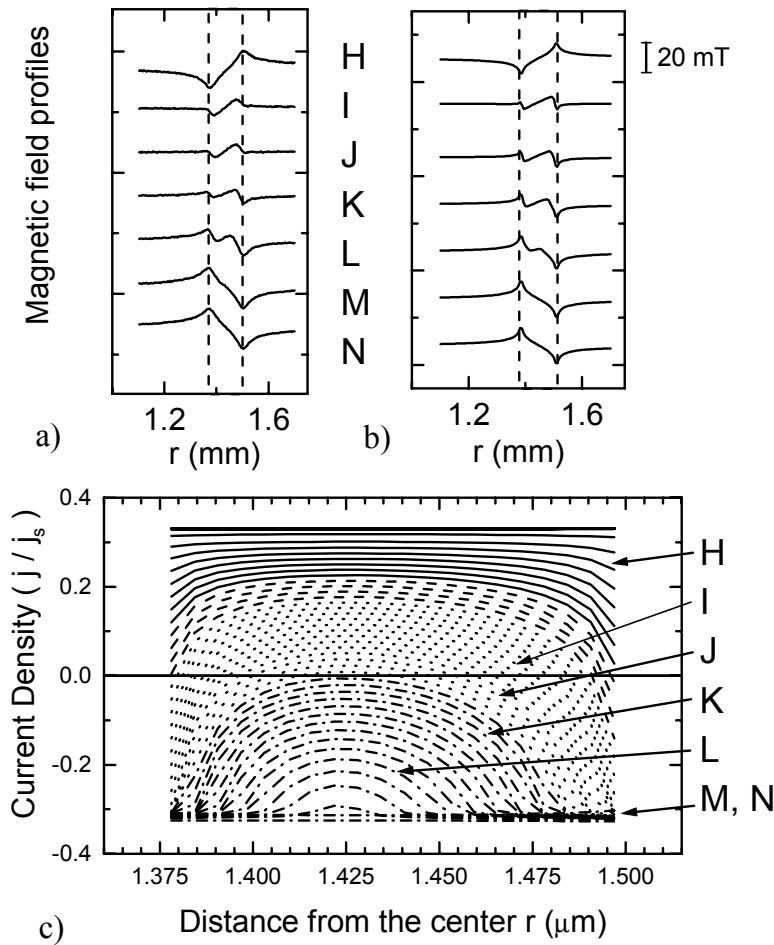
Figure 6.9: a) Experimental MO-ILIA profiles and b) calculated profiles in the narrow ring during field reversal, for (from top to bottom) $\mu_0 H = 49$ mT (H), 42 mT (I), 41 mT (J), 39 mT (K), 35 mT (L), 31 mT (M) and 24 mT (N). The positions of these fields on the hysteresis loop are indicated in figure 6.3. The dotted lines indicate the inner and outer edge of the ring. Note that the vertical scale 20 mT gives the scale within one profile, while the individual curves are shifted vertically for clarity. c) Local current density during field reversal, from the full-penetration of a positive applied field ($j = j_s$, top curve) to the full-penetration due to a negative applied field ($j = -j_s$, bottom curve). The solid lines correspond to the regime where the currents are all positive within the ring. The dashed lines correspond to currents being mainly positive but negative on the outer edge. The dotted lines correspond to the presence of negative - positive - negative currents. Finally the dot-dashed lines describe the regime where the currents are negative everywhere in the ring.

From the simulated curves in figure 6.9c it is clear that during field reversal, the current changes smoothly from say a clockwise direction (positive j) to an anti-clockwise direction (negative j). This happens, however, in a non-uniform manner over the width of the ring. First the current becomes negative at the outside edge of the ring, while at the inside there is still a positive current flowing. Hence during this crossover, there are two anti-parallel currents flowing along the whole circumference of the ring. After further reduction of the external field also a negative current starts to flow at the inner edge. In the middle of the ring, however, there is still a positive current flowing. That is, we have three concentric currents loops, flowing anti-parallel with respect to each other. When the external field is reduced further, also in the middle of the ring negative currents start to flow and the flow *direction* becomes uniform again. Upon reaching $H_{\max} - 2H_{pen}$, the current becomes (nearly) uniform again.

6.5 Conclusions

We have experimentally studied the flux penetration in a superconducting ring by torque magnetometry and magneto-optical imaging. During the first flux penetration after zero-field cooling, some negative flux is present inside the hole of the ring, immediately after applying a magnetic field. This negative flux is caused by the closure of the field lines generated by the shielding current, and it gives a (negative) peak in the magnetic field profile at the inner edge. The maximum value of the inner peak occurs at the penetration field H_{pen}, in good agreement with H_{pen} determined by torque measurements. This gives a new and unambiguous method to determine the penetration field by magneto-optics. Another second unexpected feature is the complicated field and current pattern just after reversal of the field sweep direction. Despite the small width of the rings, three concentric counter-rotating current loops are found. With numerical simulations, we can reproduce the field and current profiles, measured by magneto-optics, exceptionally well. We find from these simulations that the current density j_s is indeed uniform, except during first penetration and in a field range of width $2H_{pen}$ immediately after the reversal of the sweep rate. This illustrates that the Bean model is also valid for thin films. Even in a field range where the self-field is comparable to the applied magnetic field, the current density is uniform, provided that the sweep is coming back from a sufficiently large field $|H_{\max}| \gg 2H_{pen}$, so that the sample is fully penetrated and the not in the region of a field reversal. This indicates, that self-field and penetration effects do not interfere with the pinning properties at low magnetic fields and proves once more that the characteristic field B^* is a true pinning parameter.

References

[1]   F.C. Klaassen, G. Doornbos, J.M. Huijbregtse, R.C.F. van der Geest, B. Dam, and R. Griessen, Phys. Rev. B **64**, 184523 (2001), and chapter 5 of this thesis

[2]   B. Dam, J.M. Huijbregtse, F.C. Klaassen, R.C.F. van der Geest, G. Doornbos, J.H. Rector, A.M. Testa, S. Freisem, J.C. Martinez, B. Stäuble-Pümpin, and R. Griessen, Nature **399**, 439 (1999)

[3]   A.J.J. van Dalen, R. Griessen, S. Libbrecht, Y. Bruynseraede, and E. Osquiguil, Phys. Rev. B **54**, 1366 (1996)

[4]   E.V. Matizen, P.P. Bezverkhy, V.G. Martynets, and S.M. Ishikaev, Phys. Rev. B **59**, 9649 (1999)

[5]   S.A.L. Foulds, J. Smithyman, G.F. Cox, C.M. Muirhead, and R.G. Humphreys, Phys. Rev. B **55**, 9098 (1997)

[6]   H. Zheng, M. Jiang, R. Nikolova, V. Vlasko-Vlasov, U. Welp, B.W. Veal, G.W. Crabtree, and H. Claus, Physica C **309**, 17 (1998)

[7]   I.L. Landau and H.R. Ott, Phys. Rev. B **61**, 727 (2000)

[8]   C.P. Bean, Phys. Rev. Lett. **8**, 250 (1962)

[9]   Th. Herzog, H.A. Radovan, P. Ziemann, and E.H. Brandt, Phys. Rev. B **56**, 2871 (1997)

[10]   E.H. Brandt, Phys. Rev. B **55**, 14513 (1997)

[11]   R.J. Wijngaarden, K. Heeck, M. Welling, R. Limburg, M. Pannetier, K. van Zetten, V.L.G. Roorda, and A.R. Voorwinden, Rev. Sci. Instrum. **72**, 2661 (2001)

[12]   M.R. Koblischka and R.J. Wijngaarden, Supercond. Sci. Technol. **8**, 199 (1995)

[13]   A.E. Pashitski, A. Gurevich, A.A. Polyanskii, D.C. Larbalestier, A. Goyal, E.D. Specht, D.M. Kroeger, J.A. DeLuca, and J.E. Tkaczyk, Science **275**, 367 (1997)

[14]   R.J. Wijngaarden, H.J.W. Spoelder, R. Surdeanu, and R. Griessen, Phys. Rev. B **54**, 6742 (1996)

[15]   R.J. Wijngaarden, K. Heeck, H.J.W. Spoelder, R. Surdeanu, and R. Griessen, Physica C **295**, 177 (1998)

[16]   R.J. Wijngaarden, R. Griessen, J. Fendrich, and W.K. Kwok, Phys. Rev. B **55**, 3268 (1997)

[17]   L.A. Dorosinskii, M.V. Indenbom, V.I. Nikitenko Yu. A. Ossip'yan, A.A. Polyanskii, and V.K. Vlasko-Vlasov, Physica C **216**, 205 (1993)

[18]   R.C. Surdeanu, *Magneto-optical study of vortex dynamics in superconductors*, PhD thesis, Vrije Universiteit Amsterdam (2001)

[19]   M. Qvarford, K. Heeck, J.G. Lensink, R.J. Wijngaarden, and R. Griessen, Rev. Sci. Instrum. **63**, 5726 (1992)

[20] J.M. Huijbregtse, B. Dam, J.H. Rector, and R. Griessen, J. Appl. Phys. **86**, 6528 (1999)

[21] Jeroen Huijbregtse, *Growth, Defect Structure and Critical Currents in $YBa_2Cu_3O_{7-\delta}$ Thin Films*, PhD thesis, Vrije Universiteit Amsterdam (2001)

[22] J.D. Jackson, *Classical Electrodynamics* 2nd edition, John Wiley & Sons Inc. (1975), page 177-178

[23] M. Baziljevich, *Investigation of magnetic flux behavior in $YBa_2Cu_3O_{7-\delta}$ thin films and single crystals using magneto-optic imaging*, PhD thesis, University of Oslo (1996)

[24] E.H. Brandt and M. Indenbom, Phys. Rev. B **48**, 12893 (1993)

[25] V. Ivaska, V. Jonkus, and V. Palenskis, Physica C **319**, 79 (1999)

Chapter 7

Surface and thickness effects in thin YBa$_2$Cu$_3$O$_{7-\delta}$ films

Using a post-anneal treatment we modify the surface structure of thin pulsed laser deposited YBa$_2$Cu$_3$O$_{7-\delta}$ films. Post-annealing reduces the thickness modulations at the surface and improves the crystallinity of the film, the effect being larger for films with many dislocations. We find, that in films with a low dislocation density the current density is unaffected by post-annealing. In films with a high dislocation density the current density $j_s(0)$ increases, due to the improved crystallinity, and the characteristic field B^* decreases in accordance with a decrease in dislocation density. The high field behaviour remains unchanged. These results confirm the domination of linear defect pinning in thin films, and show that surface effects and point defects play a minor role in vortex pinning[1].

The thickness dependence of the current density indicates that screening affects vortex pinning. The zero field current density initially increases sharply at small thicknesses, has a maximum at thickness $d = 100 - 150$ nm, and decreases as $j_s(d) \sim 1/d$ for large thicknesses. We find that two competing effects are responsible for the observed behaviour. For very thin films, with thickness $d < \lambda$, the increase of the effective penetration depth $\lambda_{eff} \simeq 2\lambda^2/d$ reduces the pinning energy ε_r and, consequently, the current density. In thicker films the currents run primarily in a layer of thickness $\lambda_{eff} \approx 70$ nm near the surface and the film-substrate interface, where vortices are strongly pinned by linear defects.

For thick films a peculiar peak in the magnetization is observed, at a *positive* magnetic field on the decreasing branch of a hysteresis loop, i.e. shifted towards the sweep direction. We give a preliminary explanation involving vortex bending and Meissner holes that appear in the film due to large self-fields.

7.1 Introduction

In thin films of YBa$_2$Cu$_3$O$_{7-\delta}$ linear defects are the most important pinning centers at low magnetic fields, exhibiting a plateau in j_s up to the characteristic field $B^* = 0.7n_{disl}\Phi_0$ [1]. However, at low magnetic fields also other effects may play an important role. In this chapter we address two issues: i) the influence of the surface on vortex pinning and ii) the effect of film thickness on the pinning of vortices.
YBa$_2$Cu$_3$O$_{7-\delta}$ films are known to exhibit rough surfaces [2], which can provide for additional pinning [3, 4]. Because a vortex wants to minimize its total length, it will be pinned at a position where the film thickness is minimal. The thickness variations due to the rough surface can thus form efficient pinning centers. Various groups found evidence for surface roughness pinning by investigating films with varying thickness, as the surface structure depends strongly on the film thickness [5, 6, 7].
A second aspect, which we have given little attention up to now, is the bending of vortices due to the self-field of the large critical currents. Especially at low magnetic fields large self-fields cause vortices to be curved. Indenbom *et al.* [8] claimed that pinning by columnar defects in irradiated single crystals cannot take place due to large self-fields. Instead the creation of vortex kinks at the surface determines the critical current density, whereas in the bulk the critical current is low due to easy kink sliding. In thin films vortex bending is also large due to the large aspect ratio $r/d \approx 10^4$, with r the sample radius and d the film thickness. On the other hand the vortex has to be straight and perpendicular to the surface within a layer of length $\ell_{scr} \simeq \lambda/\gamma$, with λ the bulk penetration depth and γ the anisotropy [9]. Since the screening length ℓ_{scr} is comparable to the film thickness, we expect a crossover in behaviour when increasing the film thickness from $d \ll \lambda$ to $d \gg \lambda$, i.e. from pinning of straight vortices (by linear defects) to the pinning of curved vortices, which is probably less effective.
Note, that surface pinning was investigated by looking at films with various *thickness* [5, 6, 7], because the surface roughness was found to increase with film thickness. But by changing the thickness, also the self-field and the screening of flux are influenced. We can therefore not identify whether the film thickness (i.e. the screening properties) or the surface roughness itself is responsible for the observed pinning behaviour. We thus need a different technique that changes the surface without affecting the film thickness.
In this chapter we investigate both the effect of the surface roughness and of the film thickness on the pinning in YBa$_2$Cu$_3$O$_{7-\delta}$ thin films. We show that by performing an additional post-anneal treatment on pulsed laser deposited (PLD) films, we can change the surface structure drastically. The surface roughness is reduced by a factor $1.5 - 2$, and the crystallinity of the film is improved. We therefore have the opportunity to study directly the influence of surface modulations on the pinning properties. Additionally we measured a thin film with thickness $d = 35$ nm $\ll \lambda$ and a thick film with $d = 450$ nm $\gg \lambda$. Combining the results with the YBa$_2$Cu$_3$O$_{7-\delta}$ films with an intermediate film thickness, treated in chapter 5, we investigate how vortex bending and surface currents determine the pinning properties of films with various thickness. This chapter is organized as follows. After explaining the film preparation and the post-anneal treatment, we present our results concerning the effect of post-annealing

on the defect microstructure (section 7.3.1) and the pinning properties (section 7.3.2). In section 7.4 we discuss the results in connection with surface roughness pinning and point defect pinning at high magnetic fields. We find that there is no evidence for pinning by surface modulations nor by point defects. Instead our results provide additional evidence for linear defect pinning. In section 7.5 we present the current density and magnetic hysteresis loops of films with various thickness. We show that the thickness dependence of the current density $j_s(B=0)$ can be explained by intrinsic screening effects. In thick films with $d \gg \lambda$ vortex bending introduces a very peculiar asymmetry in the hysteresis loop, which may be explained by the formation of Meissner holes. Finally, in section 7.6 we summarize our results and conclusions.

7.2 Experimental

YBa$_2$Cu$_3$O$_{7-\delta}$ thin films with low, average and high dislocation density were deposited by means of Pulsed Laser Deposition (PLD) on (100) SrTiO$_3$ substrates [10, 11]. The PLD-system consists of a KrF excimer laser (wavelength 248 nm, pulse time 30 ns) and a UHV system in combination with projection optics. The films are c-axis oriented and have a thickness of $d \approx 110$ nm. The dislocation density varies from $n_{disl} = 28$ (low), 50 (average) to 68 μm^{-2} (high). Each film is divided into two parts. One part is measured untreated (as-deposited, AD) and the other part is post-annealed (PA). By measuring the structural and superconducting properties on both as-deposited and post-annealed part of the *same* film, we can directly compare the effect of post-annealing on the defect microstructure and on the pinning properties.

To perform critical current measurements the films were patterned by standard UV photolithography into rings of diameter $D = 3$ mm and width $w = 125$ μm, in order to have a well-defined current distribution and relaxation rate [12]. The surface morphology of the films is studied by a tapping mode AFM, using a NANOSCOPE IIIA. Additionally, we measure the crystallinity with X-ray diffraction and Rutherford Back Scattering (RBS). The superconducting transition temperature is determined by means of resistivity measurements.

To investigate the effect of the film thickness, we deposited two films with thicknesses $d = 35$ nm (LP174) and $d = 450$ nm (LP193). These two thicknesses are complementary to the thicknesses of films measured before. Specifically, most films treated in this thesis have thicknesses $d = 140$ nm and $d = 110$ nm, whereas in chapter 5 also results for films with $d = 70$ nm and $d = 192$ nm are shown.

The superconducting current density $j_s(B, T)$ is measured at temperatures up to 70 K and in magnetic fields up to 7 T by means of capacitive torque magnetometry [13]. We assure that the sample is in the fully penetrated state by performing sweeps over a much larger range than the penetration field. Since the current in a thin film is confined to the film plane, we can directly calculate the current density $j_s \propto \tau_{irr}/(\mu_0 H \sin \vartheta)$ from the irreversible torque τ_{irr}. The proportionality factor depends on the dimensions of the ring and the properties of the torquemeter, which is calibrated by means of a copper calibration coil (see chapter 2 for more details about the measurement setup).

7.2.1 Post-anneal treatment

We change the microstructural properties of the films by performing a two-step post-anneal. In the first step the samples are heated in a quartz tube oven to $T_{a1} = 800°C$ in a 97% Ar + 3% O_2 mixture, flowing at a total rate of 1.0 l/min. At this anneal temperature the samples are kept for 30 minutes. After the first anneal step the samples are slowly (2°C/min) cooled down to $T_{a2} = 500°C$, while changing the gas atmosphere to pure O_2 at $T = 600°C$. The samples are kept at $T_{a2} = 500°C$ for 30 minutes, and finally cooled down slowly ($< 2°C/min$). During the first heat step the samples undergo a structural phase transition from orthorhombic to tetragonal, as oxygen effuses into the low oxygen background atmosphere. In the tetragonal phase (at $T_{a1} = 800°C$) a rearrangement of atoms takes place. During the cool-down the films take up oxygen again and the orthorhombic crystal structure is restored. The second anneal step at $T = 500°C$ is done to ensure that the samples are fully oxygenated.

7.3 Results

7.3.1 Effect of post-annealing on the defect structure

Surface roughness

The effect of post-annealing on the surface morphology is shown in figure 7.1, depicting AFM images of three films, before and after a post-anneal treatment. From the images it becomes clear that the additional heat treatment has profound effects on the surface. Whereas the surface of as-deposited films is characterized by growth islands, separated by deep trenches [14], after post-annealing the surface has become much smoother. For the film with many dislocations the islands are bigger and much flatter after the post-anneal treatment. Apparently the heat treatment rearranges the surface to a great extent, the effect being larger for films with many dislocations. In figure 7.2 we show a height profile, indicating that the surface modulations are reduced; only some edges remain. Consequently the rms surface roughness R_q is reduced appreciably, decreasing from $R_q \approx 5$ nm to $R_q < 3$ nm in films with many dislocations.

Due to the flattening effect of post-annealing on the surface, we can investigate whether thickness modulations due to the rough surface are important for the pinning of vortices, eventually in combination with linear defect pinning. Moreover, we expect that the relation between the island density and the dislocation density is lost upon post-annealing. As we saw in chapter 3, the linear defects are mostly situated at the place where three growth islands meet. During post-annealing the island structure is rearranged appreciably, but at the same time it is hard to anneal out dislocations. We expect therefore that the dislocation density is hardly affected by post-annealing, which provides us with an extra test to check the relationship
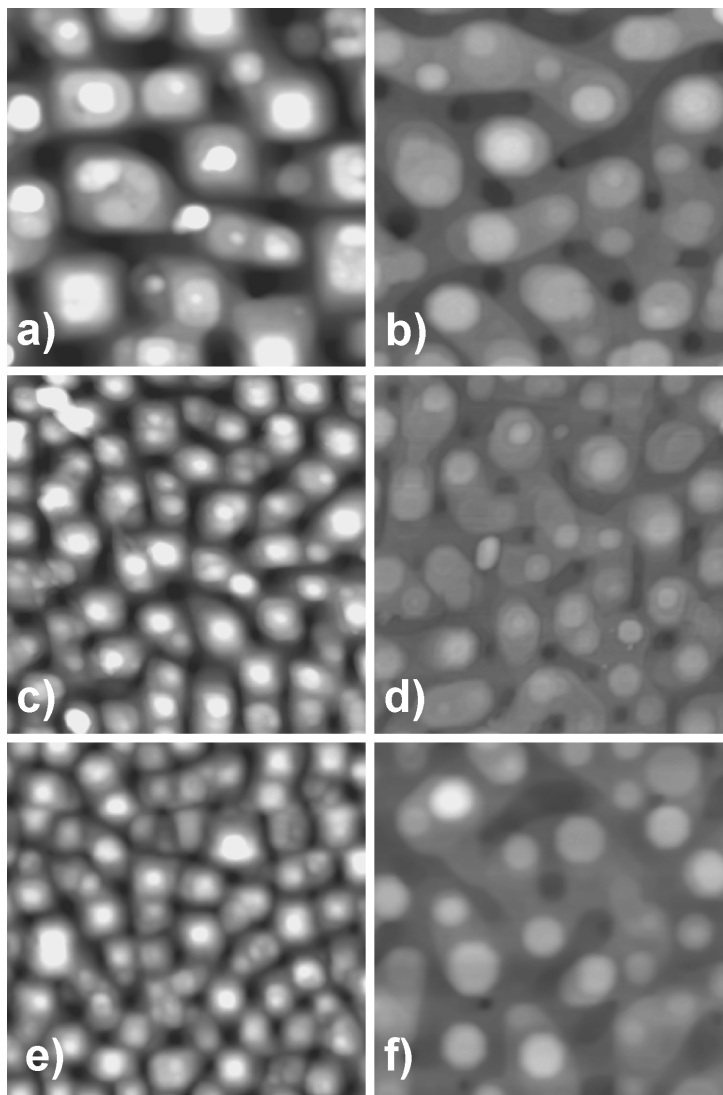
Figure 7.1: $1 \times 1 \ \mu\text{m}^{-2}$ AFM height images of three $\text{YBa}_2\text{Cu}_3\text{O}_{7-\delta}$ films on (100) SrTiO_3, with low $n_{disl} = 28 \ \mu\text{m}^{-2}$ (a, b), average $n_{disl} = 50 \ \mu\text{m}^{-2}$ (c, d) and high $n_{disl} = 68 \ \mu\text{m}^{-2}$ (e, f). The left panels show the as-deposited surface morphology, and the right panels the surface after post-annealing. The images indicate that the surface becomes much flatter after post-annealing, and the island size increases. The effect is larger in films with many dislocations. The height scale is 50 nm for all images.

between B^* and n_{disl}, independently of the island density. This was not possible in the untreated PLD films,where there is always a 1 to 1 ratio between island and dislocation density (see ref. [14] and chapter 3).

Dislocation density

The anneal temperature $T_{a1} = 800°$C is comparable to the substrate temperature during deposition. It is not a priori clear how the dislocations react to the annealing, but generally it takes a higher anneal temperature to annihilate dislocations. The dislocation density is determined by wet chemical etching, as outlined in chapter 3. We find that only for films with a high dislocation density (see figure 7.3), the number of linear defect is decreased by 37%, from $n_{disl} = 68$ to $n_{disl} = 43$ μm^{-2}, whereas in the other films n_{disl} is virtually unchanged[2]. In fact this is somewhat surprising, since, as we mentioned, the anneal temperature is rather low for dislocations to annihilate. On the other hand, in the high dislocation density film, the distance d_r between adjacent dislocations is lower, which facilitates annihilation. We find, that upon annihilation the distribution of the dislocations becomes more random. Moreover, the linear defects are not connected any more with the growth island structure, like in as-deposited PLD films.

Crystallinity

As a measure of the quality of an YBa$_2$Cu$_3$O$_{7-\delta}$ film, often the full width at half maximum (FWHM) of the (005) rocking-curve peak is taken. In our films, the FWHM of this peak is typically $\Delta\omega_{(005)} \simeq 0.1 - 0.2°$ [11]. In figure 7.4 the (005) peak is depicted for the as-deposited and post-annealed part of film LAD669. The width of the (005) peak is reduced upon post-annealing, indicating that the crystallinity improves. This trend was confirmed by channeling RBS-measurements in the [001] direction, showing a similar decrease of the FWHM as observed in X-ray measurements [15]. The improvement of crystallinity is larger for films with a high dislocation density. This is not surprising, since films with many dislocations are grown at a lower substrate temperature, and show a somewhat broader (005) peak (i.e. a reduced crystallinity). This does not mean, however, that the crystallinity of the as-deposited films with many dislocations is poor. Channeling RBS-measurements show that the crystallinity is already fine [15], but is enhanced even further by post-annealing. We conclude that post-annealing provides a way to optimize the crystalline quality, especially of high dislocation density YBa$_2$Cu$_3$O$_{7-\delta}$ films.

Oxygen content

In figure 7.5a we show the superconducting transition of the film LAD673 AD and PA. We find that both the resistivity ρ and the critical temperature T_c decrease. This suggests that upon post-annealing the films become somewhat overdoped. Probably the oxygen content has increased as a result of the phase transition from orthorhombic

---

[2]Also for the low dislocation density film LAD670, the dislocation density decreases somewhat, from $n_{disl} = 28$ to $n_{disl} = 24$ μm^{-2}, but this effect is too small to be statistically significant.

film	d (nm)	n_{disl} (μm^{-2})	R_q (nm)	T_c (K)	ΔT_c (K)	$\Delta\omega_{(005)}$ (°)	c-axis (Å)
LAD670AD	110	28	4.91	90.4	0.6	0.18	11.701
LAD670PA	110	24	3.73	89.8	0.6	0.16	11.6914
LAD669AD	110	50	5.13	90.1	0.5	0.16	11.698
LAD669PA	110	51	3.48	89.3	0.5	0.14	11.6931
LAD673AD	110	68	4.18	90.1	0.4	0.23	11.7045
LAD673PA	110	43	2.45	89.4	0.4	0.20	11.6954

Table 7.1 General properties of the as-deposited (AD) and post-annealed (PA) YBa$_2$Cu$_3$O$_{7-\delta}$ films investigated in this work. d is the film thickness, obtained from X-ray diffraction. From AFM and etching experiments we determined the dislocation density n_{disl} and the rms surface roughness R_q. T_c is the transition temperature and ΔT_c the width of the transition. The crystalline quality is characterized by the FWHM of the (005) rocking curve peak $\Delta\omega_{(005)}$ and the c-axis unit cell length.

to tetragonal and back during the post-anneal treatment. Additional proof of an increased oxygen content we find from X-ray diffraction. In figure 7.5b we plotted a $\theta - 2\theta$ X-ray scan around the (007) reflection. While the reflection angle shifted to higher values for the post-annealed sample, the peak intensity increased, and the peak width decreased. The change of shape of the reflection peak confirms the increased crystallinity after post-annealing, whereas the angle shift means that the c-axis has decreased slightly. Averaging over all (00ℓ) reflections with $\ell = 1 - 8$, we find that the c-axis unit cell length decreases from 11.70 to 11.69 Å. A smaller c-axis can be due to either an increase in oxygen content or to the improved crystallinity. However, a better crystallinity alone would *increase* T_c, whereas an increase of the charge carrier density beyond the optimal doping content *decreases* T_c. Since we observe a small decrease of T_c (7.5a) we conclude that the PA films are indeed slightly overdoped.

Summary

To summarize the influence of the post-anneal treatment on the microstructure, we show in table 7.1 the structural parameters of the films, as-deposited and post-annealed. The most important effect concerns the change of surface morphology, which becomes flatter and smears out the original island structure. Secondly the dislocation density is affected for films with many dislocations with $n_{disl} > 50$ μm^{-2}. Finally the heat treatment causes an improved crystallinity and a slight overdoping in the post-annealed YBa$_2$Cu$_3$O$_{7-\delta}$ films. All structural changes due to the annealing procedure are more substantial for films that are deposited with a low substrate temperature (i.e. having a large dislocation density), such as LAD673.
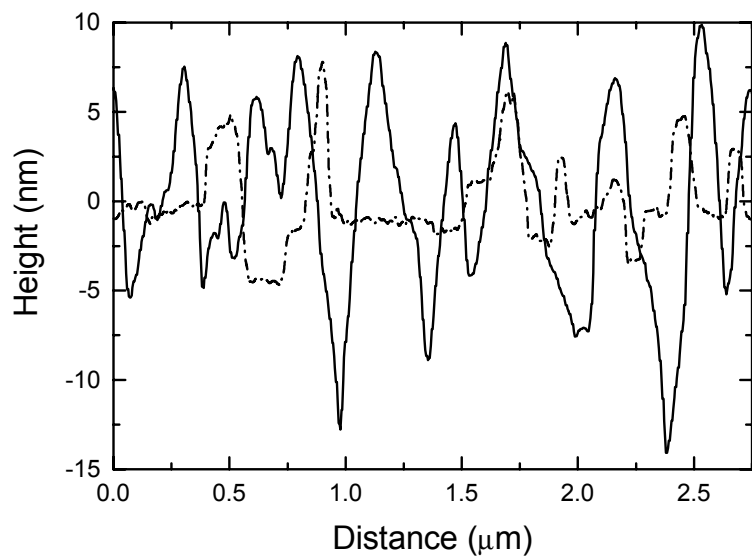
Figure 7.2: AFM cross section image of an YBa$_2$Cu$_3$O$_{7-\delta}$ film, showing the height variations at the surface before post-annealing (solid line) and after a post-anneal treatment (dash-dotted line). The reduction of the surface roughness is clearly visible.
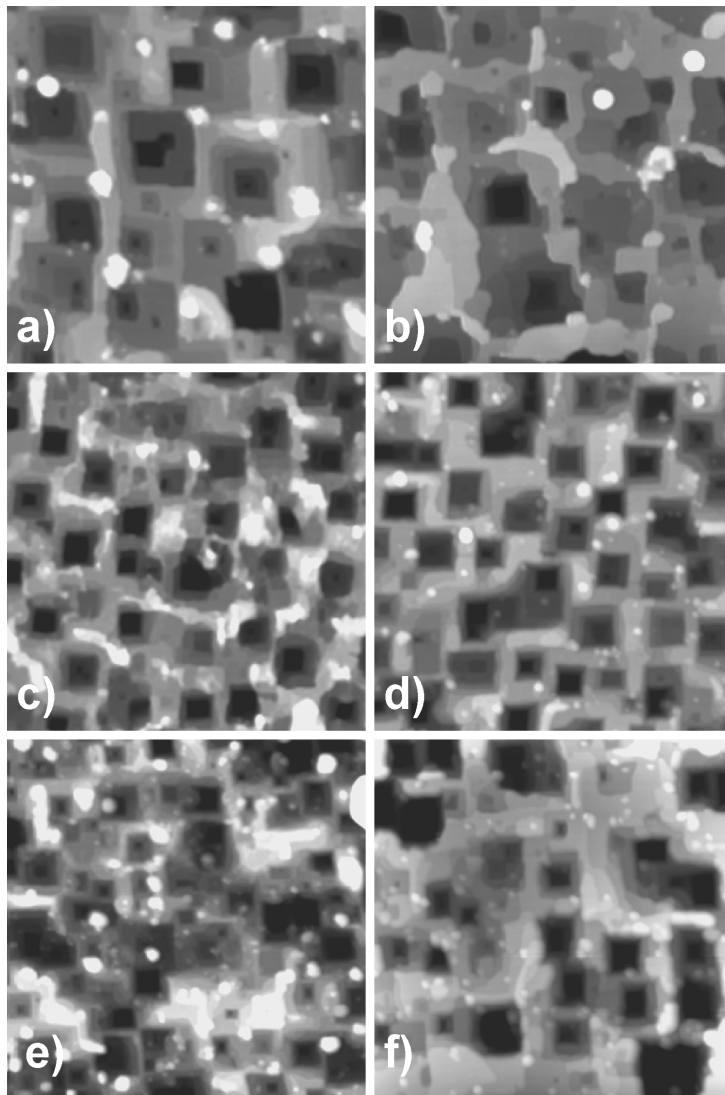
Figure 7.3: The dislocation density n_{disl} of the $YBa_2Cu_3O_{7-\delta}$ films of figure 7.1 is determined by counting the number of etch pits after wet chemical etching. The left panels show the as deposited films with a) $n_{disl} = 28$ μm^{-2}, c) $n_{disl} = 50$ μm^{-2}, and e) $n_{disl} = 68$ μm^{-2}. The right panels show the post-annealed films with b) $n_{disl} = 24$ μm^{-2}, d) $n_{disl} = 51$ μm^{-2}, and f) $n_{disl} = 43$ μm^{-2}. The dislocation density is not affected by the post-anneal treatment, except for the film with a large dislocation density, where the linear defect density was reduced from $n_{disl} = 68$ to 43 μm^{-2}. The height scale is 50 nm for all images.
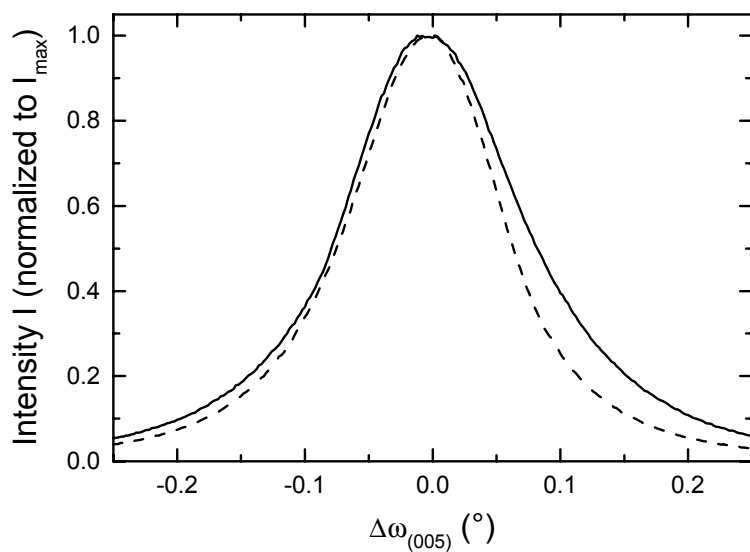
Figure 7.4: XRD rocking curve of the (005) direction for film LAD669 ($n_{disl} = 50 \ \mu\text{m}^{-2}$), as-deposited (solid line) and post-annealed (dashed line). The width of the rocking curve decreases after post-annealing, which is indicative for an improved crystallinity in the post-annealed sample.
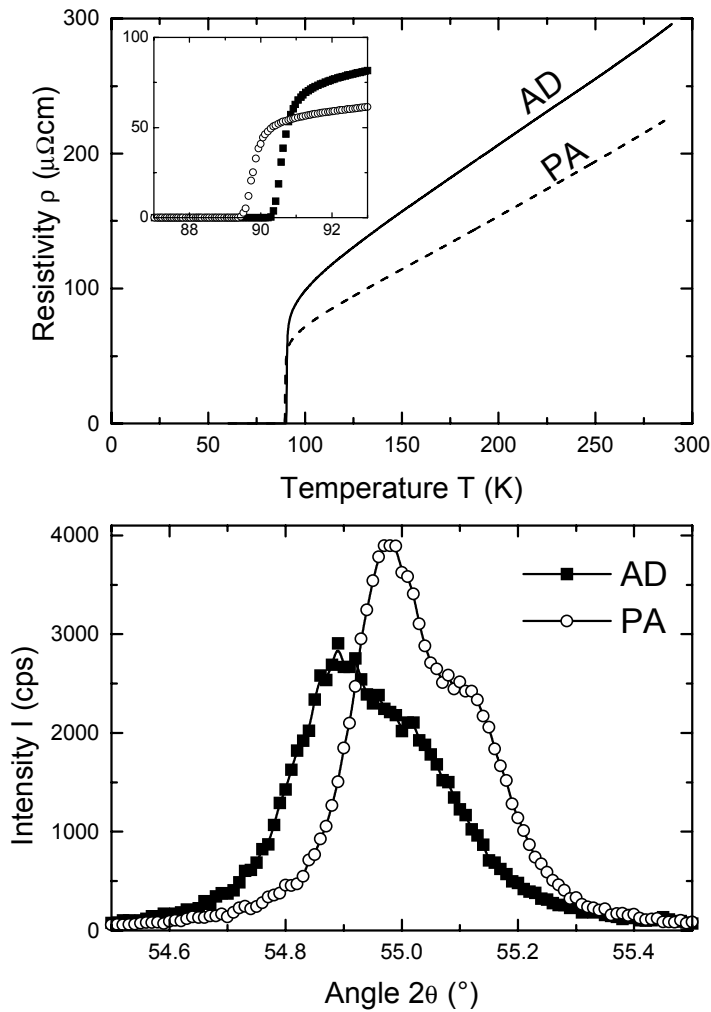
Figure 7.5: The effect on post-annealing on the crystallinity and the oxygen content is illustrated by a) a resistivity measurement and b) a XRD $\theta - 2\theta$ scan around the (007) direction. a) The resistivity $\rho(T)$ as a function of temperature shows a reduction both in ρ and in T_c after post-annealing. This indicates that the post-annealed film has a slightly overdoped oxygen content. b) The shift of the (007) peak to higher angles points to a small reduction of the c-axis length, in agreement with oxygen overdoping, whereas the decreased peak width illustrates the improved crystallinity. AD = as-deposited, PA = post-annealed.

## 7.3.2 Effect of post-anneal on the pinning properties

The changes in the microstructure of post-annealed thin films provide many opportunities to investigate the influence of various types of defects on the current density. By comparing the as-deposited and post-annealed part of the same film, we directly observe the influence of post-annealing on the pinning properties. In figure 7.6a the current density of film LAD670 (low n_{disl}) is plotted for $T = 10$, 20 and 30 K, before and after post-annealing. We observe the general features of the current density, described already in chapter 5, i.e. a plateau up to the characteristic field B^*, a crossover regime and the power law decrease $j_s(B) \sim B^\alpha$ at high magnetic fields. From figure 7.6a we find that the current density $j_s(B)$ has not changed after post-annealing, neither in field nor temperature dependence. Only at very high magnetic fields, we observe that $j_s(B)$ decreases faster in the as-deposited film (dotted arrows in figure 7.6a). This effect is rather subtle, but it may be a signature of the improved crystallinity.

Whereas for LAD670 (low n_{disl}) the differences between the AD and PA sample are small, for LAD673 with many dislocations the post-anneal treatment has a substantial impact on the behaviour of the current density. In figure 7.6b $j_s(B)$ for LAD673AD and LAD673PA is plotted at $T = 10$ and 50 K. We distinguish two important effects of the post-annealing upon $j_s(B)$. First the characteristic field B^* decreases from $B^* = 90$ mT to 65 mT. This is not surprising since we found previously, that the dislocation density decreases after post-annealing from $n_{disl} = 68$ μm^{-2} to $n_{disl} = 43$ μm^{-2} (see table 7.1). Secondly, the current density at zero magnetic field increases from $j_s(B{=}0) = 2.7 \cdot 10^{11}$ Am^{-2} to $5.0 \cdot 10^{11}$ Am^{-2} at zero magnetic field. That a post-anneal treatment can increase the current density was observed earlier [16]. To our view this is related to the increase of crystallinity, allowing for a larger *intrinsic* current density. As the crystallinity of film LAD670AD, with low dislocation density, is already excellent, an increase of $j_s(B)$ in this film is not observed.

In figure 7.7 the three pinning parameters $B^*(T)$, $j_s(B{=}0, T)$ and $\alpha(T)$ are summarized for the films LAD670 and LAD673. The parameter $\alpha \equiv d\ln j_s / d\ln B$, characterizing the high field behaviour of the current density, remains unchanged for both films after post-annealing. The increase of $j_s(0, T)$ upon post-annealing in film LAD673, accompanied by a decrease of the surface roughness, indicates that the surface probably does not play a vital role in pinning. Instead the decrease of B^* follows, as expected, the decrease of the dislocation density. In the next section we discuss the implications of post-annealing for alternative pinning mechanisms in more detail.

7.4 Discussion

The results of our post-anneal investigation elucidate the role of alternative pinning mechanisms in thin YBa$_2$Cu$_3$O$_{7-\delta}$ films. In particular we can evaluate the importance of i) surface modulations for vortex pinning and ii) pinning by point defects at high magnetic fields.
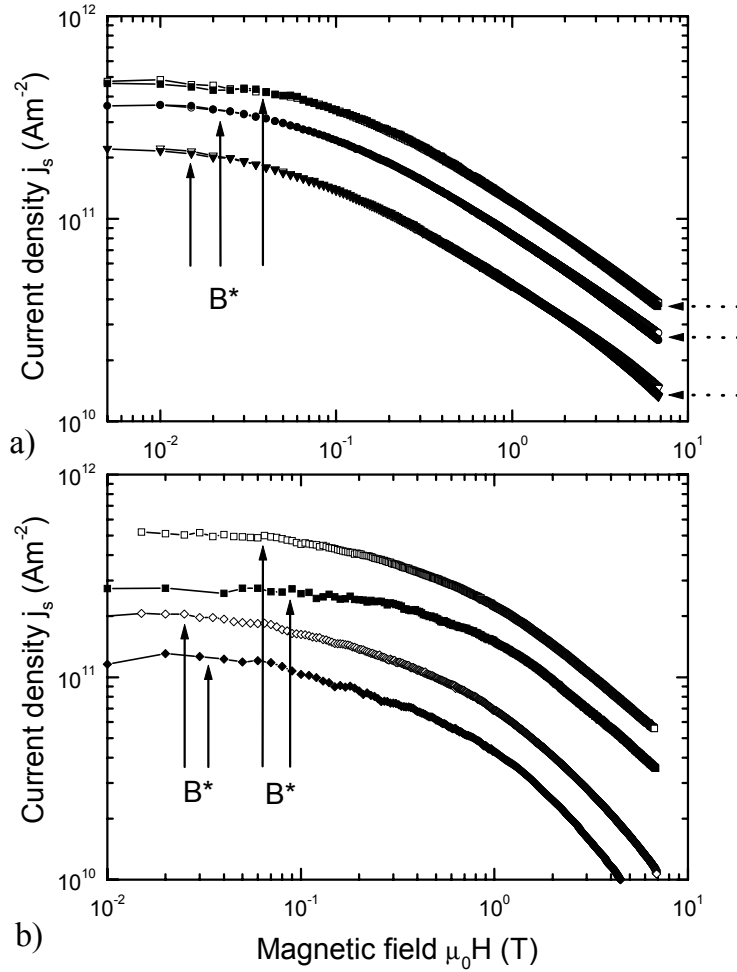
Figure 7.6: Superconducting current density $j_s(B)$ for a) both as-deposited and post-annealed part of LAD670, $n_{disl} = 28 / 24 \ \mu\mathrm{m}^{-2}$, at $T = 10$ (■, □), 20 (•, ○), and 30 K (▼, ▽). Solid symbols denote the as-deposited part, open symbols the post-annealed sample. Solid arrows indicate the value of the characteristic field. It is clear that for films with low n_{disl}, post-annealing has no influence on $j_s(B)$, except for a subtle feature at very high magnetic fields (dotted arrows), where as-deposited films develop a fast decrease of $j_s(B)$ at lower magnetic fields. b) Idem, for LAD673, $n_{disl} = 68 / 43 \ \mu\mathrm{m}^{-2}$ at $T = 10$ (■, □) and 50 K (◆, ◇). As in panel a), the solid symbols denote the AD part, and the open symbols the PA film. For films with high n_{disl}, the current density increases, whereas the dislocation density and characterstic field decrease. The behaviour at high magnetic fields is not affected by post-annealing.
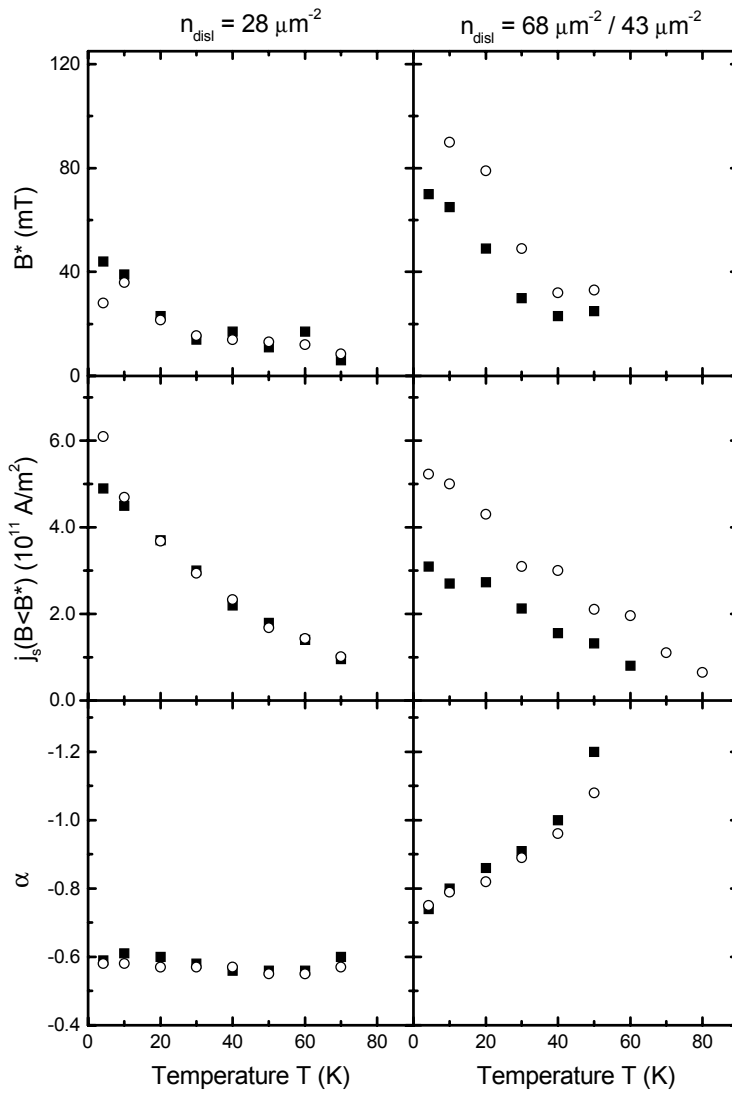
Figure 7.7: Summary of the three parameters, characterizing linear defect pinning, as a function of temperature; $B^*(T)$ (top), $j_s(B = 0, T)$ (middle) and $\alpha(T)$ (bottom) for LAD670 (left panels) and LAD673 (right panels), both as deposited (■) and post-annealed (○). The summary clearly shows that the post-anneal treatment has no effect on films with low n_{disl}, whereas in films with many dislocations, $j_s(0)$ increases to a characteristic value $j_s(B=0, d=110$ nm$) \approx 5 \cdot 10^{11}$ Am^{-2}, and B^* decreases in agreement with a reduced dislocation density.

Vortex pinning by planar defects, such as twin or anti-phase boundaries, was discussed by Huijbregtse *et al.* [15]. He showed that planar defects play a negligible role in *naturally* grown thin films. Twin boundaries would lead to lower current densities than observed, especially at low temperatures [17], and anti-phase boundaries are not formed in our films due to the use of high quality SrTiO$_3$-substrates with a low miscut angle (vicinal angle $\lesssim 0.15°$).

7.4.1 Zero-field current density and characteristic field

Comparing the results on the as-deposited and post-annealed part of the films LAD670 and LAD673, we can draw a few important conclusions. The most important effect of the post-anneal treatment, is the smoothing of the surface. The intrinsically rough surface of PLD YBa$_2$Cu$_3$O$_{7-\delta}$ films has been interpreted by some authors as an important source for vortex pinning [5, 7]. Since a vortex wants to minimize its length, thickness modulations can provide for this extra pinning. Assuming a sinusoidal thickness variation $\delta d \sin(2\pi x/D)$, with D the island size or, more generally, the wavelength of the thickness variation, the pinning force per unit length is given by [4]:

$$f_p \simeq 2\pi\varepsilon_l(\delta d/d)/D \qquad\qquad (7.1)$$

with ε_l the vortex line energy. With typical thickness variations $\delta d/d \simeq 10 - 20\%$ and island size $D = 150$ nm, we find pinning forces of $f_{p,\max} \approx 1 - 2 \cdot 10^{-5}$ Nm^{-1}, leading to critical currents $j_c \simeq 10^{10}$ Am^{-2}, which are much smaller than the current densities, that are usually observed in thin YBa$_2$Cu$_3$O$_{7-\delta}$ films. Jooss *et al.* [6] use a more sophisticated model, that takes into account the various contributions to the pinning energy more explicitly, and which separates bulk pinning from surface pinning. With a typical thickness variation $\delta d = 15$ nm, measured by AFM on our films, the contribution of the surface to the current density according to Jooss' model, is $j_s^{surface} \lesssim 10^{10}$ Am^{-2}, which is in the same range as the estimates from Kes [4].

As the critical currents, estimated from surface pinning, are rather low, we expect at most a minor contribution of the surface to the current density. Indeed, from figure 7.6a we learn that the surface modifications due to the post-anneal treatment have no measurable effect on the pinning properties of LAD670, whereas the surface roughness is reduced appreciably. In LAD673 there is even an increase of $j_s(B = 0)$, although the surface roughness decreases. The increase of the superconducting current in LAD673 therefore cannot be caused by surface modulations. From the structural information (rocking curve width and c-axis length) one concludes that the initial film quality of LAD673 is somewhat worse. It is generally observed, that films with many dislocations, such as LAD673, show a smaller current density $j_s(B = 0)$ than films with less dislocations (see, for example, figure 3.5 on page 35). After post-annealing the current density of LAD673 increases to $j_s(B = 0) \approx 5 \cdot 10^{11}$ Am^{-2}, which is the same current density as observed in film LAD670. Obviously, the film quality of LAD673 improved upon post-annealing to become comparable to the quality of low

dislocation density films. This suggests, that $j_s(B = 0) \approx 5 \cdot 10^{11}$ Am^{-2} is a universal value for the current density for films with $d = 110$ nm.

The observed behaviour is again strong evidence that linear defects are the most important pinning centers: the post-anneal treatment annihilates part of the dislocations, and the characteristic field B^* is reduced accordingly from $B^* = 90$ mT to 65 mT. Note, that in chapter 3 we investigated the influence of etching on the superconducting properties. We found that etching increases the thickness variations, whereas the current density *decreases*. If any, the surface has an *opposite* effect on the pinning properties: the shallower the surface modulations, the higher the intrinsic current density.

Some groups claim that the island structure of $YBa_2Cu_3O_{7-\delta}$ PLD films is associated with a (low angle) grain boundary or weak link [18]. Already in chapter 5 we argued that the existence of a low angle grain boundary in our films is not very likely, because the distance between the linear defects is too large to form a coherent planar defect. Moreover, whereas the post-anneal treatment does not affect the superconducting current density of LAD670, the island structure is changed dramatically. If we would assume vortex matching to the island structure, we can define an island matching field like in chapter 3, assuming that the trenches between the islands are filled with vortices until the average vortex spacing becomes comparable to λ (see section 3.5 and also ref. [19]):

$$B_\Phi^{island} \simeq \frac{2\Phi_0}{\lambda \cdot D} \tag{7.2}$$

with D the island diameter. Already in chapter 3 we argued that eq. (7.2) cannot explain the characteristic field in *as-deposited* films, since B_Φ^{island} should increase with the square root of the dislocation density, instead of linearly (section 3.5). Secondly, after post-annealing we find no change of the matching field in LAD670, although the island structure has changed considerably. Calculating the ratios between the island size before and after post-annealing for LAD673, we find $n_{island}^{AD}/n_{island}^{PA} = 0.45$, whereas $n_{disl}^{PA}/n_{disl}^{AD} = 0.63 \simeq B_{PA}^*/B_{AD}^* = 0.72$, confirming that the characteristic field is indeed connected to the dislocation density, and not to the island density. In addition, TEM observations on our films reveal a perfectly layered epitaxial structure without grain boundary over a region of several microns [15].

In conclusion the current density behaviour of as-deposited and post-annealed films does not support any grain boundary or surface roughness pinning model. Instead, our results are completely consistent with linear defect pinning.

7.4.2 Behaviour at high magnetic fields

At high magnetic fields the vortices outnumber all (extended) defects, but there are still point defects in abundance. It was therefore suggested, that in that field regime vortices are pinned by point defects [21, 22]. Especially oxygen vacancies and large precipitates, such as Y_2O_3 and Y_2BaCuO_5-inclusions (211-precipitates) are known to increase j_c [23, 24, 25]. In thin $YBa_2Cu_3O_{7-\delta}$ films Y_2O_3 inclusions are the most abundant secondary phases [26]. From planar view TEM measurements we find for

a typical density of large precipitates $n_{precip} \approx 4 \ \mu m^{-2}$ [15], which is very little compared to the dislocation density.

By giving an additional heat treatment to our films we expect that the concentration of point defects decreases, since during the post-anneal the film has more time to relax to an epitaxial equilibrium than during pulsed laser deposition. Therefore, if point defects were important pinning sites at high magnetic fields, we would expect a smaller j_s in the post-annealed film, which we do not observe. Instead, in films with many dislocations j_s even increases. Also the high field *behaviour*, characterized by the power-law slope α, does not change. This confirms that point defects play only a minor role.

In the literature it has been reported that the critical current increases due to precipitates [25]. However, it may well be, that the increase of j_c is caused by linear defects, that were induced by the precipitates, and not principally by the secondary phases themselves. In thin $YBa_2Cu_3O_{7-\delta}$ films precipitates and linear defects are closely related [26]. For example Huijbregtse *et al.* showed, that it is possible to artificially increase the dislocation density in thin $YBa_2Cu_3O_{7-\delta}$ films, by depositing Y_2O_3 droplets onto a clean $SrTiO_3$ substrate prior to the film deposition [14].

As already mentioned in section 7.3.2, a small difference is observed in $j_s(B)$ of LAD670, at magnetic fields $\mu_0 H > 4$ T (indicated by dotted arrows in figure 7.6a). In the as-deposited film a faster decrease of $j_s(B)$ develops, whereas in the post-annealed part the current decrease $j_s(B) \sim 1/\sqrt{B}$ extends up to the maximum attainable field of 7 T. Apparently the plastic pinning regime, where vortices are shearing through the lattice of the strongly pinned vortices on the linear defects, can be maintained up to higher magnetic fields, before a breakdown occurs. Possibly the increased crystallinity induces a better ordering of the vortex lattice, thus allowing for more effective "shear channels" for the unpinned vortices. However, as the effect is quite small, it is hard to draw definite conclusions from this observation.

In LAD673 the high field behaviour has not changed after post-annealing. This is rather surprising, since the dislocation density in this film decreases from $n_{disl} = 68$ to 43 μm^{-2}. As shown in chapter 5, in films with $n_{disl} < 60 \ \mu m^{-2}$ vortices are plastically pinned, with $\alpha \approx -0.58$, and in films with $n_{disl} > 60 \ \mu m^{-2}$, vortices are pinned collectively with $\alpha \approx -0.8$ to -1.1. We would therefore expect a crossover from collective to plastic pinning in LAD673, but a change of the power-law slope from $\alpha \approx -0.8$ to $\alpha \approx -0.58$ is not observed. We believe that this is due to the fact, that the island structure after post-annealing is not related any more to the positions of the linear defects. In the as-deposited films the linear defects are located in the trenches where three growth islands meet. This results in a relatively regular array of linear defects [14]. After post-annealing the island structure has flattened, but *no positional rearrangement* of the dislocations has taken place. As a result, the distribution of the linear defects of LAD673PA is still associated with the regular dislocation array of the original as-deposited film, with some of the defects annealed out. This means that the distance between nearest neighbours is mainly related to the original $n_{disl} = 68$ μm^{-2}, with a distance between many adjacent defects of $d_r \approx 1/\sqrt{68 \ \mu m^{-2}} = 120$ nm (although the *average* distance between defects is $\overline{d_r} = 1/\sqrt{43 \ \mu m^{-2}} = 152$ nm).

film	d (nm)	n_{disl} (μm^{-2})	R_q (nm)	T_c (K)	ΔT_c (K)	$\Delta\omega_{(005)}$ (°)
LP174	35	39	2.30	89.3	1.2	0.20
LP193	450	25	3.93	89.5	-	0.25

Table 7.2 Structural properties of the investigated thin and thick YBa$_2$Cu$_3$O$_{7-\delta}$ film. d is the film thickness, n_{disl} the dislocation density, R_q the rms surface roughness, T_c the transition temperature, ΔT_c the width of the transition, and $\Delta\omega_{(005)}$ denotes the FWHM of the (005) rocking curve. The critical temperature of LP193 was not determined by means of a resistivity measurement, but obtained from the extrapolation of the irreversibility field $H_{irr}(T)$ to zero field.

Consequently the distribution of the linear defects of LAD673PA is more random after post-annealing, which is indeed observed in figure 7.3f. Apparently, due to the relatively short distance between many adjacent defects, collective pinning instead of plastic pinning dominates the high magnetic field behaviour in LAD673PA, which explains why the power law slope α has not changed.

7.5 Thickness effects

7.5.1 Effect of the thickness on vortex pinning by linear defects

To investigate the effect of film thickness on the pinning properties, we measured a very thin film (LP174, $d = 35$ nm) and a thick film (LP193, $d = 450$ nm). The structural features of both films are summarized in table 7.2. The film quality is still excellent, albeit with slightly higher rocking curve widths of $\Delta\omega_{(005)} \simeq 0.2°$. Moreover, the surface roughness in both films is comparable to that observed in films of average thickness (see table 7.1). We do not observe an increase of R_q with film thickness.

The zero field current density at low temperatures is plotted in figure 7.8 together with the films from chapter 5, LAD493 ($d = 70$ nm), LAD554 ($d = 140$ nm) and Y67 ($d = 192$ nm). Also plotted are data reported by Sheriff *et al.* [7] and by Liu and Schlenker [27]. We find that the typical shape of $j_s(d)$, observed by other groups, is reproduced by our data. All data show the same trend, a sharp increase of $j_s(B=0)$ for very thin films, a maximum at around $d = 100 - 150$ nm and a slow decrease for thicker films. The maximum in current density seems to indicate a crossover, corresponding to a critical film thickness $d \simeq 2\ell_{scr}$, the maximum length over which the vortex can be straight. Note that Civale *et al.* [28], investigating the dependence of the irreversibility line on the film thickness, found a similar crossover at $d = 100$ nm. For all films with thickness $d > 100$ nm, the irreversibility line was found to coincide
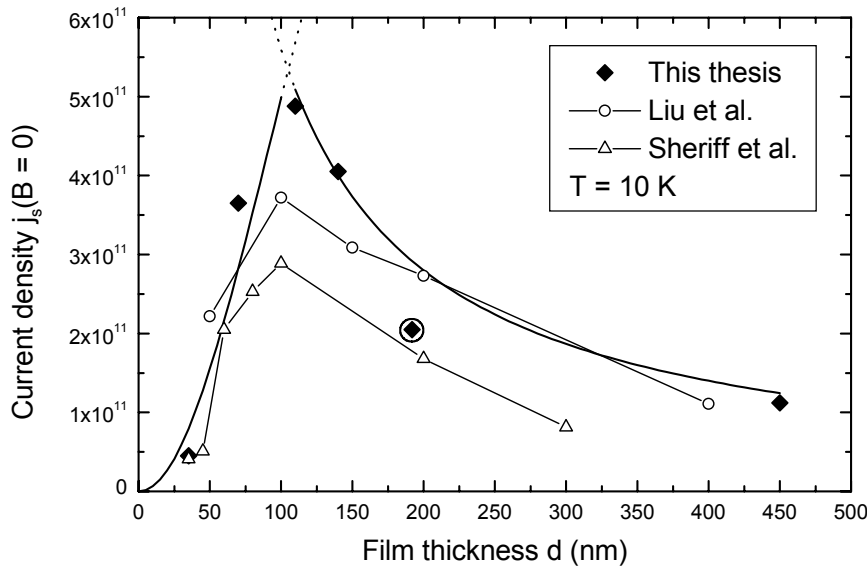
Figure 7.8: Zero field current density as a function of the film thickness for various YBa$_2$Cu$_3$O$_{7-\delta}$ films, at $T = 10$ K. Data are shown from films, studied in this thesis ($\blacklozenge$), from Liu *et al.* ($- \circ -$) [27], and from Sheriff *et al.* ($-\triangle-$) [7]. All data show the same trend, with a maximum at $d \approx 100$ nm. The solid line is the expected thickness dependence according to eqs. (7.3) and (7.4), with $j_s(d=2\lambda_{eff}) = 4 \cdot 10^{11}$ Am^{-2} and $\lambda_{eff} = 70$ nm. The agreement with our data is excellent, except for film Y67 (circled $\blacklozenge$), which has a smaller average defect size (see the main text for a discussion).

with the single crystal irreversibility line. For thinner films with $d < 100$ nm, the irreversibility line $H_{irr}(T)$ lies lower, i.e. dH_{irr}/dT decreases.

For $d < 100$ nm, the current density decreases rapidly with decreasing thickness. For LP174 we find $j_s(B=0) = 5 \cdot 10^{10}$ Am^{-2} at low temperatures, which is one order of magnitude lower compared to the films with $d = 100 - 150$ nm. The structural parameters, such as $T_c = 89.3$ K and the rocking curve width $\Delta\omega_{(005)} = 0.2°$ indicate, that the film quality is not much reduced, although the transition width ΔT_c is somewhat larger. The low current density may be caused by an increased effective penetration depth. For thin films with $d \ll \lambda$, the effective penetration depth is given by $\lambda_{eff} \simeq 2\lambda^2/d$ [29] or, alternatively, by $\lambda_{eff}(d) \simeq \lambda \coth(d/2\lambda)$ [30]. The latter has the correct asymtotic behaviour, approaching the original formula of Pearl *et al.*

[29] for small d, and reducing to λ for large film thicknesses. The larger effective penetration depth reduces the pinning energy $\varepsilon_r \sim 1/\lambda_{eff}^2$ and therefore the critical current.

After a maximum at $d = 110$ nm the current density decreases with the thickness. This may be due to vortex bending, occurring when the film thickness is larger than $d > 2\lambda_{eff}$. The maximum at $d \approx 100 - 150$ nm suggests, that the typical length, over which the vortices are straight, is $\lambda_{eff} = 50 - 75$ nm. This explains qualitatively the observed behaviour of $j_s(d)$, and coincides reasonably well with estimates of Brandt [9] and Prozorov *et al.* [31], $\ell_{scr} \simeq \lambda/\gamma \simeq 30$ nm.

Taking into account both effects we can establish the following relationship between the zero field current density and the film thickness:

$$
\begin{aligned}
j_s(d) &\approx \frac{\varepsilon_r(\lambda_{eff})}{\Phi_0 \xi} = \frac{\lambda_B^2}{\lambda_{eff}^2(d)} j_{s\,\text{max}}, & \text{for } d < 2\lambda_{eff} & \qquad (7.3)
\end{aligned}
$$

$$
\begin{aligned}
j_s(d) &\approx \frac{2\lambda_{eff}}{d} j_{s\,\text{max}}, & \text{for } d > 2\lambda_{eff} & \qquad (7.4)
\end{aligned}
$$

with $\lambda_B = 140$ nm the bulk penetration depth and $j_{s\,\text{max}} \equiv j_s(d{=}2\lambda_{eff})$ the crossover current density, exactly at the film thickness where a vortex is pinned over its maximum length ($= 2\lambda_{eff}$) by a linear defect, without being bent by the curved magnetic field lines. Eq. (7.3) stems from the linear defect pinning energy, calculated in chapter 4, with λ_{eff} instead of λ_B. Eq. (7.4) assumes, that the total current runs in a layer of length λ_{eff} at the surface and the film-substrate interface. Note, that this does not imply surface *pinning*. Vortices are still pinned by linear defects, just not over their full length. In figure 7.8 both eqs. (7.3) and (7.4) are plotted, with $j_s(d{=}2\lambda_{eff}) = 4 \cdot 10^{11}$ Am^{-2} and $\lambda_{eff} = 70$ nm. The agreement with experiment is remarkably good.

Only film Y67 ($d = 192$ nm, with circle in figure 7.8) has a low current density compared to eq. (7.4). However, Y67 is a sputtered film, which has on average more edge dislocations with a smaller defect radius, as argued in chapter 5. We find that the theoretically expected current density $j_s(192 \text{ nm}) = 2.92 \cdot 10^{11}$ Am^{-2} and the measurement $j_s(\text{Y67}) = 2.05 \cdot 10^{11}$ Am^{-2} deviate by a factor 1.4. A similar difference is found in the *true* critical current density $j_c(T{=}0, B{=}0)$ between LAD554 and Y67, $j_c = 5.2 \cdot 10^{11}$ Am^{-2} and $j_c = 2.9 \cdot 10^{11}$ Am^{-2} respectively (figure 5.9 on page 91). When corrected for the thickness, we get $j_c(\text{PLDfilms})/j_c(\text{SPUTfilms}) = 1.31$, which confirms our hypothesis in chapter 5, that sputtered films have indeed a smaller average defect size compared to PLD-films.

In conclusion, the thickness dependence of the current density $j_s(B{=}0)$ is governed by two phenomena. For small thicknesses the effective penetration depth causes a sharp reduction of the pinning strength. For thick films the currents run effectively in a small layer of $\lambda_{eff} \approx 70$ nm at the surface and the film substrate interface. In the 'bulk' of the film vortices are strongly curved, following the magnetic field lines. They could be weakly pinned, for example by point defects, but the 'bulk' currents are probably very small compared to the surface currents. In figure 7.9 we summarize schematically the situation for thin ($d \ll \lambda$) and thick ($d \gg \lambda$) films.
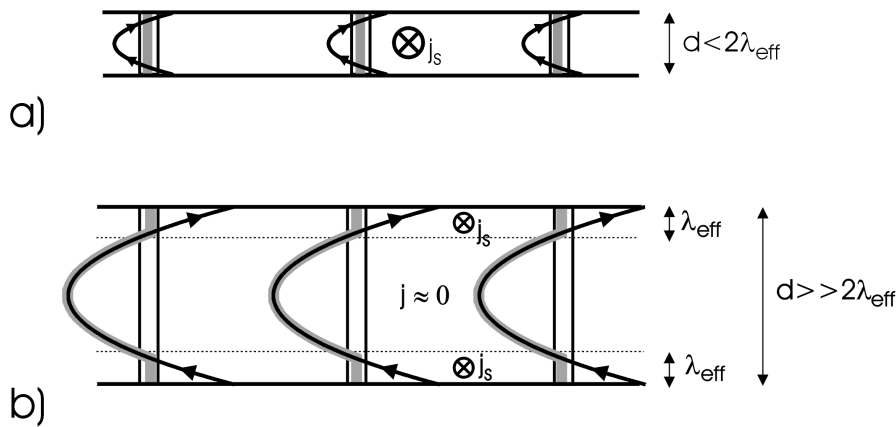
Figure 7.9: Schematic picture of the magnetic field lines (black lines) and the vortices (grey) for a) a very thin film with $d < 2\lambda_{eff}$ and b) a thick film with $d \gg 2\lambda_{eff}$. In a thin film the vortices are straight and do not follow the magnetic field lines. They are pinned over their full length by linear defects. In a thick film the vortices are straight and perpendicular to the surface over a distance $\ell_{scr} \simeq \lambda_{eff}$. Linear defects pin the vortices only in this surface layer. Consequently large superconducting currents run only near the surface. Within the bulk of the film the vortices follow the magnetic field and are weakly pinned ($j_c \approx 0$).

7.5.2 Asymmetric hysteresis loops in thick films

In figure 7.10 the hysteresis curve of the 450 nm thick LP193 is plotted for various temperatures between $T = 4.2$ and 40 K. Whereas in all films we measured, the hysteresis loop is symmetric around $\mu_0 H = 0$ T, in LP193 we find a peculiar peak in the magnetization curve, which is shifted towards *positive* fields when sweeping down in the hysteresis loop. It is therefore different from the usual magnetization peak, which is observed in single crystals *after* the zero-crossing of the hysteresis loop. The magnetization peak is situated at $\mu_0 H = 0.46$ T for $T = 4.2$ K, and decreases with temperature. Note, that the peak position is at much larger magnetic field than the characteristic field $B^* \simeq 35$ mT, which is therefore not observed experimentally, or the penetration field $\mu_0 H_{pen} \simeq 25$ mT.

The dynamical relaxation rate for LP193 is plotted in figure 7.11. Also Q exhibits some unexpected features. The most remarkable feature is a peak in $Q(B)$, situated at $\mu_0 H = 1$ T for $T = 10$ K. With increasing temperature the peak in $Q(B)$ sharpens and shifts to lower field values. The position of the peak seems to be about twice the field, where the central peak in the hysteresis loop is observed. Exactly when the central peak is reached in the hysteresis loop, the relaxation rate becomes independent of magnetic field, at least at low temperatures.
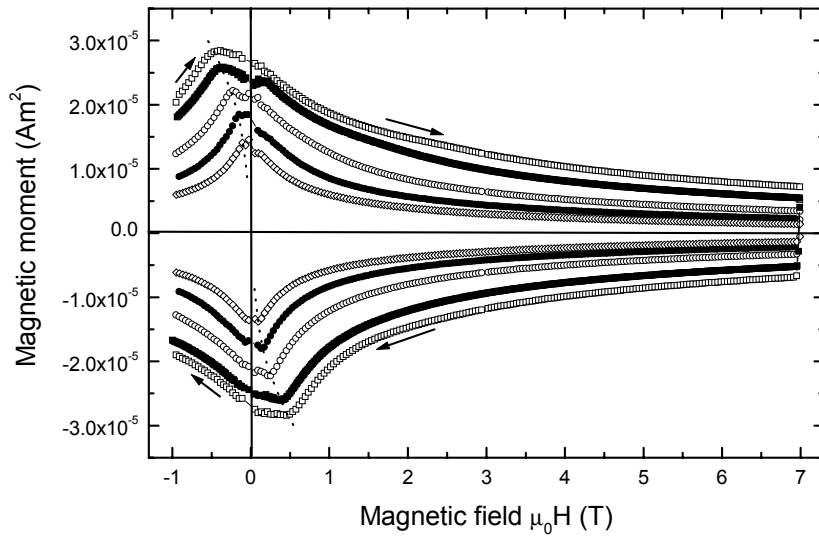
Figure 7.10: Hysteresis loops for film LP193 (d = 450 nm), taken by sweeping from $\mu_0 H = -1 \longleftrightarrow 7$ T with sweep rate $\mu_0 dH/dt = 2.4$ T/min, at temperatures $T = 4.2$ ($-\square-$), 10 ($-\blacksquare-$), 20 ($-\circ-$), 30 ($-\bullet-$), and 40 K ($-\diamondsuit-$). The arrows indicate the sweep direction. We observe a peculiar shift of the central peak *towards* the sweep direction. The dashed lines indicate the position of the central peak at various temperatures.

Both the hysteresis loop and the behaviour of the relaxation rate show, that thicker films exhibit quite different behaviour compared to thin films. This has consequences for the interpretation of the relaxation and current density data. Up to now we used the irreversible torque to determine $j_s(B)$ and $Q(B)$. However, because the magnetization curve is not symmetric in thick films, the current density behaves differently when sweeping the magnetic field up or down. By simply taking the irreversible magnetization to calculate $j_s(B)$ and $Q(B)$, we neglect this asymmetry. In this way we may introduce experimental artifacts, and it is not clear at present how we should interpret, for example, the peak in $Q(B)$.

A similar anomalous peak shift in the magnetization curve has been observed before, although it was not always noticed, in YBa$_2$Cu$_3$O$_{7-\delta}$ single crystals [32], in rotation measurements on Bi$_2$Sr$_2$CaCu$_2$O$_8$ (Bi2212) crystals [33], in polycrystalline Nb$_3$Sn samples [34] and also in Ag-sheathed (Bi,Pb)$_2$Sr$_2$Ca$_2$Cu$_3$O$_{10+\delta}$ (Bi2223) tapes [35, 36, 37]. Usually the anomalous peak shift is, however, much smaller. The variety of samples, techniques and experimental conditions suggest that the effect is rather
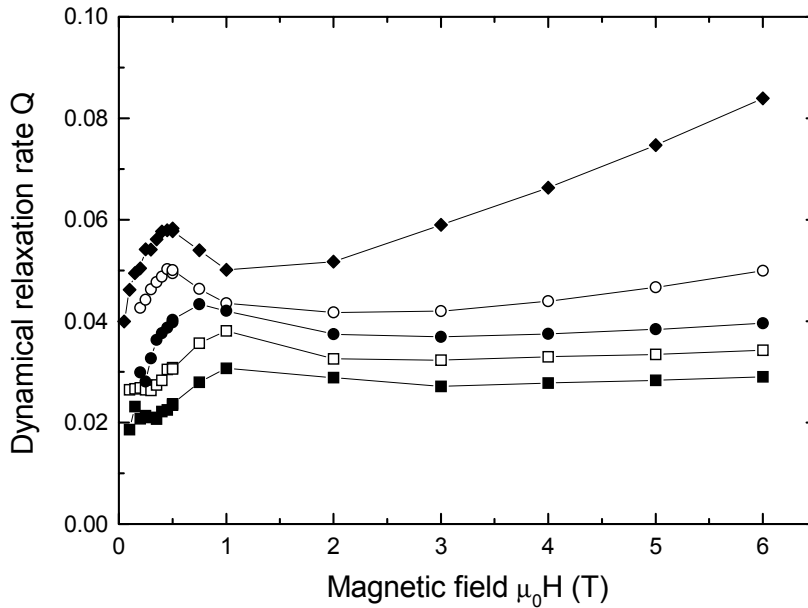
Figure 7.11: Dynamical relaxation rate $Q(B)$ for a thick film (LP193, $d = 450$ nm) for temperatures $T = 10$ ($-\blacksquare-$), 15 ($-\square-$), 20 ($- \bullet -$), 30 ($- \circ -$) and 50 K ($-\blacklozenge-$). An unexpected peak is observed in $Q(B)$, which is shallow at low temperatures, but becomes sharper and shifts to lower field values with increasing temperature. The maximum of the peak is positioned at larger magnetic fields than the central peak in a hysteresis loop, but vortex bending might well be responsible for the increased relaxation rate.

general. Recently, Shantsev *et al.* [38] showed, that for crystalline films the central peak is symmetric around $\mu_0 H = 0$, but for granular samples the central peak may shift towards the positive axis. This was investigated further by Koblischka *et al.* [39] by patterning a film into small circular disks, thereby mimicking granularity. Also Müller *et al.* [35] explained the anomalous peak with the behaviour of *inter-* and *intra*granular critical currents, running in granular samples. Although granularity plays an eminent role in tapes, in our films we have no indication for granularity. The observation, that the central peak shifts, depending on the sample dimensions [34, 40], suggests that shape effects could also be responsible for an anomalous peak shift.

One important ingredient for thick films, which we think may provide for an alternative explanation, is the curvature of the magnetic field lines due to self-fields. In thin films the curvature of the magnetic field does not have implications for vortex pinning, as the vortices are confined to be straight within a layer of thickness near the surface λ_{eff}, which is about 70 nm (see the previous section). But for LP193, with $d = 450$ nm, vortices are definitely bent due to the large current density present. In the next section we investigate how vortex bending affects the hysteresis loop. When sweeping the magnetic field back, i.e. on the decreasing branch of an hysteresis loop, Meissner areas develop in the film as soon as the applied magnetic field becomes comparable to the self-fields created by the current. This was first observed with magneto-optics by Vlasko-Vlasov *et al.* [41]. We show that these so-called Meissner holes can indeed cause the anomalous peak in the magnetization.

7.5.3 Vortex curvature due to self fields

To investigate whether vortex bending can be responsible for the observed peak shift in thicker $YBa_2Cu_3O_{7-\delta}$ films, we first calculate the self-field, taking the film thickness explicitly into account. We consider only the right half of the ring, assuming that we can approximate it by an infinitely long thin strip of width w and thickness d with an applied current density j. This approximation is justified if the ring has a large diameter compared to its width, so that the thin strip represents the cross-section of one side of the ring, and the opposite side has a negligible influence on the self-field at the first leg. The geometry is chosen such that the origin is at the center of the strip, the current density j_y is running in the y-direction, and the magnetic field is applied in the z-direction perpendicular to the film plane. The self field is found by integrating the law of Biot-Savart over the strip:

$$B_x(x,z) \quad = \quad \frac{\mu_0}{2\pi} \int_{-d/2}^{d/2} \int_{-w/2}^{w/2} \frac{j_y(x,z) \cdot (z-z')\, dx'dz'}{(x-x')^2 + (z-z')^2} \tag{7.5}$$

$$B_z(x,z) \quad = \quad \frac{\mu_0}{2\pi} \int_{-d/2}^{d/2} \int_{-w/2}^{w/2} \frac{j_y(x,z) \cdot (x-x')\, dx'dz'}{(x-x')^2 + (z-z')^2} \tag{7.6}$$

For thin films with $d \ll w$ and assuming that $j_s = j_y$ uniform[3], eqs. (7.5) and (7.6) can be simplified appreciably. In this case $B_{self,x}(x,z)$ *within the film* does not depend on the position x, and $B_{self,z}(x,z)$ does not depend on the position z within the film. Therefore we can calculate B_x and B_z, setting $x = 0$ or $z = 0$, respectively, and solve eqs. (7.5) and (7.6) for both components of the self-field analytically. The results are:

---

[3]In chapter 6 we have shown that the current density j_s in ring shaped thin films is indeed uniform to a good approximation.
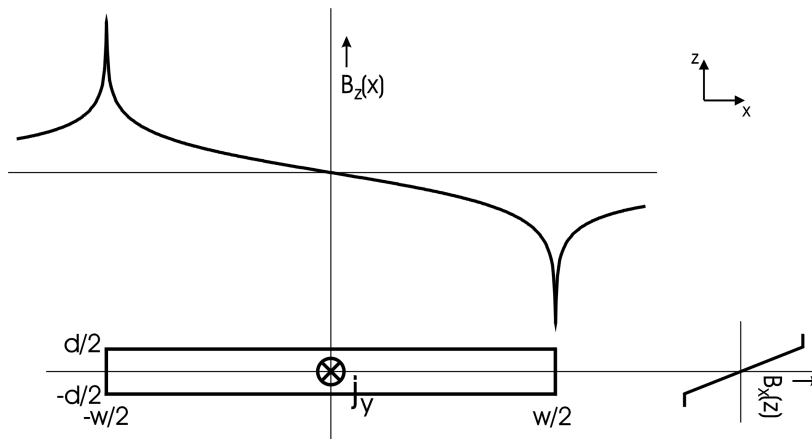
Figure 7.12: Schematic picture of the right half of the ring, depicted as an infinitely long strip. Compared to the original ring geometry, the point $x = -w/2$ represents the inner radius of the ring r_i, whereas $x = w/2$ denotes the outer radius r_o. The self-field components, calculated by integrating the law of Biot-Savart, $B_z(x)$ and $B_x(z)$ are indicated at the top and on the right, respectively.

$$B_z(x) \approx \frac{\mu_0 j_y}{2\pi} \left\{ \sum_{k=0,1} \left(2x + (-1)^k w\right) \left(\arctan \frac{d}{2(-1)^k x + w}\right) + d \ln \left| \frac{2x + w}{-2x + w} \right| \right\}$$

$$\tag{7.7}$$

$$B_x(z) \approx \mu_0 j_y z \tag{7.8}$$

In figure 7.12 a schematic drawing of the geometry of the strip and the self-field components $B_x(z)$ and $B_z(x)$ is given. In fact one can evaluate eqs. (7.5) and (7.6) for any current distribution within the strip numerically.

An externally applied magnetic field $\mu_0 H_z$ adds directly to $B_z(x)$, shifting the whole field profile upwards or downward, depending on the size of $\mu_0 H_z$, if j_y does not depend on B. The lateral field $B_x(z)$ is of course not affected by an applied field in the z-direction.

Next we look closely at the experimental situation when the hysteresis loop approaches the anomalous peak. When starting from a large positive field and lowering the applied magnetic field, the self-field profile, drawn schematically in figure 7.12, is lowered as the applied magnetic field decreases. To simplify the calculation, we assume, that the current density does not depend on magnetic field. In figure 7.13 we show three consecutive field profiles, and the corresponding field lines *within* the film, when the
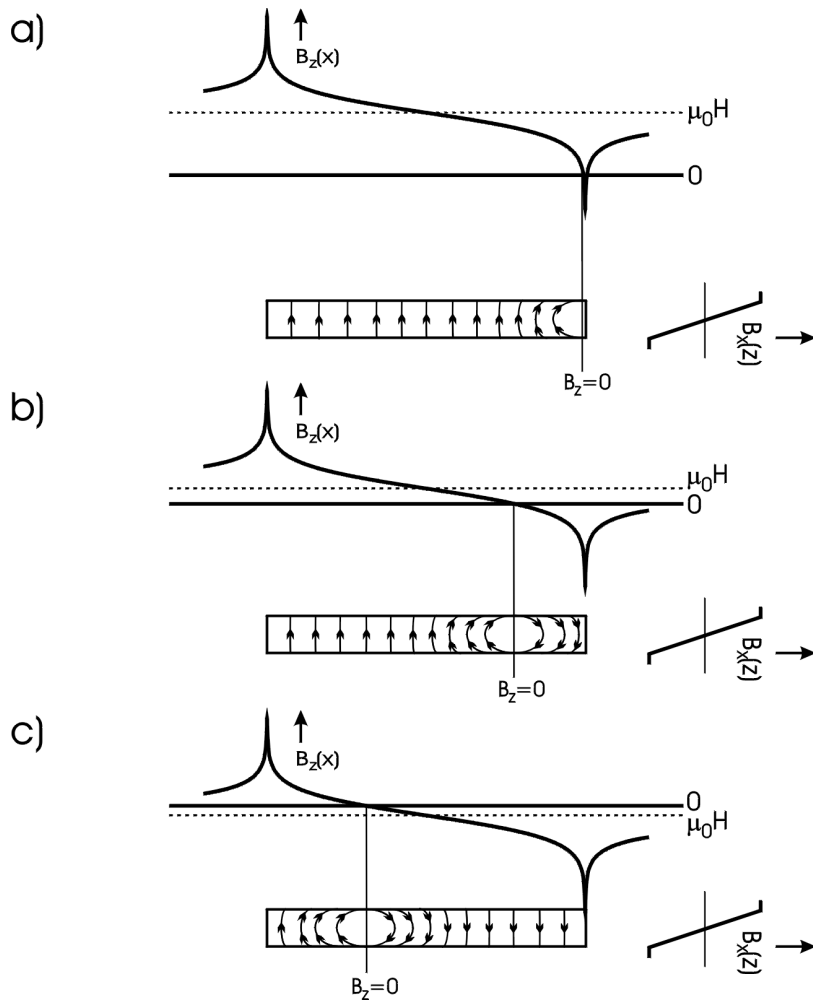
Figure 7.13: Schematic picture about how a Meissner hole is formed in thin films. We show only the right half of the ring. The magnetic field is swept back from a large magnetic field. a) At a positive applied magnetic field $\mu_0 H = B_{z,\mathrm{max}}$ the tail of the self-field reaches zero induction $B_z = 0$ at the outer edge of the ring. The magnetic field lines curve strongly and a Meissner area is formed. b) As the applied magnetic field is lowered the point with $B_z = 0$ moves to the left. Consequently the Meissner hole moves in from the edge. c) At slightly negative magnetic fields the Meissner hole has crossed more than half the width of the ring. Eventually it will cross the whole width, and disappear for negative fields $\mu_0 H < -B_{z,\mathrm{max}}$.
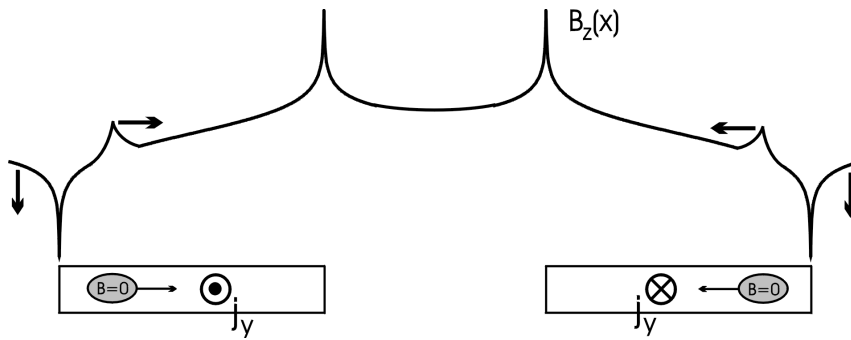
Figure 7.14: Full cross section of the ring with the $B_z(x)$ field profile. The excess current in the Meissner hole (grey) results in a peak in the magnetization, which moves inwards, as the Meissner hole itself. This causes the anomalous peak in the hysteresis loop.

magnetic field is lowered to $\mu_0 H_z \lesssim 0$. When the large tail of $B_z(x)$ crosses $B = 0$, a Meissner area forms on the edge of the superconductor (figure 7.13a).

To illustrate what happens we turn to figure 7.13b, where the Meissner area has moved in already, which makes the explanation more transparent. Exactly where $B_{z,tot} = 0$, the magnetic field has only an x-component. Slightly to the left the $B_{z,tot}$ is positive, but much smaller than $B_x(z)$, and slightly to the right $B_{z,tot}$ is negative and much smaller than $B_x(z)$. The resulting field lines point in opposite directions almost perpendicularly to the c-axis, leaving a flux free area in the middle. This so-called Meissner hole was observed already by Vlasko-Vlasov *et al.* [41]. Note that figure 7.13 shows only half of the ring.

In figure 7.14 a cross section of the ring is depicted schematically, indicating how the Meissner hole moves inwards as the applied magnetic field is lowered. The Meissner hole carries an excess screening current $j_M > j_s$ [41]. Therefore the total magnetic moment is larger due to the Meissner hole than calculated by pure electrodynamic considerations. Since the Meissner hole moves inwards from both sides of the ring (figure 7.14) the total magnetic moment is largest as soon as the self-field tail reaches $B_z = 0$, i.e. when the Meissner hole forms at the outer edge of the sample (figure 7.13a). As the Meissner hole moves inwards, the magnetic moment decreases. Thus in a hysteresis loop we find a maximum in the magnetic moment when the tail of the self-field profile reaches $B_z = 0$.

From this qualitative discussion it follows, that the magnetic moment is maximum, when the applied magnetic field is as large as the tail of the self-field. Eq. (7.7), with $j_y = 1.12 \cdot 10^{11}$ Am^{-2} as in film LP193, yields for the maximum self-field at the tail $B_{\mathrm{max}} = 0.08$ T. This is too small to explain a central peak, shifted to $\mu_0 H = 0.46$ T. However, one should realize that vortex bending sets in already before the tail of the self-field reaches $B_z = 0$. Moreover, the formation of the Meissner hole itself is a very unstable process. Since the curvature of the field lines depends on the current density,

an increased current, due to the Meissner hole, curves the magnetic field lines even more and blows up the Meissner hole. This can eventually lead to avalanches, which have indeed been observed [42]. The size of the Meissner hole can be calculated by comparing the line tension with the pinning energy [43]. If the line tension is larger than the pinning force, the vortex loop collapses towards the middle, which leads to a critical diameter $D_M \simeq 2\varepsilon_l/\Phi_0 j_s$ [41]. With the line tension $\varepsilon_l = 0.2\varepsilon_0$ and $j_c = 1 \cdot 10^{11}$ Am^{-2}, we get $D_M \approx 26$ nm, which is smaller than the current free layer, given by $D_{j=0} = d - 2\lambda_{eff} \approx 310$ nm. However, from a simple thermodynamic argument, i.e. $\int Bd\ell = \mu_0 \int jdA$, the current density needed to shield a magnetic field $\mu_0 H = 0.46$ T, taking $D_M = D_{j=0} = 310$ nm as critical diameter, is $j_M \approx 5 \cdot 10^{12}$ $Am^{-2} \approx j_0$, the depairing current (with the film thickness as critical diameter $D_M = 450$ nm, we find $j_M \approx 3 \cdot 10^{12}$ Am^{-2}). This suggests that the Meissner hole is formed as soon as the depairing current is able to completely screen the applied magnetic field.

Note, that kink sliding, as described by Indenbom *et al.* [8] leads to the formation of Meissner holes as well. The curved vortices experience a Lorentz force, directed towards the midplane of the ring $z = 0$ (see figure 7.9b). Therefore, if the pinning energy is not sufficient, easy kink sliding makes the vortex loops collapse towards the middle, leaving a similar Meissner hole as we described.

Note, that in ref. [8] the applied magnetic field was applied under an angle. The Lorentz force in that case is directed in one direction only, and the vortices do not collapse, but just slide off the sample via easy kink sliding.

We conclude that the formation of Meissner holes is a possible scenario, which could explain the anomalous shift of the central peak. However, the explanation is very preliminary, and further research is needed to clarify why the peak shifts to such large magnetic fields.

7.6 Conclusions

In this last chapter we explored the influence of post-annealing and film thickness on the pinning properties of $YBa_2Cu_3O_{7-\delta}$ films. Post-annealing flattens the surface and improves the crystallinity. This makes post-annealing a convenient technique to study the effect of various pinning mechanisms. In *thin* films thickness modulations and point defects play a negligible role, whereas our results are completely consistent with linear defect pinning, also at high magnetic fields. The thickness dependence of the zero-field current density can be explained by two effects: at very small thicknesses the effective vortex diameter widens, which reduces the pinning energy and, consequently, the critical current. Beyond a critical thickness $d \simeq 100$ nm the current density again decreases, because the currents are confined to a small layer near the surface and the substrate-film interface. Linear defects only pin the vortices near the surface. In the 'bulk' of the film they disconnect from the linear defects and are curved to coincide with the magnetic field lines.

In thicker $(d = 450$ nm) films the magnetization curve becomes asymmetric and develops a peak, shifted to positive magnetic fields on the decreasing branch of the hysteresis loop. A similar anomalous peak has been interpreted to be the result of

granularity [35, 38, 39]. We propose an alternative explanation involving the formation of Meissner holes in the ring due to large self-fields. Because vortex bending can be substantial in thicker films, one should be very cautious with the interpretation of current and relaxation data on films with $d \gg 2\lambda_{eff} = 150$ nm. For example, the relaxation data $Q(B)$ show a peak at $\mu_0 H = 1$ T at low temperatures, which could be related to vortex bending, but which could also be an experimental artifact caused by the asymmetry of the torque loop. On the other hand, the Meissner hole itself is an interesting subject of investigation in thick $YBa_2Cu_3O_{7-\delta}$ films. With magneto-optical imaging one should be able to observe Meissner holes directly, just like in single crystals [41]. The instability of Meissner holes could lead to avalanches and flux roughening. We have performed a preliminary magneto-optical measurement, which indeed revealed flux roughening at low temperatures in LP193 [44]. Finally, a post-anneal treatment, which reduces the thickness modulations, on thicker films should affect the surface currents running in thick films, and this could be used to study vortex bending in more detail.

References

[1]   B. Dam, J.M. Huijbregtse, F.C. Klaassen R.C.F. van der Geest, G. Doornbos, J.H. Rector, A.M. Testa, S. Freisem, J.C. Martínez, B. Stäuble-Pümpin, and R. Griessen, Nature **399**, 439 (1999), and chapter 3 of this thesis

[2]   M. Hawley, I.D. Raistrick, J.G. Beery, and R.J. Houlton, Science **251**, 1587 (1991)

[3]   M. McElfresh, T.G. Miller, D.M. Schaiffer, R. Reifenberger, R.E. Muenchenhausen, M. Hawley, S.R. Foltyn, and X.D. Wu, J. Appl. Phys. **71**, 5099 (1992)

[4]   P.H. Kes, in E. Kaldis (ed.), *Materials and Crystallographic Aspects of HTc-Superconductivity*, Kluwer Academic Publishers, 401 (1994)

[5]   Ch. Jooss, A. Forkl, R. Warthmann, H.-U. Habermeier, B. Leibold, and H. Kronmüller, Physica C **266**, 235 (1996)

[6]   Ch. Jooss, A. Forkl, and H. Kronmüller, Physica C **268**, 87 (1996)

[7]   E. Sheriff, R. Prozorov, Y. Yeshurun, A. Shaulov, G. Koren, C. Chabaud-Villard, J. Appl. Phys. **82**, 4417 (1997)

[8]   M.V. Indenbom, C.J. van der Beek, M. Konczykowski, and F. Holtzberg, Phys. Rev. Lett. **84**, 1792 (2000)

[9]   E.H. Brandt, Phys. Rev. B **48**, 6699 (1993)

[10]   B. Dam, J.H. Rector, J.M. Huijbregtse, and R. Griessen, Physica C **305**, 1 (1998)

[11]   J.M. Huijbregtse, B. Dam, J.H. Rector, and R. Griessen, J. Appl. Phys. **86**, 6528 (1999)

[12]   M. Pannetier, F.C. Klaassen, R.J. Wijngaarden, M. Welling, K. Heeck, J.M. Huijbregtse, B. Dam, and R. Griessen, Phys. Rev. B **64**, 144505, and chapter 6 of this thesis

[13]   M. Qvarford, K. Heeck, J.G. Lensink, R.J. Wijngaarden and R. Griessen, Rev. Sci. Instrum. **63**, 5726 (1992)

[14]   J.M. Huijbregtse, B. Dam, R.C.F. van der Geest, F.C. Klaassen, R. Elberse, J.H. Rector, and R. Griessen, Phys. Rev. B **62**, 1338 (2000)

[15]   J.M. Huijbregtse, *Growth, Defect Structure and Critical Currents in $YBa_2Cu_3O_{7-\delta}$ Thin Films*, PhD thesis, Vrije Universiteit, Chapter 4

[16]   H. Huhtinen, E. Lähderanta, and P. Paturi, J. Low Temp. Phys. **117**, 795 (1999)

[17]   L.J. Schwartzendruber, D.L. Kaiser, F.W. Gayle, L.H. Bennet, and A. Roytburd, Appl. Phys. Lett. **58**, 1566 (1991)

[18]   E. Mezzetti, R. Gerbaldo, G. Ghigo, L. Gozzelino, B. Minetti, C. Camerlingo, A. Monaco, G. Cuttone, and A. Rovelli, Phys. Rev. B **60**, 7623 (1999)

[19]   G. Doornbos, B. Dam, J.C. Martínez, R. Surdeanu, U. Poppe, and R. Griessen, Physica C **282-287**, 2303 (1997)

[20] F.C. Klaassen, G. Doornbos, J.M. Huijbregtse, R.C.F. van der Geest, B. Dam, and R. Griessen, Phys. Rev. B **64**, 184523 (2001), and chapter 5 of this thesis

[21] T.L. Hylton and M.R. Beasley, Phys. Rev. B **41**, 11669 (1990)

[22] G. Blatter, M.V. Feigel'man, V.B. Geshkenbein, A.I. Larkin and V.M. Vinokur, Rev. Mod. Phys. **66**, 1125 (1994)

[23] H. Douwes, P.H. Kes, Ch. Gerber, and J. Mannhart, Cryogenics **33**, 486 (1993)

[24] M. Murakami, M. Morita, K. Doi, and K. Miyamoto, Jap. J. Appl. Phys. **28**, 1189 (1989)

[25] B. Martínez, X. Obradors, A. Gou, V. Gomis, S. Piñol, J. Fontcuberta, H. van Tol, Phys. Rev. B **53**, 2797 (1996),
B. Martínez, F. Sandiamenge, T. Puig, X. Obradors, L. Richard, and J. Rabier, Appl. Phys. Lett. **74**, 73 (1999)

[26] A. Catana, R.F. Broom, J.G. Bednorz, J. Mannhart, and D.G. Schlom, Appl. Phys. Lett. **60**, 1016 (1992)

[27] Chang Jun Liu and Claire Schlenker, Phys. Rev. B **48**, 13911 (1993)

[28] L. Civale, T.K. Worthington, and A. Gupta, Phys. Rev. B **43**, 5425 (1991)

[29] J. Pearl, Appl. Phys. Lett **5**, 65 (1964)

[30] D.Yu. Irz, V.N. Ryzhov, and E.E. Tareyeva, Physics Letters A **207**, 374 (1995)

[31] R. Prozorov, E.B. Sonin, E. Sheriff, A. Shaulov, and Y. Yeshurun, Phys. Rev. B **57**, 13845 (1998)

[32] M. Oussena, P.A.J. de Groot, R. Gagnon, and L. Taillefer, Phys. Rev. B **49**, 9222 (1994)

[33] H.G. Schnack, R. Griessen, P. Noordeloos, K. Heeck, Physica C **266**, 285 (1996)

[34] M. Däumling and W. Goldacker, Z. Phys. B **102**, 331 (1997)

[35] K.-H. Müller, C. Andrikidis, H.K. Liu, and S.X. Dou, Phys. Rev. B **50**, 10218 (1994),
K.-H. Müller, C. Andrikidis, and Y.C. Guo, Phys. Rev. B **55**, 630 (1997)

[36] M.R. Cimberle, C. Ferdeghini, R. Flükiger, E. Giannini, G. Grasso, D. Marrè, M. Putti, and A.S. Siri, Physica C **251**, 61 (1995)

[37] M.R. Koblischka, L. Půst, A. Galkin, and P. Nálevka, Appl. Phys. Lett. **70**, 514 (1997),
M.R. Koblischka, T.H. Johansen, H. Bratsberg, L. Půst, A. Galkin, P. Nálevka, M. Maryško, M. Jirsa, M. Bentzon, P. Bodin, P. Vase, and T. Freltoft, J. Appl. Phys. **83**, 6798 (1998)

[38] D.V. Shantsev, M.R. Koblischka, Y.M. Galperin, T.H. Johansen, L. Půst, and M. Jirsa, Phys. Rev. Lett. **82**, 2947 (1999)

[39] M.R. Koblischka, L. Půst, A. Galkin, and P. Nálevka, M. Jirsa, T.H. Johansen, H. Bratsberg, B. Nilsson, and T. Claeson, Phys. Rev. B **59**, 12114 (1999),

M.R. Koblischka, L. Půst, M. Jirsa, and T.H. Johansen, Physica C **320**, 101 (1999)

[40]   M. Däumling, E. Walker, and R. Flükiger, Phys. Rev. B **50**, 13024 (1994)

[41]   V.K. Vlasko-Vlasov, U. Welp, G.W. Crabtree, D. Gunter, V. Kabanov, and V.I. Nikitenko, Phys. Rev. B **56**, 5622 (1997)

[42]   V.K. Vlasko-Vlasov, U. Welp, G.W. Crabtree, D. Gunter, V.V. Kabanov, V.I. Nikitenko, and L.M. Paulius, Phys. Rev. B **58**, 3446 (1998)

[43]   A.M. Campbell and J.E. Evetts, *Critical Currents in Superconductors*, Taylor & Francis London, 1972

[44]   F.C. Klaassen, M.T. Pannetier, M. Welling, and R.J. Wijngaarden, unpublished

Samenvatting: zijn supergeleiders super geleiders?

Inleiding

Supergeleiders zijn materialen waarvan de electrische weerstand verdwijnt beneden een kritische temperatuur T_c. Door deze eigenschap zijn supergeleiders zeer interessant voor toepassingen, aangezien electrische weerstand voor ongewenste (warmte)verliezen zorgt, bijvoorbeeld in electriciteitskabels en electromagneten. Veel materialen vertonen supergeleiding, maar de kritische temperaturen zijn zeer laag (tot 1986 lag het record bij $T_c = 23$ K $= -250°$C), waardoor supergeleiders maar beperkt worden toegepast. De ontdekking in 1986 van supergeleiding in bepaalde keramische materialen was een belangrijke stap vooruit. De kritische temperatuur in deze materialen is veel hoger dan in conventionele supergeleiders, met als huidige record $T_c = -137°$C. Dit lijkt nog steeds erg laag, maar zulke temperaturen kunnen eenvoudig bereikt worden door te koelen met vloeibare stikstof ($-196°$C), waarmee de nieuwe klasse van supergeleiders (die hoge-T_c supergeleiders worden genoemd) op goedkope(re) wijze kan worden toegepast. Inmiddels zijn de eerste grootschalige toepassingen geïmplementeerd. Zo liggen in Detroit (VS) electrische stroomkabels in de grond die gemaakt zijn van hoge-T_c supergeleiders.

Het spreekt voor zich, dat er veel wetenschappelijk onderzoek wordt verricht naar de hoge-T_c supergeleiders. Een essentiële parameter die de kwaliteit van een supergeleider aangeeft, althans voor toepassingen, is de kritische stroom. Dit is de maximale stroom die weerstandsloos (i.e. zonder verliezen) door een supergeleider kan stromen. Met andere woorden, de grootte van de kritische stroom bepaalt of een supergeleider ook een super geleider is. De kritische stroom hangt af van het soort en de kwaliteit van het materiaal, van de temperatuur en van het aangelegde magneetveld.

In mijn promotie-onderzoek heb ik de eigenschappen onderzocht van de kritische stroom van $YBa_2Cu_3O_{7-\delta}$ (yttrium-barium-koperoxyde), een van de bekendste hoge-T_c supergeleiders met $T_c = -181°$C. Specifiek heb ik dunne lagen van $YBa_2Cu_3O_{7-\delta}$, met een dikte van ongeveer 0.1 μm (een μm is een duizendste millimeter) onderzocht. De reden voor deze keuze is, dat dunne $YBa_2Cu_3O_{7-\delta}$ lagen een heel hoge stroom kunnen dragen.

Tijdens mijn onderzoek heb ik mij onder andere bezig gehouden met de volgende vragen:

- Waardoor wordt de hoogte van de kritische stroom in dunne $YBa_2Cu_3O_{7-\delta}$ lagen bepaald?

- Wat is de invloed van belangrijke parameters als de temperatuur en magneetveld op de kritische stroom?

- Hoe kan men met onze inzichten de kritische stroom verhogen?

In deze samenvatting zal ik, na een algemene uiteenzetting van de magnetische eigenschappen van supergeleiders, deze drie vragen achtereenvolgens behandelen.

Supergeleiding en magneetveld, een haat-liefde verhouding

Naast het feit, dat er geen electrische weerstand is, is er een tweede, minstens zo belangrijke eigenschap van supergeleiders: een supergeleider kan geen magneetveld verdragen. Dit zogenaamde Meissner effect heeft vergaande implicaties. Immers, in een extern aangelegd magneetveld moet een supergeleider zijn inwendige "magneetveldvrij" houden. Dit kan op twee manieren. Allereerst door volledige afscherming: in de supergeleider gaan stromen lopen die precies een tegengesteld magneetveld als het aangelegde genereren, zodat het totale magneetveld nul blijft binnen in het materiaal. In het tweede geval dringt het aangelegde magneetveld toch gedeeltelijk door de supergeleider heen. In het supergeleidende materiaal ontstaan cylindrische buisjes van niet-supergeleidend materiaal, waar de magnetische flux doorheen gaat. Deze flux buisjes noemen we vortices. Een electrische stroom loopt door het supergeleidende gedeelte langs de vortices, en ondervindt dus nog steeds geen weerstand. Het magneetveld wordt door de vortices (van normaal materiaal) geleid en heeft geen last van de supergeleidende fase ernaast. Elke vortex heeft een vaste hoeveelheid magnetische flux, dus hoe hoger het aangelegde magneetveldveld, hoe meer vortices er in het materiaal aanwezig zijn.

De gemengde fase met vortices is dus een perfecte compromis-oplossing, waarbij supergeleiding en magneetvelden toch samen kunnen gaan: het poldermodel in optima forma. Dankzij het bereikte compromis kunnen veel hogere magneetvelden en hogere stromen aangelegd worden dan in het geval van volledige afscherming.

Er doet zich echter nog een probleempje voor zodra een stroom door een supergeleider in de gemengde fase wordt gestuurd. Aangezien vortices een zekere magnetische flux hebben, werkt er in de aanwezigheid van een stroom een Lorentz-kracht[4] op de vortex, die haar in beweging zet. Aangezien de vortex een verstoorde supergeleidende fase heeft, zorgt een bewegende vortex voor een weerstand: weg super geleiding!

De enige manier om toch een eindige stroom zonder dissipatie door een supergeleider te leiden, is door de vortex op een of andere manier vast te pinnen op haar plaats. In het algemeen bieden materialen de mogelijkheid tot vortex pinning via altijd aanwezige roosterfouten. Een materiaal is nooit helemaal perfect opgebouwd, en op de plaats van

---

[4]De Lorentz-kracht is de kracht die een bewegende lading in een magneetveld ondervindt.

een roosterfout (bijvoorbeeld een vreemd of ontbrekend atoom in de kristalstructuur, of een vlak dat niet goed aansluit) kan een vortex gepind worden. De kritische stroom wordt nu bepaald door de maximale pinning kracht, die natuurlijk direct afhangt van het soort materiaaldefect.

Om een goede verklaring te geven voor de grootte van de kritische stroom in supergeleiders, moeten we dus bepalen hoe en door welk defect vortices gepind worden. Omdat in een materiaal altijd vele soorten defecten aanwezig zijn, die elk op verschillende wijze een vortex kunnen pinnen, is het bepalen van de belangrijkste bron van vortex pinning geen eenvoudige opgave. Hiervoor moet men een eenduidig verband aangeven tussen de aanwezige defecten en het gedrag van de kritische stroom.

Waardoor wordt de hoge kritische stroom in dunne $YBa_2Cu_3O_{7-\delta}$ lagen bepaald?

De belangrijkste defecten voor vortex pinning in dunne $YBa_2Cu_3O_{7-\delta}$ lagen blijken zogenaamde lineaire defecten te zijn. Het aantal lineaire defecten kunnen we meten door de dunne $YBa_2Cu_3O_{7-\delta}$ laagjes te etsen, dat wil zeggen, langzaam op te lossen, in een oplossing van 1% broom in ethanol. Doordat chemisch etsen sneller verloopt op plaatsen waar lineaire defecten aan het oppervlak komen, worden alle lijndefecten zichtbaar als vierkante putjes (zie figuur 3.1 op pagina 30). Door het ets-proces te volgen tot aan substraat waarop de film is gedeponeerd, kunnen we een diepteprofiel maken van de lijndefecten, en ook kunnen we bepalen waar de lijndefecten zich bevinden ten opzichte van het originele oppervlak. Uit de resultaten blijkt:

- De lijndefecten zitten in valleien tussen de eilanden die het oppervlak van de dunne $YBa_2Cu_3O_{7-\delta}$ lagen kenmerken.

- De lijndefecten lopen vanaf het substraat verticaal (parallel aan de c-as) door de hele film tot aan het oppervlak.

Door deze nauwkeurige karakterisatie van de defectstructuur kunnen we een directe koppeling maken met de supergeleidende eigenschappen, en in het bijzonder met de kritische stroom. In figuur 3.4 op pagina 34 is de kritische stroom als functie van het magneetveld weergegeven van drie films met verschillende lijndefect-dichtheden. We zien bij lage velden dat de kritische stroom constant is tot een karakteristiek veld B^*. Het plateau wordt groter naarmate het aantal lijndefecten in een film groter is. Voor verschillende films krijgen we een lineair verband tussen n_{disl} en B^* (figuur 3.5a op pagina 35). Er is dus een directe relatie tussen de defect-structuur en de kritische stroom van dunne $YBa_2Cu_3O_{7-\delta}$ lagen, wat aangeeft dat lijndefecten inderdaad de belangrijkste bron van pinning zijn.

We hebben het volgende model. Bij een laag magneetveld zijn er minder vortices in de supergeleider dan lijndefecten. Alle vortices zijn dus optimaal vastgepind door een lijndefect. Als het magneetveld verhoogt wordt, komen er meer vortices. Elke extra vortex gaat in een leeg defect zitten en is tevens sterk gepind. Dit geeft een constante

kritische stroom, totdat natuurlijk alle lijndefecten opgevuld zijn met vortices. Als
dan het magneetveld verhoogd wordt, kunnen de extra vortices niet meer optimaal
gepind worden, en gaat de kritische stroom omlaag. Uiteraard, hoe meer defecten,
hoe meer vortices sterk gepind kunnen worden, en hoe groter het plateau.

Wat is de invloed van de temperatuur?

Het zojuist besproken pinning mechanisme is zeer effectief bij lage temperaturen
en lage magneetvelden. In het algemeen worden hogere temperaturen gebruikt in
toepassingen (zodat bijvoorbeeld minder hard gekoeld hoeft te worden). Daarom
hebben we uitgerekend hoe de kritische stroom van de temperatuur afhangt.

De invloed van temperatuur kan heel precies bepaald worden door een beschrijving
van de zogenaamde pinning potentiaal. Deze geeft de pinning energie aan voor elke
positie van een vortex ten opzichte van een lijndefect. In figuur 4.2 op pagina 57
is de pinning potentiaal in een grafiek weergegeven. Uiteraard is de pinning het
sterkst als de vortex in het midden van het defect zit (de pinning potentiaal is het
diepst voor $R = 0$). Naar de randen toe wordt de pinning minder efficiënt, wat de
karakteristieke vorm geeft als weergegeven in figuur 4.2. De maximale helling geeft
precies de maximale pinning kracht op een vortex, en is dus evenredig met de kritische
stroom.

De pinning potentiaal is sterk temperatuur-afhankelijk. Drie belangrijke effecten spe-
len een rol:

- De grootte en de energie van een vortex hangt af van de temperatuur. Dit
  kunnen we uitrekenen door voor elke temperatuur de pinning potentiaal te
  berekenen.

- De thermische beweging van vortices zorgt ervoor, dat de gemeten kritische
  stroom lager is dan de theoretische kritische stroom. Door de thermische ac-
  tivering te meten kunnen we voor dit effect corrigeren.

- Een gepinde vortex is gelocaliseerd en heeft daardoor minder bewegingsvrijheid.
  Dit zorgt voor een effectief minder diepe pinning-potentiaal doordat de entropie
  (de wanorde) van het systeem lager is. In het geval van $YBa_2Cu_3O_{7-\delta}$ is dit
  effect relatief klein.

Wat is de invloed van magneetveld?

Bij laag magneetveld worden de lijndefecten één voor één bezet door vortices. Als alle
defecten bezet zijn, worden de extra vortices minder goed gepind. Als gevolg hiervan
neemt de kritische stroom af bij hoge magneetvelden. Er blijken twee scenario's te
zijn. In dunne lagen met weinig defecten is het plateau klein, maar de kritische
stroom neemt niet zo sterk af bij grotere magneetvelden. In dunne lagen met veel
lijndefecten, is er weliswaar een groot plateau, maar de stroom neemt ook sneller af bij
hoge magneetvelden. Welke van de twee uiteindelijk de hoogste stroom heeft, hangt
dus sterk af van het magneetveld waarbij, en is niet op voorhand te zeggen.

Hoe kan men de kritische stroom optimaliseren?

Dit is natuurlijk de hamvraag. Ruwweg kan men twee dingen proberen. Allereerst kan men proberen *meer* defecten te creëren in het materiaal, of men kan kijken of *grotere* defecten vortices beter pinnen. Wat betreft meer defecten hebben we al gezien, toen we de invloed van het magneetveld bespraken, dat het niet eenduidig is of de kritische stroom inderdaad hoger wordt. Dit hangt geheel af van de toepassing, en bij welk magneetveld het geheel moet functioneren. Voor wat betreft grotere defecten moeten we naar de temperatuur-afhankelijkheid kijken. De temperatuur-afhankelijkheid is namelijk zeer gevoelig voor de grootte van het defect. Bij lage temperaturen maakt het weinig verschil of je een groot of een klein defect hebt, maar bij hogere temperaturen kunnen grotere defecten veel beter pinnen. Dit komt omdat de vortex zelf ook groter wordt, en minder goed past in de kleine defecten, maar nog wel in de grote. Wil men dus een hogere kritische stroom, en echte super geleiding, dan is het groter maken van de defecten dé oplossing.

Dankwoord

Nu ik terugkijk op een toch redelijk lang promotie-onderzoek, met leuke momenten, maar ook met hobbels, kan ik niet anders constateren dan dat ik veel steun van vele kanten heb gehad. Voor allen mijn oprechte dank, ook als ik u niet met name noem. Allereerst Ronald, dank voor de mooie jaren in jouw groep. Het is een voorrecht om bij jou te promoveren, aangezien wetenschap en sfeer in een goede mix aanwezig zijn. Je aanname-beleid mag er wezen. Jouw enthousiasme voor de fysica werkt heel inspirerend. Ik hoop toch wel dat je je realiseert, dat met mij de torsiemetrie definitief het loodje legt.

Bernard, jij bent een superbegeleider. Ik heb bijzonder veel van je geleerd en niet alleen materiaalkunde. Vooral ook kon ik altijd op je bouwen, als het weer eens tegen zat, of als er nieuwe input moest komen. Zonde, dat ik waarschijnlijk je laatste oxyde-OiO zal blijken te zijn.
Zonder Jeroen, mijn promotie-maatje, was ik waarschijnlijk nergens geweest. Dankzij jouw conscientieuze aanpak van de materiaalkunde en de hoge kwaliteit van de films. Je merkte terecht op in je proefschrift dat de combinatie tussen ons perfect gewerkt heeft. Ik ben je bijzonder veel dank verschuldigd.

De magneto-optica is bij mij in hoofdstuk 6 vertegenwoordigd. Voor de eerste stappen op het gebied van de magneto-optica moet ik Radu de schuld geven. Myriam, you are a great companian, and we had succes in science as well. Thank you for your nice company and scientific support. Rinke als de grote magneto-optica man en van hele nuttige simulaties. Het is en blijft verhelderend om te zien hoever je met Maxwell ingewikkelde fysica kunt nabootsen.

De technische ondersteuning was altijd in veilige handen bij de heren Koeman, Heeck en Rector, en het ging met een gezonde dosis nuchterheid en gezelligheid, en een biertje natuurlijk, of niet, Nico? Gerrie bedankt voor alle organisatorische ondersteuning.

Een inspirerende en ook gezellige bezigheid was het begeleiden van studenten. Ik heb het genoegen gehad om. Ronny en Remco wat meer zijdelings, full-time met Chris, Aneta en Agnieszka. Thank you for your help and assistance.

Ik heb het voorrecht gehad om ruim vijf jaar in een heel gezellige en inspirerende sfeer te mogen vertoeven. Vele AiO's, OiO's, Post-Docs, gasten en studenten kwamen voorbij, wat altijd veel dynamiek gaf. Dank u allen.

Mijn ouders en Ginie waren er altijd met hun onvoorwaardelijke steun. Anja en Nikolai, dank voor jullie grote geduld, en de vreugde die jullie me geven! Zonder mijn familie was ik nergens.

List of publications

B.J. Feenstra, F.C. Klaassen, D. van der Marel, Z.H. Barber, R. Pérez Pinaya, and M. Decroux, *Characterization of superconducting thin films using mm-wave transmission*, in:
M.N. Afsar (ed.), Proceedings of the International Conference on Millimeter and Submillimeter Waves and Applications III
SPIE **2842**, 480 (1996)

B.J. Feenstra, F.C. Klaassen, D. van der Marel, Z.H. Barber, R. Pérez Pinaya, and M. Decroux, *Penetration depth and conductivity of NbN and $DyBa_2Cu_3O_{7-\delta}$ thin films measured by mm-wave transmission*
Physica C **278**, 213-222 (1997)

J.M. Huijbregtse, B. Dam, F.C. Klaassen, G. Doornbos, R. Van Der Geest, R. Elberse, and R. Griessen, *Strong pinning mechanisms in pulsed laser deposited $YBa_2Cu_3O_{7-\delta}$ films*, in:
P. Vincenzini (ed.), *Science and Engineering of HTC superconductivity*
Techna Srl, Faenza, Advances in Science and Technology **23**, 617-624 (1999)

F.C. Klaassen, J.M. Huijbregtse, B. Dam, R. van der Geest, G. Doornbos, J.H. Rector, R. Elberse, and R. Griessen, *Strong pinning mechanisms in high-T_c superconducting $YBa_2Cu_3O_{7-\delta}$ thin films*, in:
R. Kossowsky *et al.* (eds.), *Physics and Materials Science of Vortex States, Flux Pinning and Dynamics*
Kluwer Academic Publishers, Nato Science Series E **356**, 331-343 (1999)

B. Dam, J.M. Huijbregtse, F.C. Klaassen, R.C.F. van der Geest, G. Doornbos, J.H. Rector, A.M. Testa, S. Freisem, J.C. Martínez, B. Stäuble-Pümpin, and R. Griessen, *Origin of high critical currents in $YBa_2Cu_3O_{7-\delta}$ superconducting thin films*
Nature **399**, 439-442 (1999)

B. Dam, J.M. Huijbregtse, F.C. Klaassen, R.C.F. van der Geest, G. Doornbos, J.H. Rector, en R. Griessen, *Oorsprong van de hoge kritische stromen*
Nederlands Tijdschrift voor Natuurkunde **65**, 230-231 (1999)

J.M. Huijbregtse, F.C. Klaassen, R.C.F. van der Geest, B. Dam, and R. Griessen, *Growth-induced strong pinning sites in laser ablated $YBa_2Cu_3O_{7-\delta}$ films with a non-random distribution*
Journal of Low Temperature Physics **117**, 663-667 (1999)

F.C. Klaassen, G. Doornbos, J.M. Huijbregtse, B. Dam, and R. Griessen, *Critical current density and dynamical relaxation rate below the matching field in thin films of $YBa_2Cu_3O_{7-\delta}$*
Journal of Low Temperature Physics **117**, 1549-1553 (1999)

J.M. Huijbregtse, B. Dam, R.C.F. van der Geest, F.C. Klaassen, R. Elberse, J.H. Rector, and R. Griessen, *Natural strong pinning sites in laser ablated $YBa_2Cu_3O_{7-\delta}$ films*
Physical Review B **62**, 1338-1349 (2000)

I.A. Khrebtov, B. Dam, A.D. Tkachenko, F.C. Klaassen, J.M. Huijbregtse, and K.V. Ivanov, *YBCO films on $SrTiO_3$ substrates with recordly low 1/f noise for bolometer applications*, in:
Proceedings of the 4th European Workshop on Low Temperature Electronics - Wolte 4, 335-339 (2000)

I.A. Khrebtov, A.D. Tkachenko, K.V. Ivanov, B. Dam, F.C. Klaassen, and J.M. Huijbregtse, *The noise characteristics of YBCO films with strong pinning*
Technical Physics Letters **26**, 1078-1080 (2000)

F.C. Klaassen, G. Doornbos, J.M. Huijbregtse, B. Dam, and R. Griessen, *Vortex pinning regimes in thin films of $YBa_2Cu_3O_{7-\delta}$*
Physica C **341-348**, 1463-1464 (2000)

J.M. Huijbregtse, B. Dam, F.C. Klaassen, J.H. Rector, and R. Griessen, *$YBa_2Cu_3O_{7-\delta}$ films with self-organized natural linear defects*
Physica C **341-348**, 1985-1986 (2000)

B. Dam, J.M. Huijbregtse, R.C.F. van der Geest, F.C. Klaassen, J.M. Huijbregtse, and R. Griessen, *Natural strong pinning sites in laser ablated $YBa_2Cu_3O_{7-\delta}$ films*
Physica C **341-348**, 2327-2330 (2000)

A.V. Bobyl, I.A. Khrebtov, A.D. Tkachenko, K.V. Ivanov, B. Dam, F.C. Klaassen, and J.M. Huijbregtse, *Nature of sharp temperature dependency of normal phase flicker noise of epitaxial $YBa_2Cu_3O_{7-x}$ films*, in:
G. Bosman (ed.), *Noise in physical systems and 1/f fluctuations*, Proceedings of 16th

International Conference ICNF 2001
World Scientific Publishing Co. (2001)

I.A. Khrebtov, A.D. Tkachenko, K.V. Ivanov, B. Dam, F.C. Klaassen, and J.M. Huijbregtse, *Noise, transport and structural properties of high-T_c $YBa_2Cu_3O_{7-x}$ films with noise Hooge-parameter in normal state near to 10^{-6}*, in:
G. Bosman (ed.), *Noise in physical systems and 1/f fluctuations*, Proceedings of 16th
International Conference ICNF 2001
World Scientific Publishing Co. (2001)

M. Pannetier, F.C.Klaassen, R.J.Wijngaarden, M.Welling, K. Heeck, J.M.Huijbregtse, B.Dam, and R.Griessen, *Magneto-optical investigation of flux penetration in a superconducting ring*
Physical Review B **64**, 144505 1-7 (2001)

F.C. Klaassen, G. Doornbos, J.M. Huijbregtse, R.C.F. van der Geest, B. Dam, and R. Griessen, *Vortex pinning by natural linear defects in thin films of $YBa_2Cu_3O_{7-\delta}$*
Physical Review B **64**, 184523 1-20 (2001)

J.M. Huijbregtse, F.C. Klaassen, A. Szepielow, J.H. Rector, B. Dam, R. Griessen, B.J. Kooi, and J.Th.M. de Hosson, *Vortex pinning by natural defects in thin films of $YBa_2Cu_3O_{7-\delta}$*
Superconductor Science & Technology **15**, 1-10 (2002)

Curriculum Vitae

Frodo Klaassen werd op 8 januari 1973 geboren te 's-Hertogenbosch. Hij doorliep de middelbare school op het Dominicus College in Nijmegen, waar hij in 1991 zijn examen Gymnasium β haalde.

Van 1991 tot 1996 studeerde hij natuurkunde aan de Rijksuniversiteit Groningen. Tijdens zijn studie specialiseerde hij zich in de experimentele vaste stof fysica, onder andere via een stage aan het Ludwig Boltzmann Institut für Festkörperphysik in Wenen (oktober 1994 - januari 1995). Het afstudeeronderzoek, verricht in de groep van professor D. van der Marel, betrof een studie naar de mm-golf optische eigenschappen van dunne supergeleidende $DyBa_2Cu_3O_{7-\delta}$ films en naar ver-infrarood lasers.

Vanaf september 1996 was hij als onderzoeker in opleiding werkzaam in FOM-dienst aan de Vrije Universiteit, in de groep van professor R. Griessen. Hij onderzocht de pinning eigenschappen van dunne supergeleidende $YBa_2Cu_3O_{7-\delta}$ films in relatie tot de defect microstructuur. Dit proefschrift vormt het resultaat van zijn promotie-onderzoek.

Sinds januari 2002 werkt hij bij de Nuclear Research and consultancy Group (NRG) in Petten, waar hij onderzoek doet naar het verwerken van radio-actief afval.

Frodo Klaassen was born on the 8th of January 1973 in 's-Hertogenbosch. He attended high school at the Dominicus College in Nijmegen, where he passed his examination in 1991.

From 1991 to 1996 he studied physics at the Rijksuniversiteit Groningen. During his studies he specialized in experimental solid state physics. From October 1994 to January 1995 he did a short practise at the Ludwig Boltzmann Institut für Festkörperphysik in Vienna. His graduation project, conducted in the group of professor D. van der Marel, was an investigation concerning the mm-wave optical properties of thin superconducting $DyBa_2Cu_3O_{7-\delta}$ films and about far-infrared lasers.

From September 1996 he worked as a Ph.D.-student at the Vrije Universiteit, in the group of professor R. Griessen. He investigated the pinning properties of thin superconducting $YBa_2Cu_3O_{7-\delta}$ films in relation to the defect microstructure. This thesis forms the result of this research.

Since January 2002 he is working at the Nuclear Research and consultancy Group (NRG) in Petten, where his research focuses on the processing of radio-active waste.